UNIVERSITAT POLITÈCNICA DE CATALUNYA
BARCELONATECH

Escola Tècnica Superior d'Enginyers de Camins, Canals i Ports de Barcelona

Departament de Resistència de Materials i Estructures a l'Enginyeria

Finite element modeling of delamination in advanced composite beams and plates using one- and two-dimensional finite elements based on the refined zigzag theory

A thesis submitted for the degree of Doctor of Structural Analysis

by

Ariel Eijo

Barcelona - 2014

Advisor: Prof. Dr. Eugenio Oñate
Co-advisor: Prof. Dr. Sergio Oller

UNIVERSITAT POLITÈCNICA DE CATALUNYA
BARCELONATECH
Escola de Doctorat

Acta de calificación de tesis doctoral

Curso académico:

Nombre y apellidos

Programa de doctorado

Unidad estructural responsable del programa

Resolución del Tribunal

Reunido el Tribunal designado a tal efecto, el doctorando / la doctoranda expone el tema de la su tesis doctoral titulada_____

_____

Acabada la lectura y después de dar respuesta a las cuestiones formuladas por los miembros titulares del tribunal, éste otorga la calificación:

☐ NO APTO ☐ APROBADO ☐ NOTABLE ☐ SOBRESALIENTE

(Nombre, apellidos y firma) Presidente/a		(Nombre, apellidos y firma) Secretario/a
(Nombre, apellidos y firma) Vocal	(Nombre, apellidos y firma) Vocal	(Nombre, apellidos y firma) Vocal

_____, _____ de _____ de _____

El resultado del escrutinio de los votos emitidos por los miembros titulares del tribunal, efectuado por la Escuela de Doctorado, a instancia de la Comisión de Doctorado de la UPC, otorga la MENCIÓN CUM LAUDE:

☐ SÍ ☐ NO

(Nombre, apellidos y firma) Presidente de la Comisión Permanente de la Escuela de Doctorado	(Nombre, apellidos y firma) Secretaria de la Comisión Permanente de la Escuela de Doctorado

Barcelona a _____ de _____ de _____

Declaración inicial

De acuerdo con la Normativa Interna de la Escuela de Doctorado sobre *la elaboración y defensa de Tesis Doctorales como compendio de publicaciones*, esta tesis doctoral se presenta como un compendio de cuatro artículos de investigación publicados en diferentes revistas indexadas.

A continuación se detallan las referencias de dichos artículos indicando el factor de impacto (IF) de cada revista.

- Oñate, E., Eijo, A., and Oller, S. Simple and accurate two-noded beam element for composite laminated beams using a refined zigzag theory. *Computer Methods in Applied Mechanics and Engineering* (IF: 2.617), 213–216: 362-382, 2012.
  DOI: http://dx.doi.org/10.1016/j.cma.2011.11.023.

- Eijo, A., Oñate, E., and Oller, S. A four-noded quadrilateral element for composite laminated plates/shells using the refined zigzag theory. *Int. J. Numer. Meth. Engng* (IF: 2.068), 95: 631-660, 2013.
  DOI: http://dx.doi.org/10.1002/nme.4503.

- Eijo, A., Oñate, E., and Oller, S. A numerical model of delamination in composite laminated beams using the LRZ beam element based on the refined zigzag theory. *Composite Structures* (IF: 2.231), 104: 270-280 2013.
  DOI: http://dx.doi.org/10.1016/j.compstruct.2013.04.035.

- Eijo, A., Oñate, E., and Oller, S. Delamination in laminated plates using the 4-noded quadrilateral QLRZ plate element based on the refined zigzag theory. *Composite Structures* (IF: 2.231), 108: 456–471, 2014.
  DOI: http://dx.doi.org/10.1016/j.compstruct.2013.09.052.

To my mother and my wife

Acknowledgments

It gives me pleasure to acknowledge to my supervisor Eugenio Oñate for giving me the opportunity to develop my thesis at the International Center for Numerical Methods in Engineering (CIMNE). I further want to thank him for guidance and scientific support, which considerably contributed to the success of my work.

My special acknowledgment to my second supervisor Sergio Oller who gave me continues support and advices through my thesis with patience and knowledge. It was a pleasure to work with his assistance.

I wish to express my sincere appreciation to Omar Faure for believing in me and giving me the confidence to start this doctoral journey. Furthermore, thanks for all his rewarding and helpful advices.

I am grateful to CIMNE, the Polytechnic University of Catalonia (UPC) and the Ministry of Education of Spain for their financial support which made this work possible.

My most sincere gratitude to all my colleges at CIMNE and the RMEE department of the UPC. Particularly many thanks to Enrique Ortega for his appreciated recommendations on the writing and edition of this document.

Special thanks to my mother Mari for her numerous sacrifices. She always tried to make everything possible and impossible to build a better future for me. This led me to be the person I am now.

Above all I would like to thank my wife Ana for her love and constant support during these hard years. But most of all, thank you for being my “compañera de la vida”.

Abstract

Although laminated materials have been used for decades, their employment has increased nowadays in the last years as a result of the gained confidence of the industry on these materials. This has provided the scientific community many reasons to dedicate considerable amount of time and efforts to address a better understanding of their mechanical behavior. With this objective both, experimental and numerical simulation have been working together to give response to a variety of problems related with these materials.

Regarding numerical simulation, a correct modeling of the kinematics of laminated materials is essential to capture the real behavior of the structure. Moreover, once the kinematics of the structure has been accurately predicted other non-linear phenomena such as damage and/or plasticity process could be also studied.

In consequence, in order to contribute to the constant development of simpler and more efficient numerical tools to model laminated materials, a numerical method for modeling mode II/III delamination in advanced composite materials using one- and two-dimensional finite elements is proposed in this work. In addition, two finite elements base on a zigzag theory for simulating highly heterogeneous multilayered beams and plates structures are developed here.

The document is written based on results of four papers published in indexed journals. Copies of all these papers are included in Appendix. The main body of this thesis is constituted by Chapters 2 to 4. Chapter 2 deals with the numerical treatment of laminated beams and plates. Chapter 3 presents the formulation of the LRZ beam and the QLRZ plate finite elements based on the Refined Zigzag Theory. Finally, the main contribution of this thesis, the LRZ/QLRZ delamination model, is developed in Chapter 4.

Resumen

Aunque los materiales laminados se han utilizado durante décadas, su uso ha aumentado en los últimos años como resultado de una mayor confianza por parte de la industria. Esto ha proporcionado a la comunidad científica muchas razones para dedicar una considerable cantidad de tiempo y esfuerzos en aras de una mejor comprensión de su comportamiento mecánico. Con este objetivo tanto la simulación experimental como numérica han estado trabajando juntos para dar respuesta a una variedad de problemas relacionados con estos materiales.

En cuanto a la simulación numérica, un correcto modelado de la cinemática de los materiales laminados es esencial para capturar el comportamiento real de la estructura. Por otra parte, una vez que la cinemática de la estructura se ha predicho con precisión otros fenómenos no lineales como los proceso de daño y/o plasticidad podrían ser también estudiados.

En consecuencia, con el fin de contribuir al constante desarrollo de herramientas numéricas más simples y eficaces para modelar materiales laminados, un método numérico para el modelado de la delaminación (modo II/III) en materiales compuestos avanzados utilizando elementos finitos de una y dos dimensiones es propuesto en este trabajo. Además, dos elementos finitos para la simulación de vigas y placas de varias capas altamente heterogéneos son desarrollados aquí.

El documento está escrito en base a los resultados de cuatro artículos publicados en revistas indexadas. Copias de estos artículos se incluyen en el Apéndice. El cuerpo principal de esta tesis está constituido por los Capítulos 2-4. El Capítulo 2 aborda el tratamiento numérico de vigas y placas laminadas. El capítulo 3 presenta la formulación de los elementos finitos de viga LRZ y placa QLRZ basados en la Teoría Zigzag Refinada. Finalmente, la principal contribución de esta tesis, el modelo de delaminación LRZ/QLRZ, se desarrolla en el capítulo 4.

Contents

1 Introduction

A laminated material is an orderly stacking of a finite number of relatively thin layers perfectly linked together, designed for achieving, among other properties, improved strength, stability, energy absorption and resistance to fatigue and correction. Nowadays, the varieties of materials to be combined available on the market and the different techniques of manufacturing made their design extremely customizable according to the needs, which is the key attribute.

Laminated or multilayered materials have a multitude of applications in a diversity of sectors. Aviation, astronautics, automotive, marine, civil engineering, sports equipment, musical instruments and information technology are a sample of them. Laminated materials are present in our daily life. For example, the modern windshields (Figure 1.1a), which generally consist of a sandwich of glass sheets with a plastic layer between them. Ballistic glasses (Figure 1.1b) are a special multilayered material, which are usually constructed by an alternation of plastic sheets and hard and soft glass layers that make the laminate stronger and more elastic. A very important laminated material in the electronic industry is the Printed Circuit Board (PCB) (Figure 1.2), which is a stacking of prepregs and copper layers. Laminated wood beams are also a multilayered material commonly used in civil engineering. These are constructed by stacking up wood plies bonded by adhesives. A special case of multilayered laminates are the sandwich-structured materials, which consist of two thin but stiff skins and a lightweight but thick core between them (Figure 1.3). One of the most interesting multilayered materials are the advanced composites (Figure 1.4). These are widely employed in many high-performance applications where conventional materials cannot be used. Each layer of these laminates consists of a composite material known as fiber-reinforced polymer (FRP), which is made of continuous fibers surrounded by a polymeric matrix.

a) b)

Figure 1.1 – Modern windshields for automobiles (a) (From: http://www.titanmotorsports.com) and ballistic glasses for windshields (b) (From: http://www.miller-holzwarthinc.com/).

Figure 1.2 – Printed circuit board. From: http://www.clarydon.com/.

a) b) c)

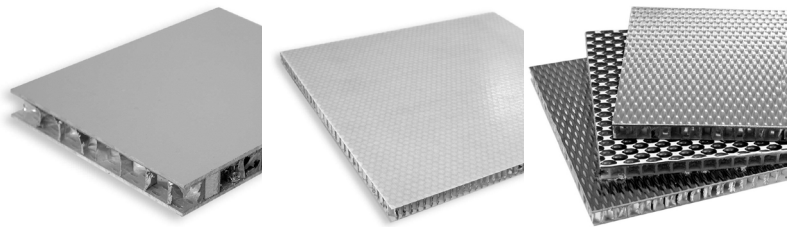

Figure 1.3 – Sandwich laminated formed by an aluminium honeycomb as core with skins of aluminium (a), fiber-glass composites (b) and fiber-carbon composites (c). From: http://www.cel.eu/.

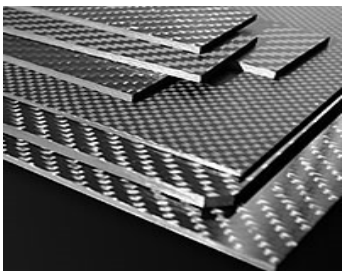

Figure 1.4 – Advanced composites of carbon fibers (CFRP). From: http://www.zero-carbon.com.

Although laminated materials have been used for decades, their employment has increased nowadays in the last years as a result of the gained confidence of the industry

on these materials. This has provided the scientific community many reasons to dedicate considerable amount of time and efforts to address a better understanding of their mechanical behavior. With this objective both, experimental and numerical simulation have been working together to give response to a variety of problems related with these materials.

Regarding numerical simulation, the subject covered in this work, a correct modeling of the kinematics of laminated materials is essential to capture the real behavior of the structure. Moreover, once the kinematics has been accurately predicted other phenomena such as damage process could be also studied.

In order to correctly predict the kinematics of complex structures, 3D finite elements analysis can be the best alternative. However, the simulation of large multilayered structures with many plies can be unaffordable with 3D analyses because of the excessive computational cost, especially when non-linear studies are required. In addition, the discretization of very thin layers can lead to highly distorted elements carrying numerical issues.

These difficulties made the simpler models [1, 2], such as the Equivalent Single Layer (ESL) or the Layer-Wise (LW), a proper alternative to model multilayered laminates. In ESL theories governing equations are written for the whole plate, which leads to a constant number of variables through the thickness. This characteristic makes ESL models very efficient. However, they suffer from limitations to correctly simulate the kinematics of highly heterogeneous laminates.

Unlike ESL theories, LW models define each layer as an independent laminate which implies that the number of variables dependent on the number of analysis layers. Although LW theories accurately describe the behavior of multilayered laminates with independence of the level of transverse heterogeneity, they may result unattractive for simulating large laminated structures with many plies.

A good compromise between the accuracy of LW models and the computational efficiency of ESL models are the Zigzag theories (ZZT). ZZT models are a special case of LW models where the number of unknowns is independent of the number of analysis layer.

Among many other, the Refined Zigzag Theory (RZT) developed by Tessler et al. [3, 4] is a simple, efficient and robust ZZT theory to be considered for developing numerical tools able to simulate multilayered laminated materials.

According to the fracture process of advanced composites materials, different failure mechanisms can occur. These can be grouped into intra- and inter-laminar fracture modes, depending where the failure occurs: within or between the layers. The fiber fracture, the matrix cracking and the fiber-matrix shear failure (debonding) are

distinguished as intra-laminar failure modes since they occur within the layer. Delamination, i.e. the relative displacement between neighboring layers, is a common inter-laminar failure mode that once it has been occurred the load carrying capacity of the composite member could be considerately reduced. Furthermore, this phenomenon may take place suddenly without any notice. These characteristics made delamination a really dangerous failure mechanism in advanced composite materials.

During the design phases of composite laminates, may be important to know how the global response of the structure is affected by delamination. For this purpose, the numerical simulation results very helpful.

Numerical techniques based on the linear elastic fracture mechanics (LEFM), the cohesive zone models (CZM) or the continuum damage mechanics (CDM) are usually applied for simulating delamination in a variety of engineering problems. Some applications examples are the skin-stiffness debonding [5] (CZM), the ply drop-off test [6] (CDM), the skin-core delamination and sub-laminate buckling [7] (LEFM) and the delamination in low-energy impact [8] (CZM). In these problems, the structures are discretized by means of 3D finite elements [6], by a combination between 3D elements and interface elements [8] or by employing shell elements and interface elements [5]. Although a detailed discretization of the structure is needed to accurately capture mix-mode delamination process in complex studies, simpler structural discretization may be enough for simulating delamination in cases where the opening mode (mode I) could be neglected. For instance, such case is found in low energy impact analyses, where fracture mode I appears usually after the shear modes (mode II and mode III) when the impact energy is considerably increased [8]. Thus, numerical methods based on a simpler discretization can be an acceptable approximation for modeling cases where delamination process is governed by the shear modes.

1.1 Objectives

This research aims at contributing to the development of simpler and more efficient numerical tools for simulating laminated materials.

Thus, this thesis is focused on two topics: the modeling of the kinematics of multilayered beam and plate structures (i) and the simulation of delamination in advanced composite materials (ii). At point (i), robust, efficient and effective finite elements are looked for. Regarding to point (ii), a simple delamination model that only uses reduced model to discretize the laminate is desired.

The main goals of this thesis are:

- The development of a numerical method based on one- and two-dimensional finite elements for simulating delamination processes (mode II and mode III) in beams and plates of advanced composite materials.

- The development of one- and two-dimensional finite elements based on the RZT theory in order to simulate the lineal behavior of highly heterogeneous multilayered beams and plates.

1.2 Organization

In order to achieve the objectives listed above, this work is structured as follows:

- Chapter 2 deals with the numerical treatment of laminated beams and plates. A review of more common reduced models employed to simulate multilayered beam/plate structures is presented first. Then, a complete description of the RZT plate theory used for developing the beam (LRZ) and plate (QLRZ) finite elements is given. Furthermore, the influence on the zigzag in-plane displacement of both, the transverse anisotropy and the span-to-thickness ratio is analyzed. In the second part of the Chapter, the failure mechanisms in advanced composite materials are dealt. In particular, special attention is given to the delamination process. Moreover, the most common numerical methods to model the failure mechanisms are presented.

- Chapter 3 presents the formulation of the LRZ beam and the QLRZ plate finite elements. The performance of these elements is studied through several numerical examples. Verification and convergence analyses are also performed. Furthermore, the problem of shear locking and the techniques employed to overcome it are addressed.

- Chapter 4 proposes the numerical model based on the LRZ and QLRZ finite element to model delamination process in advanced composite materials. A description about the isotropic damage model used for managing the onset and growth of delamination is also given. In addition, the modified Newton-Raphson scheme and the implicit integration algorithm used for solving the non-linear problem are presented. The performance of the method is analyzed by different numerical examples.

The potential of this method to simulate multi-delamination is also investigated. Moreover, the limitations of the model due to the LRZ/QLRZ kinematics are also studied.

- Chapter 5 summarizes the main achievements of this work and gives some aspects which deserve future attention.

- Appendix includes copies of all four papers on which this document is based.

2 Numerical treatment of laminated beam/plate structures

In the first part of this Chapter, a review of reduced models for modeling multilayered beams and plates is presented. Furthermore, the Refined Zigzag Plate Theory (RZT) proposed by Tessler et al. [4] is fully described. Then, the influence on the zigzag in-plane displacement of the material transverse anisotropy and the laminate span-to-thickness ratio is studied.

The second part is focused on advanced composite materials and their failure mechanisms. In particular, special attention is given to the inter-laminar damage or delamination. Moreover, usual damage models to simulate intra- and inter-laminar failure modes are treated.

2.1 Multilayered beam/plate theories

The most precise technique for simulating laminated structures are the micro-models, where 3D finite elements are used for discretizing not only each ply but also the constituents within layer or even the interface between them. Although macroscopic approach at layer level could be considered, i.e. the constituents are not discretized, simulation of large laminated structures with many of plies can be unaffordable with 3D analyses due to the excessive computational cost, especially for non-linear analyses. In addition, the discretization of very thin layers can lead to highly distorted elements carrying numerical issues.

Multi-scale approaches [9, 10] can be also used to model multilayered materials. In this method a macroscopic model is used to obtain the global response of the structure whereas the material behavior is solved with a microscopic model. Basically, the macro-model transfers the structural deformation field onto the micro-model as boundary conditions. Then, within the micro-scale, the material response is evaluated and transferred back to the macroscopic model as a constitutive law. Subsequently the

structural equilibrium is found in the macro-scale and a new deformation field is computed and so forth. The simulation of large structures having complex geometries by means of this method results computationally unattractive.

Thus, simpler and more efficient techniques than that above-mentioned are required for modeling laminated structures. 3D descriptions can be reduced to 2D models by introducing hypotheses on the displacements or/and on the stresses field, since laminate thickness is at least one order of magnitude lower than in-plane dimensions.

However, in order to develop precise reduced models, the through-thickness discontinuity of mechanical properties within a laminated material has to be accounted for. From a qualitative point of view, the influence of the transverse anisotropy on the thickness distribution of the displacement and stress fields is schematized in Figure 2.1.

The in-plane displacement, outlined in Figure 2.1a, could exhibit abrupt changes of their slope along the thickness direction at each interface because large differences on the transverse shear properties between layers exist. This slope change leads to an in-plane displacement with zigzag pattern whose amplitude and shape depend not only on the transverse anisotropy but also on the laminate span-to-thickness ratio, as discussed in Section 2.1.4. Furthermore, all displacements are continuous along the thickness.

Although in-plane stresses can be discontinuous at each interface (Figure 2.1b), transverse stresses must be continuous for equilibrium reasons (Figure 2.1c). However, like in-plane displacement, the first derivatives along z are discontinuous at each interface.

As a result, it is desirable that multilayered models satisfy the following two conditions: zigzag pattern of in-plane displacements (ZZ condition) and the continuity of transverse stresses along the thickness direction (TC condition) [11].

Many 2D approaches have been developed and improved since 19th century [12]. In order to facilitate their classification, they could be distinguished according what type of unknown variables is chosen (i) and how these variables are described (ii). At point (i), displacements are defined as variable in the so-called "displacement-based theories" (DB) whereas stresses are employed in "stress-based theories" (SB). In case of both, the displacement and the stress are considered as unknown, a "mixed[1] approach" (MB) is obtained. Regarding to point (ii), unknowns could be described by means of Equivalent Single Layer (ESL) or Layer-Wise (LW) descriptions.

[1] Mixed approaches can be distinguished between full or partial models. In full mixed approaches all stresses are considered as variable whereas in partial mixed approach only the transverse shear stresses are accounted for.

In ESL description, governing equations are written for the whole plate, i.e. unknown variables are not defined for each layer but for the whole laminate. Thus, the number of variables is independent of the number of analysis layers.

On the contrary, each layer is treated as an independent plate in LW description, assuming separate displacement/stress field within each ply. In other words, governing equations are written for each layer. Moreover, in order to enforce compatibility conditions at the interface between layers, interface constraints on displacements and transverse stresses are required. Hence, the number of variables is dependent on the number of analysis layers.

A special case of LW models where the number of unknowns is independent of the number of analysis layer are the Zigzag theory (ZZT).

Useful overviews of available theories for modeling laminated plate structures have been written by Carrera [1] and Reddy [2].

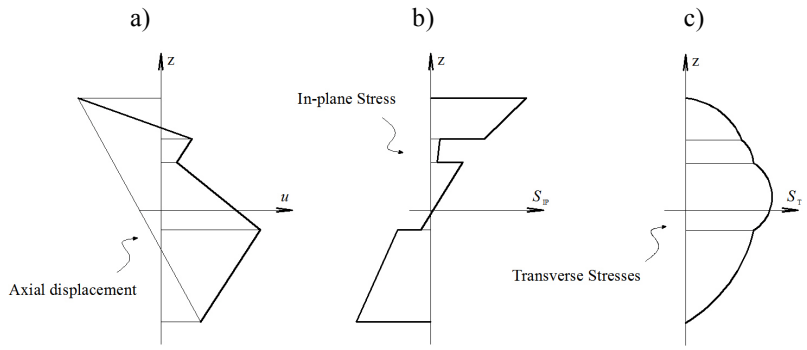

Figure 2.1 – Continuous zigzag in-plane displacement a), discontinuous in-plane stresses b), and continuous transverse stresses c).

2.1.1 Equivalent Single Layer models

Displacement-based models with ESL description (DB-ESL) have been widely developed for decades. An interesting review of DB-ESL models has been written by Wanji et al. [13].

The most basic DB-ESL model is the Classical theory (CT) [12, 14], which propose that transversal sections remain plane and normal to the reference surface after deformation, i.e. transverse shear strains are postulated to be negligible with respect to other strains. Because of these assumptions, the CT theory is limited to thin beams/plates where transverse shear effects can be neglected. In addition, this model despises the transverse normal deformation. The CT plate theory has only 5 unknown variables. Classical beam and plate models are also known as Euler-Bernoulli and Kirchhoff theories, respectively.

An improvement of the CT model are the First Order Shear Deformation theory (FSDT) [15-17], which enhance the CT kinematics by adding shear effects. This model establishes that transversal sections remain plane but not necessarily normal to the axis after deformation. Therefore, the transverse shear strain is defined constant through the thickness but not zero as in the CT theory. Like the CT model, strain along the thickness is not accounted for. Also, the plate FSDT contains only 5 unknown variables. However, in order to accurately compute transverse shear stresses, a shear correction factor[2] is required. FSDT beam and plate models are also known as Timoshenko and Reissner-Mindlin theories, respectively.

Although CT and FSDT theories are excellent alternatives to accurately model homogenous thin and thick structures, respectively, they gives poor predictions when applied to laminated structures having high level of transverse anisotropy. The cause is found in the linear thickness distribution of the axial displacement, which does not match the ZZ pattern schematized in Figure 2.1a.

FSDT theory can be improved by adding high-order terms of thickness coordinate z to the in-plane and transverse displacement fields. These improvements are known as High Order Shear Deformation theories (HSDTs).

One of first HSDTs model, where only the in-plane displacements are improved by a third-order polynomial, has been proposed by Reddy [18]. This model proposes a constant distribution of the transverse displacement.

Usually, both, the in-plane and the transverse displacement fields are defined by means of third-order polynomials [19]. However, it is also possible to find HSDTs models where fifth- and ninth-order polynomials are employed to describe the displacement field [20].

One advantage of HSDTs theories is that no shear correction factor is needed. Furthermore, those HSDTs models where a high-order description of the transverse displacement is used allow obtaining better through-thickness distribution of the transverse stresses.

With the aim to accurately satisfy the continuity of the transverse stresses along the thickness, mixed formulations should be employed.

For instance, Auricchio et al. [21] have proposed a partially mixed-based ESL model (MB-ESL) where the transverse shear stresses are a priori defined by means of the equilibrium equations assuming piecewise quadratic functions. Furthermore, the displacement field is described by the FSTD kinematics. Although the thickness

[2] This factor is equal to 5/6 for homogeneous rectangular transversal sections.

distribution of transverse shear stresses is well predicted, the axial displacement does not match the ZZ form because of the linear FSTD kinematic.

Another way to achieve through-thickness continuity of the transverse stresses is by integrating a posteriori of the equilibrium equations[3]. However, the accuracy of this method depends on how precise the displacement field is modeled. A comprehensive analysis of the available techniques for computing transverse stresses in multilayered plates has been presented by Carrera [22].

Summarizing, although the TC condition could be satisfied by some ESL models, any of them is able to capture the zigzag shape of in-plane displacements.

2.1.2 Layer-Wise models

A LW description of the in-plane displacement is an accurate alternative to fulfill the ZZ condition. Displacement-based LW models (DB-LW) employs ESL theories, such as the CT, FSDT and HSDTs, to describe the displacement field of each layer.

Some DB-ESL and DB-LW models have been evaluated and compared by Reddy and Robbins [23].

Although the ZZ condition is satisfied by DB-LW models the TC condition is not fulfilled unless appropriate interface constraints are considered. For example, Robbins and Reddy [24] have improved a DB-LW theory by assuming a piecewise continuous distribution of the transverse strain, which allows to compute the inter-laminar continuity of transverse stresses.

Models that accurately fulfill the ZZ and TC conditions are those in which both, the displacement and the stress field are described by means of LW description. These models are known as mixed-based LW models (MB-LW).

Among many works related with MB-LW theories, readers are referred to Carrera's papers [25, 26] to go deeper on these models.

Although LW theories accurately fulfill both, the ZZ and the TC condition, the number of unknown variables is proportional to the number of analysis layers. As a result, these models yield not only a high level of accuracy but also an amount of unknown variables similar to the 3D analysis. For this reason, LW models may result unattractive for simulating large laminated structures with many plies. Therefore, these models should be employed to analyze complex problems where other less expensive approaches fail to give realistic predictions.

[3] The equilibrium equations for computing "a posteriori" the transverse shear stresses are defined by $\mathrm{div}[\boldsymbol{\sigma}] = 0$, where $\boldsymbol{\sigma}$ is the stresses tensor.

2.1.3 Zigzag models

A good compromise between the accuracy of MB-LW theories and the computational efficiency of DB-ESL models are the ZZT theories. One of the most important advantages of these theories is that the number of kinematics unknowns is independent of the number of analysis layers.

In ZZT models the in-plane displacement is defined by a superposition of a piecewise continuous function, called zigzag function henceforth, over a linear, quadratic, cubic or even higher order displacement field. The zigzag functions allow these models to reproduce the abrupt change in the slope of the in-plane displacement at each interface, as shown in Figure 2.1a. Moreover, in order to fulfill the TC condition and to reduce the number of unknown variables, constraint equations at the interface between layers must be enforced.

One of first attempt to refine an ESL model by means a zigzag function has proposed by Murakami [27]. In this model, the FSDT kinematics is enhanced by adding a piecewise linear zigzag function. It is important to remark that the slope of the Murakami's zigzag function is defined positive for odd layers and negative for even plies, which implies that the shape of this function depends on the stacking sequence of the laminate only. Then, Murakami et al. [28] have also proposed an improvement of a high-order ESL theory.

It should be mentioned that approaches where the displacement field is improved by means of the Murakami's zigzag function are unable to a priori satisfy the TC condition.

In order to provide the through-thickness continuity of the transverse shear stress, Carrera [29] has developed a refined FSDT plate model based on Murakami's concepts [27]. In Carrera's model the TC condition is fulfilled a priori by assuming a piecewise quadratic function and a set of equilibrium conditions at each interface.

Demasi [30] has investigated the numerical performance of Murakami's zigzag function by means of FEM analysis.

At around the same period Murakami was developing his refined FSDT model [27], Di Sciuva [31] was working in his ZZT model. He proposed a refinement of the FSDT theory by adding a linear zigzag function also. However, the transverse shear strain is defined as a kinematic variable instead of a bending rotation as in the FSDT model. Moreover, in order to compute the zigzag function, constant shear stresses along the thickness are enforced, which is a very strict constraint for simulating multilayered materials.

Furthermore, Di Sciuva [32] and Cho et al. [33] have independently provided a refinement of a third-order ESL models by adding a linear zigzag function.

Many ZZT theories, including those mentioned above, require C^1-continuity when solved via finite element analysis, which implies a disadvantage versus simpler C^0-continuity theories, such as the FSDT model.

In order to overcome this drawback, Averill [34] formulated a refined linear zigzag theory where the FSDT model is used as its baseline. Then, the FSTD kinematics variables, i.e. the deflection, the axial displacements and the bending rotation, are considered as unknowns together with a kinematics variable associated with the zigzag function. All these variables can be interpolated with C^0-continuious polynomials. Moreover, the through-thickness continuity of the transverse shear stress is enforced using a penalty method. A cubic zigzag model was also provided by Averill et al. [35]. Although C^0-continuity is achieved, Averill's theories suffer from their inability to model correctly clamped boundary conditions.

With the goal to avoid these shortcomings and propose an amiable theory to formulate robust C^0-continuity finite element, Tessler et al. [3, 4, 36, 37] have developed the Refined ZigZag Theory (RZT). The plate[4] RZT theory proposed by Tessler et al. [36] is described below in next section.

The RZT displacement field is defined by a superposition of a linear zigzag function over the FSDT kinematics. In these models, constraint conditions on the distribution of the zigzag functions are imposed, which leads to a constant piecewise distribution of transverse shear stress along the thickness. However, the TC condition of transverse shear stresses could be computed a posterior by using equilibrium equations [38, 39]. This post-process gives accurate results because the zigzag in-plane displacements are correctly predicted. On the other hand, transverse normal strain is despised. The RZT kinematics variables are the displacements and the bending rotations of the FSDT theory together with a variable associated with the zigzag function. The key attributes of the RZT are, first, the zigzag function vanishes at the top and bottom surfaces of the laminate section. Second, it does not require full transverse shear stress continuity across the thickness coordinates. Third, in order to formulate finite elements, C^0 continuous polynomials are needed for discretizing the kinematic variables. Fourth, all boundary conditions can be effectively simulated. Finally, the zigzag function is defined as a function of the transverse shear modulus of each layer, which results useful in non-linear material analysis [40, 41].

The simplicity, efficiency and effectiveness of the RZT theory allowed develop in this thesis two robust C^0 continuous finite elements for simulating multilayered beams

[4] The beam RZT displacement field is easy obtained from the plate RZT theory by neglecting the in-plane transverse displacement *v*.

[38] and plates [39]. The formulation of these elements is presented in Chapter 3. Simultaneously, Gherlone et al. [42] and Versino et al. [43] have also formulated beam and plate finite elements based on the RZT theory.

Recently, Barut et al. [44] have extended the RZT plate theory [4] for taking into consideration the transverse normal strain. In this model, the in-plane displacement consist of a piecewise quadratic function, whereas a quadratic polynomial is used for describing the transverse displacement component. Based on this extended RZT model, Barut et al. [45] have formulated a C^0 continuous triangular plate element.

2.1.3.1 Refined zigzag theory (RZT)

Let us consider a laminated plate of uniform thickness h formed by N orthotropic layers of thickness h^k (k = 1, 2, … , N). The orthogonal Cartesian coordinates system (x,y,z) is employed as reference coordinates. The ordered pair (x,y) is set as the in-plane coordinates whereas z denotes the thickness coordinate which ranges from $-h/2$ and $+h/2$. The in-plane reference surface is placed at the middle plane for z = 0.0.

The displacement field in the RZT plate theory is written as

$$\begin{aligned} u^k(x,y,z) &= u_0(x,y) - z\cdot\theta_x(x,y) + \overline{u}^k(x,y,z) \\ v^k(x,y,z) &= v_0(x,y) - z\cdot\theta_y(x,y) + \overline{v}^k(x,y,z) \\ w\,(x,y) &= w_0(x,y) \end{aligned} \qquad 2.1$$

where the axial displacement zigzag function $\overline{u}^k$ and $\overline{v}^k$ are defined as

$$\begin{aligned} \overline{u}^k &= \phi_x^k(z)\cdot\psi_x(x,y) \\ \overline{v}^k &= \phi_y^k(z)\cdot\psi_y(x,y) \end{aligned} \qquad 2.2$$

and superscript k indicates quantities within the kth layer. The uniform axial displacements along the coordinate directions x and y are denoted by u_0 and v_0, respectively; θ_x and θ_y represent the average bending rotation of the transverse normal about the negative y and positive x directions; and w_0 is the uniform transverse deflection. $\phi_i^k\ (i = x, y)$ denote the known piecewise linear *zigzag function*, and ψ_i is a primary kinematics variable defining the amplitude of the zigzag function. Summarizing, the unknown variables are

$$\mathbf{a} = \begin{bmatrix} u_0 & v_0 & w_0 & \theta_x & \theta_y & \psi_x & \psi_y \end{bmatrix}^T \qquad 2.3$$

where the uniform displacement u_0, v_0 and w_0, and the bending rotation θ_x and θ_y are derivate from the FSDT theory, where the ψ_i variables are associated with the added displacement zigzag functions $\overline{u}^k$ and $\overline{v}^k$.

The in-plane (ε_p^k) and transverse shear (ε_t^k) strains are defined as

$$\boldsymbol{\varepsilon}_p^k = \begin{bmatrix} \varepsilon_x \\ \varepsilon_y \\ \gamma_{xy} \end{bmatrix}^k = \begin{bmatrix} \dfrac{\partial u_0}{\partial x} - z\dfrac{\partial \theta_x}{\partial x} + \phi_x^k(z)\dfrac{\partial \psi_x}{\partial x} \\ \dfrac{\partial v_0}{\partial y} - z\dfrac{\partial \theta_y}{\partial y} + \phi_y^k(z)\dfrac{\partial \psi_y}{\partial y} \\ \left(\dfrac{\partial u_0}{\partial y} + \dfrac{\partial v_0}{\partial x}\right) - z\left(\dfrac{\partial \theta_x}{\partial y} + \dfrac{\partial \theta_y}{\partial x}\right) + \left(\phi_x^k(z)\dfrac{\partial \psi_x}{\partial y} + \phi_y^k(z)\dfrac{\partial \psi_y}{\partial x}\right) \end{bmatrix} \quad 2.4$$

$$\boldsymbol{\varepsilon}_t^k = \begin{bmatrix} \gamma_{xz} \\ \gamma_{yz} \end{bmatrix}^k = \begin{bmatrix} \left(\partial w/\partial x - \theta_x\right) + \beta_x^k \psi_x \\ \left(\partial w/\partial y - \theta_y\right) + \beta_y^k \psi_y \end{bmatrix} = \begin{bmatrix} \gamma_{xz} + \beta_x^k \psi_x \\ \gamma_{yz} + \beta_y^k \psi_y \end{bmatrix} \quad 2.5$$

being γ_{iz}^k and β_i^k $\left(i = x, y\right)$, the transverse shear strain and the slope of ϕ_i^k in the thickness direction ($\beta_i^k = \partial \phi_i^k / \partial z$) for the kth layer, respectively. γ_{iz} represent the average transverse shear strains of the FSDT ($\gamma_{iz} = \partial w/\partial i - \theta_i$).

The stress-strain constitutive relationship for the kth orthotropic layer is written as

$$\begin{bmatrix} \sigma_x \\ \sigma_y \\ \underline{\tau_{xy}} \\ \tau_{xz} \\ \tau_{yz} \end{bmatrix}^k = \begin{bmatrix} D_{p11} & D_{p12} & D_{p13} & 0 & 0 \\ D_{p21} & D_{p22} & D_{p23} & 0 & 0 \\ D_{p31} & D_{p32} & D_{p33} & 0 & 0 \\ 0 & 0 & 0 & D_{t11} & D_{t12} \\ 0 & 0 & 0 & D_{t21} & D_{t22} \end{bmatrix}^k \begin{bmatrix} \varepsilon_x \\ \varepsilon_y \\ \underline{\gamma_{xy}} \\ \gamma_{xz} \\ \gamma_{yz} \end{bmatrix}^k \quad 2.6$$

or

$$\boldsymbol{\sigma}^k = \mathbf{D}^k \boldsymbol{\varepsilon}^k \quad 2.7$$

where $\mathbf{D}^k$ is the constitutive matrix referred to the reference coordinate system (x,y,z). Matrix $\mathbf{D}^k$ is computed by Eq.(3.50) in Section 3.3.3.

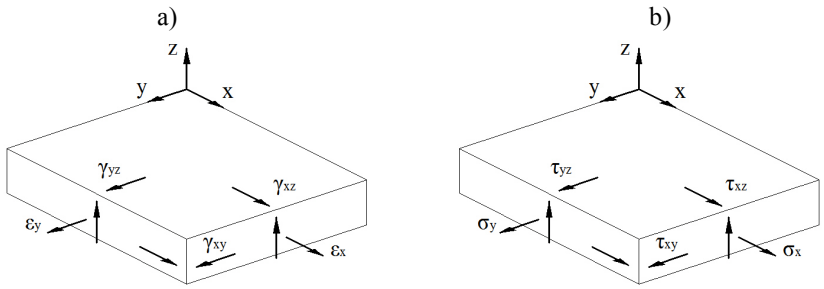

Figure 2.2 – Strain (a) and stress (b) field.

The zigzag functions ϕ_i^k are defined by piecewise linear continuous functions through the laminate thickness as

$$\phi_i^k = \frac{1}{2}(1-\xi)\bar{\phi}_i^{k-1} + \frac{1}{2}(1+\xi)\bar{\phi}_i^k = \frac{\bar{\phi}_i^k + \bar{\phi}_i^{k-1}}{2} + \frac{\bar{\phi}_i^k - \bar{\phi}_i^{k-1}}{2}\xi^k \qquad 2.8$$

where $\bar{\phi}_i^k$ and $\bar{\phi}_i^{k-1}$ are the zigzag function valued at k and $k-1$ interface, respectively, with $\bar{\phi}_i^0 = \bar{\phi}_i^N = 0$ and $\xi^k = 2\dfrac{\left(z - z^{k-1}\right)}{h^k} - 1$.

Figure 2.3 schematizes the zigzag function ϕ_x^k, the zigzag displacements $\bar{u}^k$, and the axial displacements u^k along x direction for a four-layered laminate. Similar distributions of these values are found for the y direction.

The computation of β_i^k is obtained by computing the derivative of ϕ_i^k (Eq.(2.8)) with respect to the z coordinate as

$$\beta_i^k = \frac{\partial \phi_i^k}{\partial z} = \frac{\left(\bar{\phi}_i^k - \bar{\phi}_i^{k-1}\right)}{h^k} \qquad 2.9$$

which result in piecewise constant functions.

The piecewise linear zigzag functions of Eq.(2.8) can be written as functions of β_i^k as

$$\phi_i^k = \bar{\phi}_i^{k-1} + \frac{h^k \beta_i^k}{2}\left(\zeta^k + 1\right) \qquad 2.10$$

Because the zigzag function vanishes on the top and bottom surfaces, the through-the-thickness integrals of the slope functions β_i^k is equal to zero, i.e.

$$\int_{-h/2}^{+h/2} \beta_i^k dz = \sum_{k=1}^{N} \int_{-h^k/2}^{+h^k/2} \left(\frac{\bar{\phi}_i^k - \bar{\phi}_i^{k-1}}{h^k} \right) dz = \sum_{k=1}^{N} \left(\bar{\phi}_i^k - \bar{\phi}_i^{k-1} \right) = \bar{\phi}_i^N - \bar{\phi}_i^{k-1} = 0 \quad 2.11$$

Integrating the layer transverse shear strains of Eq.(2.5) across the laminate thickness and using Eq.(2.11) reveals that

$$\gamma_{iz} = \frac{1}{h}\int_{-h/2}^{+h/2} \gamma_{iz}^{k} dz = \partial w / \partial_i - \theta_i \qquad 2.12$$

which verifies that γ_{iz} represent the average transverse shear strains of the FSDT. Moreover, Eq.(2.12) shows that the zigzag amplitude variables ψ_i do not contribute to γ_{iz}.

For convenience, a new difference function η_i is defined as

$$\eta_i = \gamma_{iz} - \psi_i \qquad 2.13$$

which leads to the following expression of the transverse shear strains for the kth layer as

$$\gamma_{iz}^{k} = \eta_i + \left(1 + \beta_i^k\right)\psi_i \qquad 2.14$$

Using Eqs.(2.14) and (2.6), the transverse shear stresses are written in matrix form as

$$\begin{bmatrix} \tau_{xz} \\ \tau_{yz} \end{bmatrix}^k = \begin{bmatrix} D_{t11} & D_{t12} \\ D_{t21} & D_{t22} \end{bmatrix}^k \left(\begin{bmatrix} \eta_x \\ \eta_y \end{bmatrix} + \begin{bmatrix} \left(1+\beta_x^k\right) & 0 \\ 0 & \left(1+\beta_y^k\right) \end{bmatrix} \begin{bmatrix} \psi_x \\ \psi_y \end{bmatrix} \right) \qquad 2.15$$

or, alternatively, they can be expressed as

$$\begin{bmatrix} \tau_{xz} \\ \tau_{yz} \end{bmatrix}^k = \begin{bmatrix} D_{t11} & D_{t12} \\ D_{t21} & D_{t22} \end{bmatrix}^k \begin{bmatrix} \eta_x \\ \eta_y \end{bmatrix} + \\ + \left\{ D_{t11}\left(1+\beta_x^k\right) \right\} \begin{bmatrix} \psi_x \\ \dfrac{D_{t21}}{D_{t11}}\psi_x \end{bmatrix} + \left\{ D_{t22}\left(1+\beta_y^k\right) \right\} \begin{bmatrix} \dfrac{D_{t12}}{D_{t22}}\psi_y \\ \psi_y \end{bmatrix} \qquad 2.16$$

In this equation, the first stress vector associated with η_i functions is independent of the zigzag functions. The second and third stress vectors contain the coefficients $\left\{ D_{t11}\left(1+\beta_x^k\right) \right\}$ and $\left\{ D_{t22}\left(1+\beta_y^k\right) \right\}$, which are dependent on the zigzag functions. In this theory, both coefficients are set to be constant quantities, denoted as G_{iz} $\left(i = x, y\right)$, whose constraint leads to constraint conditions on the distribution of the zigzag function. Thus, the continuity of the transverse shear stresses at each layer

interface, i.e. $\tau_{iz}^{k} = \tau_{iz}^{k+1}$, is not enforced. In addition, Eq.(2.16) revels that τ_{iz}^{k} is piecewise constant across the thickness.

The constraints give

$$\begin{bmatrix} \beta_x \\ \beta_y \end{bmatrix}^k = \begin{bmatrix} \dfrac{G_{xz}}{D_{t11}^k} - 1 \\ \dfrac{G_{yz}}{D_{t22}^k} - 1 \end{bmatrix} \qquad 2.17$$

where the explicit form of G_{iz} is obtained by substituting Eq.(2.17) in the integral of Eq.(2.11), i.e.

$$\begin{bmatrix} G_{xz} \\ G_{yz} \end{bmatrix} = \begin{bmatrix} h\left[\sum_{k=1}^{N} \dfrac{h^k}{D_{t11}^k}\right]^{-1} \\ h\left[\sum_{k=1}^{N} \dfrac{h^k}{D_{t22}^k}\right]^{-1} \end{bmatrix} \qquad 2.18$$

The coefficients G_{iz} are considered as an average transverse shear stiffness properties of the laminate referred to the reference coordinates system (x,y,z).

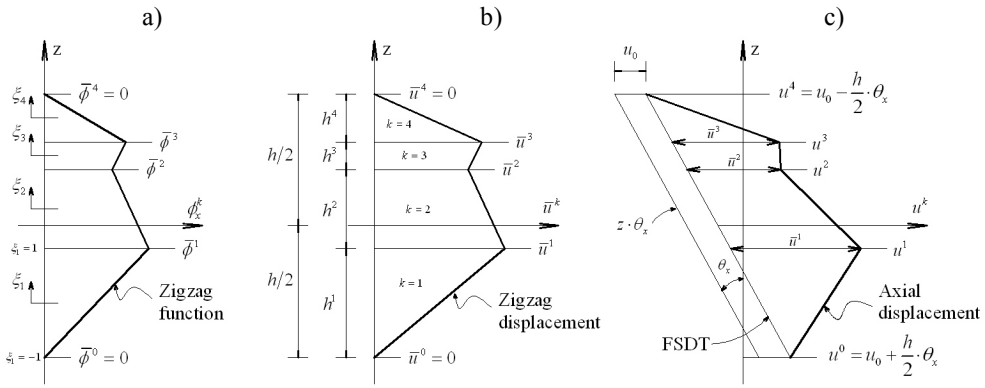

Figure 2.3 - Thickness distribution of the zigzag function ϕ_x^k a), zigzag displacement $\bar{u}^k$ b), and axial displacement u^k c) in the RZT theory.

2.1.4 Influence of the span-to-thickness ratio and the transverse heterogeneity on the zigzag pattern of the in-plane displacements

This section aims to analyze how the amplitud and shape of the zigzag in-plane displacement is afected by not only the through-thickness anisotropy of transverse shear stiffness but also the laminate span-to-thickness ratio.

In order to assess the objective, a clamped beam of thickness h = 1and span-to-thickness ratio λ = 5, 10, 20 and 50 is studied. The beam is submitted under a unitary vertical displacement Δw at the free end (Figure 2.4a). The laminated material is formed by three layers of thickness $h^k = h/3$ (k = 1,2,3) with symmetry distribution (Figure 2.4b). Four levels of transverse heterogeneity are performed defining different transverse shear modulus for the middle layer (G_M) (Table 2.1). Heterogeneity ranges from the "lowest" (H1) to the "highest" (H4) level for which the shear modulus of the middle layer is two to thousand times smaller than that of the top/bottom layers ($G_{T/B}$), respectively. All cases were solved via plane stress analysis.

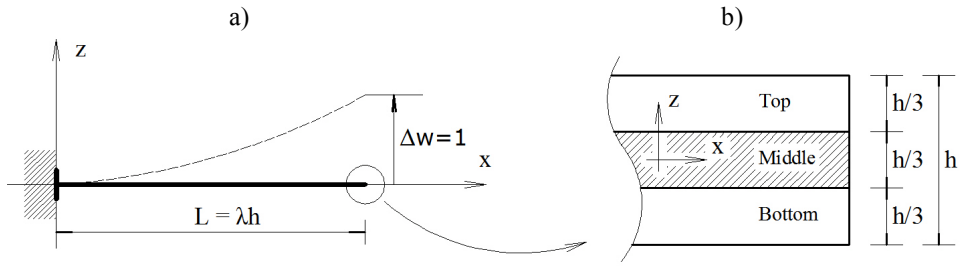

Figure 2.4 - Cantilever beam under vertical displacement a) and symmetric three-layered material b).

Transverse heterogeneities	
	$G_{T/B}$ / G_M
H1	2
H2	10
H3	100
H4	1000

Table 2.1 – Relation between the shear moduli of the top/bottom layer and the middle layer. The less and most heterogeneous configurations are the heterogeneity H1 and H4, respectively.

Figure 2.5 show the normalized axial displacement for all span-to-thickness ratios. Figure 2.5a shows that only a difference of ten times (H2) between the shear moduli is enough to obtain a zigzag distribution of the axial displacement for the less slender beam (λ = 5). On the contrary, a difference of thousand times (H4) gives a slight zigzag distribution for the most slender beam (λ = 50) (Figure 2.5c). Another interesting observation is that a difference of two orders of magnitude (H3) between the shear moduli provokes an almost linear distribution for the most slender beam and a slight zigzag pattern for the beam of λ = 20. Furthermore, a difference of one order of

magnitude (H2) gives a zigzag kinematics for the less slender beam only whereas the lowest heterogeneity (H1) provokes a linear distribution for all span-to-thickness ratios.

Therefore, the amplitude of the zigzag in-plane displacement is increased according the transverse anisotropy of the shear modulus is higher whereas it is reduced according the laminate is more slender.

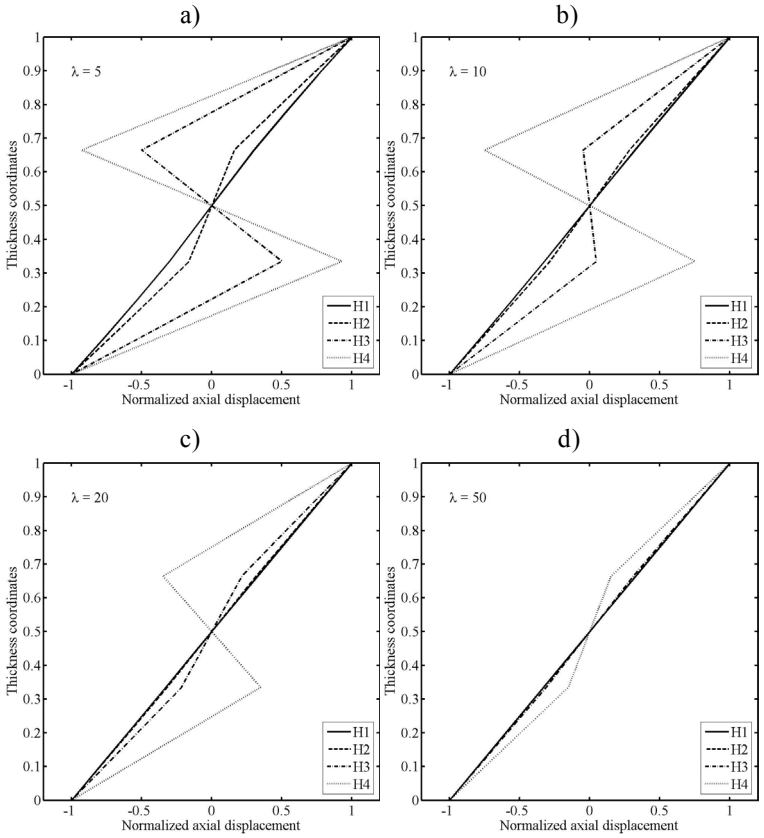

Figure 2.5 – Normalized axial displacement for span-to-thickness ratio $\lambda = 5$ a), $\lambda = 10$ b), $\lambda = 20$ c) and $\lambda = 50$ d).

2.2 Advanced composite materials and delamination phenomenon

Advanced composites laminates are a stacking of fiber reinforced plastic (FRP) layers. FRP plies are composed of continuous fibers embedded in a polymeric matrix. Although there is a large bandwidth of fiber materials, carbon are the most widely used for high-performance applications. In addition, there are a countless number of different carbon fibers, e.g. high strength, high stiffness, surface treated or non-surface-treated, etc., and polymeric matrixes, e.g. thermosetting, thermostable or thermoplastic. This wide variety of material leads to an almost infinite number of potential mixtures. Moreover, the chance to orient the fibers according an optimum distribution of strength

and stiffness provides a very customizable design. Furthermore, the use of very light and strong raw materials leads to lightweight laminates with a considerable high specific strength and stiffness[5]. Other well valued characteristics of these materials are the fatigue and corrosion resistance and the high energy absorption capacity.

These features made the advanced composites a good alternative for applications where the weight saving implies substantial cost reductions. Moreover, they are also the material of choice for structures under high strengths. Aviation and astronautics are some examples of application. The use of advanced composites in aeronautics has been considerable increased in last decades [46]. For example, about 25 and 50 percent of the airplanes Airbus A380 and Boing 787 Dreamliner are made of composite materials. In addition, composite materials represent about 80 percent of the structure weight in the construction of satellites. Automotive, marine, civil engineering, sport and medical industries are also interested in advanced composite materials.

In order to define the load carrying capacity of the structure, the study of material fracture process is a very important topic. Advanced composite laminate may suffer from different failure mechanisms. These can be grouped into intra- and inter-laminar fracture modes, depending where the failure occurs: within or between the layers. The fiber fracture[6], the matrix cracking[7] and the fiber-matrix shear failure[8] (debonding) are distinguished as intra-laminar failure modes since they occur within the layer. Delamination, i.e. the relative displacement between neighboring layers, is a common inter-laminar failure mode that once it has been occurred the load carrying capacity of the composite member could be considerately reduced. Moreover, this phenomenon may take place suddenly without any notice. These characteristics made the delamination a really dangerous failure mechanism in advanced composite materials.

Although all these failure modes have to be accounted for accurately simulating the fracture behavior of advanced composites materials, this thesis is focused on the numerical simulation of delamination only. However, for the sake of completeness, the modeling of intra-laminar fracture modes is also treated below.

---

[5] The specific strength is the strength per unit weight. It is also known as the strength/weight ratio. The same holds for specific stiffness.

[6] Fiber fracture can be provoked by not only tensile but also compressive stresses. Failure due to tensile stress occurs when the fiber strength is achieved. Longitudinal compressive stress can induce micro-buckling of fiber if the matrix is unable to hold the fibers in their position.

[7] When matrix strength is exceeded a crack is produced which tends to propagate perpendicularly to the stress direction until the fiber. If fiber strength is enough strong the crack can be stopped, otherwise, the discontinuity will be continue causing fiber fracture. Furthermore, fracture can grow parallel to the fiber at the fiber-matrix interface, i.e. debonding.

[8] Debonding occurs when fibers are disjointed from the matrix due to the fiber-matrix interface is unable to support the shear stresses acting parallel to the fibers.

2.2.1 Modeling of intra-laminar fracture modes

In order to simulate intra-laminar fracture modes, intra-laminar damage models or also called failure models can be employed. These models consist of failure criteria, which evaluate if stress leads to the failure, and degradation models, which manage the material degradation.

A simple and well known failure criterion is the maximum stress/strain criterion, which is computed by comparing the uni-axial stresses/strains with their threshold value for each component. Despite its simplicity, no interaction of stresses is taken into account.

Failure criteria that consider interactions between stresses can be subdivided into two classes, namely the global criteria, which use only one equation for all failure modes, and the physically-based criteria, which employ different criteria for different failure modes.

One of first attempts to develop a global criterion was presented by Hill [47], who proposed a single formula that take into account different strengths in various principal directions. Another very interesting global criterion has been proposed by Tsai and Wu [48], where a strength-based second order polynomial is proposed for all intra-laminar failures modes.

Among hundreds of physically-based criteria, a well-known damage criterion and widely used by commercial finite element codes is the Hashin's failure criterion [49]. This damage model is able to model fiber fracture and matrix cracking under tensile and compressive stress state. An improvement of the Hashin's model was proposed by Goyal et al. [50] where fiber-matrix shear failure is also considered. Goyal's model is also known as the extended Hashin's model. Based on Hashin's ideas, Puck [51] proposed a failure criterion where three different types of matrix cracking are considered. Dávila et al. [52] have developed a damage model, denoted LaRC03, that consists of six phenomenological failure criteria which can predict matrix and fiber failures without curve-fitting parameters. An improvement of the LaRC03 failure criteria, denoted LaRC04, was proposed by Pinho et al. [53].

Intra-laminar material properties of FRP composite laminates, such as stiffness/strengths parallel and transverse to the fiber, can be characterized according the American [54, 55] and the European [56-58] standards. These experimental tests are carried out under tensile and compressive load states.

Oller et al. [59] and Martínez [60] proposed another way for modeling the non-linear mechanical behavior of FRP laminated structures. Their methods are based on the combination of the constitutive models of each phase, i.e. fibers and matrix, together with governing equations that control the mechanical behavior of the composite. In other words, the mechanical behavior of each component is treated separately whereas the global response of the composite is obtained by assembling all contributions of components. In order to separately model the phases in a uni-directional (UD) composite material, the Classical mixing theory [61, 62] or the Serial/Parallel mixing theory [63] can be employed.

2.2.2 Inter-laminar fracture mode - Delamination phenomenon

According to Bolotin [64], two kinds of delamination can be distinguished: internal and near-surface delamination. The first one is situated within the bulk of material (Figure 2.6a) whereas the second one, as its name suggests, is placed near the surface of the laminate (Figure 2.6b).

After near-surface delamination, delaminated part does not necessarily have the same deformation as the rest of laminate. That leads to a complex fracture process where have to be accounted for not only the delamination growth but also local stability of the delaminated part.

Unlike near-surface delamination, the delaminated parts after internal delamination have similar deformation because of the interaction between them. Moreover, local instabilities are almost improbable to occur after internal delamination. However, this type of delamination may considerably modify the stiffness of the composite member provoking a substantial reduction of the load carrying capacity.

Furthermore, many delamination processes can take place within the laminate, which is known as multi-delamination (Figure 2.6c).

Local forces, thermal actions and low-energy impacts may serve as sources of delamination during transportation, storage, montage or service life of the structure. In addition, geometry discontinuities such as access holes, notches, free edges or bonded and bolted joints can also induce delamination due to high stress gradients.

At a microscopic scale, delamination is preceded by the formation of micro-cracks in a resin-rich zone between layers (Figure 2.7). Although micro-cracks could migrate through the plies [65], delamination is usually assumed to propagate parallel to the ply planes within the interface, which is an acceptable idealization for its numerical

modeling. Furthermore, according to fracture mechanics, delamination may occur as a single fracture mode I, mode II, mode III (Figure 2.8), or more likely as any combination of these (mixed mode). Mode I or opening mode corresponds to transverse normal tensile stress where mode II and III are provoked by the sliding and the scissoring shear stresses[9], respectively. These stresses are known as inter-laminar stresses also.

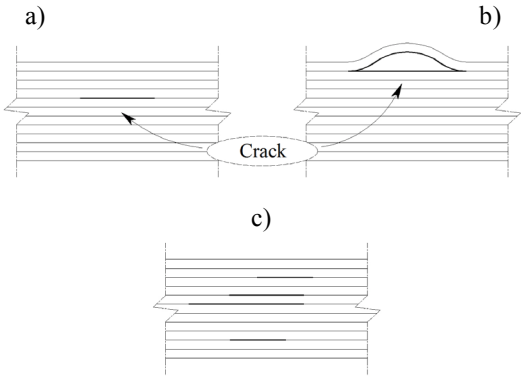

Figure 2.6 – Internal (a), near-surface (b) and multiple (c) delamination according to Bolotin.

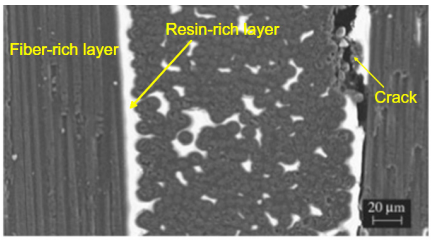

Figure 2.7 – Photomicrograph of an advanced composite where resin-rich zones and delamination are shown, from Barut et al. [44].

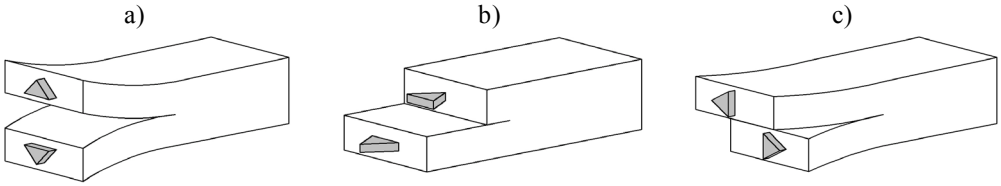

Figure 2.8 – Fracture mode I a), mode II b) and mode III c).

Delamination process, i.e. the onset and the growth, are governed by two inter-laminar properties, namely the strength and the fracture toughness (G_c). These

[9] Sliding and scissoring shear stresses correspond to the transverse shear stresses parallel and transversal to fiber direction, respectively.

properties depend on the delamination mode. The fracture toughness is also known as fracture energy, since it is defined as the amount of energy dissipated per unit area during the fracture process.

Both inter-laminar properties can be characterized via experimental tests. The mode II strength can be determined by the American standard ASTM D2344 [66]. It is not clear to the author if exist experimental tests to characterize strength for modes I and III. However, mode I strength is usually considered equal to the in-plane transverse tensile strength because the opening mode is matrix-dominated. Regarding to mode III strength, an assumption of safe design is to define it equal to mode II strength.

Fracture toughness for pure modes I (G_{Ic}) and II (G_{IIc}) can be determined via the double cantilever beam (DCB) [67, 68] and the end notched flexure (ENF) [69] standardized tests, respectively. Mode III fracture energy (G_{IIIc}) can be characterized via the no standardized edge crack torsion (ECT) test proposed by Lee [70].

In order to compute the fracture toughness (G_c) for different mode mixing ratios ($\rho = G_{II}/G_T$)[10] from the pure mode I (DCB) to the pure mode II (ENF), the mixed mode bending (MMB) [71] standardized test can be employed. However, the experimental characterization of the fracture energy for all possible mixed mode results impossible to carry out. For this reason, the fracture toughness is usually determined by means of curves that approximately fit the data generated by experimental tests. For example, among many others [65, 72], the BK model [73], the power law model [74] and the polynomial curve [75] (Table 2.2) are some of the most common mixed mode criteria. The fracture energy characterization is schematized in Figure 2.9.

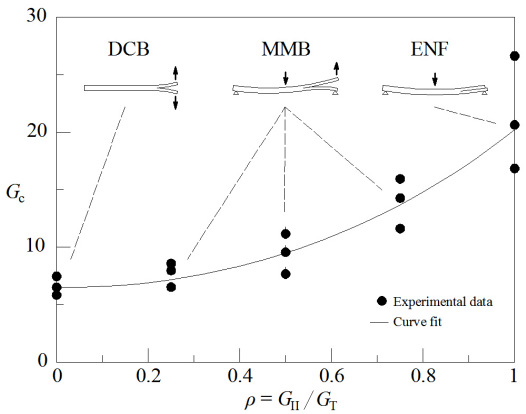

Figure 2.9 – Characterization of the fracture toughness for different mode mixing ratios.

[10] The mode mixing ratio ρ relates the mode II energy release rate (G_{II}) with the total energy release rate (G_T) in order to distinguish different mixed modes. This value ranges from 0 (pure mode I - DCB) to 1 (pure mode II – ENF).

Mixed mode criteria	
BK	$G_c = G_{Ic} + \left(G_{IIc} - G_{Ic}\right)\rho^{\kappa}$
Power law	$\left(\frac{G_I}{G_{Ic}}\right)^{\kappa_1} + \left(\frac{G_{II}}{G_{IIc}}\right)^{\kappa_2} = 1$ For $\kappa_1 = \kappa_2 = \kappa$ $G_c = \left[\left(\frac{1-\rho}{G_{Ic}}\right)^{\kappa} + \left(\frac{\rho}{G_{IIc}}\right)^{\kappa}\right]^{-1/\kappa}$
Polynomial	$G_c = G_{Ic} + \kappa_1\rho + \kappa_2\rho^2$

Table 2.2 – Mixed mode criteria for computing the mixed mode fracture toughness. ρ is the mode mixing ratio defined as G_{II}/G_T, whereas κ_1, κ_2 and κ are curve fitting parameters.

2.2.2.1 Modeling of delamination

Methods based on the linear elastic fracture mechanics (LEFM), such as the Virtual Crack Closure Technique (VCCT) [7, 76], the J-integral method [77, 78] and the virtual crack extension method [79], have proved to be suitable for predicting delamination growth. These methods are used to compute the energy release rate by means of results obtained from finite elements analyses. Then, delamination propagation occurs when the energy release rate is higher than the fracture thoroughness.

Nowadays, the VCCT technique is widely used to study several delamination cases, such as delamination buckling [80-82] and skin-stiffener debond [83-85], where the structure can be discretized with 3D, plane stress and/or plate finite elements. An interesting overview of this technique is presented by Kruger [7], where expressions to compute the energy release rate with different kinds of finite elements are also derived.

LEFM-based methods can be also employed together with simpler models such as the LW theories. Recently, Saeedi et al. [86] formulated a delamination model based on a LW description where the energy release rate is computed via the VCCT technique. In addition, Saeedi's model is contrasted with a 3D analysis that employs the J-integral method. Also, Barbero et al. [87] proposed a model based on a LW description where the virtual crack extension method is employed.

Although the efficacy of these techniques to predict delamination growth is well known, an initial crack must be predefined since they are unable to predict delamination onset. This is a significant drawback for certain geometries and load cases where the predefined crack can be difficult to locate.

Nowadays, cohesive or interface finite elements are other effective numerical method to fully simulate the delamination process. These elements are based on the cohesive zone approach (CZM) proposed by Dudgale [88] and Barenblatt [89] where it is assumed that molecular forces or cohesive forces act in the close vicinity of the crack tip. As a result, the crack is extended within a fracture process zone where a softening process takes place instead of a sudden decohesion.

The softening process is described by cohesive laws[11] which use different criteria[12] to control not only the onset but also the growth of delamination. Usually, onset criteria relate inter-laminar stress and strength whereas delamination growth is governed by the energy dissipated during the process[13].

Interface elements can be formulated based on solid-like [90, 91] or zero-thickness [92-97] approaches.

Solid-like interface elements are based on hexahedral solid elements with finite thickness. However, the transverse normal and shear stresses are accounted for only. All other stresses are set to zero. In addition, the initial thickness of the element has to be thin enough[14] in order to avoid membrane effects.

Unlike solid-like elements, zero-thickness elements are defined by two surfaces that are initially coincident, i.e. the thickness is equal to zero. These surfaces are held together by inter-laminar tractions as long as the interface is intact.

Cohesive laws are usually written in stress-strain and traction-displacement relationships for solid-like and zero-thickness elements, respectively. An interesting comparison between both types of interface element can be found in Balzani's PhD thesis [5].

Cohesive elements do not require initial crack to provide delamination onset, which is an important advantages respect to the LEFM-based methods, but they have to be placed between the plies where delamination is expected to occur. Thus, in cases where delamination paths are unknown it would be necessary to place interface elements between all layers. As a result, the computational resources needed for carrying out the simulation is considerably increased, especially in laminates of many plies. For this reason interface elements are peculiar suitable for studies where delamination path is known a priori, such as skin-stiffener delamination problems [5, 94, 95, 98].

Methods based on the continuum damage mechanics (CDM) are also able to simulate delamination. Martinez et al. [6] successfully analyzed delamination in a ply

[11] Cohesive laws are frequently defined by means of bi-linear and exponential curves.
[12] These criteria are usually formulated taking into account mixed-mode delamination.
[13] When the area under cohesive law curve is equal to the fracture toughness complete decohesion occurs and delamination is propagated.
[14] A thickness of 1/100 of the thinnest layer thickness is usually adopted.

drop-off test using 3D finite elements to discretize the laminate and an isotropic damage model to manage the material mechanical behavior.

For this method, it is not necessary to know a priori where delamination is expected to occur because any layer can suffer from damage. However, 3D finite elements are required to describe the laminate. Because of this, the study of delamination in large laminated structures of many layers may be unaffordable with this method. In addition, the discretization of very thin layers can lead to highly distorted elements carrying numerical issues.

Reduced models, such as those treated in Section 2.1, can be also employed to simulate delamination.

ESL-based finite elements can be employed together with LEFM-based techniques [7] or interface elements [5, 91]. However, these elements cannot simulate delamination by themselves since their kinematics are unable to predict discontinuities in the displacement field.

LW models can be also used in conjunction with LEFM-based methods [86, 87, 99], as already mentioned. In addition, it is also possible to use interface elements in LW descriptions as proposed by Hosseini-Toudeshky et al. [100]. Furthermore, delamination can be simulated via LW models by incorporating constitutive laws to manage the non-linear behavior of the interface continuity condition [101]. However, the main disadvantage of LW-based models is that the number of variable depends on the number of analysis layers, which could result computationally too expensive to simulate large composite structures of many layers.

To the knowledge of the author, the use of ZZT theories to model delamination in advanced composite laminates has been quite limited so far.

Di Sciuva and Gherlone [102] developed a refined version of the cubic zigzag theory, where both, the displacement and the transverse shear stress are defined as variables on the surfaces of the laminate. This feature allows the model to be employed in sub-laminate approaches[15] [103]. Although these approaches are able to simulate discontinuities on the displacement field, they may require excessive computational resources since the number of variables depends on the number of analysis layer.

Icardi et al. [104-106] have proposed a model based on a refined 3D cubic zigzag theory to analyze damage induced by low velocity impacts on composites laminates. However, in order to overcome the C^2 continuity requirement, FSDT-based C^0 plate elements are employed to approximate the solution. Then, stresses and other quantities of the zigzag theory are computed by a post-processing procedure based on strain energy updating from the FSDT model to the zigzag one.

[15] Sub-laminate approaches are special cases of the LW description where the laminate thickness is conveniently divided in several sub-domains.

RZT theory is a good alternative to simulate laminate structures with highly transverse anisotropy. Among many reason, the efficiency and efficacy to capture the zigzag in-plane displacement are some of the most important, as already mentioned in Section 2.1.3. However, in order to predict the relative displacement between layers, the definition of the zigzag function is the key feature. This function depends on the transverse shear modulus of each layer, which provides to the RZT theory the ability of changing the shape of the in-plane displacement by simply modifying the shear properties of the plies. Thus, the relative displacement between neighboring layers can be modeled by simply locating a thin enough ply between them and then reduce the shear modulus of the added ply.

Based on this idea, the author and advisors of this thesis have recently proposed a numerical model for predicting delamination in advanced composite beams [40] and plates [41] using the LRZ [38] and QLRZ [39] finite elements, respectively. This delamination model is presented in Chapter 4.

3 Formulation of the beam LRZ and the plate QLRZ multilayered finite elements

Formulation of the two-noded beam LRZ [38] and four-noded plate QLRZ [39] finite elements are presented in this Chapter. These elements are based on the refined zigzag theory of Tessler et al. [4, 36] presented in Section 2.1.3.1.

Both finite elements are formulated under the following consideration:

- Small deformations and displacements.
- Quasi-static application of loads and displacements.

3.1 Weak form of equilibrium equations via the principle of virtual work

The strong form of the differential equations is defined by the local Lagrangian equation of motion given by

$$\operatorname{div}[\boldsymbol{\sigma}] + \mathbf{b} - \rho\ddot{\mathbf{a}} = \mathbf{0} \tag{3.1}$$

being $\boldsymbol{\sigma}$ the stresses tensor, $\mathbf{b}$ the body forces and $\rho\ddot{\mathbf{a}}$ the dynamics forces vectors. This equation must be satisfied at each point within the volume of the body, denoted by Ω.

Now, boundary conditions have to be defined in order to formulate a complete boundary value problem. Thus, the stress-like (Newmann) and the displacement (Dirichlet) boundary condition, which are prescribed at the surfaces of the body Γ_t and Γ_u, respectively, are defined by

$$\mathbf{t} = \boldsymbol{\sigma}\mathbf{n} = \bar{\mathbf{t}} \quad \text{on} \quad \Gamma_t \qquad \text{and} \qquad \mathbf{u} = \bar{\mathbf{u}} \quad \text{on} \quad \Gamma_u \tag{3.2}$$

where $\mathbf{n}$ is the unit normal vector. $\bar{\mathbf{t}}$ and $\bar{\mathbf{u}}$ are the external forces and displacement vector, respectively.

Eqs.(3.1) and (3.2) define a complete boundary value problem, where its weak form is obtained via the principle of virtual work (PVW) [107] as

$$\int_{\Omega} \delta\mathbf{a}^T \rho \ddot{\mathbf{a}}\, d\Omega + \int_{\Omega} \delta\boldsymbol{\varepsilon}^T \boldsymbol{\sigma}\, d\Omega - \int_{\Omega} \delta\mathbf{a}^T \mathbf{b}\, d\Omega - \int_{\Gamma_t} \delta\mathbf{a}^T \overline{\mathbf{t}}\, d\Gamma_t = 0 \qquad 3.3$$

Since dynamic effects forces are not considered in this work, Eq.(3.3) is rewritten as

$$\int_{\Omega} \delta\boldsymbol{\varepsilon}^T \boldsymbol{\sigma}\, d\Omega - \int_{\Gamma_t} \delta\mathbf{a}^T \overline{\mathbf{t}}\, d\Gamma_t = 0 \qquad 3.4$$

where $\int_{\Omega} \delta\boldsymbol{\varepsilon}^T \boldsymbol{\sigma}\, d\Omega = \mathrm{W}^{\mathrm{int}}$ is the internal work and $\int_{\Gamma_t} \delta\mathbf{a}^T \overline{\mathbf{t}}\, d\Gamma_t = \mathrm{W}^{\mathrm{ext}}$ is the work of the external forces.

Here, Eq.(3.4) is solved by the finite element method. Thus, the integrand of Eq.(3.4) is computed by the summation of the contribution of each finite element *e* as

$$\int_{\Omega} \delta\boldsymbol{\varepsilon}^T \boldsymbol{\sigma}\, d\Omega - \int_{\Gamma_t} \delta\mathbf{a}^T \overline{\mathbf{t}}\, d\Gamma_t = \sum_{e=1}^{n} \left(\int_{\Omega^{(e)}} \delta\boldsymbol{\varepsilon}^{(e)^T} \boldsymbol{\sigma}^{(e)}\, d\Omega - \int_{\Gamma_t^{(e)}} \delta\mathbf{a}^{(e)^T} \overline{\mathbf{t}}^{(e)}\, d\Gamma_t^{(e)} \right) = 0 \qquad 3.5$$

being $\Omega^{(e)}$ and $\Gamma_t^{(e)}$ the volume and the contour of the element. Therefore, it is possible firstly to compute the stiffness matrix and the forces vector element by element and then assemble them all.

3.2 LRZ beam finite element

An isoparametric two-noded C^0 beam element, named LRZ, with four kinematic variables per node based on the RZT theory is formulated in this Section. This element is able to simulate thick and thin beams of highly heterogeneous laminated materials. Since this element suffers of shear looking, as shown in Section 3.2.7.1, a selective numerical integration of the transverse stiffness matrices is employed to overcoming this effect. In order to evaluate the performance of the LRZ element for simulating laminated materials, convergence and comparison studies are carried out in Section 3.2.7.2 and 3.2.7.3, respectively.

3.2.1 Beam RZT kinematics

From Eq.(2.1), the RZT kinematics for a beam is obtained by considering the axial *u* displacement and the transverse deflection *w* only. Thus, the beam displacement field is defined as

$$\begin{aligned} u^k(x,z) &= u_0(x) - z \cdot \theta(x) + \overline{u}^k(x,z) \\ w(x) &= w_0(x) \end{aligned} \qquad 3.6$$

with

$$\overline{u}^k = \phi^k(z)\cdot\psi(x)$$

The four kinematics variables of the RZT beam theory are

$$\mathbf{a} = \begin{bmatrix} u_0 & w_0 & \theta & \psi \end{bmatrix}^T \tag{3.7}$$

3.2.2 Strain and generalized strain

For convenience, the strain $\boldsymbol{\varepsilon}^k$ of the kth layer is split into the in-plane (ε_p^k) and the transverse shear (ε_t^k) strains as

$$\boldsymbol{\varepsilon}^k = \begin{bmatrix} \varepsilon_p \\ \varepsilon_t \end{bmatrix}^k = \begin{bmatrix} \dfrac{\partial u^k}{\partial x} \\ \dfrac{\partial u^k}{\partial z} + \dfrac{\partial w}{\partial x} \end{bmatrix} = \begin{bmatrix} \dfrac{\partial u_0}{\partial x} \\ 0 \end{bmatrix} + \begin{bmatrix} -z\dfrac{\partial \theta_x}{\partial x} \\ \dfrac{\partial w_0}{\partial x} - \theta_x \end{bmatrix} + \begin{bmatrix} \phi_x^k(z)\dfrac{\partial \psi_x}{\partial x} \\ \dfrac{\partial \phi_x^k}{\partial z}\psi_x \end{bmatrix} =$$

$$= \begin{bmatrix} \varepsilon_m \\ 0 \end{bmatrix} + \begin{bmatrix} \varepsilon_b \\ \varepsilon_s \end{bmatrix} + \begin{bmatrix} \varepsilon_{mb\phi} \\ \varepsilon_{s\phi} \end{bmatrix}^k = \begin{bmatrix} \mathbf{S}_p & 0 \\ 0 & \mathbf{S}_t \end{bmatrix}^k \cdot \begin{bmatrix} \hat{\boldsymbol{\varepsilon}}_p \\ \hat{\boldsymbol{\varepsilon}}_t \end{bmatrix} \tag{3.8}$$

where ε_m, ε_b and ε_s are the strain value duo to membrane, bending and transverse shear effects of the RMT theory, respectively. The in-plane and transverse shear strains values emanating from the RZT theory are denoted by $\varepsilon_{mb\phi}$ and $\varepsilon_{s\phi}$. $\hat{\boldsymbol{\varepsilon}}_p$ and $\hat{\boldsymbol{\varepsilon}}_t$ are the generalized in-plane and transverse shear strains vectors, respectively, defined as

$$\hat{\boldsymbol{\varepsilon}}_p = \begin{bmatrix} \hat{\varepsilon}_m \\ \hat{\varepsilon}_b \\ \hat{\varepsilon}_{mb\phi} \end{bmatrix} = \begin{bmatrix} \dfrac{\partial u_0}{\partial x} \\ \dfrac{\partial \theta}{\partial x} \\ \dfrac{\partial \psi}{\partial x} \end{bmatrix} \quad ; \quad \hat{\boldsymbol{\varepsilon}}_t = \begin{bmatrix} \hat{\varepsilon}_s \\ \hat{\varepsilon}_{s\phi} \end{bmatrix} = \begin{bmatrix} \dfrac{\partial w_0}{\partial x} - \theta \\ \psi \end{bmatrix} \tag{3.9}$$

$$\mathbf{S}_p^k = \begin{bmatrix} S_m \\ S_b \\ S_{mb\phi}^k \end{bmatrix}^T = \begin{bmatrix} 1 \\ -z \\ \phi^k(z) \end{bmatrix}^T \quad ; \quad \mathbf{S}_t^k = \begin{bmatrix} S_s \\ S_{s\phi}^k \end{bmatrix}^T = \begin{bmatrix} 1 \\ \dfrac{\partial \phi^k}{\partial z} \end{bmatrix}^T$$

where $(\hat{\bullet})$ denotes the generalized strain values.

3.2.3 Stress-strain constitutive relationships

The relationship between the in-plane and the transverse shear stresses and the strains for the kth layer are expressed in matrix form as

$$\boldsymbol{\sigma}^k = \begin{bmatrix} \sigma_x \\ \hline \tau_{xz} \end{bmatrix}^k = \begin{bmatrix} E & 0 \\ 0 & G \end{bmatrix}^k \cdot \begin{bmatrix} \varepsilon_p \\ \hline \varepsilon_t \end{bmatrix}^k = \mathbf{D}^k \boldsymbol{\varepsilon}^k \tag{3.10}$$

being E^k and G^k the Young and the shear modulus for the kth layer, respectively.

3.2.4 Stress resultants

According to the subdivision of the strains (Eq.(3.8)), the stress resultant vector $\hat{\boldsymbol{\sigma}}$ is subdivided into in-plane $\hat{\boldsymbol{\sigma}}_p$ and transverse shear $\hat{\boldsymbol{\sigma}}_t$ stress resultants as

$$\hat{\boldsymbol{\sigma}} = \begin{bmatrix} \hat{\boldsymbol{\sigma}}_p \\ \hline \hat{\boldsymbol{\sigma}}_t \end{bmatrix} = \begin{bmatrix} N \\ M \\ \hline M_\phi \\ Q \\ Q_\phi \end{bmatrix} \tag{3.11}$$

where N, M and Q are the membrane force, the bending moment, and the transverse shear force of standard beam theory, respectively. M_ϕ and Q_ϕ are respectively an additional bending moment and an additional shear force, which are derived from the RZT theory (Figure 3.1).

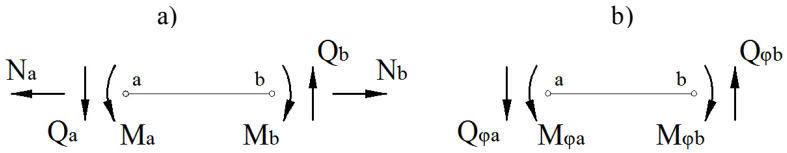

Figure 3.1 – Direction of stress resultants of standard beam theory (a) and those derived from the RZT beam theory (b).

The stress resultants for a beam are obtained by integrating stresses (Eq.(3.10)) over the transverse section A as

$$\begin{aligned} \hat{\boldsymbol{\sigma}}_p &= \int_A \mathbf{S}_p^{k^T} \sigma_x^k \mathrm{dA} = \int_A \mathbf{S}_p^{k^T} E^k \mathbf{S}_p^k \hat{\varepsilon}_p \mathrm{dA} = \left(\int_A \mathbf{S}_p^{k^T} E^k \mathbf{S}_p^k \mathrm{dA} \right) \hat{\varepsilon}_p = \hat{\mathbf{D}}_p \hat{\varepsilon}_p \\ \hat{\boldsymbol{\sigma}}_t &= \int_A \mathbf{S}_t^{k^T} \tau_{xz}^k \mathrm{dA} = \int_A \mathbf{S}_t^{k^T} G^k \mathbf{S}_t^k \hat{\varepsilon}_t \mathrm{dA} = \left(\int_A \mathbf{S}_t^{k^T} G^k \mathbf{S}_t^k \mathrm{dA} \right) \hat{\varepsilon}_t = \hat{\mathbf{D}}_t \hat{\varepsilon}_t \end{aligned} \tag{3.12}$$

being $\hat{\mathbf{D}}_p$ and $\hat{\mathbf{D}}_t$ the generalized constitutive matrices given as

$$\hat{\mathbf{D}}_p = \int_{\mathrm{A}} \mathbf{S}_p^{k^T} E^k \mathbf{S}_p^k \mathrm{dA} = \int_{\mathrm{A}} E^k \begin{bmatrix} 1 & -z & \phi^k \\ -z & z^2 & -z\phi^k \\ \phi^k & -z\phi^k & \left(\phi^k\right)^2 \end{bmatrix} \mathrm{dA}$$

$$\hat{\mathbf{D}}_t = \int_{\mathrm{A}} \mathbf{S}_t^{k^T} G^k \mathbf{S}_t^k \mathrm{dA} = \int_{\mathrm{A}} G^k \begin{bmatrix} 1 & \beta^k \\ \beta^k & \left(\beta^k\right)^2 \end{bmatrix} \mathrm{dA} \qquad 3.13$$

The generalized constitutive matrices $\hat{\mathbf{D}}$ are exactly computed using analytical integration. The ϕ^k function and its derivate β^k within each layer k are computed by Eqs.(2.10) and (2.17), respectively. Note that functions for x direction are only considered. Moreover, in case of beams, the parameter D_{t11}^k in Eqs.(2.17) and (2.18) is the shear modulus G^k.

3.2.5 Principle of virtual work

Let us consider a beam of length L and transverse section $\mathrm{A} = bh$ which is subjected to distributed **q** loads applied on the contour Γ and point loads $\mathrm{p_i}$. For this case, the differential equations of equilibrium (Eq.3.4) is rewritten as

$$\int_{\mathrm{V}} \delta\boldsymbol{\varepsilon}^{k^T} \boldsymbol{\sigma}^k \, \mathrm{dV} = \int_{\Gamma} \delta\mathbf{a}^T \mathbf{q} \, \mathrm{d}\Gamma + \sum_{i=1}^{pl} \delta\mathrm{a}_i \mathrm{p}_i \qquad 3.14$$

where the l.h.s. is the internal virtual work performed by the stresses $\boldsymbol{\sigma}^k$ and the r.h.s. is the external virtual work.

Substituting Eq.(3.8) into the l.h.s. of Eq.(3.14) gives

$$\int_{\mathrm{V}} \delta\boldsymbol{\varepsilon}^{k^T} \boldsymbol{\sigma}^k \, \mathrm{dV} = \int_{\mathrm{V}} \delta\hat{\boldsymbol{\varepsilon}}_p^T \mathbf{S}_s^{k^T} \sigma_x \, \mathrm{dV} + \int_{\mathrm{V}} \delta\hat{\boldsymbol{\varepsilon}}_t^T \mathbf{S}_t^{k^T} \tau_{xz} \, \mathrm{dV}$$

Using Eqs.(3.8), (3.10), (3.12) yields

$$\int_{\mathrm{V}} \delta\boldsymbol{\varepsilon}^{k^T} \boldsymbol{\sigma}^k \, \mathrm{dV} = \int_{\mathrm{L}} \delta\hat{\boldsymbol{\varepsilon}}_p^T \hat{\boldsymbol{\sigma}}_p \, \mathrm{dL} + \int_{\mathrm{L}} \delta\hat{\boldsymbol{\varepsilon}}_t^T \hat{\boldsymbol{\sigma}}_t \, \mathrm{dL}$$

Finally, the equilibrium equations of Eq.(3.4) can be written as

$$\int_{\mathrm{L}} \left(\delta\hat{\boldsymbol{\varepsilon}}_p^T \hat{\boldsymbol{\sigma}}_p + \delta\hat{\boldsymbol{\varepsilon}}_t^T \hat{\boldsymbol{\sigma}}_t \right) \mathrm{dL} = \int_{\Gamma} \delta\mathbf{a}^T \mathbf{q} \, \mathrm{d}\Gamma + \sum_{i=1}^{pl} \delta\mathrm{a}_i \mathrm{p}_i \qquad 3.15$$

The integrands in Eq.(3.15) contain kinematic variables derivatives up to first order only, which allows to use C0[16] continuous finite elements.

3.2.6 LRZ formulation

3.2.6.1 Discretization of the displacement field

The middle axis of the beam is discretized by using 2-noded isoparametric finite elements, where the kinematic variables **a** of Eq.(3.7) are interpolated within each element as

$$\mathbf{a}^{(e)} = \begin{bmatrix} u_0 \\ w_0 \\ \theta \\ \psi \end{bmatrix} = \sum_{i=1}^{2} \mathbf{N}_i \mathbf{a}_i^{(e)} = \begin{bmatrix} \mathbf{N}_1 & \mathbf{N}_2 \end{bmatrix} \cdot \begin{bmatrix} \mathbf{a}_1 \\ \mathbf{a}_2 \end{bmatrix}^{(e)} = \mathbf{N}_\mathbf{n} \mathbf{a}_\mathbf{n}^{(e)} \qquad 3.16$$

where

$$\mathbf{N}_i = N_i \mathbf{I}_4 \quad ; \quad \mathbf{a}_i^{(e)} = \begin{bmatrix} u_0 & w_0 & \theta & \psi \end{bmatrix}_i^T$$

being $N_i = \frac{1}{2}\left(1 + \xi\xi_i\right)$ (Table 3.1 and Figure 3.2) the linear shape function[17] of node *i*th and $\mathbf{I}_4$ is the 4x4 unit matrix.

Node	ξ_i
1	-1
2	1

Table 3.1 - Values of ξ_i for each node.

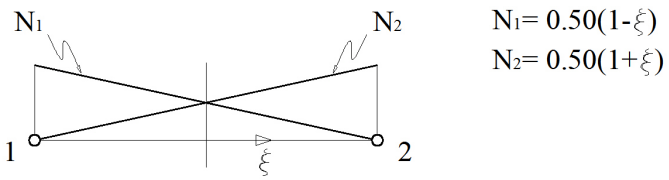

Figure 3.2 – Linear shape functions of two-noded element.

[16] In general, a finite element is Cm continuous if the displacement field and its m first derivatives are continuous between elements. Thus, a finite element is C0 continuous if the kinematic variables are inter-elements continuous only.

[17] In order to standardize the process of developing the elemental matrices, the shape functions N_i are established in the normalized natural coordinate system (ξ). In case of bilinear shape functions, N_i are normalized to the natural coordinate system (ξ,η).

The element geometry is interpolated as

$$x = \sum_{i=1}^{2} \hat{N}_i x_i \qquad 3.17$$

where $\hat{N}_i = N_i$, which leads to an isoparametric formulation[18].

Considering the length of the finite element defined by $\mathrm{L}^{(e)} = x_2 - x_1$ and the form of N_i, the value $\mathrm{d}x/\mathrm{d}\xi$ is computed from Eq.(3.17) as

$$\frac{\mathrm{d}x}{\mathrm{d}\xi} = \frac{\mathrm{d}N_1}{\mathrm{d}\xi} x_1 + \frac{\mathrm{d}N_2}{\mathrm{d}\xi} x_2 = -\frac{1}{2} x_1 + \frac{1}{2} x_2 = \frac{\mathrm{L}^{(e)}}{2}$$

wherewith

$$\mathrm{d}x = \frac{\mathrm{L}^{(e)}}{2}\mathrm{d}\xi \qquad \text{and} \qquad \frac{\mathrm{d}\xi}{\mathrm{d}x} = \frac{2}{\mathrm{L}^{(e)}} \qquad 3.18$$

Thus, the derivatives of the shape functions with respect to the Cartesian coordinates are computed using the chain rule as

$$\begin{aligned} \frac{\mathrm{d}N_1}{\mathrm{d}x} &= \frac{\mathrm{d}N_1}{\mathrm{d}\xi}\frac{\mathrm{d}\xi}{\mathrm{d}x} = -\frac{1}{2}\frac{2}{\mathrm{L}^{(e)}} = -\frac{1}{\mathrm{L}^{(e)}} \\ \frac{\mathrm{d}N_2}{\mathrm{d}x} &= \frac{\mathrm{d}N_2}{\mathrm{d}\xi}\frac{\mathrm{d}\xi}{\mathrm{d}x} = \frac{1}{2}\frac{2}{\mathrm{L}^{(e)}} = \frac{1}{\mathrm{L}^{(e)}} \end{aligned} \qquad 3.19$$

3.2.6.2 Generalized strain field

The interpolated generalized in-plane strains $\hat{\boldsymbol{\varepsilon}}_p^{(e)}$ within each finite element are obtained by substituting Eq.(3.16) into Eq.3.9 as

$$\hat{\boldsymbol{\varepsilon}}_p^{(e)} = \begin{bmatrix} \hat{\varepsilon}_m \\ \hat{\varepsilon}_b \\ \hat{\varepsilon}_{mb\phi} \end{bmatrix}^{(e)} = \begin{bmatrix} \dfrac{\partial u_0}{\partial x} \\ \dfrac{\partial \theta}{\partial x} \\ \dfrac{\partial \psi}{\partial x} \end{bmatrix}^{(e)} = \sum_{i=1}^{2} \begin{bmatrix} \dfrac{\partial N_i}{\partial x} u_0 \\ \dfrac{\partial N_i}{\partial x} \theta \\ \dfrac{\partial N_i}{\partial x} \psi \end{bmatrix}_i = \sum_{i=1}^{2} \mathbf{B}_{p_i} \mathbf{a}_i^{(e)} = \mathbf{B}_p \mathbf{a}_{\mathbf{n}}^{(e)} \qquad 3.20$$

[18] The formulation is named *isoparametric* when kinematic variables as well as element geometry are approximated using the same shape function, e.g. $N_i = \hat{N}_i$. If the polynomial degree of $\hat{N}_i$ is higher than that of N_i, then a *super-parametric* formulation is obtained; otherwise, the formulation is called *sub-parametric*.

where $\mathbf{B}_p$ and $\mathbf{B}_{p_i}$ are the in-plane generalized strain matrices for the element *e* and the *i*th node, respectively. The matrix $\mathbf{B}_{p_i}$ is split into membrane (m), bending (b) and zigzag $(mb\phi)$ contributions, which leads to

$$\mathbf{B}_{p_i} = \begin{bmatrix} \mathbf{B}_m \\ \mathbf{B}_b \\ \mathbf{B}_{mb\phi} \end{bmatrix}_i = \begin{bmatrix} \dfrac{\partial N_i}{\partial x} & 0 & 0 & 0 \\ 0 & 0 & \dfrac{\partial N_i}{\partial x} & 0 \\ 0 & 0 & 0 & \dfrac{\partial N_i}{\partial x} \end{bmatrix} \tag{3.21}$$

In the same manner, the generalized transverse strains $\hat{\boldsymbol{\varepsilon}}_t^{(e)}$ are obtained as

$$\hat{\boldsymbol{\varepsilon}}_t^{(e)} = \begin{bmatrix} \hat{\varepsilon}_s \\ \hat{\varepsilon}_{s\phi} \end{bmatrix}^{(e)} = \begin{bmatrix} \dfrac{\partial w_0}{\partial x} - \theta_x \\ \psi \end{bmatrix}^{(e)} = \sum_{i=1}^{2} \begin{bmatrix} \dfrac{\partial N_i}{\partial x} w_0 - N_i \theta \\ N_i \psi \end{bmatrix}_i = \sum_{i=1}^{2} \mathbf{B}_{t_i} \mathbf{a}_i^{(e)} = \mathbf{B}_t \mathbf{a}_{\mathbf{n}}^{(e)} \tag{3.22}$$

where $\mathbf{B}_t$ and $\mathbf{B}_{t_i}$ are the transverse generalized strain matrices for the element *e* and the *i*th node, respectively. Matrix $\mathbf{B}_{t_i}$ is split into shear (s) and zigzag $(s\phi)$ contributions as

$$\mathbf{B}_{t_i} = \begin{bmatrix} \mathbf{B}_s \\ \mathbf{B}_{s\phi} \end{bmatrix}_i = \begin{bmatrix} 0 & \dfrac{\partial N_i}{\partial x} & -N_i & 0 \\ 0 & 0 & 0 & N_i \end{bmatrix} \tag{3.23}$$

3.2.6.3 Element stiffness matrix and nodal forces vector

Considering Eqs.(3.5), (3.15), the beam element stiffness matrix and the nodal forces vector are obtained via the following equation

$$\int_{\mathrm{L}^{(e)}} \left(\delta\hat{\boldsymbol{\varepsilon}}_p^{(e)^T} \hat{\boldsymbol{\sigma}}_p + \delta\hat{\boldsymbol{\varepsilon}}_t^{(e)^T} \hat{\boldsymbol{\sigma}}_t \right) \mathrm{dL} = \int_{\mathrm{L}^{(e)}} \delta\mathbf{a}^{(e)^T} \mathbf{q} \, \mathrm{dL} + \delta\mathbf{a}_{\mathbf{n}}^{(e)^T} \mathbf{p} \tag{3.24}$$

being $\mathrm{L}^{(e)}$ the length of the finite element.

Considering that

$$\delta\hat{\boldsymbol{\varepsilon}}_p^{(e)^T} = \delta\mathbf{a}_{\mathbf{n}}^{(e)^T} \mathbf{B}_p^T \quad ; \quad \delta\hat{\boldsymbol{\varepsilon}}_t^{(e)^T} = \delta\mathbf{a}_{\mathbf{n}}^{(e)^T} \mathbf{B}_t^T \quad ; \quad \delta\mathbf{a}^{(e)^T} = \delta\mathbf{a}_{\mathbf{n}}^{(e)^T} \mathbf{N}_{\mathbf{n}}^T$$

and substituting Eq.(3.12) into Eq.(3.24) gives

$$\int_{\mathrm{L}^{(e)}} \left(\delta\mathbf{a}_{\mathbf{n}}^{(e)^T} \mathbf{B}_p^T \hat{\mathbf{D}}_p \hat{\boldsymbol{\varepsilon}}_p + \delta\mathbf{a}_{\mathbf{n}}^{(e)^T} \mathbf{B}_t^T \hat{\mathbf{D}}_t \hat{\boldsymbol{\varepsilon}}_t \right) \mathrm{dL} = \int_{\mathrm{L}^{(e)}} \delta\mathbf{a}_{\mathbf{n}}^{(e)^T} \mathbf{N}_{\mathbf{n}}^T \mathbf{q} \, \mathrm{dL} + \delta\mathbf{a}_{\mathbf{n}}^{(e)^T} \mathbf{p}$$

Then, substituting Eqs.(3.20), (3.22) into the previous equation yields

$$\int_{L^{(e)}} \left(\delta \mathbf{a}_{\mathbf{n}}^{(e)^T} \mathbf{B}_p^T \hat{\mathbf{D}}_p \mathbf{B}_p \mathbf{a}_{\mathbf{n}}^{(e)} + \delta \mathbf{a}_{\mathbf{n}}^{(e)^T} \mathbf{B}_t^T \hat{\mathbf{D}}_t \mathbf{B}_t \mathbf{a}_{\mathbf{n}}^{(e)} \right) dL = \int_{L^{(e)}} \delta \mathbf{a}_{\mathbf{n}}^{(e)^T} \mathbf{N}_{\mathbf{n}}^T \mathbf{q} \; dL + \delta \mathbf{a}_{\mathbf{n}}^{(e)^T} \mathbf{p}$$

Thus, the equation can be factored as

$$\delta \mathbf{a}_{\mathbf{n}}^{(e)^T} \left\{ \left[\int_{L^{(e)}} \left(\mathbf{B}_p^T \hat{\mathbf{D}}_p \mathbf{B}_p + \mathbf{B}_t^T \hat{\mathbf{D}}_t \mathbf{B}_t \right) dL \right] \mathbf{a}_{\mathbf{n}}^{(e)} \right\} = \left(\int_{L^{(e)}} \mathbf{N}_{\mathbf{n}}^T \mathbf{q} \; dL + \mathbf{p} \right) \delta \mathbf{a}_{\mathbf{n}}^{(e)^T}$$

$$\left[\int_{L^{(e)}} \left(\mathbf{B}_p^T \hat{\mathbf{D}}_p \mathbf{B}_p + \mathbf{B}_t^T \hat{\mathbf{D}}_t \mathbf{B}_t \right) dL \right] \mathbf{a}_{\mathbf{n}}^{(e)} = \int_{L^{(e)}} \mathbf{N}_{\mathbf{n}}^T \mathbf{q} \; dL + \mathbf{p}$$

Finally, Eq.(3.24) is reduced to

$$\mathbf{K}^{(e)} \; \mathbf{a}_{\mathbf{n}}^{(e)} = \int_{L^{(e)}} \mathbf{N}_{\mathbf{n}}^T \mathbf{q} \; dL + \mathbf{p} \tag{3.25}$$

with

$$\mathbf{K}^{(e)} = \int_{L^{(e)}} \left(\mathbf{B}_p^T \hat{\mathbf{D}}_p \mathbf{B}_p + \mathbf{B}_t^T \hat{\mathbf{D}}_t \mathbf{B}_t \right) dL \tag{3.26}$$

Matrix $\mathbf{K}^{(e)}$ is the elemental stiffness matrix, which for convenience is computed as

$$\mathbf{K}^{(e)} = \mathbf{K}_p^{(e)} + \mathbf{K}_t^{(e)}$$

being $\mathbf{K}_p^{(e)}$ and $\mathbf{K}_t^{(e)}$ the in-plane and the transverse elemental stiffness matrices, respectively, defined as

$$\begin{aligned} \mathbf{K}_p^{(e)} &= \int_{L^{(e)}} \mathbf{B}_p^T \hat{\mathbf{D}}_p \mathbf{B}_p dL \\ \mathbf{K}_t^{(e)} &= \int_{L^{(e)}} \mathbf{B}_t^T \hat{\mathbf{D}}_t \mathbf{B}_t dL \end{aligned} \tag{3.27}$$

To assess the influence of the reduced integration of matrix $\mathbf{K}_t^{(e)}$ for overcoming the shear locking of the solution, matrix $\mathbf{K}_t^{(e)}$ is split as follows

$$\mathbf{K}_t^{(e)} = \mathbf{K}_s^{(e)} + \mathbf{K}_{s\phi}^{(e)} + \mathbf{K}_{ss\phi}^{(e)} + \left[\mathbf{K}_{ss\phi}^{(e)} \right]^T \tag{3.28}$$

with

$$\begin{aligned} \mathbf{K}_s^{(e)} &= \int_{L^{(e)}} \mathbf{B}_s^T \hat{\mathbf{D}}_{s(1,1)} \mathbf{B}_s dL \\ \mathbf{K}_{s\phi}^{(e)} &= \int_{L^{(e)}} \mathbf{B}_{s\phi}^T \hat{\mathbf{D}}_{s(2,2)} \mathbf{B}_{s\phi} dL \\ \mathbf{K}_{ss\phi}^{(e)} &= \int_{L^{(e)}} \mathbf{B}_s^T \hat{\mathbf{D}}_{s(1,2)} \mathbf{B}_{s\phi} dL \end{aligned} \tag{3.29}$$

The external nodal forces vector $\mathbf{F}^{\text{ext}}$ are defined by the r.h.s. of Eq.(3.25) as

$$\mathbf{F}^{\text{ext}} = \int_{\mathrm{L}^{(e)}} \mathbf{N}_{\mathbf{n}}^{T}\mathbf{q}\ \mathrm{dL} + \mathbf{p} \tag{3.30}$$

Considering Eq.(3.18), the integrals of Eq.(3.27) defined in the Cartesian coordinate are transformed to the natural coordinate as

$$\begin{aligned}\mathbf{K}_{p}^{(\mathrm{e})} &= \int_{\mathrm{L}^{(e)}} \mathbf{B}_{p}^{T}\hat{\mathbf{D}}_{p}\mathbf{B}_{p}\mathrm{dL} = \int_{-1}^{+1} \mathbf{B}_{p}^{T}\hat{\mathbf{D}}_{p}\mathbf{B}_{p}\frac{\mathrm{L}^{(\mathrm{e})}}{2}\mathrm{d}\xi \\ \mathbf{K}_{t}^{(\mathrm{e})} &= \int_{\mathrm{L}^{(e)}} \mathbf{B}_{t}^{T}\hat{\mathbf{D}}_{t}\mathbf{B}_{t}\mathrm{dL} = \int_{-1}^{+1} \mathbf{B}_{p}^{T}\hat{\mathbf{D}}_{t}\mathbf{B}_{p}\frac{\mathrm{L}^{(\mathrm{e})}}{2}\mathrm{d}\xi\end{aligned} \tag{3.31}$$

The derivatives of the shape functions with respect to the Cartesian coordinates contained into the generalized strain matrices $\mathbf{B}$ are computed by Eq.(3.19).

The integrals of the in-plane element stiffness matrix $\mathbf{K}_{p}^{(\mathrm{e})}$ (Eq.(3.31)) is exactly computed by using the one-point Gauss quadrature as

$$\begin{aligned}\mathbf{K}_{p}^{(\mathrm{e})} &= \int_{-1}^{+1} \mathbf{B}_{p}^{T}\hat{\mathbf{D}}_{p}\mathbf{B}_{p}\frac{\mathrm{L}^{(\mathrm{e})}}{2}\mathrm{d}\xi = \frac{\mathrm{L}^{(\mathrm{e})}}{2}\left[\mathbf{B}_{p}^{T}\hat{\mathbf{D}}_{p}\mathbf{B}_{p}\right]_{(\xi_{GP})} W_{GP} \\ \mathbf{K}_{p}^{(\mathrm{e})} &= \mathrm{L}^{(\mathrm{e})}\left[\mathbf{B}_{p}^{T}\hat{\mathbf{D}}_{p}\mathbf{B}_{p}\right]_{(\xi_{GP}=0.0)}\end{aligned} \tag{3.32}$$

where $W_{GP} = 2$ and $\xi_{GP} = 0.0$ are respectively the weighting factor and the natural coordinate of the center integration point (or Gauss points (GP)). Matrices $\mathbf{B}$ are evaluated at $\xi_{GP} = 0.0$.

The exact integration of matrix $\mathbf{K}_{t}^{(\mathrm{e})}$ is obtained by using two Gauss points. However, the full numerical integration of $\mathbf{K}_{t}^{(\mathrm{e})}$ leads to shear locking effects for slender beams. For this reason, a selective integration scheme is used, where matrices $\mathbf{K}_{s}^{(\mathrm{e})}$ and $\mathbf{K}_{ss\phi}^{(\mathrm{e})}$ are solved by employing a reduced integration (one integration point only) as

$$\begin{aligned}\mathbf{K}_{s}^{(\mathrm{e})} &= \int_{-1}^{+1} \mathbf{B}_{s}^{T}\hat{\mathbf{D}}_{s(1,1)}\mathbf{B}_{s}\frac{\mathrm{L}^{(\mathrm{e})}}{2}\mathrm{d}\xi = \mathrm{L}^{(\mathrm{e})}\left[\mathbf{B}_{s}^{T}\hat{\mathbf{D}}_{s(1,1)}\mathbf{B}_{s}\right]_{(\xi_{GP}=0.0)} \\ \mathbf{K}_{ss\phi}^{(\mathrm{e})} &= \int_{-1}^{+1} \mathbf{B}_{s}^{T}\hat{\mathbf{D}}_{s(1,2)}\mathbf{B}_{s\phi}\frac{\mathrm{L}^{(\mathrm{e})}}{2}\mathrm{d}\xi = \mathrm{L}^{(\mathrm{e})}\left[\mathbf{B}_{s}^{T}\hat{\mathbf{D}}_{s(1,2)}\mathbf{B}_{s\phi}\right]_{(\xi_{GP}=0.0)}\end{aligned} \tag{3.33}$$

and matrix $\mathbf{K}_{s\phi}^{(\mathrm{e})}$ (Eq.(3.29)) is full integrated using two Gauss point as

$$\mathbf{K}_{s\phi}^{(e)} = \int_{-1}^{+1} \mathbf{B}_{s\phi}^{T} \hat{\mathbf{D}}_{s(2,2)} \mathbf{B}_{s\phi} \frac{\mathrm{L}^{(e)}}{2} \mathrm{d}\xi = \sum_{GP=1}^{2} \frac{\mathrm{L}^{(e)}}{2} \left[\mathbf{B}_{s\phi}^{T} \hat{\mathbf{D}}_{s(2,2)} \mathbf{B}_{s\phi} \right]_{(\xi_{GP})} W_{GP} \qquad 3.34$$

Both natural coordinate ξ_{GP} and weighting factor W_{GP} for the two-point Gauss quadrature are listed in Table 3.2.

GP	ξ_{GP}	W_{GP}
1	$-\frac{1}{\sqrt{3}}$	1
2	$+\frac{1}{\sqrt{3}}$	1

Table 3.2 – Natural coordinates and weighting factors of integration points.

A study of the accuracy of the LRZ solution for modeling slender beams using this selective integration scheme is presented in Section 3.2.7.1.

3.2.6.4 Boundary conditions

The boundary conditions are:

- Clamped side:

$$w = u = \theta = \psi = 0$$

- Simply supported side:

$$w = 0$$

- Symmetry axis:

$$u_n = \theta_n = \psi_n = 0$$

where "n" is the orthogonal direction to the symmetry axis.

3.2.6.5 Improved computation of transverse shear stresses

Since the constitutive equation (Eq.(3.10)) yields a constant value of the transverse shear stress τ_{xz}^{k} into each layer, a discontinuous thickness distribution of τ_{xz} is obtained. A useful alternative to improve the computation of τ_{xz} is to use the equilibrium equations

$$\frac{\partial \sigma_x}{\partial x} + \frac{\partial \tau_{xz}}{\partial z} = 0 \qquad 3.35$$

from which, the transverse shear stress at a point "P" located within the finite element is computed across the thickness by

$$\tau_{xz}(z)\big|_P = -\int_{-h/2}^{z} \left.\frac{\partial \sigma_x}{\partial x}\right|_P dz \qquad 3.36$$

The axial stress σ_x at point "P" is calculated by the following approximation

$$\sigma_x(z)\big|_P = \sum_{i=1}^{2} N_i\big|_P \cdot \sigma_x^i(z) \qquad 3.37$$

where N_i is the shape function previously defined and *i* denotes the *i*th node. The nodal axial stress $\sigma_x^i(z)$ is obtained by the averaging of Gauss stresses from neighboring elements at the *i*th node.

Finally, the thickness distribution of transverse shear stress is obtained by replacing Eq.(3.37) into Eq(3.36),

$$\tau_{xz}(z)\big|_P = -\int_{-h/2}^{z} \left(\sum_{i=1}^{2} \left.\frac{\partial N_i}{\partial x}\right|_P \cdot \sigma_x^i(z) \right) \qquad 3.38$$

3.2.7 LRZ studies

3.2.7.1 Shear locking

The selective integration scheme, as solution of the shear locking effects, is studied by analyzing a cantilever beam of length L subjected to a unit point load F = 1 N (Figure 3.3). The beam is formed by a three-layered laminate, whose properties are listed on Table 3.3.

The study is performed for four span-to-thickness ratios: λ = 5, 10, 50, 100 (λ = L/h) using a mesh of 100 LRZ beam elements. The reference solution was obtained by a plane stress analysis (PS) using a mesh of 27000 4-noded quadrilateral (Figure 3.4).

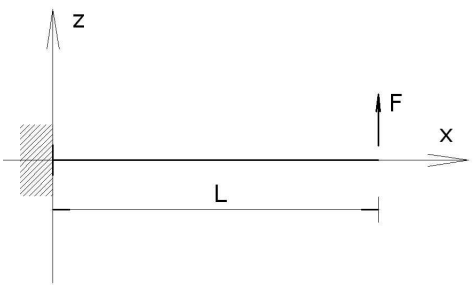

Figure 3.3 – Cantilever beam under point load.

Laminated Material			
	Layer 1 (bottom)	Layer 2 (core)	Layer 3 (top)
h [mm]	6.6667	6.6667	6.6667
E [MPa]	$2.19\text{x}10^5$	$2.19\text{x}10^3$	$2.19\text{x}10^5$
G [MPa]	$0.876\text{x}10^5$	$8.80\text{x}10^2$	$0.876\text{x}10^5$

Table 3.3 – Material properties of shear locking study.

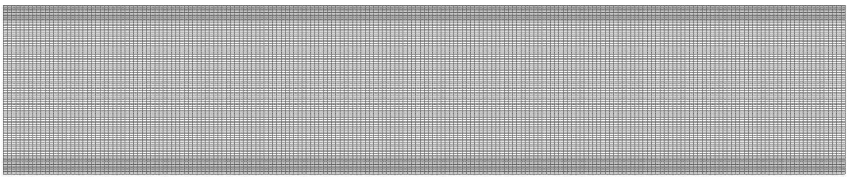

Figure 3.4 – Structured mesh of 27000 four-noded plane stress quadrilaterals elements.

The ratio $r = w_{LRZ} / w_{PS}$ between the vertical displacement at the free end computed with the LRZ element mesh (w_{LRZ}) and with the PS analysis (w_{PS}) for each span-to-thickness λ is shown in Figure 3.5. Results for the LRZ mesh have been obtained using exact two-point integration for all terms of matrix $\mathbf{K}_t^{(e)}$ (Eq.(3.28)) and a one-point reduced integration for the following three groups of matrices: $\mathbf{K}_s^{(e)}$; $\mathbf{K}_s^{(e)}$ and $\mathbf{K}_{s\phi}^{(e)}$; and all terms of $\mathbf{K}_t^{(e)}$. Labels "all", "S", "SPsi", and "Psi" in Figure 3.5-Figure 3.8 refer to matrices $\mathbf{K}_t^{(e)}$, $\mathbf{K}_s^{(e)}$, $\mathbf{K}_{ss\phi}^{(e)}$, and $\mathbf{K}_{s\phi}^{(e)}$, respectively.

Figure 3.5 clearly shows that the LRZ element suffers shear locking when matrix $\mathbf{K}_t^{(e)}$ is full integrated. It is also shown that the finite element is shear locking-free when the reduced integration is used.

The influence of the selective integration in the distribution of the transverse shear stress is also studied. Figure 3.6-Figure 3.8 show the thickness distribution of τ_{xz} in sections located at distances L/20, L/4, L/2 and 3L/4 from the clamped end for span-to-thickness ratios λ = 5, 10 and 100. For this analysis, the Timoshenko solution (TBT) is also analyzed using a mesh of 300 standard 2-noded elements. A shear correction factor of $5/6$ is used for all TBT results presented in this work.

Results show that for thick beams (small values of λ) similar solutions are obtained for both, the reduced and the exact integration of matrix $\mathbf{K}_t^{(e)}$. For slender beams,

however, results obtained using reduced integration of the three matrix groups are different.

It is shown that slightly more accurate results are obtained when matrices $\mathbf{K}_{s}^{(e)}$ and $\mathbf{K}_{s\phi}^{(e)}$ are integrated using a one-point quadrature, whereas matrix $\mathbf{K}_{ss\phi}^{(e)}$ is computed by using two Gauss points. Hence, this selective integration scheme is adopted to overcoming shear locking effects.

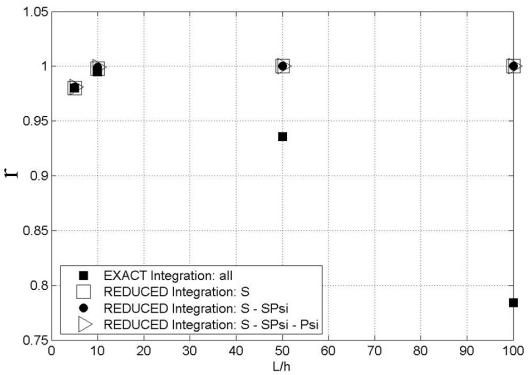

Figure 3.5 – r ratio versus λ for cantilever beam under point load.

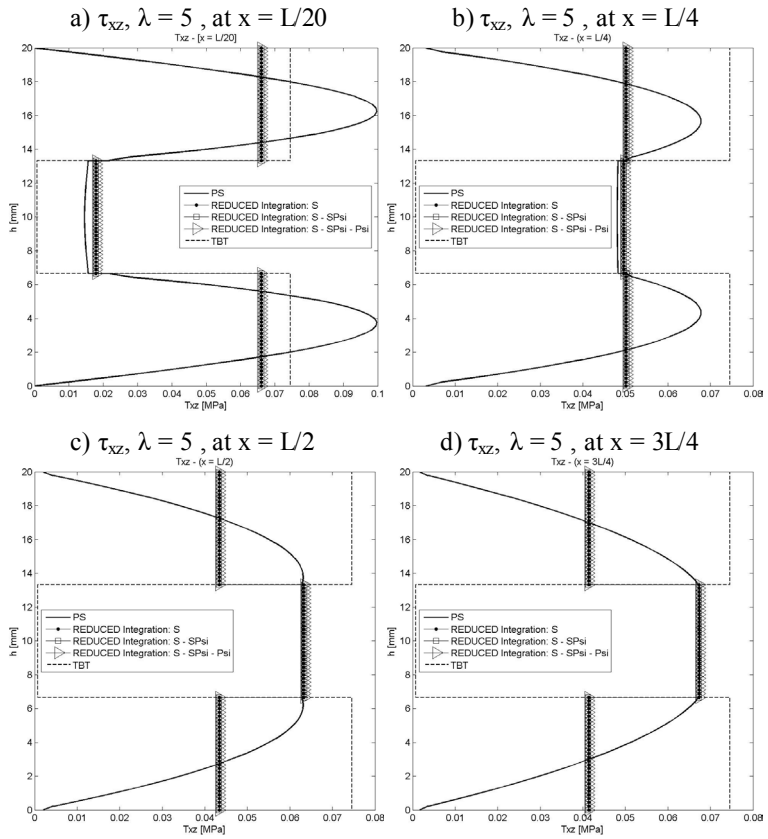

Figure 3.6 – Thickness distribution of the transverse shear stress for λ = 5 at different sections.

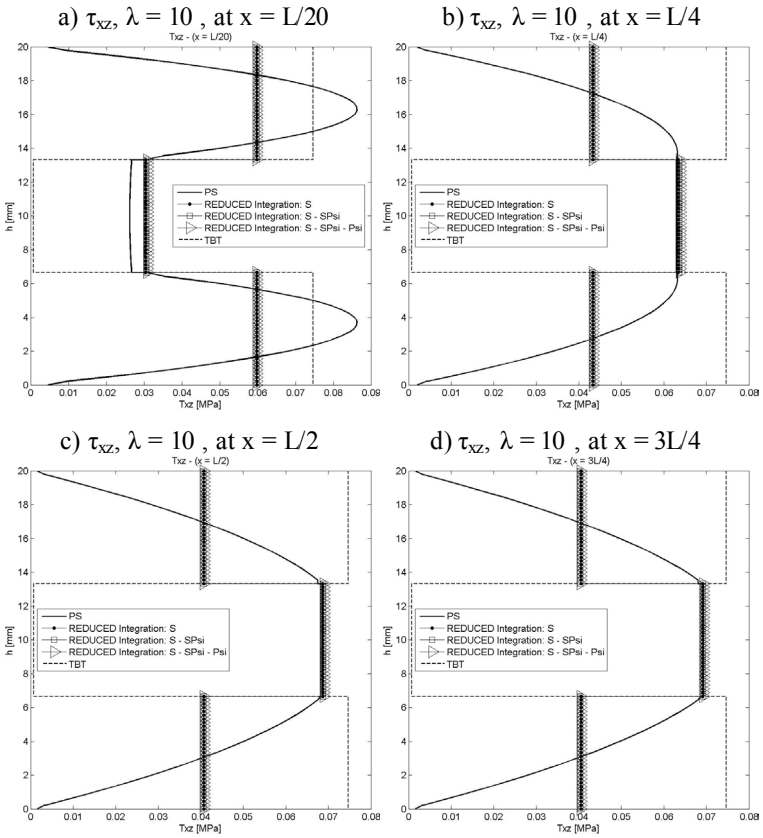

Figure 3.7 – Thickness distribution of the transverse shear stress for λ = 10 at different sections.

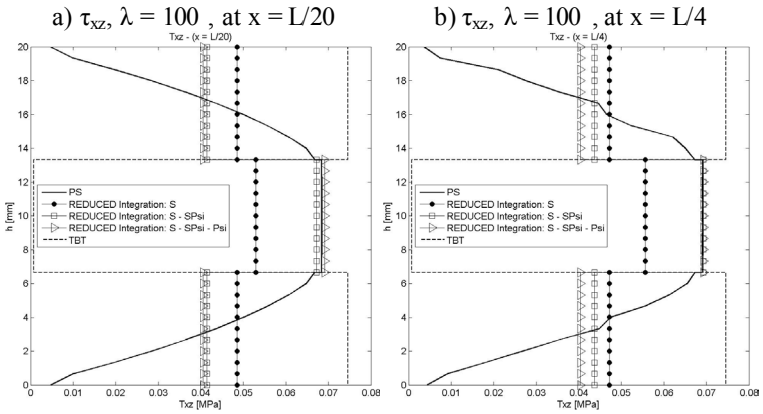

Figure 3.8 – Thickness distribution of the transverse shear stress for λ = 100 at different sections.

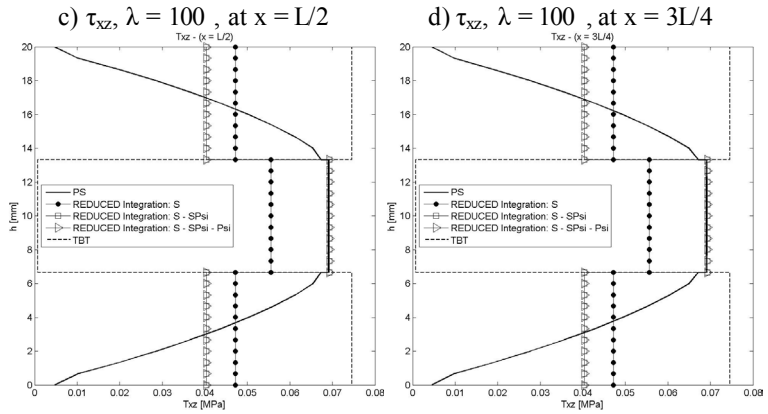

Figure 3.8 – Continuation.

3.2.7.2 Convergence

The beam of Figure 3.3 is studied for three laminated materials of different degree of heterogeneity. Materials properties are listed in Table 3.4. Material A is the most homogeneous one, while material C is clearly the most heterogeneous.

Composite Materials				
		Layer 1 (bottom)	Layer 2 (core)	Layer 3 (top)
Composite A	h [mm]	6.66	6.66	6.66
	E [MPa]	$2.19x10^5$	$2.19x10^4$	$4.4E^5$
	G [MPa]	$8.76x10^4$	$8.80x10^3$	$2.00E^5$
Composite B	h [mm]	6.66	6.66	6.66
	E [MPa]	$2.19x10^5$	$2.19x10^3$	$2.19E^5$
	G [MPa]	$8.76x10^4$	$8.80x10^2$	$8.76E^4$
Composite C	h [mm]	2	16	2
	E [MPa]	$2.19x10^5$	$0.73x10^3$	$7.3x10^5$
	G [MPa]	$0.876x10^5$	$0.29x10^3$	$2.92x10^5$

Table 3.4 – Material properties of laminated materials used for convergence study.

In order to evaluate mesh convergence of the LRZ solution, six meshes ranging from 5 to 300 elements are used.

Convergence is measured by the relative error defined as

$$e_r = \frac{m_6 - m_i}{m_6} \qquad 3.39$$

where m_6 and m_i are the values of the magnitude of interest obtained using the finest grid (300 elements) and the *i*th mesh (i = 1, 2, … 5), respectively.

Table 3.5 and Figure 3.9 show the convergence for deflection w and function ψ at the free end, the maximum axial stress σ_x at the end section and the maximum shear stress τ_{xz} at the mid-section.

Results clearly show that convergence is always slower for the most heterogeneous material. For the mesh of 25 elements the errors for all the magnitudes considered are less than 1% for materials A and B. For material C the maximum error does not exceed 5%. For the 50 element mesh errors around 1% were obtained in all cases.

Results for the 10 element mesh are good for material A (errors less than 0.4%), relatively good for material B (errors less than around 5%) and unacceptable for material C (errors ranging from around 8% to 20%).

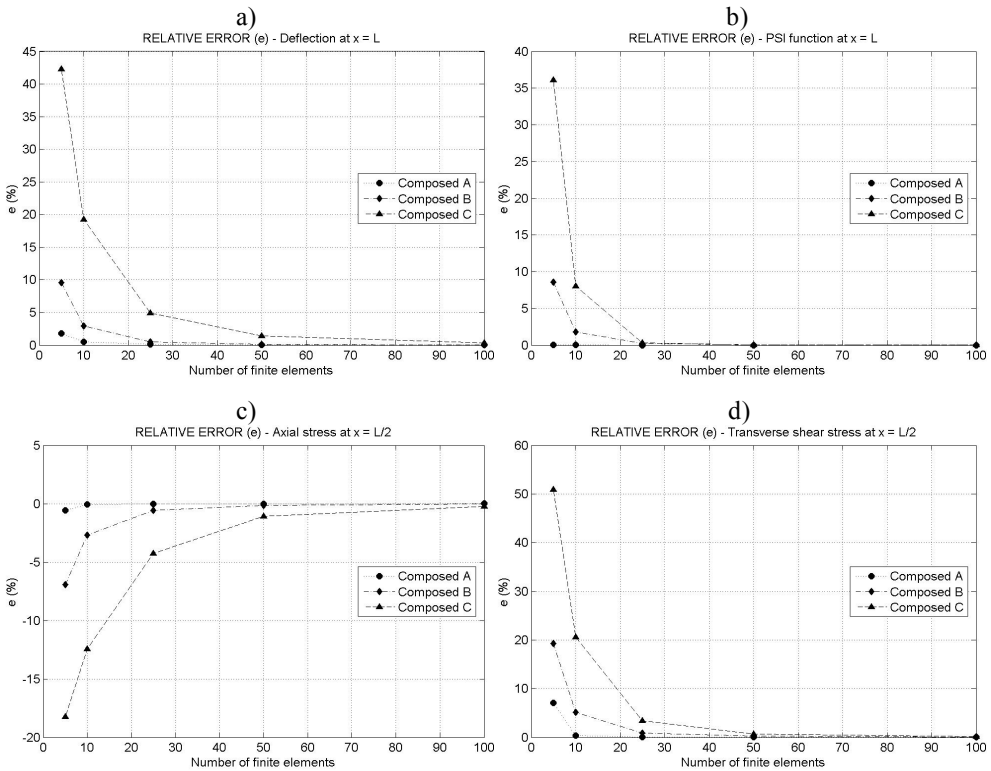

Figure 3.9 – Convergence relative error for: a) w at x = L, b) ψ at x = L, c) maximum axial stress at x = L, d) and maximum shear stress at x = L/2.

a)

$e_r(\%)$ - ***w*** **at x = L**

Number of elements	Composites A	B	C
5	1.800	9.588	42.289
10	0.506	2.901	19.277
25	0.0860	0.499	4.913
50	0.0191	0.123	1.406
100	0.0048	0.031	0.339
300	0.0000	0.0000	0.0000

b)

$e_r(\%)$ - ψ **at x = L**

Number of elements	Composites A	B	C
5	0.040	8.563	36.113
10	0.003	1.814	8.042
25	0.000	0.259	0.328
50	0.000	0.063	0.033
100	0.000	0.016	0.007
300	0.000	0.000	0.000

c)

$e_r(\%)$ - $\left(\sigma_x\right)_{\max}$ **at x = L**

Number of elements	Composites A	B	C
5	-0.568	-6.923	-18.239
10	-0.076	-2.704	-12.437
25	-0.013	-0.568	-4.266
50	-0.003	-0.131	-1.095
100	0.001	-0.029	-0.250
300	0.000	0.000	0.000

d)

$e_r(\%)$ - $\left(\tau_{xz}\right)_{\max}$ **at x = L/2**

Number of elements	Composites A	B	C
5	7.020	19.283	50.938
10	0.352	5.176	20.602
25	0.052	0.888	3.408
50	0.010	0.210	0.707
100	0.003	0.049	0.147
300	0.000	0.000	0.000

Table 3.5 – Convergence relative error for: a) w at x = L, b) ψ at x = L, c) maximum axial stress at x = L, d) and maximum shear stress at x = L/2.

3.2.7.3 Numerical examples

Cantilever beam under an end point load

The beam material is the highly heterogeneous laminate C defined in the previous analysis (Table 3.4). The span-to-thickness ratio is $\lambda = 5$.

The reference solution is a PS analysis using the structured mesh of 27000 four-node quadrilaterals shown in Figure 3.4. TBT theory is also compared employing a mesh of 300 two-node beam elements. Labels “LRZ-300”, “LRZ-50”, “LRZ-25”, and “LRZ-10” refer to the solution obtained by the LRZ meshes of 300, 50, 25 and 10 elements, respectively.

Deflection w along the beam length is shown in Figure 3.10. Very good agreement with the PS solution is obtained already for the LRZ-50 mesh. TBT results are considerable stiffer. Deflection value computed by TBT is about six times stiffer at the free edge.

Figure 3.11 shows the distribution of the axial displacements at the top and bottom surfaces of the top layer along the beam length. Excellent results are again obtained with the LRZ-50 mesh. The TBT results are far from the correct ones.

The thickness distribution for the axial displacement at sections located at distances $L/4$, $L/2$ and $3L/4$ from the clamped end are shown in **Figure 3.12**. Results for the LRZ element are in good agreement with the reference solution. The standard linear distribution of TBT theory is far from the correct zigzag results.

Figure 3.16 shows the distribution of the axial stress σ_x at the top and bottom surfaces of the beam cross section along the beam length. Very good results are obtained for the LRZ-50 and LRZ-300 meshes. Results for the LRZ-25 mesh compare reasonably well with the PS solution except in the vicinity of the clamped edge. However, this error is corrected for the LRZ-50 and LRZ-300 meshes. The TBT results yield a linear distribution of the axial stress along the beam, as expected. This introduces large errors in the axial stress values in the vicinity of the clamped support.

Thickness distribution for the transverse shear stress τ_{xz} at different sections are shown in Figure 3.13. LRZ results provide an accurate estimate of the average transverse shear stress value for each layer. The distribution of τ_{xz} across the thickness can be improved by using Eq.(3.38).

Figure 3.14 shows the thickness distribution of the axial stress σ_x at the clamped end and at the center of the beam. LRZ results are well approximated to the reference solution. TBT results have an erroneous stress distribution for the top and bottom layers at the clamped end. These differences are less important at the central section.

LRZ and TBT results for the distribution of the tangential shear stress τ_{xz} for each layer along the beam length are shown in Figure 3.15.

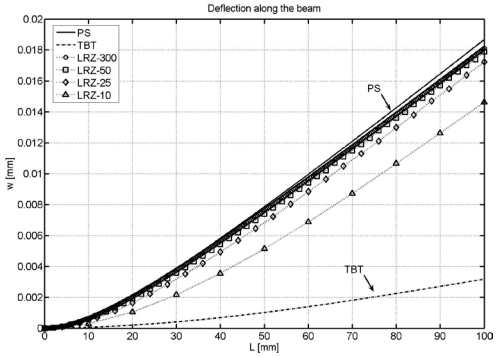

Figure 3.10 – Distribution of vertical displacement *w* along the beam length.

a) b)

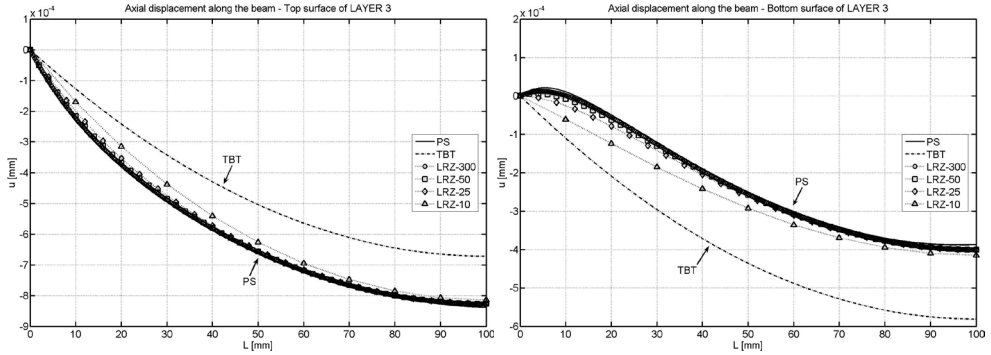

Figure 3.11 – Axial displacement *u* at the upper (a) and lower (b) surfaces of the top layer along the beam length.

a) b)

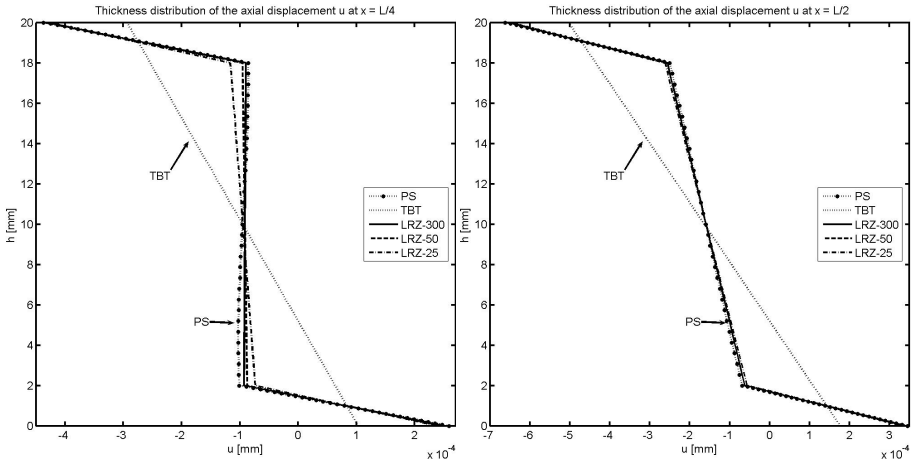

Figure 3.12 – Thickness distribution of the axial displacement u at x = L/4 (a), x = L/2 (b), and x = 3L/4 (c).

c)

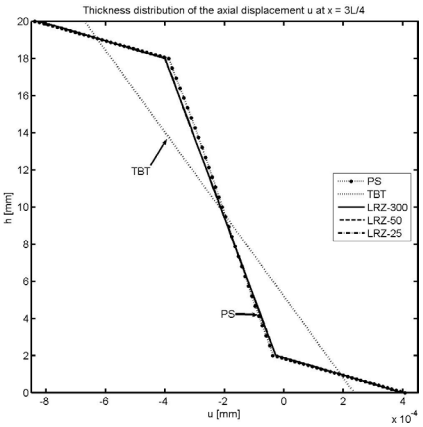

Figure 3.12 – Continuation.

a) b)

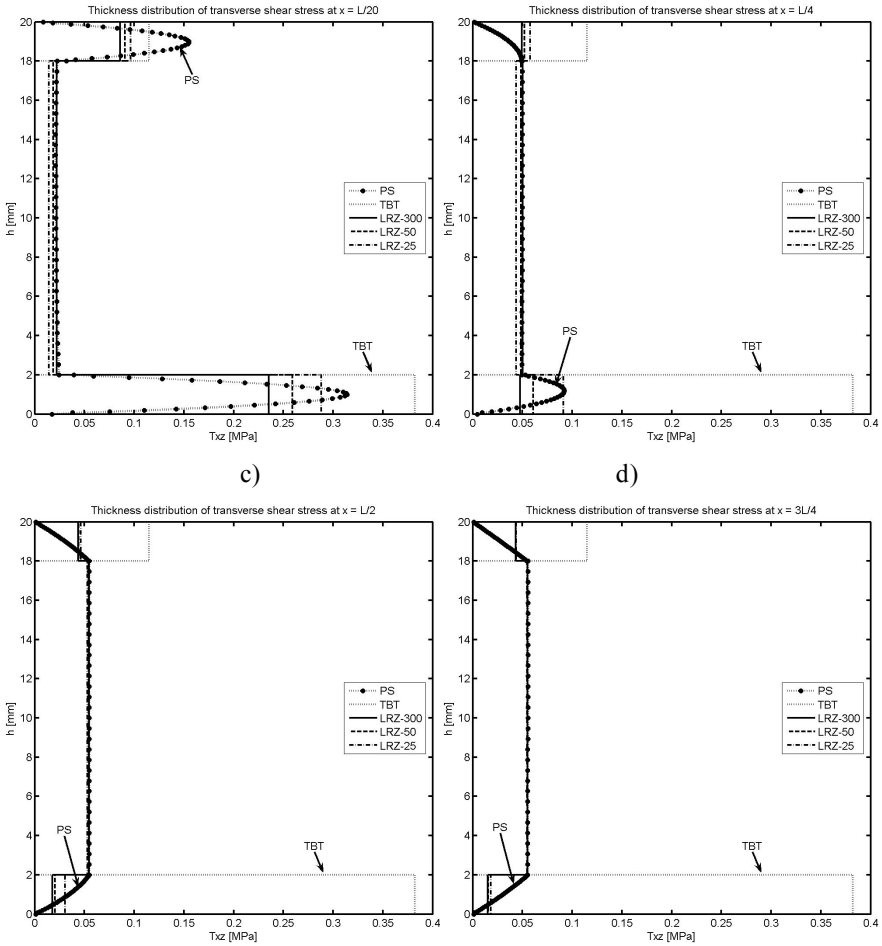

c) d)

Figure 3.13 – Thickness distribution of the transverse shear stress at x= L/20 (a), x = L/4 (b), x = L/2 (c), and x = 3L/4 (d).

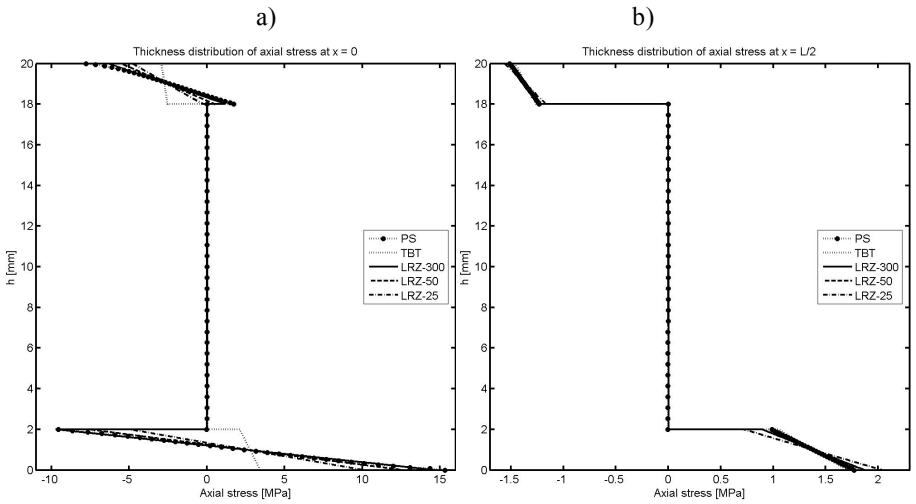

Figure 3.14 – Thickness distribution of the axial stress at x= 0 (a) and x = L/2 (b).

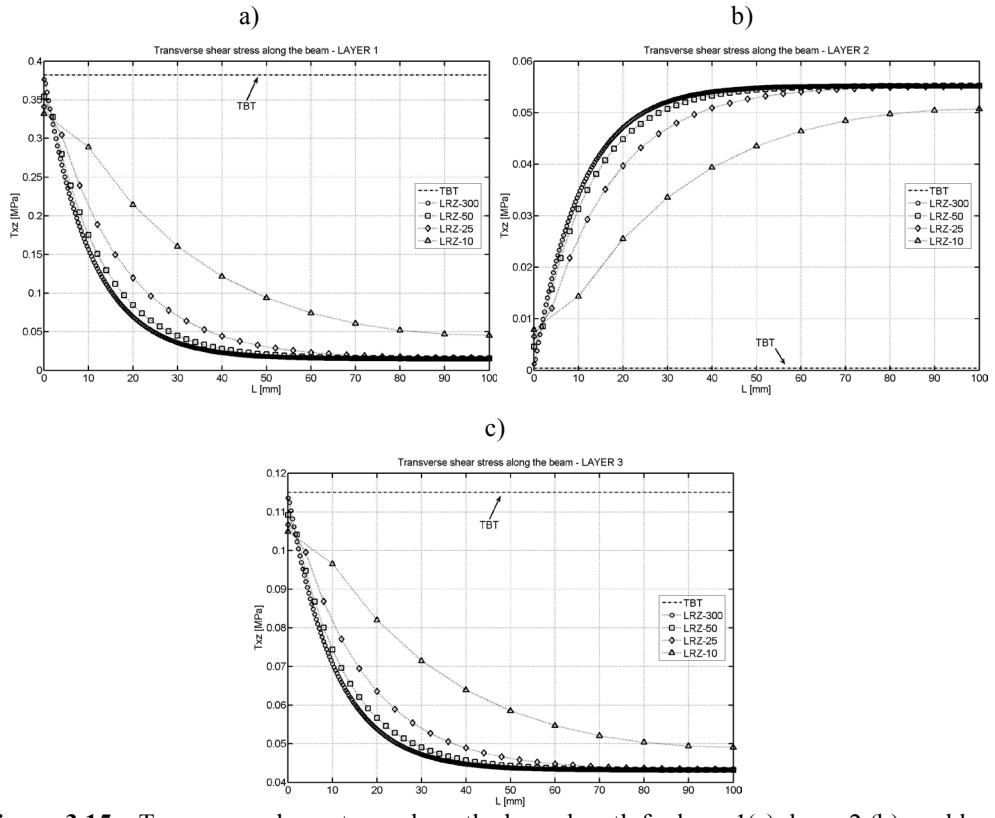

Figure 3.15 – Transverse shear stress along the beam length for layer 1(a), layer 2 (b), and layer 3 (c).

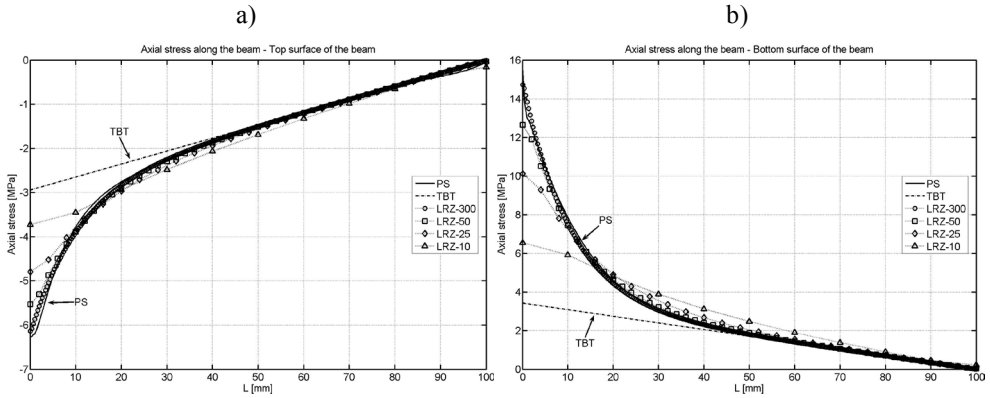

Figure 3.16 – Axial stress at the upper (a) and lower (b) surfaces of the cross section along the beam length.

Simple supported beam under uniformly distributed unit load

Laminated material properties are listed in Table 3.6. The span-to-thickness ratio is $\lambda = 5$.

	Laminated Material		
	Layer 1 (bottom)	Layer 2 (core)	Layer 3 (top)
h [mm]	6.6667	6.6667	6.6667
E [MPa]	2.19×10^5	5.30×10^5	7.39×10^5
G [MPa]	0.876×10^5	2.90×10^2	2.92×10^5

Table 3.6 – Material properties.

LRZ results are once more compared with those obtained with the TBT mesh of 300 two-noded elements and with a structured mesh of 27000 4-noded plane stress quadrilateral elements. PS solution is obtained by fixing the vertical displacement of all nodes at the end sections and the horizontal displacement for the mid-line edge nodes only. No advantage of symmetry was taken into account.

The distribution of the vertical deflection along the beam length is shown in Figure 3.17. For the finest LRZ mesh the central deflection is around 12% stiffer than the PS solution. The discrepancy is due to the difference in the way the simple support condition is modelled in beam and PS theories, as well as to the limitations of beam theory to model accurately very thick beams. TBT results are inaccurate, as expected.

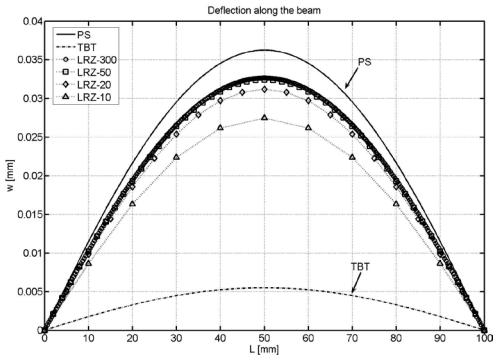

Figure 3.17 – Distribution of vertical displacement *w* along the beam length.

Figure 3.18 shows the distribution of the axial stress σ_x along the beam at the top surface for the second and third layer. Results show an acceptable accuracy of the LRZ solution with a maximum error of 10% for the finest mesh. On the contrary, the TBT model gives a too poor solution.

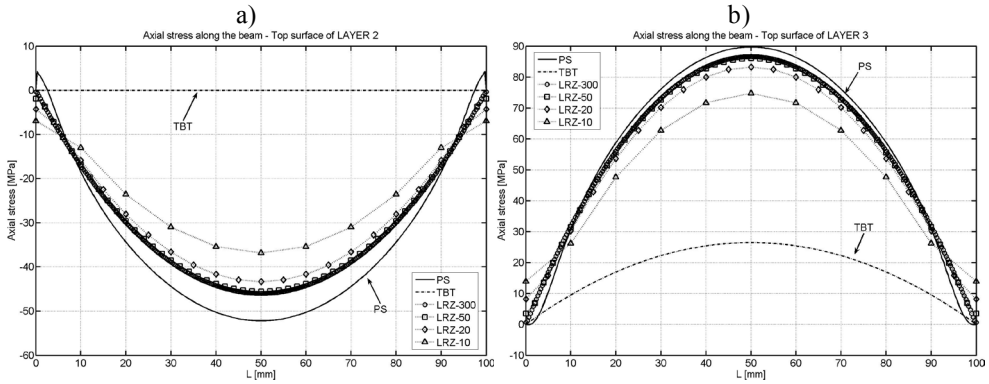

Figure 3.18 – Axial stress at the top surface for the second (a) and third (b) layer along the beam length.

Figure 3.19 shows the thickness distribution of the axial displacement at the left end section (x = 0) and at x = $L/4$. The LRZ element captures very well the zigzag shape of the axial displacement field even for a coarse mesh of 10 elements. The TBT element yields an unrealistic linear distribution.

Thickness distribution of the axial stress (at x = L/4, L/2) and the transverse shear stress (at x = L/20, L/4) are shown in Figure 3.20 and Figure 3.21, respectively. The accuracy of the LRZ results is again noticeable (even for the coarse 10 element mesh). The TBT element fails to capture the zigzag distribution of the axial stress and gives a wrong value of almost zero shear stress at the core layer.

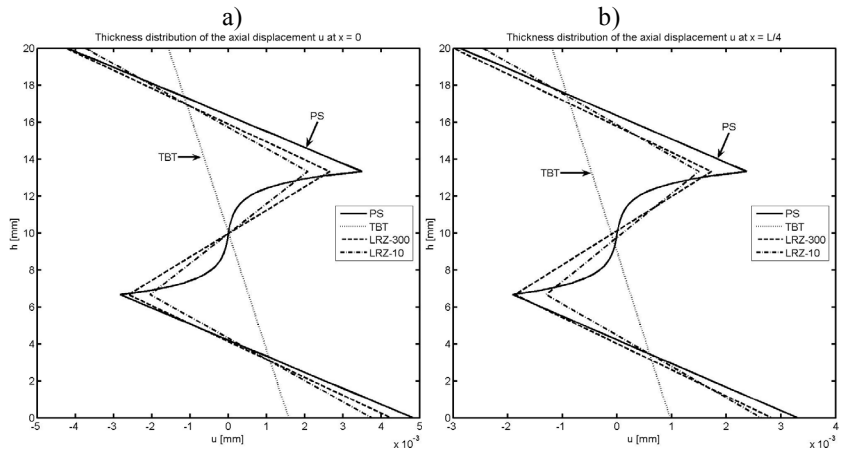

Figure 3.19 – Thickness distribution of the axial displacement *u* at x = 0 (a) and x = L/4 (b).

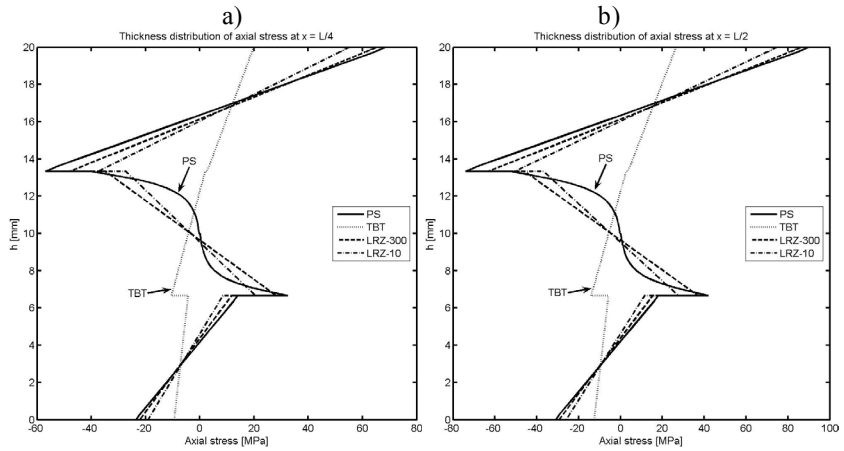

Figure 3.20 – Thickness distribution of the axial stress at x= L/4 (a) and x = L/2 (b).

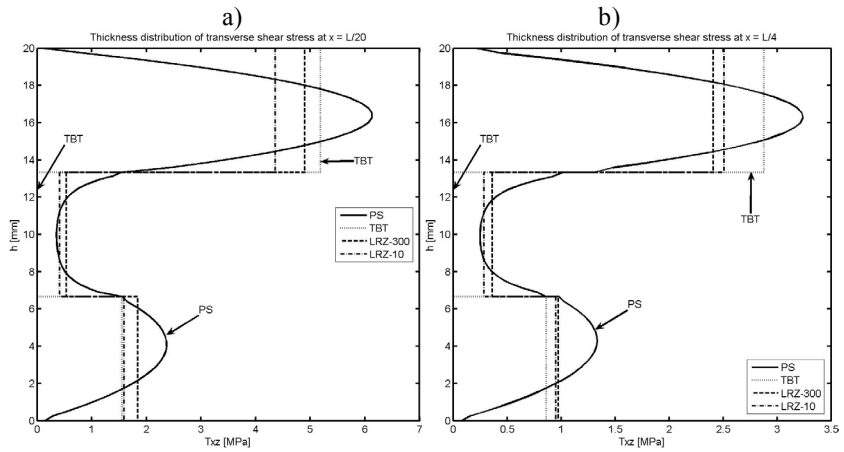

Figure 3.21 – Thickness distribution of the transverse shear stress at x= L/20 (a) and x = L/4 (b).

Figure 3.22 shows the distribution of the transverse shear stress along the beam for each ply obtained with the LRZ and TBT elements.

Figure 3.23 shows a similar set of results for a moderately thick SS beam (λ=10) and the same material properties. The distribution of the deflection and the axial stress along the beam length are shown in Figure 3.23a and Figure 3.23b, respectively. The accuracy of the LRZ element is again noticeable.

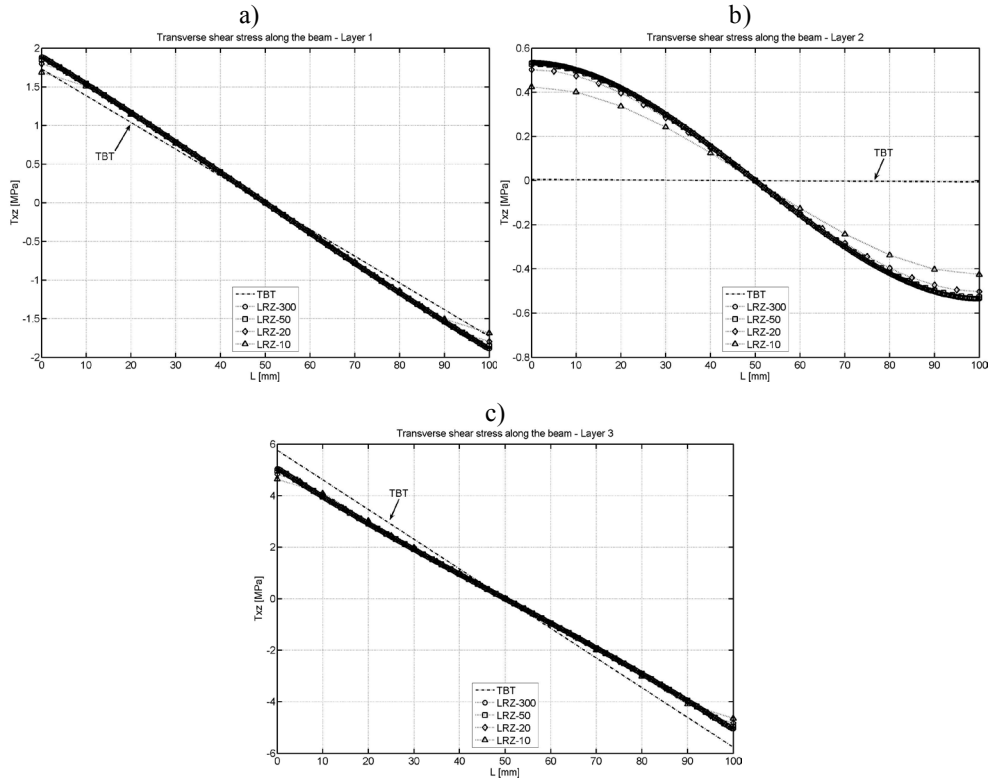

Figure 3.22 – Transverse shear stress along the beam length for layer 1(a), layer 2 (b), and layer 3 (c).

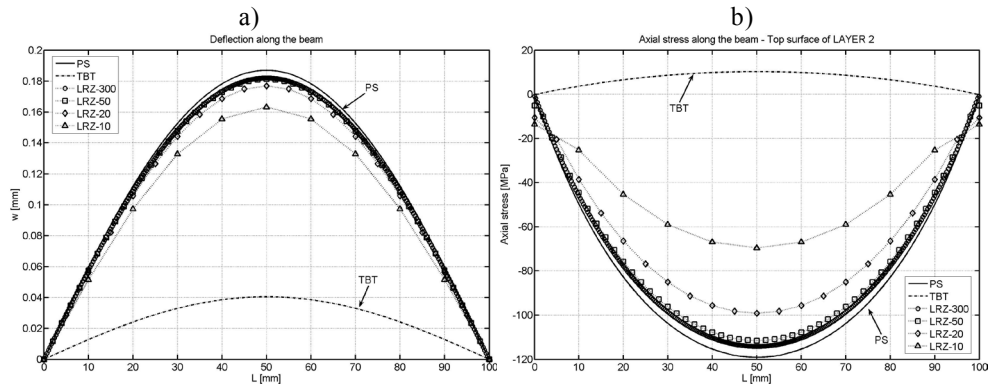

Figure 3.23 – Distribution of the vertical displacement *w* (a) and the axial stress at the top surface of second layer (b) along the beam length.

Non-symmetric ten-layered clamped beam under uniformly distributed unit load

In this example a ten-layered clamped slender beam (L = 100 mm, h = 5 mm, b = 1 mm, $\lambda = 20$) under uniformly distributed loading (q = 1KN/mm) is analyzed. Laminated material properties are listed in Table 3.7.

a)

Layer	h_i	Material
1	0.5	IV
2	0.6	I
3	0.5	V
4	0.4	III
5	0.7	IV
6	0.1	III
7	0.4	II
8	0.5	V
9	0.3	I
10	1	II

b)

Material	E [MPa]	G [MPa]
I	2.19×10^5	0.876×10^5
II	7.30×10^5	2.92×10^5
III	7.30×10^2	2.92×10^2
IV	5.30×10^5	2.12×10^5
V	0.82×10^5	0.328×10^5

Table 3.7 – Layer distribution (a) and material properties (b).

Figure 3.24 shows the deflection along the beam for LRZ meshes of 10 and 300 elements (LRZ-10 and LRZ-300). LRZ results are compared with PS and TBT results. A mesh of 27.000 4-noded PS quadrilaterals and a mesh of 300 TBT elements are used. Even for the coarse 10 element mesh the LRZ deflection is good approximated to the PS solution.

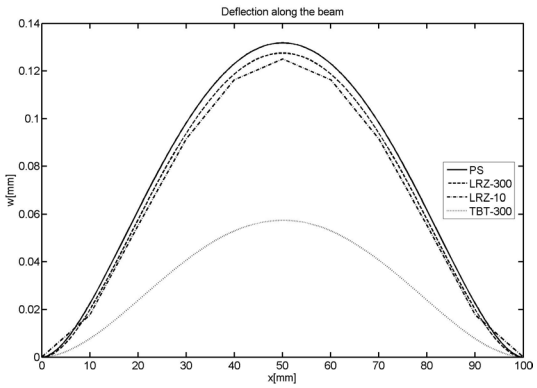

Figure 3.24 – Distribution of vertical displacement w along the beam length.

Figure 3.25 shows the thickness distribution of the axial displacement and the axial stress for the section at $x = L/4$. The accuracy of the LRZ results is once more remarkable.

Thickness distribution of the transverse shear stress at x = L4 is shown in Figure 3.26. Figure 3.26a shows the values obtained by the constitutive equation Eq.(3.10). These results are clearly better than those obtained with the TBT element but only coincide in an average sense with the plane stress FEM solution. The improved computation of the transverse shear stress using Eq.(3.38) is shown in Figure 3.26b, where a very good approximation to the PS result is observed even for the coarse mesh of 10 LRZ elements.

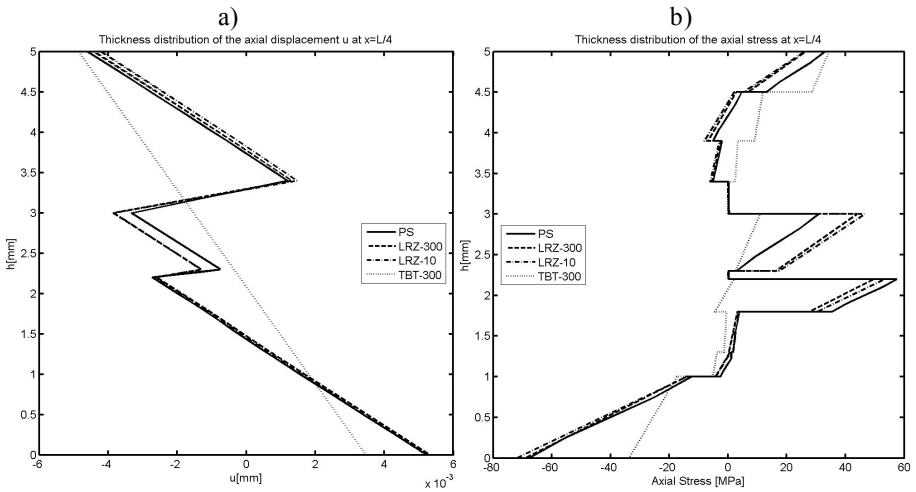

Figure 3.25 – Thickness distribution of the axial displacement *u* (a) and the axial stress (b) at x = L/4.

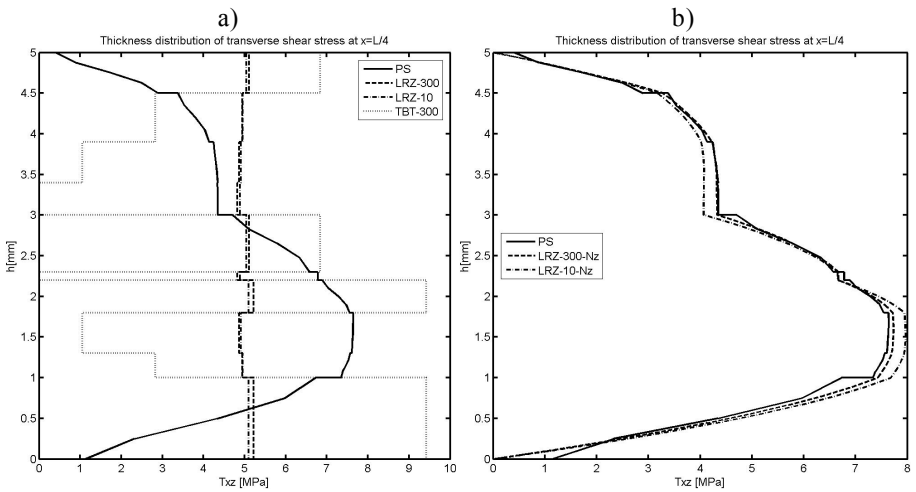

Figure 3.26 – Thickness distribution of the transverse shear stress at x = L/4 computed by the constitutive equation 3.10 (a) and by the improved equation 3.38 (b).

3.3 QLRZ plate finite element

The formulation of an isoparametric four-node C^0 quadrilateral plate element, named QLRZ, with seven kinematic variables per node based on the RZT theory is

presented in this Section. This element is designed for modeling thick and thin plate/shell structures of highly heterogeneous laminated materials. The original form of this element suffers of shear looking, as shown in Section 3.3.7.1, which is avoided by means of an *assumed linear shear strain field*. The performance of QLRZ is analyzed in three different studies: *verification*, *convergence* and *comparison*. The *verification* study (Section 3.3.7.2) aims at evaluating the performance of this element when the material is homogenous, i.e. when the zigzag function vanishes. The influence of the material transverse heterogeneity on convergence and accuracy of the QLRZ element is analyzed in the *convergence* study (Section 3.3.7.3). Finally, the performance of the QLRZ element for modeling highly heterogeneous materials is evaluated in the *comparison* analysis (Section 3.3.7.4).

3.3.1 Plate RZT kinematics

The QLRZ kinematics is defined by Eq.(2.1) in Section 2.1.3.1 as

$$\begin{aligned} u^k(x,y,z) &= u_0(x,y) - z\cdot\theta_x(x,y) + \overline{u}^k(x,y,z) \\ v^k(x,y,z) &= v_0(x,y) - z\cdot\theta_y(x,y) + \overline{v}^k(x,y,z) \\ w\,(x,y) &= w_0(x,y) \end{aligned} \qquad 3.40$$

where the axial displacement zigzag function $\overline{u}^k$ and $\overline{v}^k$ are defined as

$$\begin{aligned} \overline{u}^k &= \phi_x^k(z)\cdot\psi_x(x,y) \\ \overline{v}^k &= \phi_y^k(z)\cdot\psi_y(x,y) \end{aligned} \qquad 3.41$$

The unknown variables for the plate RZT theory are

$$\mathbf{a} = \begin{bmatrix} u_0 & v_0 & w_0 & \theta_x & \theta_y & \psi_x & \psi_y \end{bmatrix}^T \qquad 3.42$$

where the uniform displacement u_0, v_0 and w_0, and the bending rotation θ_x and θ_y are derivate from the FSDT theory, where the ψ_i variables are associated with the added displacement zigzag functions $\overline{u}^k$ and $\overline{v}^k$.

3.3.2 Stain and generalized strain

For convenience, the strain $\boldsymbol{\varepsilon}^k$ of the kth layer is split into the in-plane ($\boldsymbol{\varepsilon}_p^k$) and the transverse shear ($\boldsymbol{\varepsilon}_t^k$) strains as

$$\boldsymbol{\varepsilon}^k = \begin{bmatrix} \boldsymbol{\varepsilon}_p \\ \boldsymbol{\varepsilon}_t \end{bmatrix}^k = \begin{bmatrix} \varepsilon_x \\ \varepsilon_y \\ \gamma_{xy} \\ \gamma_{xz} \\ \gamma_{yz} \end{bmatrix}^k = \begin{bmatrix} \dfrac{\partial u^k}{\partial x} \\ \dfrac{\partial v^k}{\partial y} \\ \dfrac{\partial u^k}{\partial y} + \dfrac{\partial v^k}{\partial x} \\ \dfrac{\partial u^k}{\partial z} + \dfrac{\partial w}{\partial x} \\ \dfrac{\partial v^k}{\partial z} + \dfrac{\partial w}{\partial y} \end{bmatrix} =$$

$$= \begin{bmatrix} \dfrac{\partial u_0}{\partial x} \\ \dfrac{\partial v_0}{\partial y} \\ \dfrac{\partial u_0}{\partial y} + \dfrac{\partial v_0}{\partial x} \\ 0 \\ 0 \end{bmatrix} + \begin{bmatrix} -z\dfrac{\partial \theta_x}{\partial x} \\ -z\dfrac{\partial \theta_y}{\partial y} \\ -z\left(\dfrac{\partial \theta_x}{\partial y} + \dfrac{\partial \theta_y}{\partial x}\right) \\ \dfrac{\partial w_0}{\partial x} - \theta_x \\ \dfrac{\partial w_0}{\partial y} - \theta_y \end{bmatrix} + \begin{bmatrix} \phi_x^k(z)\dfrac{\partial \psi_x}{\partial x} \\ \phi_y^k(z)\dfrac{\partial \psi_y}{\partial y} \\ \phi_x^k(z)\dfrac{\partial \psi_x}{\partial y} + \phi_y^k(z)\dfrac{\partial \psi_y}{\partial x} \\ \dfrac{\partial \phi_x^k}{\partial z}\psi_x \\ \dfrac{\partial \phi_y^k}{\partial z}\psi_y \end{bmatrix} =$$

$$= \begin{bmatrix} \boldsymbol{\varepsilon}_m \\ 0 \end{bmatrix} + \begin{bmatrix} \boldsymbol{\varepsilon}_b \\ \boldsymbol{\varepsilon}_s \end{bmatrix} + \begin{bmatrix} \boldsymbol{\varepsilon}_{mb\phi} \\ \boldsymbol{\varepsilon}_{s\phi} \end{bmatrix}^k = \begin{bmatrix} \mathbf{S}_p & 0 \\ 0 & \mathbf{S}_t \end{bmatrix}^k \cdot \begin{bmatrix} \hat{\boldsymbol{\varepsilon}}_p \\ \hat{\boldsymbol{\varepsilon}}_t \end{bmatrix} \qquad 3.43$$

where $\boldsymbol{\varepsilon}_m$, $\boldsymbol{\varepsilon}_b$ and $\boldsymbol{\varepsilon}_s$ are the strain vectors duo to membrane, bending and transverse shear effects of the RMT theory, respectively. The in-plane and transverse shear strains vectors emanating from the RZT theory are denoted by $\boldsymbol{\varepsilon}_{mb\phi}$ and $\boldsymbol{\varepsilon}_{s\phi}$. $\hat{\boldsymbol{\varepsilon}}_p$ and $\hat{\boldsymbol{\varepsilon}}_t$ are the generalized in-plane and transverse shear strains vectors, respectively, defined as

$$\hat{\boldsymbol{\varepsilon}}_p = \begin{bmatrix} \hat{\boldsymbol{\varepsilon}}_m \\ \hat{\boldsymbol{\varepsilon}}_b \\ \hat{\boldsymbol{\varepsilon}}_{mb\phi} \end{bmatrix} \quad ; \quad \hat{\boldsymbol{\varepsilon}}_t = \begin{bmatrix} \hat{\boldsymbol{\varepsilon}}_s \\ \hat{\boldsymbol{\varepsilon}}_{s\phi} \end{bmatrix} \qquad 3.44$$

$$\mathbf{S}_p^k = \begin{bmatrix} \mathbf{S}_m & \mathbf{S}_b & \mathbf{S}_{mb\phi}^k \end{bmatrix} \quad ; \quad \mathbf{S}_t^k = \begin{bmatrix} \mathbf{S}_s & \mathbf{S}_{s\phi}^k \end{bmatrix}$$

where $(\hat{\bullet})$ denotes the generalized strain vectors given by

$$\hat{\boldsymbol{\varepsilon}}_m = \begin{bmatrix} \dfrac{\partial u_0}{\partial x} & \dfrac{\partial v_0}{\partial y} & \dfrac{\partial u_0}{\partial y} + \dfrac{\partial v_0}{\partial x} \end{bmatrix}^T \quad ; \quad \hat{\boldsymbol{\varepsilon}}_s = \begin{bmatrix} \dfrac{\partial w_0}{\partial x} - \theta_x \\ \dfrac{\partial w_0}{\partial y} - \theta_y \end{bmatrix} = \begin{bmatrix} \gamma_{xz} \\ \gamma_{yz} \end{bmatrix}$$

$$\hat{\boldsymbol{\varepsilon}}_b = \begin{bmatrix} \dfrac{\partial \theta_x}{\partial x} & \dfrac{\partial \theta_y}{\partial y} & \dfrac{\partial \theta_x}{\partial y} + \dfrac{\partial \theta_y}{\partial x} \end{bmatrix}^T \quad ; \quad \hat{\boldsymbol{\varepsilon}}_{s\phi} = \begin{bmatrix} \psi_x \\ \psi_y \end{bmatrix} \qquad 3.45$$

$$\hat{\boldsymbol{\varepsilon}}_{mb\phi} = \begin{bmatrix} \dfrac{\partial \psi_x}{\partial x} & \dfrac{\partial \psi_y}{\partial y} & \dfrac{\partial \psi_x}{\partial y} & \dfrac{\partial \psi_y}{\partial x} \end{bmatrix}^T$$

and matrix operators $\mathbf{S}$ are defined as

$$\mathbf{S}_m = \begin{bmatrix} 1 & 0 & 0 \\ 0 & 1 & 0 \\ 0 & 0 & 1 \end{bmatrix} = \mathrm{I}_3 \quad ; \quad \mathbf{S}_b = -z\,\mathbf{I}_3 \quad ; \quad \mathbf{S}_s = \begin{bmatrix} 1 & 0 \\ 0 & 1 \end{bmatrix} = \mathbf{I}_2$$

$$\mathbf{S}^k_{mb\phi} = \begin{bmatrix} \phi^k_x(z) & 0 & 0 & 0 \\ 0 & \phi^k_y(z) & 0 & 0 \\ 0 & 0 & \phi^k_x(z) & \phi^k_y(z) \end{bmatrix} \quad ; \quad \mathbf{S}^k_{s\phi} = \begin{bmatrix} \dfrac{\partial \phi^k_x}{\partial z} & 0 \\ 0 & \dfrac{\partial \phi^k_y}{\partial z} \end{bmatrix} \qquad 3.46$$

In Eq.(3.45) $\gamma_{iz}\ (i = x, y)$ is the average transverse shear strain of RMT. Note that ϕ^k_i is piecewise linear, hence, its derivative $\left(\dfrac{\partial \phi^k_i}{\partial z} = \beta^k_i \right)$ is constant within each layer.

3.3.3 Stress-strain constitutive relationships

The reduced elasticity matrix for the orthotropic kth layer is given by

$$\bar{\mathbf{D}}^k = \begin{bmatrix} \bar{\mathbf{D}}_p & \mathbf{0} \\ \mathbf{0} & \bar{\mathbf{D}}_t \end{bmatrix}^k \qquad 3.47$$

with

$$\bar{\mathbf{D}}_p^k = \frac{1}{1-\upsilon_{12}\upsilon_{21}}\begin{bmatrix} E_1 & \upsilon_{12}E_2 & 0 \\ \upsilon_{12}E_2 & E_2 & 0 \\ 0 & 0 & (1-\upsilon_{12}\upsilon_{21})G_{12} \end{bmatrix} \qquad 3.48$$

$$\bar{\mathbf{D}}_t^k = \begin{bmatrix} G_{13} & 0 \\ 0 & G_{23} \end{bmatrix}$$

being E and G the Young and the shear moduli, respectively, and υ the Poisson's ratio. It is important to note that the strains $\boldsymbol{\varepsilon}^k$ are referred to the local coordinate system (x,y,z) whereas the $\bar{\mathbf{D}}_{ij}^k$ magnitudes are referred to the material orientation (e1,e2,e3) (Figure 3.27). Direction e1 is parallel to the main in-plane direction[19], e2 is the in-plane direction transverse to the e1, and e3 is the through-thickness direction that is coincident with the local vertical direction z. The relations between the basis vectors are defined by

$$\begin{bmatrix} \mathrm{e1} \\ \mathrm{e2} \\ \mathrm{e3} \end{bmatrix} = \mathbf{T}\cdot\begin{bmatrix} \mathrm{x} \\ \mathrm{y} \\ \mathrm{z} \end{bmatrix} \qquad \text{with} \qquad \mathbf{T} = \begin{bmatrix} \mathrm{c} & \mathrm{s} & 0 \\ -\mathrm{s} & \mathrm{c} & 0 \\ 0 & 0 & 1 \end{bmatrix} \qquad 3.49$$

where $\mathrm{c} = \cos(\alpha)$ and $\mathrm{s} = \sin(\alpha)$.

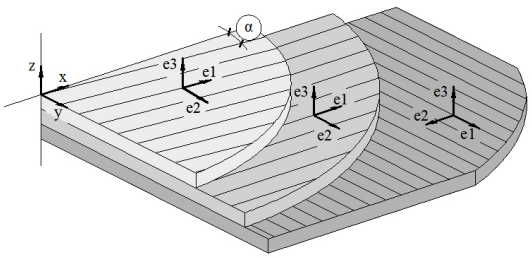

Figure 3.27 – Local coordinate system (x,y,z) and material orientation (e1,e2,e3). The angle between vector x and e1 is defined by α.

When material orientation is not correlated with local coordinate, e.g. the angle α between vectors x and e1 is different to cero, a transformation of the constitutive matrix $\bar{\mathbf{D}}^k$ to the local orientation has to be done by

[19] The main in-plane orientation e1 is coincident to that on which the higher in-plane Young's modulus is oriented. For advanced composite materials, direction e1 is parallel to the fibre orientation.

$$\mathbf{D}^k = \mathbf{\Pi}^T \cdot \bar{\mathbf{D}}^k \cdot \mathbf{\Pi} = \begin{bmatrix} \mathbf{D}_p & \mathbf{0} \\ \mathbf{0} & \mathbf{D}_t \end{bmatrix}^k \tag{3.50}$$

with

$$\mathbf{\Pi} = \begin{bmatrix} c^2 & s^2 & sc & 0 & 0 \\ s^2 & c^2 & -sc & 0 & 0 \\ -2sc & 2sc & c^2 - s^2 & 0 & 0 \\ 0 & 0 & 0 & c & s \\ 0 & 0 & 0 & -s & c \end{bmatrix}$$

Note, if $\alpha = 0$, that implies: $\mathbf{\Pi} = \mathbf{I}_5$ and $\mathbf{D}^k = \bar{\mathbf{D}}^k$.

Then, the stress-strain constitutive relationship of the kth layer referred to the local coordinate system (x,y,z) is defined as

$$\boldsymbol{\sigma}^k = \begin{bmatrix} \boldsymbol{\sigma}_p \\ \hline \boldsymbol{\sigma}_t \end{bmatrix}^k = \begin{bmatrix} \sigma_x \\ \sigma_y \\ \tau_{xy} \\ \hline \tau_{xz} \\ \tau_{yz} \end{bmatrix}^k = \begin{bmatrix} \mathbf{D}_p & \mathbf{0} \\ \mathbf{0} & \mathbf{D}_t \end{bmatrix}^k \cdot \begin{bmatrix} \boldsymbol{\varepsilon}_p \\ \boldsymbol{\varepsilon}_t \end{bmatrix}^k = \mathbf{D}^k \boldsymbol{\varepsilon}^k \tag{3.51}$$

where $\boldsymbol{\sigma}_p^k$ and $\boldsymbol{\sigma}_t^k$ are the in-plane and the transverse shear stresses vectors, respectively.

Finally, the stresses $\bar{\boldsymbol{\sigma}}^k$ and strains $\bar{\boldsymbol{\varepsilon}}^k$ vector referred to the material coordinate system (e1,e2,e3) for the kth layer are computed by

$$\begin{aligned} \bar{\boldsymbol{\sigma}}^k &= \left(\mathbf{\Pi}^{k^T}\right)^{-1} \cdot \boldsymbol{\sigma}^k = \bar{\mathbf{D}}^k \cdot \bar{\boldsymbol{\varepsilon}}^k \\ \bar{\boldsymbol{\varepsilon}}^k &= \mathbf{\Pi}^k \cdot \boldsymbol{\varepsilon}^k \end{aligned} \tag{3.52}$$

Although layers are treated as isotropic or orthotropic material in this work, the mechanical behavior of each component within FRP laminates (e.g. fibers and matrix) can be separately modeled using the well-known Mixing theory [61, 62] or a more advanced mixing theory called Serial/Parallel [63].

3.3.4 Stress resultants

Due to the subdivision of the strains (Eq.(3.43)) also the stress resultant vector $\hat{\boldsymbol{\sigma}}$ is subdivided into membrane forces $\hat{\boldsymbol{\sigma}}_m$, bending moments $\hat{\boldsymbol{\sigma}}_b$, transverse shear forces

$\hat{\boldsymbol{\sigma}}_s$, pseudo-bending moments $\hat{\boldsymbol{\sigma}}_{mb\phi}$ and pseudo-shear forces $\hat{\boldsymbol{\sigma}}_{s\phi}$ (Figure 3.28). $\hat{\boldsymbol{\sigma}}_m$, $\hat{\boldsymbol{\sigma}}_b$, and $\hat{\boldsymbol{\sigma}}_s$ derives from the standard plate theory, whereas $\hat{\boldsymbol{\sigma}}_{mb\phi}$ and $\hat{\boldsymbol{\sigma}}_{s\phi}$ are pseudo stress resultants from the RZT plate theory.

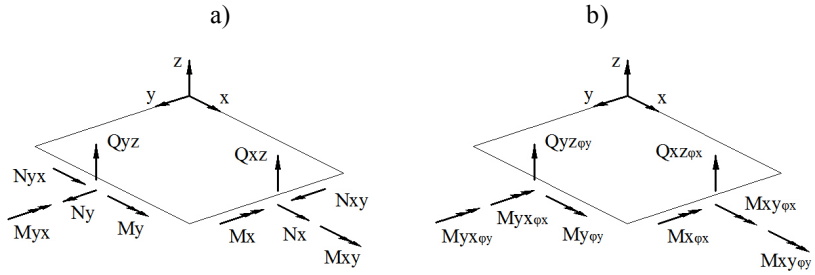

Figure 3.28 – Direction of stress resultants of standard plate theory (a) and those derived from the RZT plate theory (b).

The stress resultants for a plate are obtained by integrating stresses (Eq.(3.51)) over the thickness as

Membrane forces $\hat{\boldsymbol{\sigma}}_m$

$$\hat{\boldsymbol{\sigma}}_m = \begin{bmatrix} N_x \\ N_y \\ N_{xy} \end{bmatrix} = \int_z \mathbf{S}_m^T \boldsymbol{\sigma}_p^k \mathrm{d}z \qquad 3.53$$

$$\hat{\boldsymbol{\sigma}}_m = \left(\int_z \mathbf{S}_m^T \mathbf{D}_p^k \mathbf{S}_m \mathrm{d}z\right)\hat{\boldsymbol{\varepsilon}}_m + \left(\int_z \mathbf{S}_m^T \mathbf{D}_p^k \mathbf{S}_b \mathrm{d}z\right)\hat{\boldsymbol{\varepsilon}}_b + \left(\int_z \mathbf{S}_m^T \mathbf{D}_p^k \mathbf{S}_{mb\phi}^k \mathrm{d}z\right)\hat{\boldsymbol{\varepsilon}}_{mb\phi}$$

$$\hat{\boldsymbol{\sigma}}_m = \hat{\mathbf{D}}_m \hat{\boldsymbol{\varepsilon}}_m + \hat{\mathbf{D}}_{mb} \hat{\boldsymbol{\varepsilon}}_b + \hat{\mathbf{D}}_{mmb\phi} \hat{\boldsymbol{\varepsilon}}_{mb\phi}$$

$$\hat{\mathbf{D}}_m = \int_z \mathbf{S}_m^T \mathbf{D}_p^k \mathbf{S}_m \mathrm{d}z$$

$$\hat{\mathbf{D}}_{mb} = \int_z \mathbf{S}_m^T \mathbf{D}_p^k \mathbf{S}_b \mathrm{d}z$$

$$\hat{\mathbf{D}}_{mmb\phi} = \int_z \mathbf{S}_m^T \mathbf{D}_p^k \mathbf{S}_{mb\phi}^k \mathrm{d}z$$

Bending moments $\hat{\boldsymbol{\sigma}}_b$

$$\hat{\boldsymbol{\sigma}}_b = \begin{bmatrix} M_x \\ M_y \\ M_{xy} \end{bmatrix} = \int_z \mathbf{S}_b^T \boldsymbol{\sigma}_p^k \mathrm{d}z \qquad 3.54$$

$$\hat{\boldsymbol{\sigma}}_b = \left(\int_z \mathbf{S}_b^T \mathbf{D}_p^k \mathbf{S}_m \mathrm{dz}\right)\hat{\boldsymbol{\varepsilon}}_m + \left(\int_z \mathbf{S}_b^T \mathbf{D}_p^k \mathbf{S}_b \mathrm{dz}\right)\hat{\boldsymbol{\varepsilon}}_{\boldsymbol{b}} + \left(\int_z \mathbf{S}_b^T \mathbf{D}_p^k \mathbf{S}_{mb\phi}^k \mathrm{dz}\right)\hat{\boldsymbol{\varepsilon}}_{\boldsymbol{mb\phi}}$$

$$\hat{\boldsymbol{\sigma}}_b = \hat{\mathbf{D}}_{bm}\hat{\boldsymbol{\varepsilon}}_m + \hat{\mathbf{D}}_b\hat{\boldsymbol{\varepsilon}}_{\boldsymbol{b}} + \hat{\mathbf{D}}_{bmb\phi}\hat{\boldsymbol{\varepsilon}}_{\boldsymbol{mb\phi}}$$

$$\hat{\mathbf{D}}_{bm} = \int_z \mathbf{S}_b^T \mathbf{D}_p^k \mathbf{S}_m \mathrm{dz}$$
$$\hat{\mathbf{D}}_b = \int_z \mathbf{S}_b^T \mathbf{D}_p^k \mathbf{S}_b \mathrm{dz}$$
$$\hat{\mathbf{D}}_{bmb\phi} = \int_z \mathbf{S}_b^T \mathbf{D}_p^k \mathbf{S}_{mb\phi}^k \mathrm{dz}$$

Transverse shear forces $\hat{\boldsymbol{\sigma}}_s$

$$\hat{\boldsymbol{\sigma}}_s = \begin{bmatrix} Q_{xz} \\ Q_{yz} \end{bmatrix} = \int_z \mathbf{S}_s^T \boldsymbol{\sigma}_t^k \mathrm{dz} \qquad 3.55$$

$$\hat{\boldsymbol{\sigma}}_s = \left(\int_z \mathbf{S}_s^T \mathbf{D}_t^k \mathbf{S}_s \mathrm{dz}\right)\hat{\boldsymbol{\varepsilon}}_s + \left(\int_z \mathbf{S}_s^T \mathbf{D}_t^k \mathbf{S}_{s\phi}^k \mathrm{dz}\right)\hat{\boldsymbol{\varepsilon}}_{s\phi}$$

$$\hat{\boldsymbol{\sigma}}_s = \hat{\mathbf{D}}_s\hat{\boldsymbol{\varepsilon}}_s + \hat{\mathbf{D}}_{ss\phi}\hat{\boldsymbol{\varepsilon}}_{s\phi}$$

$$\hat{\mathbf{D}}_s = \int_z \mathbf{S}_s^T \mathbf{D}_t^k \mathbf{S}_s \mathrm{dz}$$
$$\hat{\mathbf{D}}_{ss\phi} = \int_z \mathbf{S}_s^T \mathbf{D}_t^k \mathbf{S}_{s\phi}^k \mathrm{dz}$$

Pseudo-bending moments $\hat{\boldsymbol{\sigma}}_{mb\phi}$

$$\hat{\boldsymbol{\sigma}}_{mb\phi} = \begin{bmatrix} M_{x\phi_x} \\ M_{y\phi_y} \\ M_{xy\phi_x} \\ M_{xy\phi_y} \end{bmatrix} = \int_z \mathbf{S}_{mb\phi}^{k^T} \boldsymbol{\sigma}_p^k dz \qquad 3.56$$

$$\hat{\boldsymbol{\sigma}}_{mb\phi} = \left(\int_z \mathbf{S}_{mb\phi}^{k^T} \mathbf{D}_p^k \mathbf{S}_m \mathrm{dz}\right)\hat{\boldsymbol{\varepsilon}}_m + \left(\int_z \mathbf{S}_{mb\phi}^{k^T} \mathbf{D}_p^k \mathbf{S}_b \mathrm{dz}\right)\hat{\boldsymbol{\varepsilon}}_{\boldsymbol{b}} + \left(\int_z \mathbf{S}_{mb\phi}^{k^T} \mathbf{D}_p^k \mathbf{S}_{mb\phi}^k \mathrm{dz}\right)\hat{\boldsymbol{\varepsilon}}_{\boldsymbol{mb\phi}}$$

$$\hat{\boldsymbol{\sigma}}_{mb\phi} = \hat{\mathbf{D}}_{mb\phi m}\hat{\boldsymbol{\varepsilon}}_m + \hat{\mathbf{D}}_{mb\phi b}\hat{\boldsymbol{\varepsilon}}_{\boldsymbol{b}} + \hat{\mathbf{D}}_{mb\phi}\hat{\boldsymbol{\varepsilon}}_{\boldsymbol{mb\phi}}$$

$$\hat{\mathbf{D}}_{mb\phi m} = \int_z \mathbf{S}_{mb\phi}^{k^T} \mathbf{D}_p^k \mathbf{S}_m \mathrm{dz}$$

$$\hat{\mathbf{D}}_{mb\phi b} = \int_z \mathbf{S}_{mb\phi}^{k^T} \mathbf{D}_p^k \mathbf{S}_b \mathrm{dz}$$

$$\hat{\mathbf{D}}_{mb\phi} = \int_z \mathbf{S}_{mb\phi}^{k^T} \mathbf{D}_p^k \mathbf{S}_{mb\phi}^k \mathrm{dz}$$

and finally *pseudo-shear forces* $\hat{\boldsymbol{\sigma}}_{s\phi}$

$$\hat{\boldsymbol{\sigma}}_{s\phi} = \begin{bmatrix} Q_{xz\phi_x} \\ Q_{xz\phi_y} \end{bmatrix} = \int_z \mathbf{S}_{s\phi}^{k^T} \boldsymbol{\sigma}_t^k \mathrm{dz} \qquad 3.57$$

$$\hat{\boldsymbol{\sigma}}_{s\phi} = \left(\int_z \mathbf{S}_{s\phi}^{k^T} \mathbf{D}_t^k \mathbf{S}_s \mathrm{dz} \right) \hat{\boldsymbol{\varepsilon}}_s + \left(\int_z \mathbf{S}_{s\phi}^{k^T} \mathbf{D}_t^k \mathbf{S}_{s\phi}^k \mathrm{dz} \right) \hat{\boldsymbol{\varepsilon}}_{s\phi}$$

$$\hat{\boldsymbol{\sigma}}_{s\phi} = \hat{\mathbf{D}}_{s\phi s} \hat{\boldsymbol{\varepsilon}}_s + \hat{\mathbf{D}}_{s\phi} \hat{\boldsymbol{\varepsilon}}_{s\phi}$$

$$\hat{\mathbf{D}}_{s\phi s} = \int_z \mathbf{S}_{s\phi}^{k^T} \mathbf{D}_t^k \mathbf{S}_s \mathrm{dz}$$

$$\hat{\mathbf{D}}_{s\phi} = \int_z \mathbf{S}_{s\phi}^{k^T} \mathbf{D}_t^k \mathbf{S}_{s\phi}^k \mathrm{dz}$$

The matrix expression for the stress resultants $\hat{\boldsymbol{\sigma}}$ can be written as

$$\hat{\boldsymbol{\sigma}} = \begin{bmatrix} \hat{\boldsymbol{\sigma}}_p \\ \hat{\boldsymbol{\sigma}}_t \end{bmatrix} = \begin{bmatrix} \tilde{\mathbf{D}}_p & \mathbf{0} \\ \mathbf{0} & \tilde{\mathbf{D}}_t \end{bmatrix} \cdot \begin{bmatrix} \hat{\boldsymbol{\varepsilon}}_p \\ \hat{\boldsymbol{\varepsilon}}_t \end{bmatrix} \qquad 3.58$$

where $\hat{\boldsymbol{\sigma}}_p$ and $\hat{\boldsymbol{\sigma}}_t$ contain the in-plane and transverse shear stress resultants, respectively,

$$\hat{\boldsymbol{\sigma}}_p = \begin{bmatrix} \hat{\boldsymbol{\sigma}}_m \\ \hat{\boldsymbol{\sigma}}_b \\ \hat{\boldsymbol{\sigma}}_{mb\phi} \end{bmatrix} \quad ; \quad \hat{\boldsymbol{\sigma}}_t = \begin{bmatrix} \hat{\boldsymbol{\sigma}}_s \\ \hat{\boldsymbol{\sigma}}_{s\phi} \end{bmatrix} \qquad 3.59$$

and the in-plane and transverse shear generalized constitutive matrices, $\tilde{\mathbf{D}}_p$ and $\tilde{\mathbf{D}}_t$ respectively, are given by

$$\tilde{\mathbf{D}}_p = \begin{bmatrix} \hat{\mathbf{D}}_m & \hat{\mathbf{D}}_{mb} & \hat{\mathbf{D}}_{mmb\phi} \\ \hat{\mathbf{D}}_{bm} & \hat{\mathbf{D}}_b & \hat{\mathbf{D}}_{bmb\phi} \\ \hat{\mathbf{D}}_{mb\phi m} & \hat{\mathbf{D}}_{mb\phi b} & \hat{\mathbf{D}}_{mb\phi} \end{bmatrix} \quad ; \quad \tilde{\mathbf{D}}_t = \begin{bmatrix} \hat{\mathbf{D}}_s & \hat{\mathbf{D}}_{ss\phi} \\ \hat{\mathbf{D}}_{s\phi s} & \hat{\mathbf{D}}_{s\phi} \end{bmatrix} \qquad 3.60$$

Analytical integration is used to compute the generalized constitutive matrices $\hat{\mathbf{D}}$.

3.3.5 Principle of virtual work

Let us consider a plate of volume V, which is subjected to the distributed surface **q** and line **f** loads applied on the surface Γ_A and the contour Γ_L, respectively. Point loads p_i are also acting on the plate. For this case, the differential equations of equilibrium (Eq.(3.4)) is rewritten as

$$\int_V \delta\boldsymbol{\varepsilon}^{k^T}\boldsymbol{\sigma}^k \, dV = \int_{\Gamma_A} \delta\mathbf{a}^T\mathbf{q} \, d\Gamma_A + \int_{\Gamma_L} \delta\mathbf{a}^T\mathbf{f} \, d\Gamma_L + \sum_{i=1}^{pl} \delta a_i p_i \qquad 3.61$$

where the l.h.s. is the internal virtual work performed by the stresses $\boldsymbol{\sigma}^k$ and the r.h.s. is the external virtual work.

Substituting Eq.(3.43) into the l.h.s. of Eq.(3.61) gives

$$\begin{aligned}\int_V \delta\boldsymbol{\varepsilon}^{k^T}\boldsymbol{\sigma}^k \, dV &= \int_V \left(\delta\hat{\boldsymbol{\varepsilon}}_m^T\mathbf{S}_m^T + \delta\hat{\boldsymbol{\varepsilon}}_b^T\mathbf{S}_b^T + \delta\hat{\boldsymbol{\varepsilon}}_{mb\phi}^T\mathbf{S}_{mb\phi}^{k^T}\right)\boldsymbol{\sigma}_p^k \, dV + \\ &\quad + \int_V \left(\delta\hat{\boldsymbol{\varepsilon}}_s^T\mathbf{S}_s^T + \delta\hat{\boldsymbol{\varepsilon}}_{s\phi}^T\mathbf{S}_{s\phi}^{k^T}\right)\boldsymbol{\sigma}_t^k \, dV \\ &= \int_V \left(\delta\hat{\boldsymbol{\varepsilon}}_m^T\mathbf{S}_m^T\boldsymbol{\sigma}_p^k + \delta\hat{\boldsymbol{\varepsilon}}_b^T\mathbf{S}_b^T\boldsymbol{\sigma}_p^k + \delta\hat{\boldsymbol{\varepsilon}}_{mb\phi}^T\mathbf{S}_{mb\phi}^{k^T}\boldsymbol{\sigma}_p^k\right) dV + \\ &\quad + \int_V \left(\delta\hat{\boldsymbol{\varepsilon}}_s^T\mathbf{S}_s^T\boldsymbol{\sigma}_t^k + \delta\hat{\boldsymbol{\varepsilon}}_{s\phi}^T\mathbf{S}_{s\phi}^{k^T}\boldsymbol{\sigma}_t^k\right) dV\end{aligned}$$

Using Eq.(3.43), (3.51), (3.58) yields

$$\int_V \delta\boldsymbol{\varepsilon}^{k^T}\boldsymbol{\sigma}^k \, dV = \int_A \left(\delta\hat{\boldsymbol{\varepsilon}}_m^T\hat{\boldsymbol{\sigma}}_m + \delta\hat{\boldsymbol{\varepsilon}}_b^T\hat{\boldsymbol{\sigma}}_b + \delta\hat{\boldsymbol{\varepsilon}}_{mb\phi}^T\hat{\boldsymbol{\sigma}}_{mb\phi}\right) dA + \int_A \left(\delta\hat{\boldsymbol{\varepsilon}}_s^T\hat{\boldsymbol{\sigma}}_s + \delta\hat{\boldsymbol{\varepsilon}}_{s\phi}^T\hat{\boldsymbol{\sigma}}_{s\phi}\right) dA$$

being A the in-plate area of the plate.

Finally, the equilibrium equations of Eq.(3.4) can be written as

$$\int_A \left(\delta\hat{\boldsymbol{\varepsilon}}_p^T\hat{\boldsymbol{\sigma}}_p + \delta\hat{\boldsymbol{\varepsilon}}_t^T\hat{\boldsymbol{\sigma}}_t\right) dA = \int_{\Gamma_A} \delta\mathbf{a}^T\mathbf{q} \, d\Gamma_A + \int_{\Gamma_L} \delta\mathbf{a}^T\mathbf{f} \, d\Gamma_L + \sum_{i=1}^{pl} \delta a_i p_i \qquad 3.62$$

Theses integrands contain kinematics variables derivatives up to first order only, which allows to use C0 continuous finite elements.

3.3.6 QLRZ formulation

3.3.6.1 Discretization of the displacement field

The middle surface of the plate is discretized into 4-node planar isoparametric finite elements of quadrilateral shape.

The kinematic variables **a** of Eq.(2.3) are interpolated within each element as

$$\mathbf{a}^{(e)} = \begin{bmatrix} u_0 \\ v_0 \\ w_0 \\ \theta_x \\ \theta_y \\ \psi_x \\ \psi_y \end{bmatrix} = \sum_{i=1}^{4} \mathbf{N}_i \mathbf{a}_i^{(e)} = \begin{bmatrix} \mathbf{N}_1 & \mathbf{N}_2 & \mathbf{N}_3 & \mathbf{N}_4 \end{bmatrix} \cdot \begin{bmatrix} \mathbf{a}_1 \\ \mathbf{a}_2 \\ \mathbf{a}_3 \\ \mathbf{a}_4 \end{bmatrix}^{(e)} = \mathbf{N}_\mathbf{n} \mathbf{a}_\mathbf{n}^{(e)} \qquad 3.63$$

Where

$$\mathbf{N}_i = N_i \mathbf{I}_7 \quad ; \quad \mathbf{a}_i^{(e)} = \begin{bmatrix} u_0 & v_0 & w_0 & \theta_x & \theta_y & \psi_x & \psi_y \end{bmatrix}_i^T$$

being $N_i = \frac{1}{4}(1+\xi\xi_i)(1+\eta\eta_i)$ (Table 3.8 and Figure 3.29) the bi-linear shape function of node *i*th and I_7 is the 7x7 unit matrix.

Node	ξ_i	η_i
1	-1	-1
2	1	-1
3	1	1
4	-1	1

Table 3.8 - Values of ξ_i and η_i for each node.

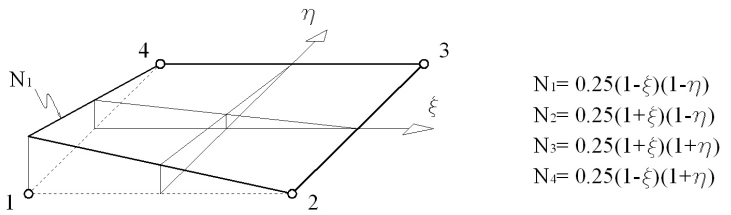

Figure 3.29 – Bi-linear shape functions of quadrilateral four-noded element.

The element geometry is interpolated as

$$x = \sum_{i=1}^{4} \hat{N}_i x_i \qquad ; \qquad y = \sum_{i=1}^{4} \hat{N}_i y_i \qquad 3.64$$

where $\hat{N}_i = N_i$, which leads to an isoparametric formulation.

The Jacobian matrix $\mathbf{J}^{(e)}$ of the transformation from the natural coordinates to the Cartesian coordinates is obtained using the chain rule as

$$\frac{\partial N_i}{\partial \xi} = \frac{\partial N_i}{\partial x}\frac{\partial x}{\partial \xi} + \frac{\partial N_i}{\partial y}\frac{\partial y}{\partial \xi}$$
$$\frac{\partial N_i}{\partial \eta} = \frac{\partial N_i}{\partial x}\frac{\partial x}{\partial \eta} + \frac{\partial N_i}{\partial y}\frac{\partial y}{\partial \eta}$$

or in a matrix form

$$\begin{bmatrix} \frac{\partial N_i}{\partial \xi} \\ \frac{\partial N_i}{\partial \eta} \end{bmatrix} = \begin{bmatrix} \frac{\partial x}{\partial \xi} & \frac{\partial y}{\partial \xi} \\ \frac{\partial x}{\partial \eta} & \frac{\partial y}{\partial \eta} \end{bmatrix} \cdot \begin{bmatrix} \frac{\partial N_i}{\partial x} \\ \frac{\partial N_i}{\partial y} \end{bmatrix} = \mathbf{J}^{(e)} \begin{bmatrix} \frac{\partial N_i}{\partial x} \\ \frac{\partial N_i}{\partial y} \end{bmatrix} \qquad 3.65$$

where $\mathbf{J}^{(e)}$ is the Jacobian matrix.

$$\begin{bmatrix} \frac{\partial N_i}{\partial x} \\ \frac{\partial N_i}{\partial y} \end{bmatrix} = \left[\mathbf{J}^{(e)}\right]^{-1} \begin{bmatrix} \frac{\partial N_i}{\partial \xi} \\ \frac{\partial N_i}{\partial \eta} \end{bmatrix}$$

with

$$\left[\mathbf{J}^{(e)}\right]^{-1} = \frac{1}{\left|\mathbf{J}^{(e)}\right|} \begin{bmatrix} \frac{\partial y}{\partial \eta} & -\frac{\partial y}{\partial \xi} \\ -\frac{\partial x}{\partial \eta} & \frac{\partial x}{\partial \xi} \end{bmatrix}$$

being $\left|\mathbf{J}^{(e)}\right|$ the Jacobian determinant. Thus,

$$\frac{\partial N_i}{\partial x} = \frac{1}{\left|\mathbf{J}^{(e)}\right|}\left(\frac{\partial y}{\partial \eta}\frac{\partial N_i}{\partial \xi} - \frac{\partial y}{\partial \xi}\frac{\partial N_i}{\partial \eta}\right)$$
$$\frac{\partial N_i}{\partial y} = \frac{1}{\left|\mathbf{J}^{(e)}\right|}\left(\frac{\partial x}{\partial \xi}\frac{\partial N_i}{\partial \eta} - \frac{\partial x}{\partial \eta}\frac{\partial N_i}{\partial \xi}\right) \qquad 3.66$$

The Jacobian determinant is also used to determinate the differential area in natural coordinates as

$$dx\, dy = \left|\mathbf{J}^{(e)}\right| d\xi\, d\eta \qquad 3.67$$

The term of $\mathbf{J}^{(e)}$ are computed using the isoparametric transformation of Eq.(3.64) as

$$\frac{\partial x}{\partial \xi}=\sum_{i=1}^{4}\frac{\partial N_i}{\partial \xi}x_i \qquad ; \qquad \frac{\partial x}{\partial \eta}=\sum_{i=1}^{4}\frac{\partial N_i}{\partial \eta}x_i$$
$$\frac{\partial y}{\partial \xi}=\sum_{i=1}^{4}\frac{\partial N_i}{\partial \xi}y_i \qquad ; \qquad \frac{\partial y}{\partial \eta}=\sum_{i=1}^{4}\frac{\partial N_i}{\partial \eta}y_i$$

Thus, the Jacobian matrix is defined by

$$\mathbf{J}^{(e)}=\begin{bmatrix}\frac{\partial x}{\partial \xi} & \frac{\partial y}{\partial \xi}\\ \frac{\partial x}{\partial \eta} & \frac{\partial y}{\partial \eta}\end{bmatrix}=\sum_{i=1}^{4}\begin{bmatrix}\frac{\partial N_i}{\partial \xi}x_i & \frac{\partial N_i}{\partial \xi}y_i\\ \frac{\partial N_i}{\partial \eta}x_i & \frac{\partial N_i}{\partial \eta}y_i\end{bmatrix} \tag{3.68}$$

3.3.6.2 Generalized strain field

The interpolated generalized in-plane strains $\hat{\boldsymbol{\varepsilon}}_p^{(e)}$ within each finite element are obtained by substituting Eq.(3.63) into Eq.(3.43) as

$$\hat{\boldsymbol{\varepsilon}}_p^{(e)}=\begin{bmatrix}\hat{\boldsymbol{\varepsilon}}_m\\ \hat{\boldsymbol{\varepsilon}}_b\\ \hat{\boldsymbol{\varepsilon}}_{mb\phi}\end{bmatrix}^{(e)}=\begin{bmatrix}\frac{\partial u_0}{\partial x}\\ \frac{\partial v_0}{\partial y}\\ \frac{\partial u_0}{\partial y}+\frac{\partial v_0}{\partial x}\\ \hline \frac{\partial \theta_x}{\partial x}\\ \frac{\partial \theta_y}{\partial y}\\ \frac{\partial \theta_x}{\partial y}+\frac{\partial \theta_y}{\partial x}\\ \hline \frac{\partial \psi_x}{\partial x}\\ \frac{\partial \psi_y}{\partial y}\\ \frac{\partial \psi_x}{\partial y}\\ \frac{\partial \psi_y}{\partial x}\end{bmatrix}^{(e)}=\sum_{i=1}^{4}\begin{bmatrix}\frac{\partial N_i}{\partial x}u_0\\ \frac{\partial N_i}{\partial y}v_0\\ \frac{\partial N_i}{\partial y}u_0+\frac{\partial N_i}{\partial x}v_0\\ \hline \frac{\partial N_i}{\partial x}\theta_x\\ \frac{\partial N_i}{\partial y}\theta_y\\ \frac{\partial N_i}{\partial y}\theta_x+\frac{\partial N_i}{\partial x}\theta_y\\ \hline \frac{\partial N_i}{\partial x}\psi_x\\ \frac{\partial N_i}{\partial y}\psi_y\\ \frac{\partial N_i}{\partial y}\psi_x\\ \frac{\partial N_i}{\partial x}\psi_y\end{bmatrix}_i=\sum_{i=1}^{4}\mathbf{B}_{p_i}\mathbf{a}_i^{(e)}=\mathbf{B}_p\mathbf{a}_{\mathbf{n}}^{(e)} \tag{3.69}$$

where $\mathbf{B}_p$ and $\mathbf{B}_{p_i}$ are the in-plane generalized strain matrices for the element and the *i*th node, respectively. The matrix $\mathbf{B}_{p_i}$ is split into membrane (m), bending (b) and zigzag $(mb\phi)$ contributions, which leads to

$$\mathbf{B}_{p_i} = \begin{bmatrix} \mathbf{B}_m \\ \mathbf{B}_b \\ \mathbf{B}_{mb\phi} \end{bmatrix}_i \tag{3.70}$$

with

$$\mathbf{B}_{m_i} = \begin{bmatrix} \frac{\partial N_i}{\partial x} & 0 & 0 & 0 & 0 & 0 & 0 \\ 0 & \frac{\partial N_i}{\partial y} & 0 & 0 & 0 & 0 & 0 \\ \frac{\partial N_i}{\partial y} & \frac{\partial N_i}{\partial x} & 0 & 0 & 0 & 0 & 0 \end{bmatrix} \qquad \mathbf{B}_{b_i} = \begin{bmatrix} 0 & 0 & 0 & \frac{\partial N_i}{\partial x} & 0 & 0 & 0 \\ 0 & 0 & 0 & 0 & \frac{\partial N_i}{\partial y} & 0 & 0 \\ 0 & 0 & 0 & \frac{\partial N_i}{\partial y} & \frac{\partial N_i}{\partial x} & 0 & 0 \end{bmatrix}$$

$$\mathbf{B}_{mb\phi_i} = \begin{bmatrix} 0 & 0 & 0 & 0 & 0 & \frac{\partial N_i}{\partial x} & 0 \\ 0 & 0 & 0 & 0 & 0 & 0 & \frac{\partial N_i}{\partial y} \\ 0 & 0 & 0 & 0 & 0 & \frac{\partial N_i}{\partial y} & 0 \\ 0 & 0 & 0 & 0 & 0 & 0 & \frac{\partial N_i}{\partial x} \end{bmatrix} \tag{3.71}$$

Generalized transverse strains $\hat{\boldsymbol{\varepsilon}}_t^{(e)}$ are also obtained by the same manner as

$$\hat{\boldsymbol{\varepsilon}}_t^{(e)} = \begin{bmatrix} \hat{\boldsymbol{\varepsilon}}_s \\ \hat{\boldsymbol{\varepsilon}}_{s\phi} \end{bmatrix}^{(e)} = \begin{bmatrix} \frac{\partial w_0}{\partial x} - \theta_x \\ \frac{\partial w_0}{\partial y} - \theta_y \\ \hline \psi_x \\ \psi_y \end{bmatrix}^{(e)} = \sum_{i=1}^{4} \begin{bmatrix} \frac{\partial N_i}{\partial x} w_0 - N_i \theta_x \\ \frac{\partial N_i}{\partial y} w_0 - N_i \theta_y \\ \hline N_i \psi_x \\ N_i \psi_y \end{bmatrix}_i = \sum_{i=1}^{4} \mathbf{B}_{t_i} \mathbf{a}_i^{(e)} = \mathbf{B}_t \mathbf{a}_{\mathbf{n}}^{(e)} \tag{3.72}$$

where $\mathbf{B}_t$ and $\mathbf{B}_{t_i}$ are the transverse generalized strain matrices for the element and the *i*th node, respectively. Matrix $\mathbf{B}_{t_i}$ is split into shear (s) and zigzag $(s\phi)$ contributions as

$$\mathbf{B}_{t_i} = \begin{bmatrix} \mathbf{B}_s \\ \mathbf{B}_{s\phi} \end{bmatrix}_i \qquad 3.73$$

where

$$\mathbf{B}_{s_i} = \begin{bmatrix} 0 & 0 & \dfrac{\partial N_i}{\partial x} & -N_i & 0 & 0 & 0 \\ 0 & 0 & \dfrac{\partial N_i}{\partial y} & 0 & -N_i & 0 & 0 \end{bmatrix} \qquad 3.74$$

$$\mathbf{B}_{s\phi_i} = \begin{bmatrix} 0 & 0 & 0 & 0 & 0 & N_i & 0 \\ 0 & 0 & 0 & 0 & 0 & 0 & N_i \end{bmatrix}$$

3.3.6.3 Element stiffness matrix and nodal forces vector

Considering Eqs.(3.5), (3.62), the element stiffness matrix and nodal forces vector are obtained via the following equation

$$\int_{A^{(e)}} \left(\delta\hat{\boldsymbol{\varepsilon}}_p^{(e)^T} \hat{\boldsymbol{\sigma}}_p + \delta\hat{\boldsymbol{\varepsilon}}_t^{(e)^T} \hat{\boldsymbol{\sigma}}_t \right) dA = \int_{A^{(e)}} \delta\mathbf{a}^{(e)^T} \mathbf{q}\ dA + \int_{S^{(e)}} \delta\mathbf{a}^{(e)^T} \mathbf{f}\ dS + \delta\mathbf{a}_{\mathbf{n}}^{(e)^T} \mathbf{p} \qquad 3.75$$

being $A^{(e)}$ the element area and $S^{(e)}$ the element side where $\mathbf{f}$ is applied.

Considering that

$$\delta\hat{\boldsymbol{\varepsilon}}_p^{(e)^T} = \delta\mathbf{a}_{\mathbf{n}}^{(e)^T} \mathbf{B}_p^T \quad ; \quad \delta\hat{\boldsymbol{\varepsilon}}_t^{(e)^T} = \delta\mathbf{a}_{\mathbf{n}}^{(e)^T} \mathbf{B}_t^T \quad ; \quad \delta\mathbf{a}^{(e)^T} = \delta\mathbf{a}_{\mathbf{n}}^{(e)^T} \mathbf{N}_{\mathbf{n}}^T$$

and substituting Eq.(3.58) into Eq.(3.75) gives

$$\int_{A^{(e)}} \left(\delta\mathbf{a}_{\mathbf{n}}^{(e)^T} \mathbf{B}_p^T \tilde{\mathbf{D}}_p \hat{\boldsymbol{\varepsilon}}_p + \delta\mathbf{a}_{\mathbf{n}}^{(e)^T} \mathbf{B}_t^T \tilde{\mathbf{D}}_t \hat{\boldsymbol{\varepsilon}}_t \right) dA = \int_{A^{(e)}} \delta\mathbf{a}_{\mathbf{n}}^{(e)^T} \mathbf{N}_{\mathbf{n}}^T \mathbf{q}\ dA + \int_{S^{(e)}} \delta\mathbf{a}_{\mathbf{n}}^{(e)^T} \mathbf{N}_{\mathbf{n}}^T \mathbf{f}\ dS + \delta\mathbf{a}_{\mathbf{n}}^{(e)^T} \mathbf{p}$$

Substituting Eqs.(3.69), (3.72) into previous equation yields

$$\int_{A^{(e)}} \left(\delta\mathbf{a}_{\mathbf{n}}^{(e)^T} \mathbf{B}_p^T \tilde{\mathbf{D}}_p \mathbf{B}_p \mathbf{a}_{\mathbf{n}}^{(e)} + \delta\mathbf{a}_{\mathbf{n}}^{(e)^T} \mathbf{B}_t^T \tilde{\mathbf{D}}_t \mathbf{B}_t \mathbf{a}_{\mathbf{n}}^{(e)} \right) dA = \int_{A^{(e)}} \delta\mathbf{a}_{\mathbf{n}}^{(e)^T} \mathbf{N}_{\mathbf{n}}^T \mathbf{q}\ dA + \int_{S^{(e)}} \delta\mathbf{a}_{\mathbf{n}}^{(e)^T} \mathbf{N}_{\mathbf{n}}^T \mathbf{f}\ dS + \delta\mathbf{a}_{\mathbf{n}}^{(e)^T} \mathbf{p}$$

Thus, the equation is factorized as

$$\delta\mathbf{a}_{\mathbf{n}}^{(e)^T} \left\{ \left[\int_{A^{(e)}} \left(\mathbf{B}_p^T \tilde{\mathbf{D}}_p \mathbf{B}_p + \mathbf{B}_t^T \tilde{\mathbf{D}}_t \mathbf{B}_t \right) dA \right] \mathbf{a}_{\mathbf{n}}^{(e)} \right\} = \left(\int_{A^{(e)}} \mathbf{N}_{\mathbf{n}}^T \mathbf{q}\ dA + \int_{S^{(e)}} \mathbf{N}_{\mathbf{n}}^T \mathbf{f}\ dS + \mathbf{p} \right) \delta\mathbf{a}_{\mathbf{n}}^{(e)^T}$$

$$\left[\int_{A^{(e)}} \left(\mathbf{B}_p^T \tilde{\mathbf{D}}_p \mathbf{B}_p + \mathbf{B}_t^T \tilde{\mathbf{D}}_t \mathbf{B}_t \right) dA \right] \mathbf{a}_{\mathbf{n}}^{(e)} = \int_{A^{(e)}} \mathbf{N}_{\mathbf{n}}^T \mathbf{q}\ dA + \int_{S^{(e)}} \mathbf{N}_{\mathbf{n}}^T \mathbf{f}\ dS + \mathbf{p}$$

Finally, Eq.(3.75) is reduced to

$$\mathbf{K}^{(\mathrm{e})}\,\mathbf{a}_{\mathbf{n}}^{(\mathrm{e})} = \int_{\mathrm{A}^{(\mathrm{e})}} \mathbf{N}_{\mathbf{n}}^{T}\mathbf{q}\;\mathrm{dA} + \int_{\mathrm{S}^{(\mathrm{e})}} \mathbf{N}_{\mathbf{n}}^{T}\mathbf{f}\;\mathrm{dS} + \mathbf{p} \tag{3.76}$$

with

$$\mathbf{K}^{(\mathrm{e})} = \int_{\mathrm{A}^{(\mathrm{e})}} \left(\mathbf{B}_{p}^{T}\tilde{\mathbf{D}}_{p}\mathbf{B}_{p} + \mathbf{B}_{t}^{T}\tilde{\mathbf{D}}_{t}\mathbf{B}_{t}\right)\mathrm{dA} \tag{3.77}$$

Matrix $\mathbf{K}^{(\mathrm{e})}$ is the elemental stiffness matrix, which for convenience is split as

$$\mathbf{K}^{(\mathrm{e})} = \mathbf{K}_{p}^{(\mathrm{e})} + \mathbf{K}_{t}^{(\mathrm{e})}$$

being $\mathbf{K}_{p}^{(\mathrm{e})}$ and $\mathbf{K}_{t}^{(\mathrm{e})}$ the in-plane and the transverse elemental stiffness matrices, respectively, defined as

$$\begin{aligned} \mathbf{K}_{p}^{(\mathrm{e})} &= \int_{\mathrm{A}^{(\mathrm{e})}} \mathbf{B}_{p}^{T}\tilde{\mathbf{D}}_{p}\mathbf{B}_{p}\mathrm{dA} \\ \mathbf{K}_{t}^{(\mathrm{e})} &= \int_{\mathrm{A}^{(\mathrm{e})}} \mathbf{B}_{t}^{T}\tilde{\mathbf{D}}_{t}\mathbf{B}_{t}\mathrm{dA} \end{aligned} \tag{3.78}$$

To facilitate subsequent shear locking studies, matrix $\mathbf{K}_{t}^{(\mathrm{e})}$ is split as follows

$$\mathbf{K}_{t}^{(\mathrm{e})} = \mathbf{K}_{s}^{(\mathrm{e})} + \mathbf{K}_{s\phi}^{(\mathrm{e})} + \mathbf{K}_{ss\phi}^{(\mathrm{e})} + \left[\mathbf{K}_{ss\phi}^{(\mathrm{e})}\right]^{T} \tag{3.79}$$

with

$$\begin{aligned} \mathbf{K}_{s}^{(\mathrm{e})} &= \int_{\mathrm{A}^{(\mathrm{e})}} \mathbf{B}_{s}^{T}\hat{\mathbf{D}}_{s}\mathbf{B}_{s}\mathrm{dA} \\ \mathbf{K}_{s\phi}^{(\mathrm{e})} &= \int_{\mathrm{A}^{(\mathrm{e})}} \mathbf{B}_{s\phi}^{T}\hat{\mathbf{D}}_{s\phi}\mathbf{B}_{s\phi}\mathrm{dA} \\ \mathbf{K}_{ss\phi}^{(\mathrm{e})} &= \int_{\mathrm{A}^{(\mathrm{e})}} \mathbf{B}_{s}^{T}\hat{\mathbf{D}}_{ss\phi}\mathbf{B}_{s\phi}\mathrm{dA} \end{aligned} \tag{3.80}$$

The external nodal forces vector $\mathbf{F}^{\mathrm{ext}}$ are defined by the r.h.s. of Eq.(3.76) as

$$\mathbf{F}^{\mathrm{ext}} = \int_{\mathrm{A}^{(\mathrm{e})}} \mathbf{N}_{\mathbf{n}}^{T}\mathbf{q}\;\mathrm{dA} + \int_{\mathrm{S}^{(\mathrm{e})}} \mathbf{N}_{\mathbf{n}}^{T}\mathbf{f}\;\mathrm{dS} + \mathbf{p} \tag{3.81}$$

Considering Eq.(3.67) and $\mathrm{dA} = dx\,dy$, the integrals of Eq.(3.78) defined in the Cartesian coordinate are transformed to the natural coordinate as

$$\begin{aligned} \mathbf{K}_{p}^{(\mathrm{e})} &= \int_{\mathrm{A}^{(\mathrm{e})}} \mathbf{B}_{p}^{T}\tilde{\mathbf{D}}_{p}\mathbf{B}_{p}\mathrm{dA} = \int_{-1}^{+1}\int_{-1}^{+1} \mathbf{B}_{p}^{T}\tilde{\mathbf{D}}_{p}\mathbf{B}_{p}\left|\mathbf{J}^{(\mathrm{e})}\right| \mathrm{d}\xi\,\mathrm{d}\eta \\ \mathbf{K}_{t}^{(\mathrm{e})} &= \int_{\mathrm{A}^{(\mathrm{e})}} \mathbf{B}_{t}^{T}\tilde{\mathbf{D}}_{t}\mathbf{B}_{t}\mathrm{dA} = \int_{-1}^{+1}\int_{-1}^{+1} \mathbf{B}_{t}^{T}\tilde{\mathbf{D}}_{t}\mathbf{B}_{t}\left|\mathbf{J}^{(\mathrm{e})}\right| \mathrm{d}\xi\,\mathrm{d}\eta \end{aligned} \tag{3.82}$$

Note that, the derivatives of the shape functions with respect to the Cartesian coordinates contained into the generalized strain matrices $\mathbf{B}$ are computed by Eq.(3.66). The integrals of Eqs.(3.82) are solved via numerical integration using the Gauss quadrature as

$$\mathbf{K}_p^{(e)} = \int_{-1}^{+1}\int_{-1}^{+1} \mathbf{B}_p^T \tilde{\mathbf{D}}_p \mathbf{B}_p \left|\mathbf{J}^{(e)}\right| d\xi\, d\eta = \sum_{GP=1}^{4} \left[\mathbf{B}_p^T \tilde{\mathbf{D}}_p \mathbf{B}_p \left|\mathbf{J}^{(e)}\right|\right]_{(\xi_{GP},\eta_{GP})} W_{GP}$$
$$\mathbf{K}_t^{(e)} = \int_{-1}^{+1}\int_{-1}^{+1} \mathbf{B}_t^T \tilde{\mathbf{D}}_t \mathbf{B}_t \left|\mathbf{J}^{(e)}\right| d\xi\, d\eta = \sum_{GP=1}^{4} \left[\mathbf{B}_t^T \tilde{\mathbf{D}}_t \mathbf{B}_t \left|\mathbf{J}^{(e)}\right|\right]_{(\xi_{GP},\eta_{GP})} W_{GP} \qquad 3.83$$

where a 2x2 integration scheme is used for providing an exact integration of both, the $\mathbf{K}_p^{(e)}$ and the $\mathbf{K}_t^{(e)}$ matrices. The subscript *GP* indicates the actual integration point (the Gauss points) under consideration, which weighting factor is W_{GP}. Matrices $\mathbf{B}$ and the Jacobian determinant are evaluated at point GP.

The natural coordinates and the weighting factor of each Gauss point (ξ_{GP},η_{GP}) are listed in Table 3.9.

GP	(ξ_{GP},η_{GP})		W_{GP}
	ξ_{GP}	η_{GP}	
1	$-\frac{1}{\sqrt{3}}$	$-\frac{1}{\sqrt{3}}$	1
2	$+\frac{1}{\sqrt{3}}$	$-\frac{1}{\sqrt{3}}$	1
3	$+\frac{1}{\sqrt{3}}$	$+\frac{1}{\sqrt{3}}$	1
4	$-\frac{1}{\sqrt{3}}$	$+\frac{1}{\sqrt{3}}$	1

Table 3.9 – Natural coordinates and weighting factors of each Gauss point.

However, when full Gauss integration is used, the QLRZ element suffers from shear locking for slender plates, which leads to too stiff solutions. Note that for homogeneous plate the QLRZ becomes to the 4-noded quadrilateral Reissner-Mindlin finite element (QLLL), which is based on the FSDT theory. Taking into account that the QLLL element also suffers from shear locking it is reasonable to think that the causes of shear locking in the QLRZ element are the same as in the QLLL element. For the QLLL element, it is demonstrated [108] that according the plate is more slender the contribution of $\mathbf{K}_s^{(e)}$ (Eq.(3.79)) in the stiffness matrix $\mathbf{K}^{(e)}$ is progressively increasing until infinity in the limit case for h = 0. Thus, it is considered that the source of shear

locking in the QLRZ element is also related to the shear stiffness contribution of $\mathbf{K}_s^{(e)}$, as showed below in this chapter.

In order to avoid this numerical problem, a reduced integration of the shear contribution using a selective integration technique, where the $\mathbf{K}_s^{(e)}$ matrix is integrated by using one Gauss point only, can be used. However, it may further lead to undesired hour-glassing, which can propagate through the finite element mesh. For this reason, it is has to be carefully used.

Another robust technique is the *assumed transverse shear strains* approach developed by Dvorkin and Bathe [109, 110], which is adopted for overcoming the shear locking effects in the QLRZ element. This approach is based on the imposition of a special transverse shear strain $\hat{\boldsymbol{\varepsilon}}_s$ field, which satisfies the Kirchhoff condition for thin plate, e.g. $\hat{\boldsymbol{\varepsilon}}_s = 0$. Note, $\hat{\boldsymbol{\varepsilon}}_s$ is the shear strain of the Reissner-Mindlin theory.

The assumed elemental shear strain $\hat{\boldsymbol{\varepsilon}}_s^{(e)}$ related to the Cartesian coordinate is defined as

$$\hat{\boldsymbol{\varepsilon}}_s^{(e)} = \overline{\mathbf{B}}_s \mathbf{a}_{\mathbf{n}}^{(e)} \tag{3.84}$$

where $\overline{\mathbf{B}}_s$ is the sought *substitute transverse shear strain matrix*. Thus, this technique leads to matrix $\mathbf{B}_s$ (Eq.(3.73)) being replaced by the substitutive matrix $\overline{\mathbf{B}}_s$ of Eq.(3.96) . Therefore, the stiffness matrices $\mathbf{K}_s^{(e)}$ and $\mathbf{K}_{s\phi}^{(e)}$ (Eq.(3.80)) of $\mathbf{K}_t^{(e)}$ are now computed by

$$\begin{aligned} \mathbf{K}_s^{(e)} &= \int_{A^{(e)}} \overline{\mathbf{B}}_s^T \hat{\mathbf{D}}_s \overline{\mathbf{B}}_s \mathrm{dA} \\ \mathbf{K}_{ss\phi}^{(e)} &= \int_{A^{(e)}} \overline{\mathbf{B}}_s^T \hat{\mathbf{D}}_{ss\phi} \mathbf{B}_{s\phi} \mathrm{dA} \end{aligned} \tag{3.85}$$

The computation of $\overline{\mathbf{B}}_s$ is briefly explained at following. A detailed description of this technique can be found in [108].

Computation of the substitutive shear strain generalized matrix $\overline{\mathbf{B}}_s$

The assumed natural transverse shear strain field is given by

$$\hat{\boldsymbol{\varepsilon}}_s^{'} = \begin{bmatrix} \gamma_\xi \\ \gamma_\eta \end{bmatrix} = \begin{bmatrix} \alpha_1 + \alpha_2\eta \\ \alpha_3 + \alpha_4\xi \end{bmatrix} = \begin{bmatrix} 1 & \eta & 0 & 0 \\ 0 & 0 & 1 & \xi \end{bmatrix} . \begin{bmatrix} \alpha_1 \\ \alpha_2 \\ \alpha_3 \\ \alpha_4 \end{bmatrix} = \mathbf{A}\boldsymbol{\alpha} \qquad 3.86$$

where coefficients α_i are obtained by sampling the natural shear strains at the four points I, II, III and IV. Points I and III are denoted by symbol + whereas points II and IV by x. Figure 3.30 shows the assumed strain field.

The transverse shear strains in the Cartesian coordinate system are expressed as

$$\hat{\boldsymbol{\varepsilon}}_s = \begin{bmatrix} \gamma_{xz} \\ \gamma_{yz} \end{bmatrix} = \mathbf{J}^{-1}\hat{\boldsymbol{\varepsilon}}_s^{'} \qquad 3.87$$

where $\mathbf{J}$ is the 2D Jacobian matrix defined by Eq.(3.68).

For convenience, a transverse shear stress along the predefined orientations $\overline{\xi}_i$ (Figure 3.31) is defined as

$$\gamma_{\overline{\xi}_i} = \left(\alpha_1 + \alpha_2\eta\right)\cdot\cos\delta_i + \left(\alpha_3 + \alpha_4\xi\right)\cdot\sin\delta_i \quad ; \quad i = 1, 4 \qquad 3.88$$

where δ_i is the angle between direction $\overline{\xi}_i$ and the natural axis ξ. The matrix form of Eq.(3.88) is written as

$$\boldsymbol{\gamma}_{\overline{\xi}} = \begin{bmatrix} \gamma_{\overline{\xi}_1} \\ \gamma_{\overline{\xi}_2} \\ \gamma_{\overline{\xi}_3} \\ \gamma_{\overline{\xi}_4} \end{bmatrix} = \begin{bmatrix} 1 & -1 & 0 & 0 \\ 0 & 0 & 1 & 1 \\ 1 & 1 & 0 & 0 \\ 0 & 0 & 1 & -1 \end{bmatrix} \cdot \begin{bmatrix} \alpha_1 \\ \alpha_2 \\ \alpha_3 \\ \alpha_4 \end{bmatrix} = \mathbf{P}\boldsymbol{\alpha} \qquad 3.89$$

where $\boldsymbol{\gamma}_{\overline{\xi}}$ contains the values of the assumed transverse shear strain at each sampling points (+ and x).

From Eq.(3.89)

$$\boldsymbol{\alpha} = \mathbf{P}^{-1}\boldsymbol{\gamma}_{\overline{\xi}} \qquad 3.90$$

where the strains $\gamma_{\overline{\xi}_i}$ are related to γ_{ξ_j} and γ_{η_j} $(j = I, IV)$ by

$$\boldsymbol{\gamma}_{\bar{\xi}} = \begin{bmatrix} \gamma_{\bar{\xi}_1} \\ \gamma_{\bar{\xi}_2} \\ \gamma_{\bar{\xi}_3} \\ \gamma_{\bar{\xi}_4} \end{bmatrix} = \begin{bmatrix} 1 & 0 & 0 & 0 & 0 & 0 & 0 & 0 \\ 0 & 0 & 0 & 1 & 0 & 0 & 0 & 0 \\ 0 & 0 & 0 & 0 & 1 & 0 & 0 & 0 \\ 0 & 0 & 0 & 0 & 0 & 0 & 0 & 1 \end{bmatrix} \cdot \begin{bmatrix} \gamma_{\xi_I} \\ \gamma_{\eta_I} \\ \gamma_{\xi_{II}} \\ \gamma_{\eta_{II}} \\ \gamma_{\xi_{III}} \\ \gamma_{\eta_{III}} \\ \gamma_{\xi_{IV}} \\ \gamma_{\eta_{IV}} \end{bmatrix} = \mathbf{T}\hat{\boldsymbol{\gamma}}' \qquad 3.91$$

Combining Eqs.(3.86), (3.90), (3.91) gives

$$\hat{\boldsymbol{\varepsilon}}_s' = \mathbf{A}\mathbf{P}^{-1}\mathbf{T}\hat{\boldsymbol{\gamma}}' \qquad 3.92$$

The Cartesian transverse shear strains $\hat{\boldsymbol{\gamma}}$ at the sampling points are related to the natural transverse shear strains $\hat{\boldsymbol{\gamma}}'$ by

$$\hat{\boldsymbol{\gamma}}' = \begin{bmatrix} \mathbf{J}_{\mathrm{I}} & \mathbf{0} & \mathbf{0} & \mathbf{0} \\ \mathbf{0} & \mathbf{J}_{\mathrm{II}} & \mathbf{0} & \mathbf{0} \\ \mathbf{0} & \mathbf{0} & \mathbf{J}_{\mathrm{III}} & \mathbf{0} \\ \mathbf{0} & \mathbf{0} & \mathbf{0} & \mathbf{J}_{\mathrm{IV}} \end{bmatrix} \cdot \begin{bmatrix} \hat{\boldsymbol{\gamma}}_{\mathrm{I}} \\ \hat{\boldsymbol{\gamma}}_{\mathrm{II}} \\ \hat{\boldsymbol{\gamma}}_{\mathrm{III}} \\ \hat{\boldsymbol{\gamma}}_{\mathrm{IV}} \end{bmatrix} = \mathbf{C}\hat{\boldsymbol{\gamma}} \qquad ; \qquad \hat{\boldsymbol{\gamma}}_j = \begin{bmatrix} \gamma_{xz} \\ \gamma_{yz} \end{bmatrix}_j \qquad 3.93$$

The Cartesian shear strains and the nodal displacements $\mathbf{a}$ are related as

$$\hat{\boldsymbol{\gamma}} = \mathbf{B}_s\mathbf{a} \qquad 3.94$$

where $\mathbf{B}_s$ is the original transverse generalized strain matrix (Eq.(3.74)) evaluated at the *j*th sampling point. Note that matrix $\mathbf{C}$ is also evaluated at each *j*th point.

Substituting Eqs.(3.92), (3.93), (3.94) into (3.87) yields

$$\hat{\boldsymbol{\varepsilon}}_s = \mathbf{J}^{-1}\mathbf{A}\mathbf{P}^{-1}\mathbf{T}\mathbf{C}\mathbf{B}_s\mathbf{a} = \overline{\mathbf{B}}_s\mathbf{a} \qquad 3.95$$

where $\overline{\mathbf{B}}_s$ is the sought substitute transverse shear strain matrix given by

$$\overline{\mathbf{B}}_s = \mathbf{J}^{-1}\mathbf{A}\mathbf{P}^{-1}\mathbf{T}\mathbf{C}\mathbf{B}_s \qquad 3.96$$

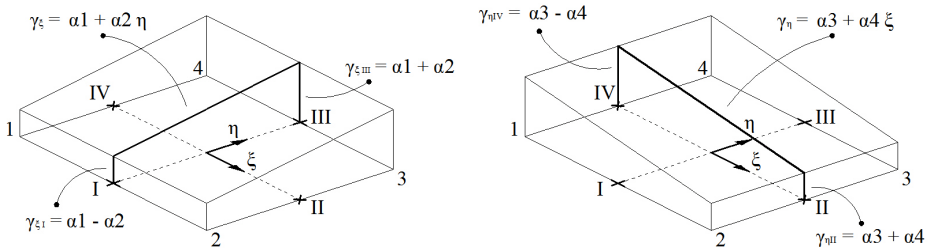

Figure 3.30 – Assumed transverse shear strain field.

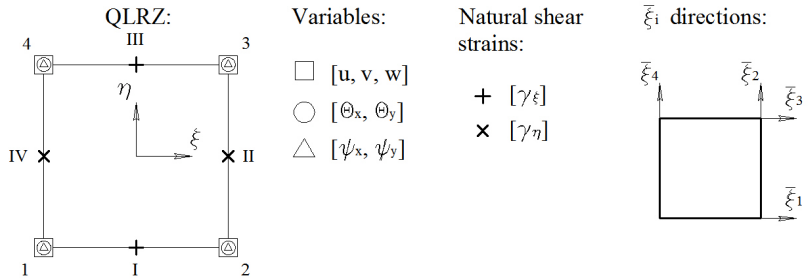

Figure 3.31 - QLRZ element. Evaluation points of the kinematics variables and the assumed shear strains.

3.3.6.4 Boundary conditions

The boundary conditions are:

- Clamped side:

$$w = 0$$
$$u = \theta_x = \psi_x = 0$$
$$v = \theta_y = \psi_y = 0$$

- Simply supported side:
  Hard Support

$$w = u_s = \theta_s = \psi_s = 0$$

  Soft Support

$$w = 0$$

  where “s” is the direction of the side.

- Symmetry axis:

$$u_n = \theta_n = \psi_n = 0$$

  where “n” is the orthogonal direction to the symmetry axis.

3.3.6.5 Improved computation of transverse shear stresses

Whereas in-plane stresses $\left(\sigma_x, \sigma_y \text{ and } \tau_{xy}\right)$ are well predicted by Eq.(3.51), the transverse shear stresses $\left(\tau_{xz} \text{ and } \tau_{yz}\right)$ are not. The reason is that the constitutive yields a constant value into each layer, leading to a discontinuous thickness distribution of τ_{xz} and τ_{yz}. A useful alternative is to compute τ_{xz} and τ_{yz} from the in-plane stresses using the equilibrium equations

$$\begin{aligned} \frac{\partial \sigma_x}{\partial x} + \frac{\partial \tau_{xy}}{\partial y} + \frac{\partial \tau_{xz}}{\partial z} = 0 \\ \frac{\partial \tau_{xy}}{\partial x} + \frac{\partial \sigma_y}{\partial y} + \frac{\partial \tau_{yz}}{\partial z} = 0 \end{aligned} \qquad 3.97$$

from which, the transverse shear stresses at a point "P" within the finite element across the thickness coordinates z are computed by

$$\begin{aligned} \tau_{xz}(z)\big|_P &= -\int_{-h/2}^{z} \left.\frac{\partial \sigma_x}{\partial x}\right|_P dz - \int_{-h/2}^{z} \left.\frac{\partial \tau_{xy}}{\partial y}\right|_P dz \\ \tau_{yz}(z)\big|_P &= -\int_{-h/2}^{z} \left.\frac{\partial \sigma_y}{\partial y}\right|_P dz - \int_{-h/2}^{z} \left.\frac{\partial \tau_{xy}}{\partial x}\right|_P dz \end{aligned} \qquad 3.98$$

The in-plane stresses at point "P" are approximated by

$$\begin{aligned} \sigma_x(z)\big|_P &= \sum_{i=1}^{4} N_i\big|_P \cdot \sigma_x^i(z) \\ \sigma_y(z)\big|_P &= \sum_{i=1}^{4} N_i\big|_P \cdot \sigma_y^i(z) \\ \tau_{xy}(z)\big|_P &= \sum_{i=1}^{4} N_i\big|_P \cdot \tau_{xy}^i(z) \end{aligned} \qquad 3.99$$

where N_i is the shape function and i denotes the ith node. The nodal stresses $\sigma_x^i(z)$, $\sigma_y^i(z)$ and $\tau_{xy}^i(z)$ are obtained by the averaging of Gauss stresses from neighboring elements at the ith node. Finally, the transverse shear stresses are obtained by replacing Eq.(3.99) into Eq.(3.98),

$$\tau_{xz}(z)\big|_P = -\int_{-h/2}^{z}\left(\sum_{i=1}^{4}\left.\frac{\partial N_i}{\partial x}\right|_P \cdot \sigma_x^i(z)\right) - \int_{-h/2}^{z}\left(\sum_{i=1}^{4}\left.\frac{\partial N_i}{\partial y}\right|_P \cdot \tau_{xy}^i(z)\right)$$
$$\tau_{yz}(z)\big|_P = -\int_{-h/2}^{z}\left(\sum_{i=1}^{4}\left.\frac{\partial N_i}{\partial y}\right|_P \cdot \sigma_y^i(z)\right) - \int_{-h/2}^{z}\left(\sum_{i=1}^{4}\left.\frac{\partial N_i}{\partial x}\right|_P \cdot \tau_{xy}^i(z)\right) \qquad 3.100$$

3.3.7 QLRZ studies

3.3.7.1 Shear locking

In order to show the efficiency of the *assumed transverse shear strain* technique for overcoming shear looking effects, a simply supported (SS) square plate of length side $L = 2$ under a uniformly distributed load of unit value ($q = 1$) is analyzed (Figure 3.32).

Moreover, the selective integration technique of $\mathbf{K}_t^{(e)}$ matrix is analyzed. Considering that

$$\mathbf{K}_t^{(e)} = \mathbf{K}_s^{(e)} + \mathbf{K}_{s\phi}^{(e)} + \mathbf{K}_{ss\phi}^{(e)} + \left[\mathbf{K}_{ss\phi}^{(e)}\right]^T$$

it is possible to define the following three different combinations of selective integration

Integration combinations		
Combinations	Exact	Reduced
C1	$\mathbf{K}_{s\phi}^{(e)}$; $\mathbf{K}_{ss\phi}^{(e)}$	$\mathbf{K}_s^{(e)}$
C2	$\mathbf{K}_{s\phi}^{(e)}$	$\mathbf{K}_s^{(e)}$; $\mathbf{K}_{ss\phi}^{(e)}$
C3	-	$\mathbf{K}_t^{(e)}$

Table 3.10 – Integration combinations used to assess the selective integration of K_t.

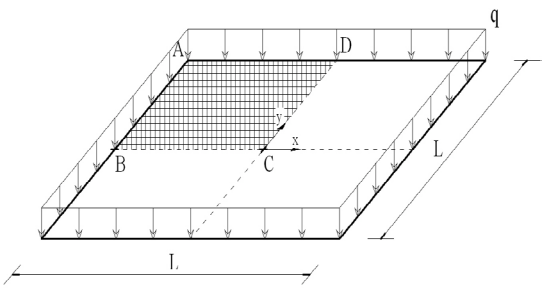

Figure 3.32 – Simply supported square plate under uniformly distributed load.

The analysis is performed for four span-to-thickness ratios: $\lambda = L/h = 5,10,50,100$. A 3-layer composite material is used, whose properties are listed in Table 3.11.

	Laminated Material		
	Layer 1 (bottom)	Layer 2 (core)	Layer 3 (top)
h_i [mm]	$L/4\lambda$	$L/2\lambda$	$L/4\lambda$
E [MPa]	$2.19\text{x}10^5$	$2.19\text{x}10^4$	$4.40\text{x}10^5$
G [MPa]	$0.876\text{x}10^5$	$8.80\text{x}10^4$	$1.76\text{x}10^5$

Table 3.11 – Material properties of shear locking study.

Only one quarter of the plate is studied due to symmetry (Figure 3.32) using a mesh of 16x16 QLRZ elements (Figure 3.33a) with 289 nodes and 1445 DOFs. The reference solution is obtained by a 3D finite element analysis using a mesh of 10x10x9 (3 elements per ply) of 20-noded hexahedral elements (HEXA20) involving 4499 nodes and 13497 DOFs (Figure 3.33b).

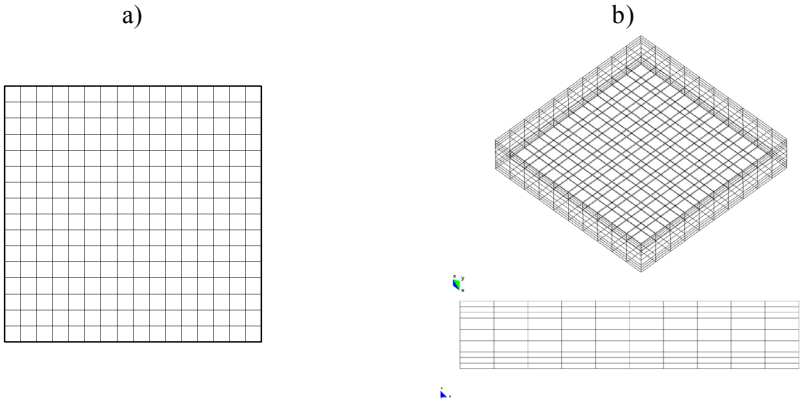

Figure 3.33 – Meshes used for the analysis of one quarter of the SS plate. 16x16 QLRZ elements (a) and 10x10x9 HEXA20 elements (b).

Figure 3.34 shows the *r* ratio defined as

$$r = \frac{w_{QLRZ}}{w_{3D}} \qquad 3.101$$

where w_{QLRZ} and w_{3D} are the middle (z = 0) deflection at the plate center obtained with the QLRZ element and the 3D finite element analysis, respectively. The QLRZ element results have been obtained with *exact* integration of matrix $\mathbf{K}_t^{(e)}$ (exact),

employing the three selective integration listed in Table 3.10 (C1, C2, and C3), and finally using the *assumed transverse shear strain field* technique (QLRZ).

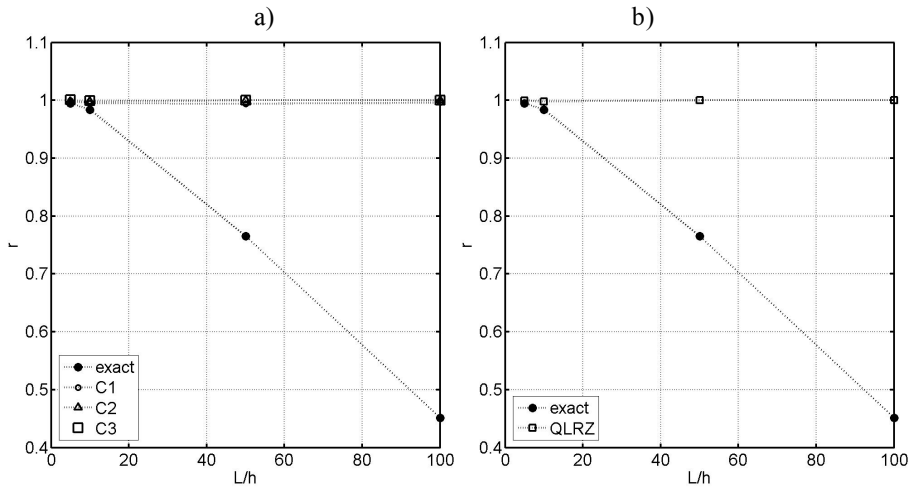

Figure 3.34 – r ratio vs. span-to-thickness ratio $\lambda = L/h$. Simply supported square plate under uniformly distributed load. Figure a): exact integration (exact) and the three integration combinations (C1, C2, and C3) of Table 3.10. Figure b): exact integration and assumed transverse shear strain fields (QLRZ).

Figure 3.34 clearly shows shear locking defects when exact integration of $\mathbf{K}_t^{(e)}$ is used. However, it is shown that this defect disappears for both techniques.

Figure 3.35 shows the distribution of the vertical deflection w along the plate central line BC (Figure 3.32). Figure 3.35a reveals the existence of mechanisms when reduced integration is used. These mechanisms do not appear if the *assumed transverse shear strain* technique is used (Figure 3.35b).

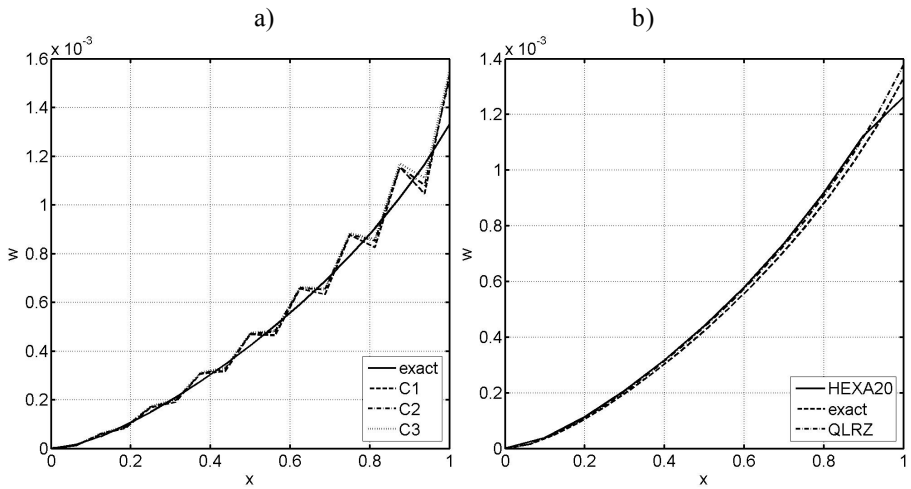

Figure 3.35 - Vertical deflection w along BC. Clamped square plate ($\lambda = 10$) under a center point load. Figure a): exact integration (exact) and the three integration combinations (C1, C2, and C3) of table AI-1. Figure b): exact integration, assumed transverse shear strain fields (QLRZ), and 3D analysis (HEXA20).

3.3.7.2 Verification

The accuracy of the *QLRZ element* for isotropic homogeneous material is studied in this section. The aim is to evaluate the behavior of the QLRZ element when ϕ_i ($i = x, y$) vanishes which leads to $\psi_i = 0$ and the RZT kinematics becomes the RMT displacement field.

This study consists in analyzing a SS and a clamped square plate of side length L = 2 and thickness h = 0.05 (λ = L/h = 40) under a uniformly distributed load q = 1 and a point load P = 4 acting at the center (Figure 3.36). Isotropic homogeneous material properties are assumed with: E = 0.219, μ = 0.25, and G = E/2(1+ μ).

Assuming symmetry along both axes, only one quarter of the plate is analyzed. Five different meshes of QLRZ elements whose properties are listed in Table 3.12 are employed (Figure 3.37).

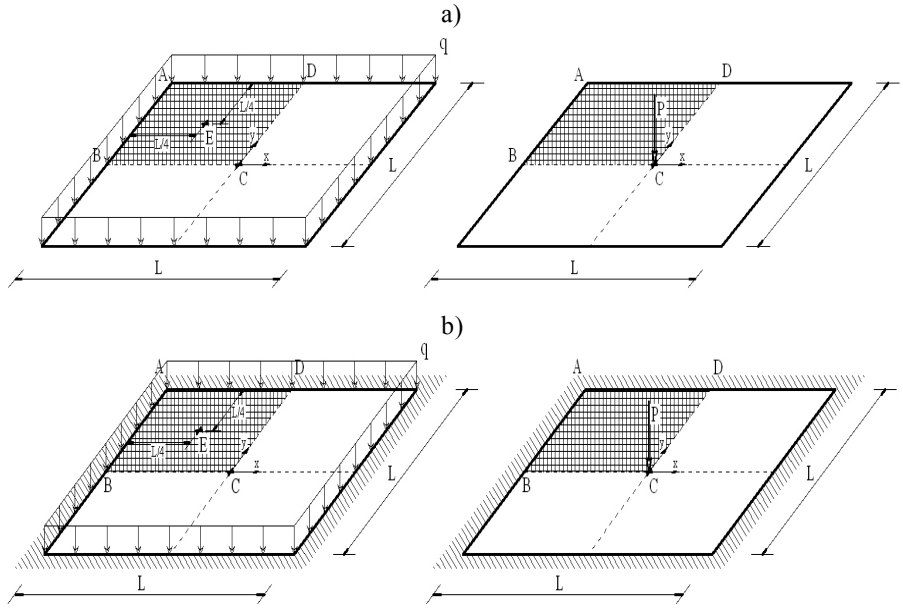

Figure 3.36 – Square plate (λ = 40) for verification and convergence analysis. SS plate (a) and clamped plate (b) under uniformly distributed load and central point load.

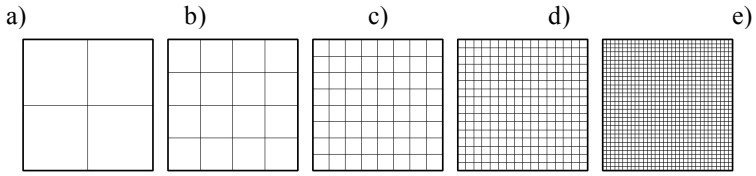

Figure 3.37 – Meshes of nxn QLRZ elements employed for verification and convergence analysis. (a) n = 2; (b) n = 4; (c) n = 8; (d) n = 16; (e) n = 32.

QLRZ meshes properties				
Mesh	N	Elements	Nodes	DOFs
1	2	4	9	45
2	4	16	25	150
3	8	64	81	405
4	16	256	289	1445
5	32	1024	1089	5445

Table 3.12 – QLRZ meshes properties.

The reference solution was obtained by a finite element analysis using a mesh of 32x32 4-noded quadrilateral Reissner-Mindlin (FSDT) element with substitute shear strain fields [111].

In order to assess the element accuracy, the following relative error is defined

$$e_r = \frac{w_i - w_{RMT}}{w_{RMT}} \qquad 3.102$$

where w_i is the vertical deflection at the center point computed with the *i*th QLRZ mesh $(i = 1, 2, ..., 5)$ and w_{RMT} is the reference solution. The w_{RMT} values for all cases are listed in Table 3.13.

Reissner-Mindlin solutions		
Boundary	Load	w_{RMT}
SS	Distributed	0.02680
	Point	0.07730
Clamped	Distributed	0.00841
	Point	0.03790

Table 3.13 – Reissner-Mindlin solutions using a mesh of 32x32 four-noded quadrilateral elements.

The QLRZ solution of the problem and the relative error are listed in Table 3.14.

Figure 3.38 shows the behavior of the error. Labels “SS-P”, “SS-q”, “C-P”, and “C-q” refer to simply-supported-point-load, simply-supported-distributed-load, clamped-point-load, and clamped-distributed-load, respectively.

Relative error (e_r%) of w at center point					
Load	Mesh	SS		Clamped	
		w	er (%)	w	er (%)
Distributed	2x2	0.026150	-2.43	0.0080239	-4.59
	4x4	0.026638	-0.60	0.0082998	-1.31
	8x8	0.026744	-0.21	0.0083747	-0.42
	16x16	0.026770	-0.11	0.0083939	-0.19
	32x32	0.026776	-0.09	0.0083988	-0.13
Point	2x2	0.076049	-1.62	0.0322470	-14.92
	4x4	0.076392	-1.17	0.0360900	-4.78
	8x8	0.076767	-0.69	0.0371910	-1.87
	16x16	0.076966	-0.43	0.0375650	-0.88
	32x32	0.077097	-0.26	0.0377400	-0.42

Table 3.14 – Relative error e_r of w at center point.

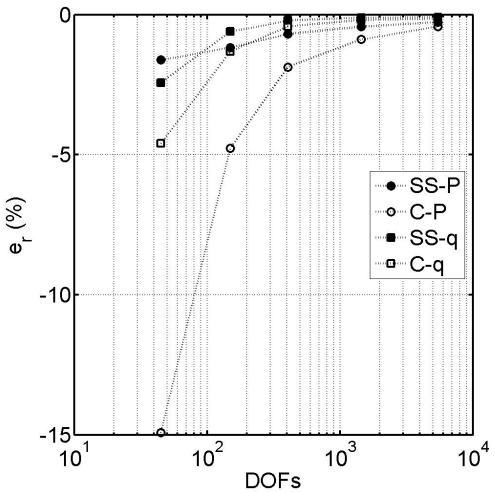

Figure 3.38 – Relative error e_r of central deflection.

Figure 3.38 clearly shows the convergence of the QLRZ solution to the Reissner-Mindlin solution for all cases. Good accuracy is obtained already for the 4x4 mesh (e_r less than 2.5%) except for the C-p case (e_r approximately equal to 5%). Results for the SS case (error < 2.5%) are better than for the clamped one. The worst result is obtained for the clamped plate under central point load for the 2x2 mesh (e_r=-14.92%).

3.3.7.3 Convergence

In order to study the influence of the heterogeneity of the laminated material on the convergence and accuracy of the QLRZ element, a SS and a clamped square plates of length side L = 2m and thickness h = 0.1m (λ = 20) under uniformly distributed load q = 1N/m^2 (Figure 3.36a and Figure 3.36c) are analyzed. Three different laminated materials, whose properties are listed in Table 3.15, are considered for each example. The material heterogeneity increases from composite C1 to C3.

Taking advantage of symmetry only one quarter of plate is analyzed using the QLRZ meshes shown in Figure 3.37. The reference solution was obtained by a 3D finite element analysis using a mesh of 10x10x9 (3 elements per ply) 20-noded hexahedral elements involving 4499 nodes and 13497 DOFs (Figure 3.39).

Composite Materials				
		Layer 1 (bottom)	Layer 2 (core)	Layer 3 (top)
Composite C1	h_i	h/3	h/3	h/3
	E [MPa]	$2.19\text{x}10^{-1}$	$2.19\text{x}10^{-2}$	$4.40\text{x}10^{-1}$
	υ	0.25	0.25	0.25
Composite C2	h_i	h/3	h/3	h/3
	E [MPa]	$2.19\text{x}10^{-1}$	$2.19\text{x}10^{-3}$	$2.19\text{x}10^{-1}$
	υ	0.25	0.25	0.25
Composite C3	h_i	h/10	4h/5	h/10
	E [MPa]	$2.19\text{x}10^{-1}$	$7.25\text{x}10^{-4}$	$7.30\text{x}10^{-2}$
	υ	0.25	0.25	0.25

Table 3.15 – Composite material properties.

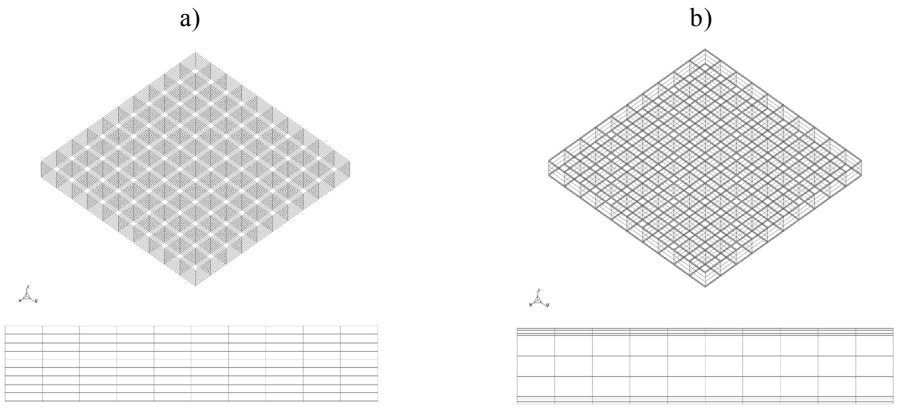

Figure 3.39 – 10x10x9 HEXA20 meshes employed to compute the reference solution for composite C1 and C2 (a), and composite C3 (b).

Convergence is quantified by the relative error defined as

$$e_r = \frac{m_i - m_{3D}}{m_{3D}} \qquad 3.103$$

where m_i and m_{3D} are the magnitudes of interest obtained with the ith QLRZ mesh (i = 1,2,…,5) and the 3D reference solution, respectively. The magnitudes studied m are: the middle (z = 0) vertical deflection w at the center point C (Figure 3.36), the axial stress σ_x on the top surface of ply 1 at point E, and ψ_x at point E. Since ψ_x does not appear in 3D finite element analyses, m_i and m_{3D} are the values of this magnitude obtained with the ith QLRZ mesh (i = 1,…,4) and the finest mesh (32x32), respectively.

Results are listed in Table 3.16 and Table 3.17, and Figure 3.40 and Figure 3.41.

It is clearly seen that convergence is always slower for the most heterogeneous material and for the clamped plate.

For the clamped plate and the three materials (Table 3.16) errors are less than 10% for the 16x16 mesh for all variables. For the SS plate (Table 3.17) errors are less than 2.3% for the 8x8 mesh in all cases.

For composite C1 (the most homogeneous) errors are less than 2.9% for the 8x8 mesh in all cases and less than 6.3% for the 4x4 mesh in all cases except for σ_x in the clamped plate.

For the most heterogeneous material (composite C3), the difference in the results between the SS and the clamped plate is larger. For the SS plate (Table 3.17) errors are less than 2.3% for the 8x8 mesh in all variables. For the clamped plate (Table 3.16) errors are less than 23% for the 8x8 mesh and less than 10% for the 16x16 mesh in all cases. The quality of results obtained for the composite C2 is between that of composites C1 and C3.

Relative error e_r (%) in clamped plate

Mesh	**w** at point C			$\boldsymbol{\sigma_x}$ at point E			$\boldsymbol{\psi_x}$ at point E		
	C1	C2	C3	C1	C2	C3	C1	C2	C3
2x2	11.71	50.28	60.99	99.99	100	100	26.13	80.09	86.48
4x4	4.65	30.16	43.47	20.86	44.14	45.53	6.28	43.34	54.80
8x8	1.60	12.32	22.44	2.90	14.35	17.24	1.47	13.68	18.58
16x16	0.29	3.67	9.25	-1.21	-0.40	-1.15	0.30	2.58	2.22
32x32	-0.14	0.69	2.85	-2.22	-4.70	-4.62	0.00	0.00	0.00

Table 3.16 – Clamped square plate ($\lambda = 20$) under uniformly distributed load. Relative error e_r (%) for w, σ_x, and ψ_x.

Relative error e_r (%) in SS plate

Mesh	**w** at point C			**σx** at point E			**ψx** at point E		
	C1	C2	C3	C1	C2	C3	C1	C2	C3
2x2	2.69	19.36	25.83	26.98	32.89	33.24	9.11	41.06	51.92
4x4	0.68	6.50	10.14	4.86	7.70	9.05	3.99	8.95	13.67
8x8	0.25	1.54	2.22	-0.30	-0.79	0.44	0.71	0.40	1.84
16x16	0.15	0.38	0.35	-1.55	-3.04	-1.92	0.07	0.45	1.44
32x32	0.12	0.12	-0.02	-1.86	-3.49	-2.07	0.00	0.00	0.00

Table 3.17 – SS square plate ($\lambda = 20$) under uniformly distributed load. Relative error e_r (%) for *w*, σ_x, and ψ_x.

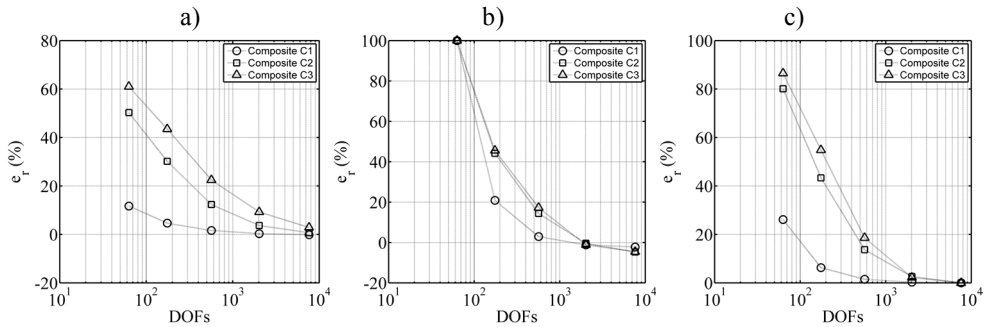

Figure 3.40 – Clamped square plate ($\lambda = 20$) under uniformly distributed load. Relative error e_r (%) for *w* (a), σ_x (b), and ψ_x (c).

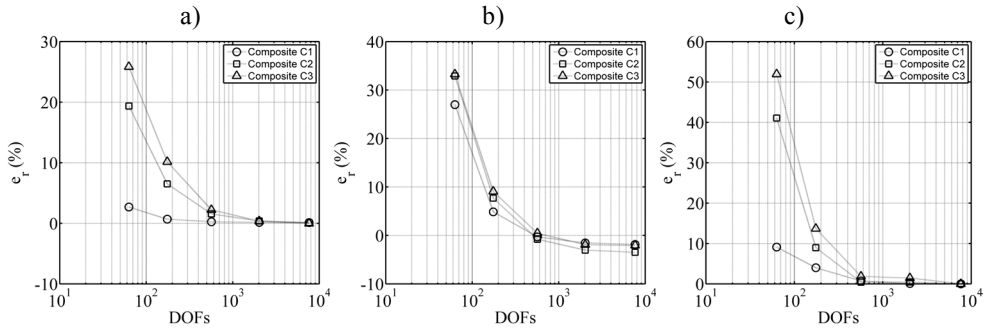

Figure 3.41 – SS square plate ($\lambda = 20$) under uniformly distributed load. Relative error e_r (%) for *w* (a), σ_x (b), and ψ_x (c).

3.3.7.4 Numerical examples

Comparison for SS square and circular composite laminated plates

In order to show the performance of the QLRZ element for highly heterogeneous composite material, a square SS plate of length L = 2m and thickness h = 0.1m, and a circular SS plate of diameter D = 2m and thickness h = 0.1m are studied. The structures are loaded under a uniformly distributed load, q=10000N/m^2 (Figure 3.42).

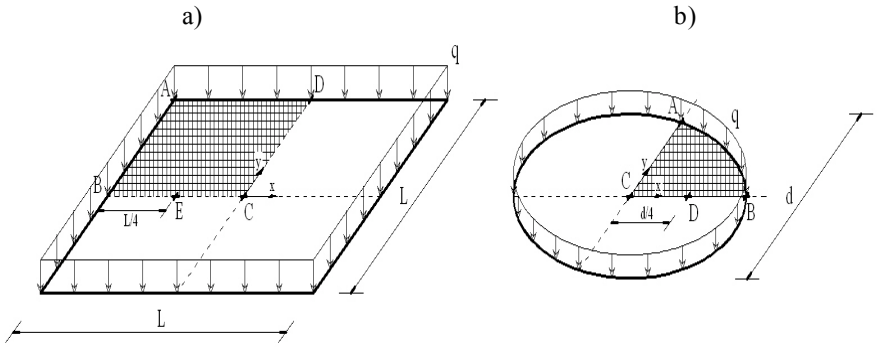

Figure 3.42 – Square SS plate (a) and circular SS plate (b) under uniformly distributed load.

Each plate is studied for different composite laminated materials with properties listed in Table 3.18 and Table 3.19. The square plate is analyzed for composites C4-7 and the circular plate for composites C6-7.

Do to symmetry only one quarter of plate is analyzed with the QLRZ meshes shown in Figure 3.43 whose properties are listed in Table 3.20. The reference solution is a 3D finite element analysis using HEXA20 elements. The different 3D meshes for each case are shown in Figure 3.44. Details of each mesh are listed in Table 3.21.

Layer material properties				
	A	B	C	D
E_1	157.9x10^2	19.15		
E_2	9.58 x10^2	19.15	0.104 x10^2	104.1 x10^2
E_3	9.58 x10^2	191.5		
μ_{12}	0.32	6.58 x10^{-4}		
μ_{13}	0.32	6.43 x10^{-8}	0.30	0.31
μ_{23}	0.49	6.43 x10^{-8}		
G_{12}	5.93 x10^2	42.3 x10^{-7}	0.04x10^2	39.73 x10^2
G_{13}	5.93 x10^2	36.51		
G_{23}	3.23 x10^2	124.8		

Table 3.18 – Layer material properties. E and G are given in MPa.

Composite laminated materials		
Composite	Layer distribution	h_i / h
C4	(A/C/A)	(0.1/0.8/0.1)
C5	(A/B)	(0.5/0.5)
C6	(A/B/C/D)	(0.1/0.3/0.5/0.1)
C7	(A/C/A/C/B/C/A/C/A)	(0.1/0.1/0.1/0.1/0.2/0.1/0.1/0.1/0.1)

Table 3.19 – Layer distribution of composite materials.

QLRZ meshes properties				
Mesh	nxn	Number of elements	Nodes	DOFs
a	8x8	64	81	567
b	16x16	256	289	2023
c	--	40	53	371
d	--	168	193	1351

Table 3.20 – QLRZ meshes properties.

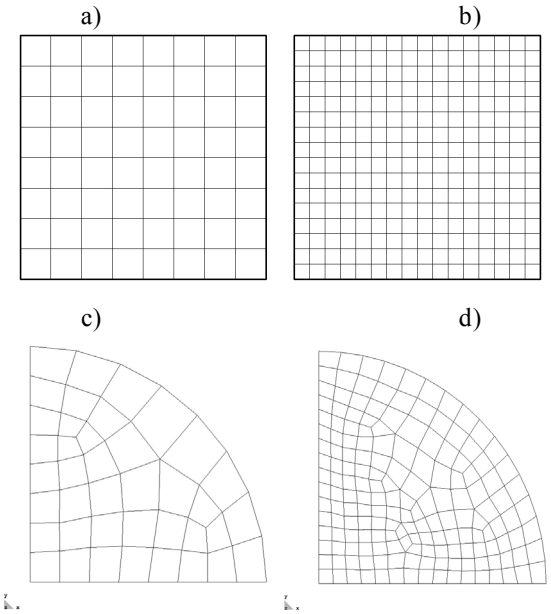

Figure 3.43 – QLRZ meshes. Square plate: 8x8 (a) and 16x16 element (b). Circular plate: 40 (c) and 168 (d) elements.

HEXA20 mesh properties				
Mesh	Composite	Number of elements	Nodes	DOFs
a	C4	640	3285	9855
b	C5	512	2673	8019
c	C6	768	3897	11691
d	C7	1728	8487	25461
e	C6	602	3094	9282
f	C7	1161	5824	17472

Table 3.21 – HEXA20 meshes properties.

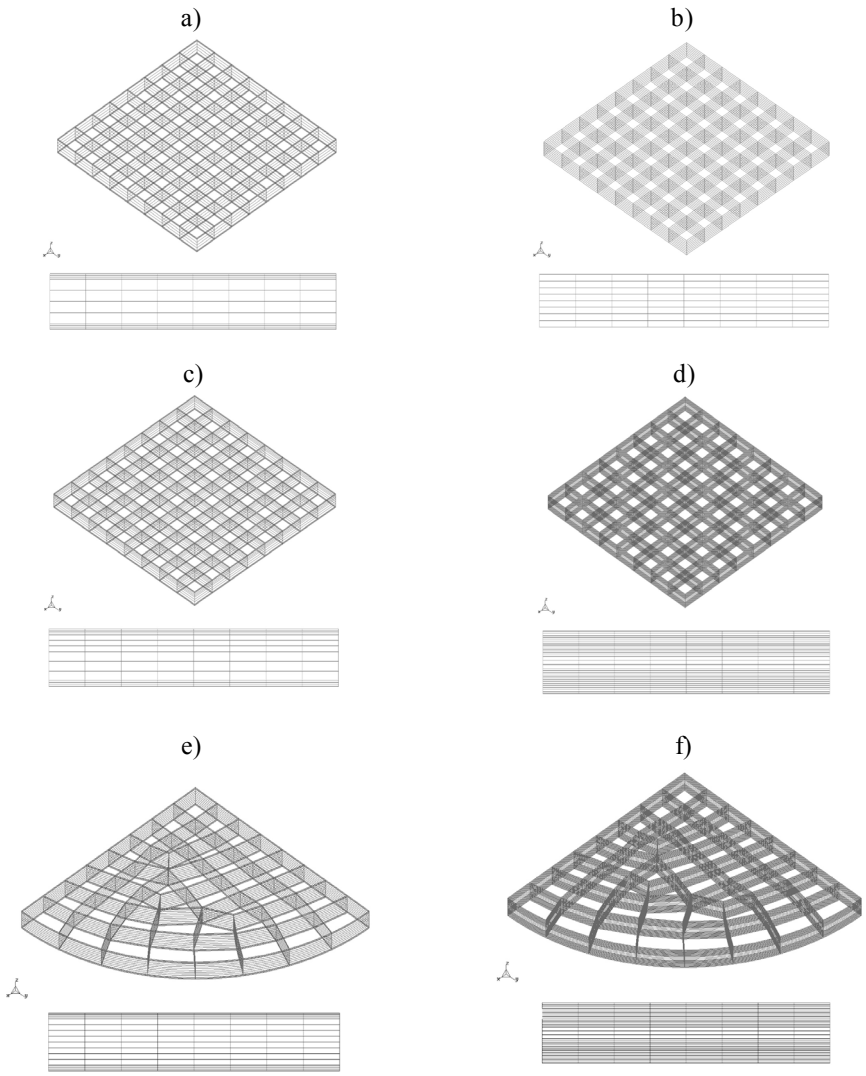

Figure 3.44 – HEXA20 reference meshes. Square meshes for composites C4 (a), C5 (b), C6 (c), C7 (d), and circular meshes for composites C6 (e) and C7 (f).

The RMT results for the square plate of composite C4 are also shown in Figure 3.45. The RMT solution was obtained by using a mesh of 16x16 four-noded QLLL plate element [108, 112].

Figure 3.45-Figure 3.50 show the computed vertical deflection w (a), the thickness distribution of the axial displacement u (b), the axial stress σ_x (c), the transverse shear stress τ_{xz} (d) for each plate under study.

The vertical deflection is accurately captured. At the center of plate, the maximum error (14%) is given by the circular plate of composite C6 for the 40-element mesh (Figure 3.46a). The errors are less than 10% for the finest mesh (168 elements).

The thickness distribution of the axial displacement is accurately predicted in all cases. The ability to capture the complex kinematics of laminated composite materials is a key feature of the QLRZ plate element. The successful axial displacement prediction leads to accurate axial stress values as shown in Figures c). Figures d) displays the good results for the thickness distribution of the transverse shear stresses computed by means of Eq.(3.100).

Figure 3.45 shows the inaccurate results when modeling a composite laminated plate using QLLL elements based on RMT. The deflection at the plate center is three times stiffer than the reference solution (Figure 3.45a). The RMT solution also yields an erroneous linear thickness distribution of the axial displacement (Figure 3.45b), which leads to a distorted distribution of the axial stress (Figure 3.45c). Finally, the RMT is unable to capture the correct transverse shear stress distribution (Figure 3.45d).

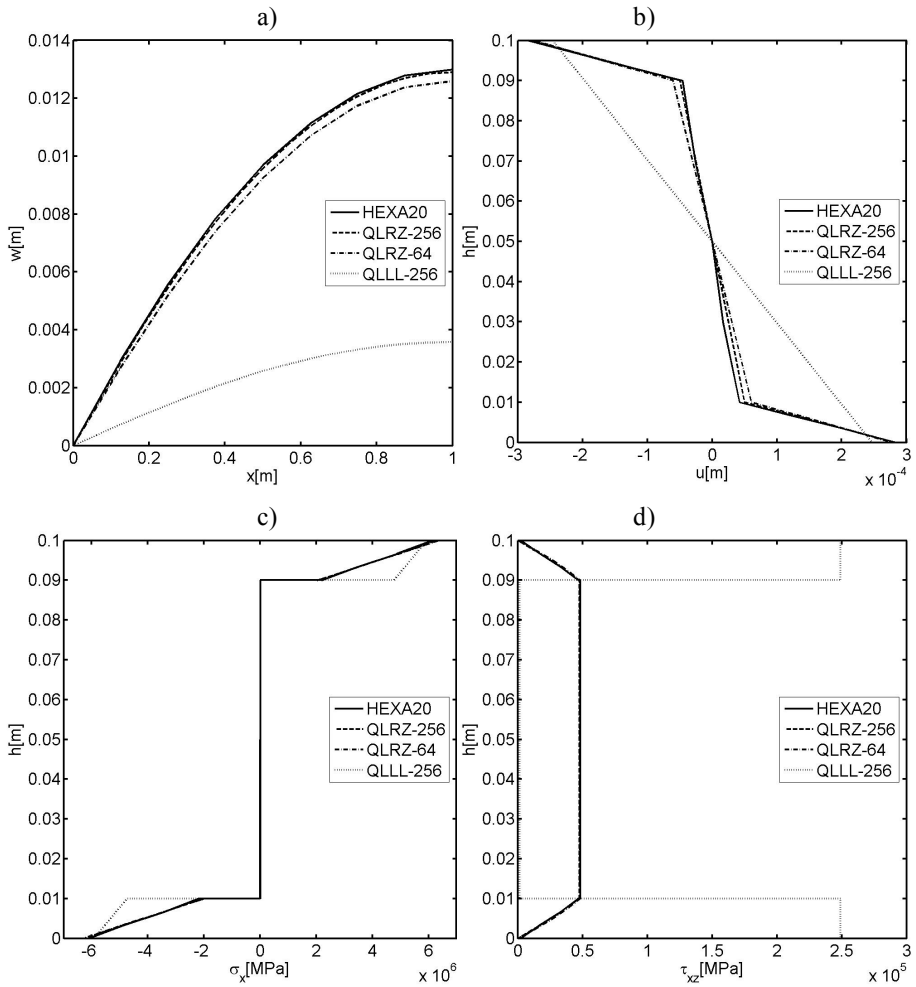

Figure 3.45 – SS square plate under uniformly distributed load. Composite C4. (a) Vertical deflection along central line BC. Thickness distribution of: (b) axial displacement *u* at point B, (c) axial stress σ_x at the center point C, and (d) transverse shear stress τ_{xz} at point E.

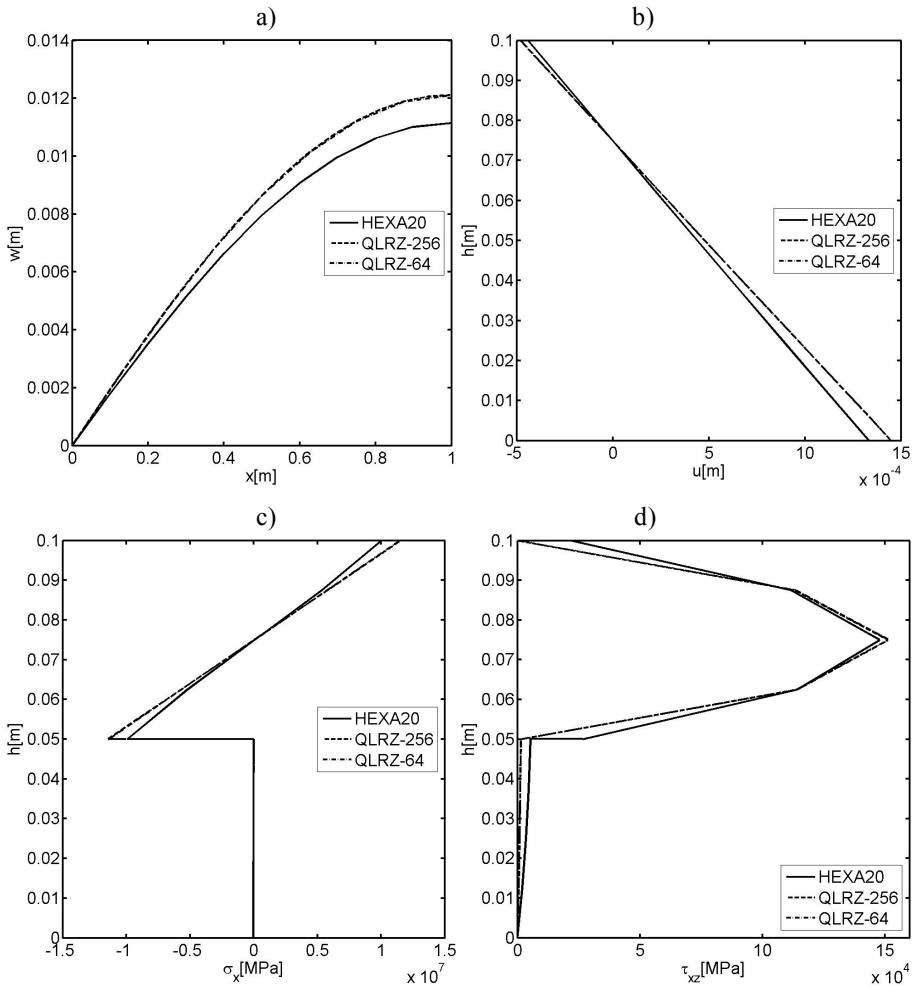

Figure 3.46 – SS square plate under uniformly distributed load. Composite C5. (a) Vertical deflection along central line BC. Thickness distribution of: (b) axial displacement *u* at point B, (c) axial stress σ_x at the center point C, and (d) transverse shear stress τ_{xz} at point E.

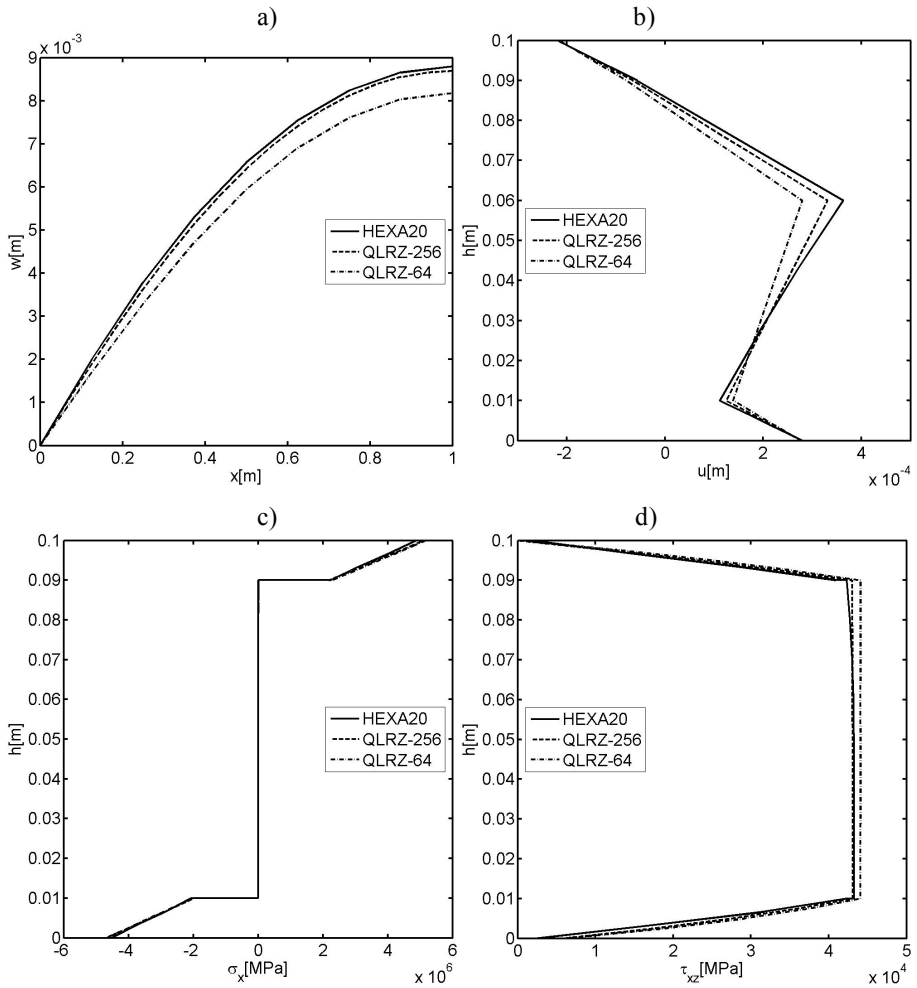

Figure 3.47 – SS square plate under uniformly distributed load. Composite C6. (a) Vertical deflection along central line BC. Thickness distribution of: (b) axial displacement *u* at point B, (c) axial stress σ_x at the center point C, and (d) transverse shear stress τ_{xz} at point E.

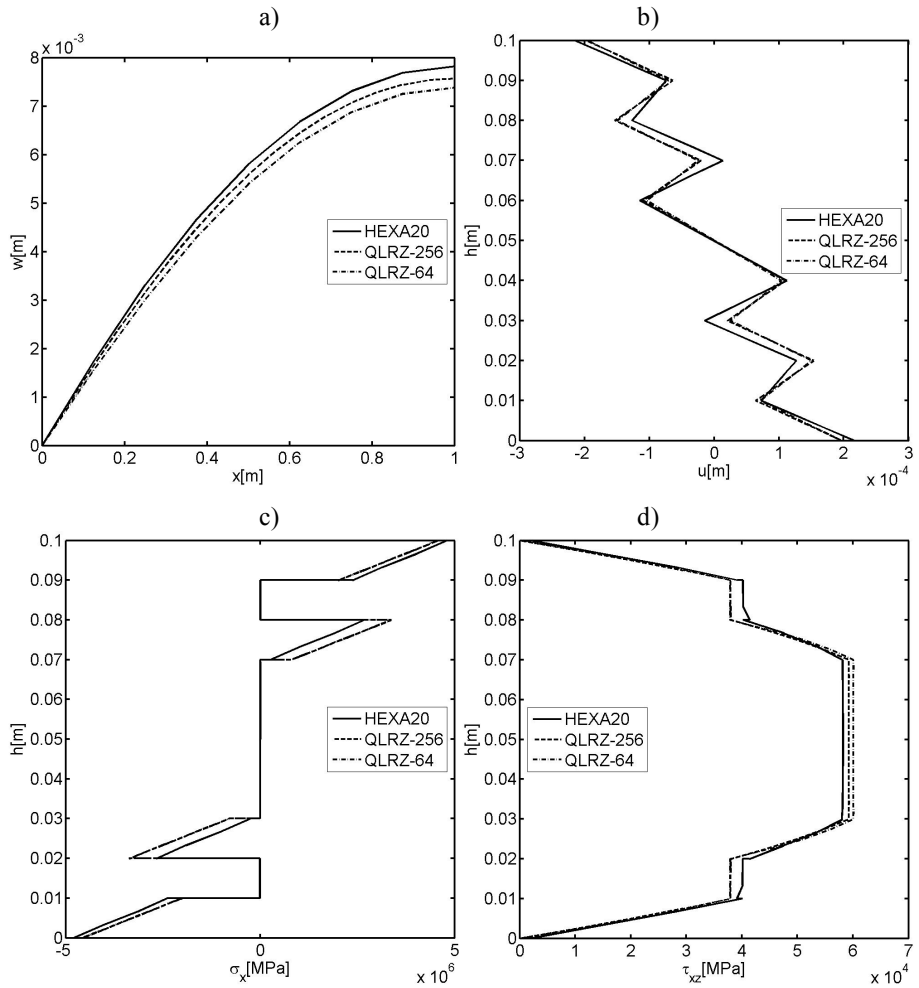

Figure 3.48 – SS square plate under uniformly distributed load. Composite C7. (a) Vertical deflection along central line BC. Thickness distribution of: (b) axial displacement u at point B, (c) axial stress σ_x at the center point C, and (d) transverse shear stress τ_{xz} at point E.

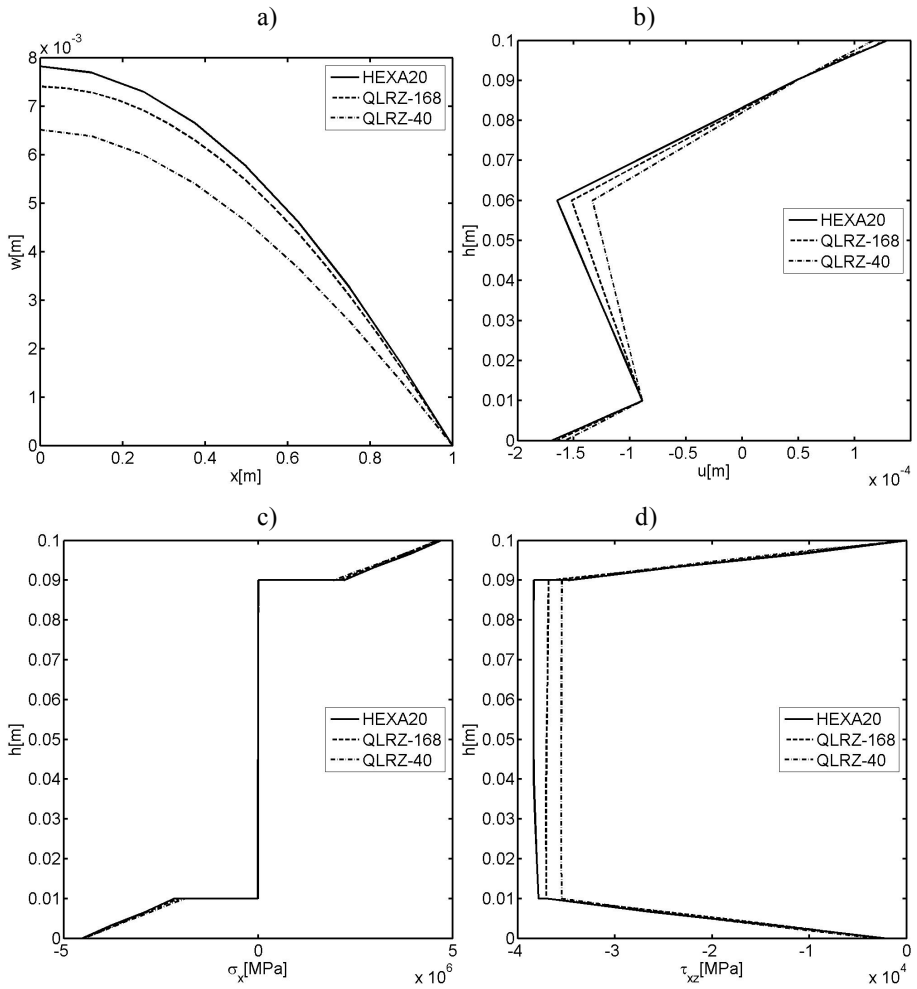

Figure 3.49 – SS circular plate under uniformly distributed load. Composite C6. (a) Vertical deflection along line BC. Thickness distribution of: (b) axial displacement *u* at point D, (c) axial stress σ_x at the center point C, and (d) transverse shear stress τ_{xz} at point D.

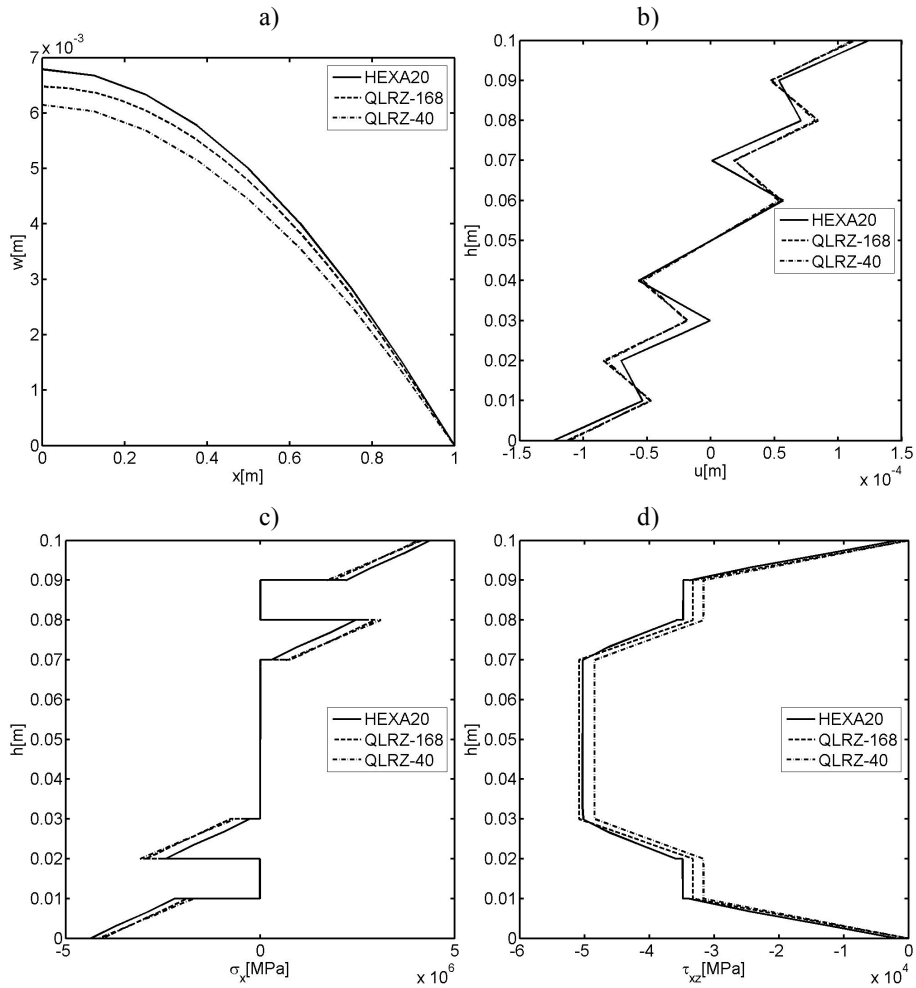

Figure 3.50 – SS circular plate under uniformly distributed load. Composite C7. (a) Vertical deflection along line BC. Thickness distribution of: (b) axial displacement *u* at point D, (c) axial stress σ_x at the center point C, and (d) transverse shear stress τ_{xz} at point D.

4 Numerical model of delamination using the beam LRZ and the plate QLRZ finite elements

A numerical model to simulate mode II/III delamination in advanced composite beams and plates based on the RZT theory is presented in this Chapter.

The method uses the LRZ and QLRZ finite elements for describing the whole laminated material including the resin-rich zone at the interface between plies where delamination occurs. In other words, no additional technique for modeling the delamination paths is required.

Some limitations of the model are discussed below in Section 4.1.

The key attribute of the RZT theory that makes it able to capture relative displacement between layers is that the zigzag function depends on the transverse shear modulus of each layer. This feature allows changing the shape of the zigzag in-plane displacement by modifying the shear properties of plies. With this in mind, the relative displacement between neighboring layers can be modeled by simply discretizing the resin-rich interface zone between them (Figure 2.7) with an additional thin enough ply and then considerately reduce its shear modulus in comparison with those of neighboring layers. It is important to note that no additional kinematics variables are introduced in the model by incorporating these interface plies.

The additional layers, which describe the delamination path, are also named as cohesive layers (cl) henceforth. Moreover, layers that make up the laminate are named as material layers (ml).

The resin-rich zone at the interface is considered as an isotropic material. Therefore, the mechanical behavior of “cl” layers is controlled by an isotropic damage model which is developed below in Section 4.2. Note that delamination process is described by the intra-laminar damage of the “cl” ply.

Intra-laminar failure mechanisms within “ml” layers are not considered. The mechanical behavior of these layers is considered as linear elastic. As a result,

delamination cannot migrate through layers but it can propagate parallel to the ply planes within the "cl" layers. Although failure mechanisms of material layers are despised in the present form of the LRZ/QLRZ delamination model, they can be accounted for in the future.

The non-linear problem induced by the degradation process is solved by the modified Newton-Raphson method presented in Section 4.3.

4.1 Kinematics limitations of the LRZ and QLRZ elements for simulation delamination

The most relevant limitations of the LRZ/QLRZ delamination model proceed from the definition of the displacement field and the zigzag function.

Definition of the through-thickness displacement: The model is unable to simulate opening fracture mode (mode I) because the vertical displacement is defined constant along the laminate thickness. Thus, sliding (mode II) and scissoring (mode III) fracture modes can be simulated only. Of course, fracture mode III is not accounted for in beams since the transversal in-plane displacement is not considered (Eq.(3.6)).

Definition of the zigzag function: After delamination, the laminate is divided into sub-laminates with their own kinematics. According to Section 2.1.4, for a given structural slenderness ratio, if the transverse anisotropy of the resultant sub-laminates is enough high, the in-plane displacement may describe a zigzag form, as shown in Figure 4.1b.

Zigzag patterns of in-plane displacement within sub-laminates after delamination cannot be captured by the present model because of the zigzag function definition. The reasons are deducted immediately below. For simplicity, no distinction between orthogonal directions (x,y) is considered.

The zigzag function is computed by Eq.(2.10) as

$$\phi^k = \overline{\phi}^{k-1} + \frac{h^k \beta^k}{2}\left(\zeta^k + 1\right)$$

where the slope of ϕ^k function for the kth layer is computed by Eq.(2.17) as

$$\beta^k = \frac{G}{D_t^k} - 1$$

being D_t^k and G the transverse shear stiffness of the kth layer and the average transverse shear stiffness properties of the laminate, respectively. G is defined by Eq.(2.18) as

$$G = h\left[\sum_{k=1}^{N}\frac{h^k}{D_t^k}\right]^{-1}$$

In order to capture relative in-plane displacement between plies with the LRZ/QLRZ delamination model, the zigzag function must be updated by reducing the shear modulus of the damaged cohesive layer, as demonstrated below in Section 4.4. Thus, when the transverse shear properties of a damaged layer d are reduced almost to zero, i.e. $D^d \rightarrow 0$, G tends to zero. As a result, the slope of the zigzag function for all undamaged layers is approximately equal to the negative unit value, i.e. $\beta^k \simeq -1$, whereas the slope for the damaged layer is defined positive by $\beta^d \simeq h / h^d - 1$. Therefore, the zigzag function is defined by a piecewise linear function, where its slope changes at the damaged ply only, as schematized in Figure 4.2a. Thus, the in-plane displacement of the sub-laminates can be represented by a linear distribution only (Figure 4.2b) because similar slopes are computed for all undamaged layers.

According to Section 2.1.4 and what has been previously stated, delamination in multilayered structures having low span-to-thickness ratio and high transverse anisotropy cannot be correctly simulated with the present model.

However, that is not the case of advanced composite materials where the shear modulus does not differ generally in more than one order of magnitude between layers [113]. Moreover, laminated structures of composite materials are generally characterized by high slenderness ratios.

Furthermore, delamination in three-layered laminates can be modeled with independence of the level of transverse anisotropy and the slenderness of the structures[20] because the in-plane displacement within each sub-laminate presents a linear distribution. For these materials, sub-laminates consist of at most two layers where the linear kinematics is governed by the stiffer ply only.

Because of this, skin-core delamination in sandwich materials can be also modeled with the LRZ/QLRZ delamination model, as shown in Section 4.6.1.

[20] In order to avoid tall beams/plates, the span-to-thickness ratio has to be at least 5.

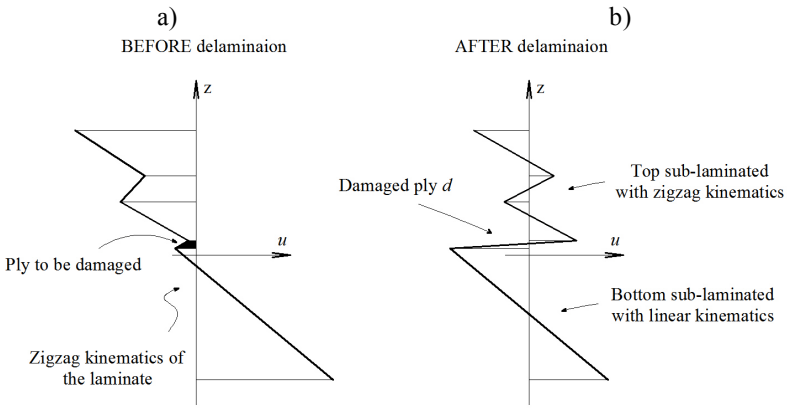

Figure 4.1 – In-plane displacement before a) and after b) delamination.

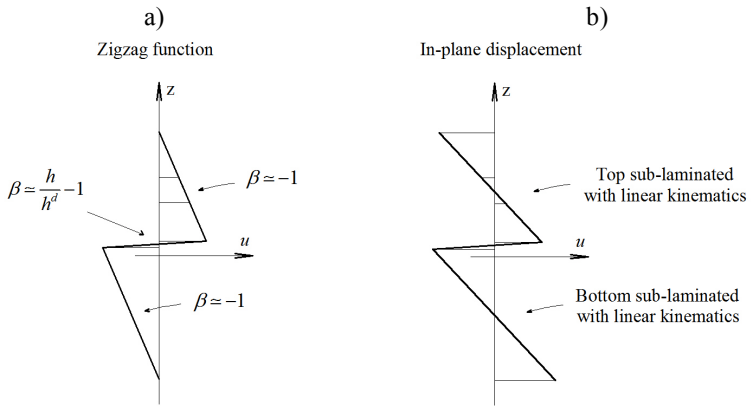

Figure 4.2 – Zigzag function a) and RZT in-plane displacement b) after delamination.

4.2 Isotropic damage model

The mechanical behavior of the cohesive layer is described by the isotropic damage model detailed below.

Among different continuum damage models such as those found in Ref. [114-117], the simple and robust isotropic damage model proposed by Oliver et al. [118] is used to manage the non-linear behavior of the “cl” layers.

The level of damage or degradation is monitored through a single internal scalar variable d, which takes values ranged between 0 (no damage) and 1 (full damage). This variable represents the loss of the material stiffness as shown in Figure 4.3a. Physically, the degradation process is characterized by the presence and the growth of micro-cracks and -cavities within the solid which leads to a reduction of the effective area of load

transfer. Thus, the real stresses vector $\boldsymbol{\sigma}$ of any isotropic layer is transformed to an effective one $\boldsymbol{\sigma}_0$ as

$$\boldsymbol{\sigma}_0 = \frac{\boldsymbol{\sigma}}{\left(1-d\right)} \tag{4.1}$$

where d measures the degradation level of the isotropic layer in all direction.

From Eq.(4.1), the real stresses vector is defines as

$$\boldsymbol{\sigma} = \left(1-d\right)\boldsymbol{\sigma}_0 = \left(1-d\right)\mathbf{D}_0\boldsymbol{\varepsilon} \tag{4.2}$$

where $\boldsymbol{\varepsilon}$ is the strain vector and $\mathbf{D}_0$ is the undamaged isotropic constitutive matrix which can be easily obtained from Eq.(3.10) and Eq.(3.48) for beams and plates, respectively.

In order to distinguish between a damage state and an undamaged one, it is necessary to define a damage criterion which is formulated here in the undamaged stress space as

$$F\left(\boldsymbol{\sigma}_0, d\right) = f\left(\boldsymbol{\sigma}_0\right) - c\left(d\right) \leq 0 \tag{4.3}$$

where f is a norm used to compare different states of deformation and c is the damage threshold. Note that f depends on the effective stresses whereas c is a function of the damage variable. Damage occurs when the value of f is larger than c. Damage starts for $f > c_0$, being c_0 the initial damage threshold value, which depends on the material properties, defined as

$$c_0 = \frac{f_t}{\sqrt{E_0}} \tag{4.4}$$

where f_t is the tensile strength and E_0 the Young modulus of the undamaged isotropic material.

The norm f adopted in this work is defined as

$$f = \sqrt{\boldsymbol{\varepsilon} : \boldsymbol{\sigma}_0} \tag{4.5}$$

For convenience, a fully equivalent expression for Eq.(4.3) is defined as

$$\overline{F} = \Theta\left(f\right) - \Theta\left(c\right) \leq 0 \tag{4.6}$$

where $\Theta\left(\cdot\right)$ is a suitable monotonic scalar function.

The evolution laws for the damage variable d and the damage threshold c are expressed as

$$\begin{aligned} \dot{c} &= \dot{\mu} \\ \dot{d} &= \dot{\mu}\frac{\partial \bar{F}}{\partial f} = \frac{\partial \Theta(f)}{\partial f} \end{aligned} \qquad 4.7$$

where μ is a damage consistency parameter which is used to define loading and unloading/reloading (Figure 4.3a) conditions according to the Kuhn-Tucker conditions

$$\dot{\mu} \geq 0 \quad ; \quad \bar{F} \leq 0 \quad ; \quad \dot{\mu}\bar{F} = 0 \qquad 4.8$$

From Eq.(4.7), the evolution of variables d and c is obtained via integrating [119] as

$$\begin{aligned} d &= \Theta(f) \\ c &= \max\{c_0 \,;\, \max\{f\}\} \end{aligned} \qquad 4.9$$

In this work an exponential evolution law is adopted for $\Theta(f)$ (Figure 4.3b) as

$$\Theta(f) = 1 - \frac{c_0}{f} e^{B\left(1-\frac{f}{c_0}\right)} \qquad 4.10$$

Considering the norm of Eq.(4.5), the exponential softening of Eq.(4.10), and the initial damage threshold value c_0 (Eq.(4.4)), the parameter B is computed as

$$B = \left(\frac{G_f \cdot E_0}{l^* \cdot (f_t)^2} - \frac{1}{2} \right)^{-1} \geq 0 \qquad 4.11$$

being G_f the fracture energy per unit area and l^* a characteristic length, which is here defined as the influence length of each Gauss point for LRZ element and is equal to the square root of the influence area of each Gauss point for QLRZ element.

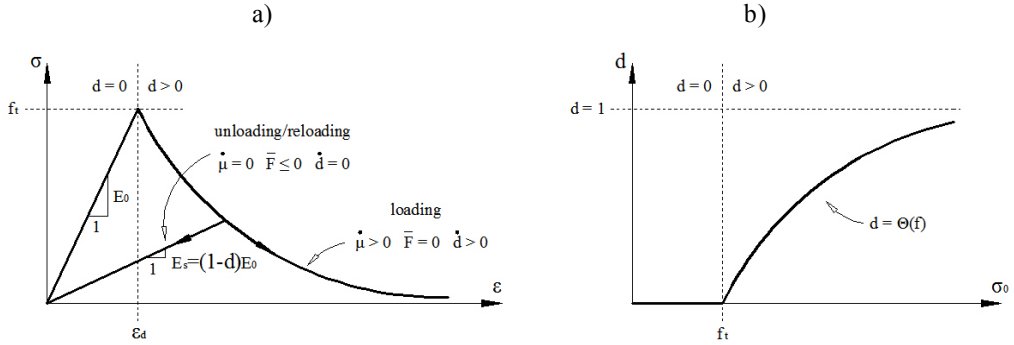

Figure 4.3 – Uniaxial stress-strain curve with softening (a) and exponential damage variable evolution (b).

4.3 Non-lineal problem solution: modified Newton-Raphson method

During a material degradation process, the structure stiffness suffers changes that induce a non-linear response of the structure. The resulting non-linear set of equilibrium equations can be written as

$$\mathbf{F}^{\text{ext}} - \mathbf{F}^{\text{int}}\left(\mathbf{q}\right) = \mathbf{R}\left(\mathbf{q}\right) = 0 \qquad 4.12$$

where $\mathbf{q}$, $\mathbf{F}^{\text{ext}}$ and $\mathbf{F}^{\text{int}}\left(\mathbf{q}\right)$ are the discretization parameters, the external and the internal forces vectors, respectively. $\mathbf{R}\left(\mathbf{q}\right)$ is the residual forces vector. Note, dynamic forces are not considered.

The solution of Eq.(4.12) is achieved by using an incremental-iterative method employing sufficiently small increment from a known solution. Thus, the non-lineal problems is formulated as the solution of

$${}_{n}\mathbf{F}^{\text{ext}} - \mathbf{F}^{\text{int}}\left({}_{n}\mathbf{q}\right) = \mathbf{R}\left({}_{n}\mathbf{q}\right) = 0 \qquad 4.13$$

for the *n*th increment and from the last known solution

$$\mathbf{q} = {}_{n-1}\mathbf{q} \quad ; \quad \mathbf{F}^{\text{ext}} = {}_{n-1}\mathbf{F}^{\text{ext}} \quad ; \quad {}_{n-1}\mathbf{R} = 0 \qquad 4.14$$

The well-known iterative Newton-Raphson method proposes a linear approximation of Eq.(4.13) via the truncated Taylor series as

$${}_{n}^{i}\mathbf{R} \approx {}_{n}^{i-1}\mathbf{R} + {}_{n}^{i-1}\left(\frac{\partial \mathbf{R}}{\partial \mathbf{q}}\right)^{i} d\mathbf{q} = 0 \qquad 4.15$$

where $d\mathbf{q}$ is the increment of the nodal DOF at *i*th iteration.

From Eq.(4.13)

$${}_{n}^{i-1}\left(\frac{\partial \mathbf{R}}{\partial \mathbf{q}}\right) = -{}_{n}^{i-1}\left(\frac{\partial \mathbf{F}^{\text{int}}}{\partial \mathbf{q}}\right) = -{}^{i-1}\mathbf{K}_{\text{T}} \qquad 4.16$$

where $\mathbf{K}_{\text{T}}$ is the tangent stiffness matrix at *i*-1th iteration.

Substituting Eq.(4.16) into Eq.(4.15) gives

$${}_{n}^{i-1}\mathbf{R} = {}^{i-1}\mathbf{K}_{\text{T}}\,{}^{i}d\mathbf{q} \qquad 4.17$$

or

$${}^{i}d\mathbf{q} = \left({}^{i-1}\mathbf{K}_{\text{T}}\right)^{-1}\,{}_{n}^{i-1}\mathbf{R} \qquad 4.18$$

Finally, the solution is found by updating the nodal DOF $\mathbf{q}$ as

$$ {}^{i}_{n}\mathbf{q} = {}^{i-1}_{n}\mathbf{q} + {}^{i}d\mathbf{q} \tag{4.19} $$

or

$$ {}^{i}_{n}\mathbf{q} = {}_{n-1}\mathbf{q} + {}^{i}\Delta\mathbf{q} \tag{4.20} $$

with

$$ {}^{i}\Delta\mathbf{q} = \sum_{m=1}^{i} {}^{m}d\mathbf{q} \tag{4.21} $$

The process is repeated until the convergence criterion $\left\|\mathbf{R}\right\| \leq \varsigma \left\|\mathbf{F}^{\text{ext}}\right\|$ is satisfied being ς a predefined error tolerance [120].

In this work a modification of the Newton-Raphson method is used, where the tangent stiffness matrix $\mathbf{K}_{\text{T}}$ is approximated by

$$ {}^{i-1}\mathbf{K}_{\text{T}} \approx {}^{i-1}\mathbf{K}_{\text{d}} \tag{4.22} $$

being $\mathbf{K}_{\text{d}}$ the damaged stiffness matrix defined as

$$ {}^{i-1}\mathbf{K}_{\text{d}} = \int_{\omega} \mathbf{B}^{T}\, {}^{i-1}\ddot{\mathbf{D}}_{\text{d}}\mathbf{B}\ \text{d}\omega \tag{4.23} $$

with

$$ {}^{i-1}\ddot{\mathbf{D}}_{\text{d}} = \int_{\zeta} \left[{}^{i-1}\mathbf{S}^{k}_{\text{d}} \right]^{T} {}^{i-1}\mathbf{D}^{k}_{\text{d}}\ {}^{i-1}\mathbf{S}^{k}_{\text{d}} \text{d}\zeta \tag{4.24} $$

being ${}^{i-1}\mathbf{D}^{k}_{\text{d}}$ and $\ddot{\mathbf{D}}_{\text{d}}$ the damaged constitutive matrix for the kth layer computed by Eqs.(3.10, 3.48) and the damaged generalized constitutive matrix of the whole laminate defined by Eqs.(3.13, 3.60), respectively. The integration domains ω and ζ depend on the finite element employed.

Note, the subscript d indicates damaged quantities which are computed by reducing the mechanical properties of those layers where damage occurs. In order to capture delamination, the zigzag function has to be updated. Thus, the matrix ${}^{i-1}\mathbf{S}^{k}_{\text{d}}$ is set as a damaged quantity since it contains the zigzag function.

Furthermore, the solution at the first iteration of a new nth step has to be calculated by means of the damaged stiffness matrix $\mathbf{K}_{\text{d}}$ computed at the last iteration of the previous n-1th step.

Figure 4.4 schematizes the original and the modified Newton-Raphson method.

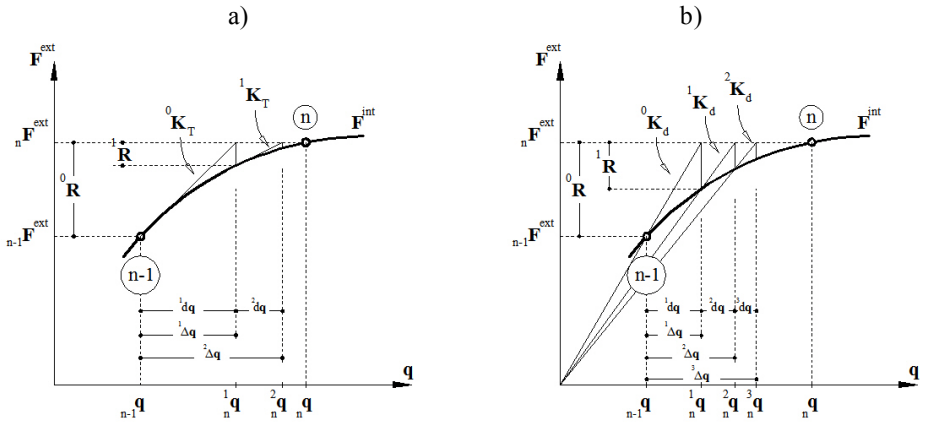

Figure 4.4 – Original (a) and modified (b) Newton-Raphson method.

4.4 Update of the zigzag function to simulate delamination

In order to capture relative displacements between layers, a technique based on updating the zigzag function during the degradation process of the "cl" plies is employed by the LRZ/QLRZ delamination model. The basics of this strategy are explained below.

In 3D finite element analyses, the nodal internal forces are obtained by integrating stresses over the finite elements volume. When a finite element suffers from softening because the damage threshold is reached, stresses within that damaged element are reduced. As a result, a lack of equilibrium between the internal forces of the damaged element and the neighboring elements happens, which induces nodal residual forces. These forces generate the relative displacement between layers that typically occurs during a delamination process. Then, equilibrium is achieved with an iterative process such as that of Section 4.3. This process is schematized in Figure 4.5a.

The kinematic variables (Eq.(2.3)) and stress resultants (Eqs.(3.11),(3.58)) of the LRZ/QLRZ finite elements are computed at the in-plane middle surface of the element ($z = 0$). Because of this, there are no forces within the laminate able to induce relative displacements between plies. Consequently, the LRZ/QLRZ elements are unable to provoke any change on the zigzag shape of the in-plane displacement by reducing stresses only.

In case stresses are reduced only, a variation of the amplitude of the previous displacement field is obtained, instead of capturing a delaminated kinematics. That is because the LRZ/QLRZ kinematics variables are not able to modify by themselves the

shape of the zigzag displacement, but they can vary the amplitude only. This is outlined in Figure 4.5b – Without ϕ update.

The kinematics of the RZT theory is defined by a superposition of a linear piecewise zigzag function over the linear FSDT displacement fields (Figure 2.3). As a result, the zigzag shape of the in-plane displacement is governed by the zigzag function ϕ only. Comprehensibly, in order to modify the zigzag form of the RZT in-plane displacement, the zigzag function must be updated according with the delamination process. Taking into account that the zigzag function depends on the transverse shear stiffness of each layer, the update of this function by reducing the shear properties of the damaged layer is a natural manner for provoking changes in the zigzag pattern of the in-plane displacement.

Taking into account that only "cl" plies are able to suffer damage in the LRZ/QLRZ delamination model and the degradation level is measured by the damage variable d, the update of the zigzag function is proposed by reducing the initial elastic shear moduli G_0^{cl} of the damaged cohesive layers "cl" as

$$G_d^{cl} = \left(1 - d^{cl}\right) G_0^{cl} \tag{4.25}$$

which leads to the definition of the average transverse shear stiffness G_{iz} as

$$\begin{bmatrix} G_{xz} \\ G_{yz} \end{bmatrix} = \begin{bmatrix} h\left[\sum_{ml=1}^{Nml} \frac{h^{ml}}{D_{t11}^{ml}} + \sum_{cl=1}^{Ncl} \frac{h^{cl}}{G_d^{cl}}\right]^{-1} \\ h\left[\sum_{ml=1}^{Nml} \frac{h^{ml}}{D_{t22}^{ml}} + \sum_{cl=1}^{Ncl} \frac{h^{cl}}{G_d^{cl}}\right]^{-1} \end{bmatrix} \tag{4.26}$$

where *Nml* and *Ncl* denote the number of material and cohesive layers, respectively. The slope of zigzag function for the material layer "ml" and the cohesive layer "cl" are computed by

$$\begin{bmatrix} \beta_x \\ \beta_y \end{bmatrix}^{ml} = \begin{bmatrix} \frac{G_{xz}}{D_{t11}^{ml}} - 1 \\ \frac{G_{yz}}{D_{t22}^{ml}} - 1 \end{bmatrix} \quad ; \quad \begin{bmatrix} \beta_x \\ \beta_y \end{bmatrix}^{cl} = \begin{bmatrix} \frac{G_{xz}}{G_d^{cl}} - 1 \\ \frac{G_{yz}}{G_d^{cl}} - 1 \end{bmatrix} \tag{4.27}$$

This simple update procedure of the zigzag function allows the method to capture the relative displacement between layers.

Figure 4.5 schematizes all mentioned above. The implicit algorithm proposed to compute delamination with the LRZ/QLRZ model is shown in Figure 4.6.

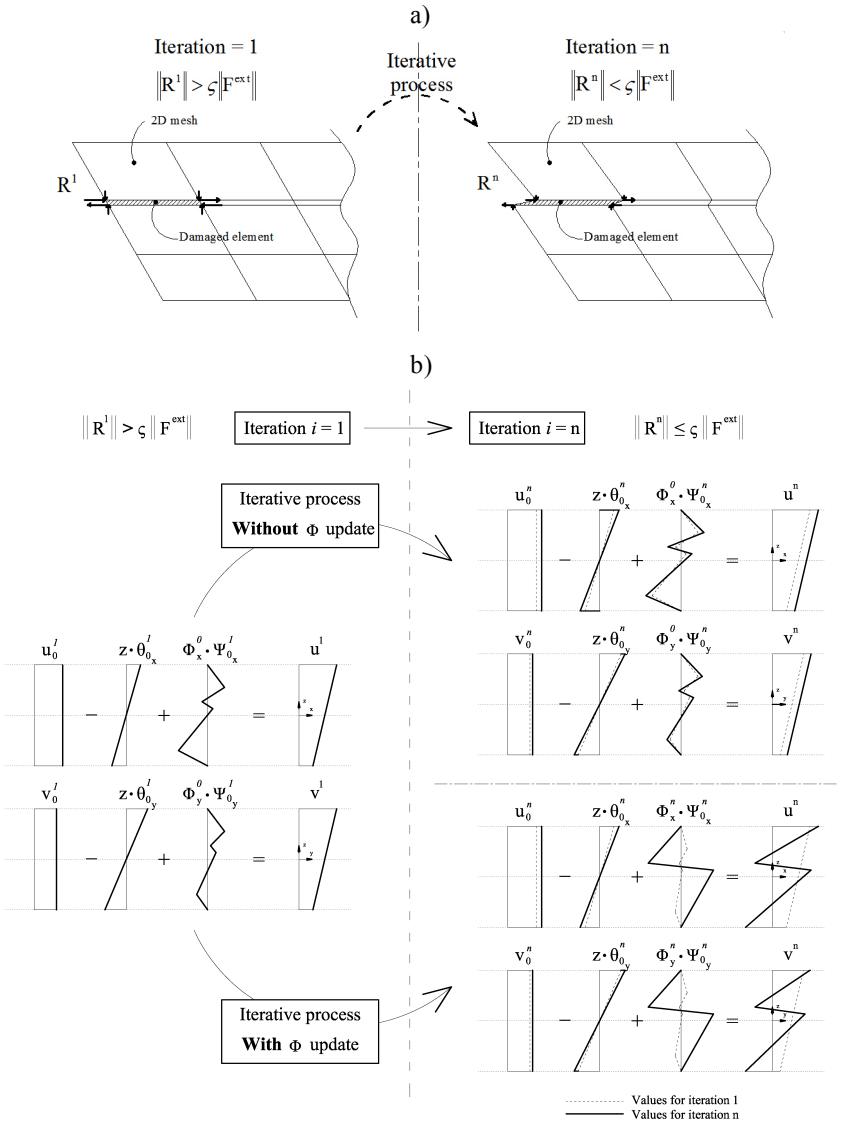

Figure 4.5 - The delaminated displacement field is achieved by the residual forces (R) in a plane stress analysis (PS) (a). Delaminación can be captured with the LRZ/QLRZ finite element when the zigzag function ϕ is updated by reducing the shear modulus of the damaged layer (b).

Loop over load increments

Update external forces $\mathbf{F}^{\text{ext}}$

Iterative process

If *i*th iteration = 1

$${}^{1}\mathbf{a} = \mathbf{K}_{\text{d}}^{-1} \cdot \mathbf{F}^{\text{ext}}$$

$${}^{1}\boldsymbol{\varepsilon}^{k} = \mathbf{S}_{d}^{k}\ \mathbf{B}\ {}^{1}\mathbf{a}$$

Note that for the first iteration $\mathbf{K}_{\text{d}}^{-1}$ and $\mathbf{S}_{d}^{k}$ are computed at the last iteration of the previous load increment.

Else

$${}^{i}d\mathbf{a} = {}^{i-1}\mathbf{K}_{\text{d}} \cdot {}^{i-1}\mathbf{R}$$

$${}^{i}\mathbf{a} = {}^{i-1}\mathbf{a} + {}^{i}d\mathbf{a}$$

$${}^{i}\boldsymbol{\varepsilon}^{k} = {}^{i-1}\mathbf{S}_{d}^{k}\ \mathbf{B}\ {}^{i}\mathbf{a}$$

Remember that ${}^{i-1}\mathbf{S}_{d}^{k}$ contains the updated ϕ function of the *i-1*th iteration. As a consequence, the strain field ${}^{i}\boldsymbol{\varepsilon}^{k}$ corresponds to the delaminated kinematics.

End if

Evaluate undamaged stresses:

$${}^{i}\boldsymbol{\sigma}^{k} = \mathbf{D}_{0}^{k} \cdot {}^{i}\boldsymbol{\varepsilon}^{k}$$

Damage evaluation in cohesive layers:

Compute damage variable:

$${}^{i}d^{cl} = 1 - \frac{c_0}{{}^{i}f} e^{B\left(1 - \frac{{}^{i}f}{c_0}\right)} \qquad \text{with} \qquad {}^{i}f = \sqrt{{}^{i}\boldsymbol{\varepsilon}^{cl} : {}^{i}\boldsymbol{\sigma}_{0}^{cl}}$$

Correct stresses and shear moduli:

$${}^{i}\boldsymbol{\sigma}^{cl} = \left(1 - {}^{i}d^{cl}\right) {}^{i}\boldsymbol{\sigma}_{0}^{cl} \quad ; \quad {}^{i}G_{d}^{cl} = \left(1 - {}^{i}d^{cl}\right) {}^{i}G_{0}^{cl}$$

Update zigzag function:

Compute average transverse shear stiffness:

$${}^{i}\begin{bmatrix} G_{xz} \\ G_{yz} \end{bmatrix} = \begin{bmatrix} h\left[\sum_{ml=1}^{Nml} \frac{h^{ml}}{D_{t11}^{ml}} + \sum_{cl=1}^{Ncl} \frac{h^{cl}}{{}^{i}G_{d}^{cl}}\right]^{-1} \\ h\left[\sum_{ml=1}^{Nml} \frac{h^{ml}}{D_{t22}^{ml}} + \sum_{cl=1}^{Ncl} \frac{h^{cl}}{{}^{i}G_{d}^{cl}}\right]^{-1} \end{bmatrix}$$

Figure 4.6 - Algorithm for solving the non-linear problem by means of the modified Newton-Raphson. Note that the zigzag function is updated at each iteration. Figure continued on the page.

Compute zigzag slope:

$$ {}^{i}\begin{bmatrix}\beta_x\\ \beta_y\end{bmatrix}^{ml} = \begin{bmatrix}\dfrac{{}^{i}G_{xz}}{D_{t11}^{ml}} - 1\\ \dfrac{{}^{i}G_{yz}}{D_{t22}^{ml}} - 1\end{bmatrix} \quad \text{for materials layers "}ml\text{"} $$

$$ {}^{i}\begin{bmatrix}\beta_x\\ \beta_y\end{bmatrix}^{cl} = \begin{bmatrix}\dfrac{{}^{i}G_{xz}}{{}^{i}G_{d}^{cl}} - 1\\ \dfrac{{}^{i}G_{yz}}{{}^{i}G_{d}^{cl}} - 1\end{bmatrix} \quad \text{for cohesive layers "}cl\text{"} $$

Compute zigzag function:

$$ {}^{i}\phi_x^k = \bar{\phi}_x^{k-1} + \frac{h^k\,{}^{i}\beta_x^k}{2}\left(\zeta^k + 1\right) \quad ; \quad {}^{i}\phi_y^k = \bar{\phi}_y^{k-1} + \frac{h^k\,{}^{i}\beta_y^k}{2}\left(\zeta^k + 1\right) $$

Computation of the damaged stiffness matrix and internal forces:

$$ {}^{i}\mathbf{K}_{\mathrm{d}} = \int_A \mathbf{B}^T\,{}^{i}\hat{\mathbf{D}}_{\mathrm{d}}\,\mathbf{B}\,dA $$

$$ {}^{i}\mathbf{F}^{\mathrm{int}} = \int_V \mathbf{B}^T\,{}^{i}\mathbf{S}^T\,{}^{i}\boldsymbol{\sigma}^k\,dV $$

Verification of convergence criteria

$$ \mathbf{F}^{\mathrm{ext}} - {}^{i}\mathbf{F}^{\mathrm{int}} = {}^{i}\mathbf{R} $$

$$ \left\| {}^{i}\mathbf{R} \right\| \le \varsigma \left\| \mathbf{F}^{\mathrm{ext}} \right\| $$

 # END iterative process

 # END loops over load increments

Figure 4.6 - Continuation.

4.5 Multi-delamination modeling with the LRZ/QLRZ delamination model

Simulation of multi-delamination with the LRZ/QLRZ delamination model is investigated in this section.

In the LRZ/QLRZ model, relative displacements are provoked by modifying the shape of the zigzag function using Eqs. (4.25)-(4.27). The alteration of this function is motived by reducing the shear modulus of damaged cohesive layers during degradation process. Note that these equations are written to simulate multi-delamination, i.e. several “cl” plies can be damaged. However, in order to capture more than one relative

displacement with the LRZ/QLRZ delamination model, some cares have to be accounted for when updating the zigzag function.

In order to analyze the potential of the QLRZ/LRZ model for simulating multi-delamination, a sandwich clamped beam with two possible delamination paths is studied.

The beam is subjected to a vertical displacement Δw = 1mm at the free end (Figure 4.7a). The length and thickness of the beam are L = 100mm and h = 20.02mm, respectively. The laminated material consists of two skins (the top and the bottom layers) and a less stiff core between them (the middle ply). The top and bottom delamination paths between skins and core are described by the cohesive layers "cl-1" and "cl-2", respectively (Figure 4.7b). Thickness and mechanical properties of each layer are listed in Table 4.1.

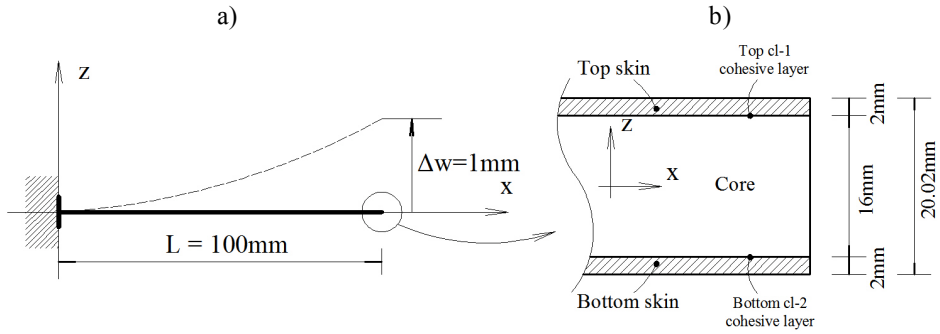

Figure 4.7 - Cantilever beam under vertical displacement a) and sandwich three-layered material b).

Thicknesses and material properties

	Top Skin	Core	Bottom Skin	Cohesive layers
h [mm]	2	16	2	0.01
E [MPa]	$2.19\text{x}10^5$	$7.30\text{x}10^2$	$7.3\text{x}10^5$	$7.30\text{x}10^2$
G [MPa]	$0.876\text{x}10^5$	$2.90\text{x}10^2$	$2.92\text{x}10^5$	$2.90\text{x}10^2$

Table 4.1 – Layer properties for multi-delamination study.

In this case, the damage of each interface layer is induced by reducing the shear modulus from G = $2.9\text{x}10^2$ MPa to G = $2.9\text{x}10^{-8}$ MPa. Note that the reduction of the "cl" shear modulus is applied over the whole beam length.

Reference solution is computed by a plane stress analysis (PS) using a mesh of 3200 4-noded quadrilateral finite elements (Figure 4.8). The beam length is discretized with 100 elements whereas the thicknesses of the skins and core are described with 3

and 24 finite elements, respectively. Only 1 finite element is required to define the cohesive layers.

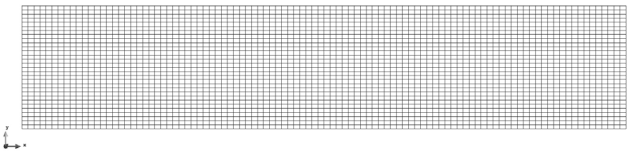

Figure 4.8 - Four-noded quadrilateral finite element mesh for the PS analysis.

Figure 4.9 shows the thickness distribution of the axial displacement *u* at the free end for the undamaged beam (a), after first delamination at the top cohesive layer "cl-1" (b) (single-delamination) and after second delamination at the bottom layer "cl-2" (c) (multi-delamination).

Despite the low span-to-thickness ratio and high transverse anisotropy of the beam, results clearly show a great agreement between the LRZ/QLRZ model and the PS analysis. It is appreciated that both, the single- (Figure 4.9b) and the multi-delamination (Figure 4.9c) are well captured.

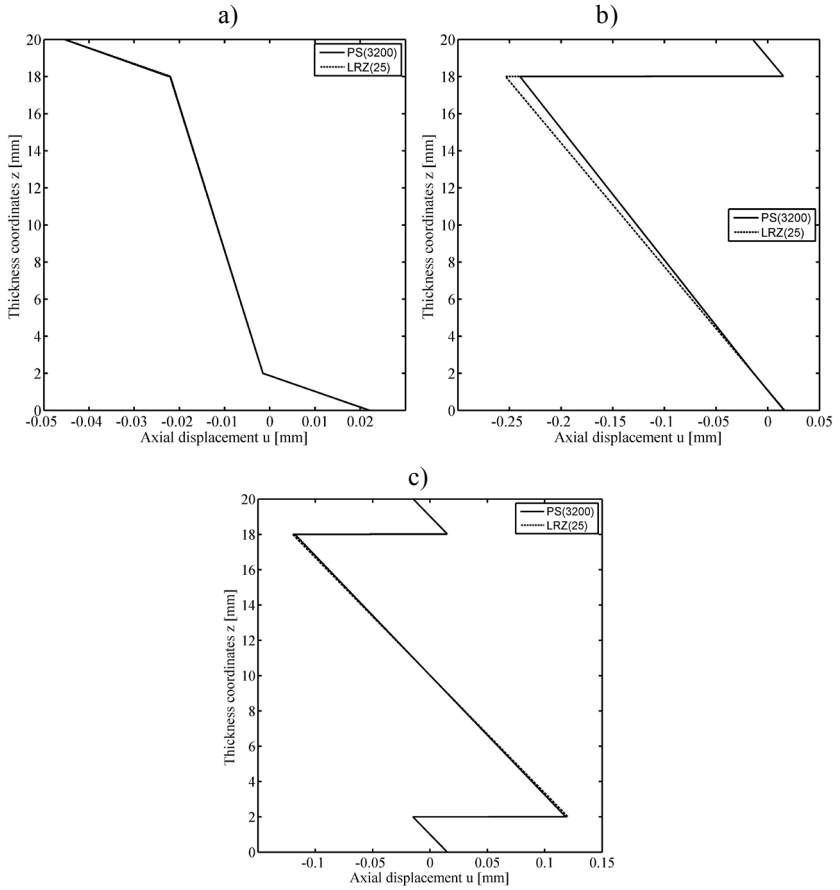

Figure 4.9 - Axial displacement u at the free end for the undamaged beam (a), for single-delamination at the cohesive layer "cl-1" (b) and for multi-delamination (c).

Before to continue analyzing results, it is important to remark that after delamination the slope of the zigzag function (Eq.(4.27)) is controlled by the average transverse shear stiffness of laminate (Eq.(4.26)) which in turn is governed by the smallest damaged shear modulus.

With this in mind, once the top delamination has been occurred, the shape of the zigzag function is controlled by the "cl-1" ply only. After second delamination, however, the zigzag function could be governed by the "cl-1" (if $G^{cl-1} < G^{cl-2}$), the "cl-2" (if $G^{cl-1} > G^{cl-2}$) or both cohesive layers (if $G^{cl-1} \approx G^{cl-2}$).

In consequence, the model was able to capture the second relative displacement at the bottom interface because the shear modulus of the "cl-2" ply have been reduced to the same value as the "cl-1" layer ($G^{cl-2} = G^{cl-1} = 2.9x10^{-8}$ MPa). Otherwise, the model could predict wrong displacement field, as detailed below.

With the aim to clarify the mentioned above, imagine a delamination process where the "cl-1" ply was full damage at the *n*th step by reducing its shear modulus to $G^{cl-1} = 2.9x10^{-8}$ MPa. As a result, the undamaged zigzag function (Figure 4.10a) has to be updated provoking a jump at the top cohesive layer (Figure 4.10b). This update of the zigzag function induces the top single-delamination of Figure 4.9b.

Then, some steps later, the shear modulus of the bottom cohesive layer is also reduced to $2.9x10^{-8}$ MPa ($G^{cl-2} = G^{cl-1}$). Consequently, the zigzag function is updated again leading to two jumps at top and bottom cohesive layers (Figure 4.10c). This new configuration of the zigzag function provokes the multi-delamination showed in Figure 4.9c.

Now, imagine that the shear modulus of the "cl-2" layer is decreased to $2.9x10^{-10}$ MPa instead of be reduced to $2.9x10^{-8}$ MPa, i.e. two orders of magnitude smaller than the shear modulus of the "cl-1" ply previously damaged.

Therefore, the updated zigzag function has only one jump at the bottom interface (Figure 4.11a), instead of having two jumps like in Figure 4.10c. In consequence, a single-delamination path at the cohesive ply "cl-2" is computed neglecting the previous delamination at layer "cl-1", as shown in Figure 4.11b. The reason is that the average transverse shear stiffness of laminate is now governed by the shear modulus of the "cl-2" because of $G^{cl-1} > G^{cl-2}$.

This situation is completely unreal since not only the double-delamination could not be captured, but also the in-plane displacement is modified to a new configuration which does not take into account the relative displacement at ply "cl-1" previously computed.

Thus, in order to maintain previous delamination state, the reduced shear modulus of new damaged cohesive layers must not be smaller than that of the first degraded cohesive layer.

It is important to note that the difference of two orders of magnitude between the damaged shear moduli (arbitrarily chosen for this example) implies a difference of the damage variable *d* between both layers approximately equal to 9.9×10^{-9} % only.

In addition, in order to capture new delamination paths, the sensibility of the zigzag function to be modified once first delamination has been occurred has to be studied.

Thus, imagine that the "cl-2" shear modulus is decreased to 2.9×10^{-6} MPa instead of 2.9×10^{-8} MPa, i.e. two orders of magnitude larger than that of the "cl-1" layer previously damaged. As a result, the update of the zigzag function does not provoke significant changes on its previous delaminated shape (Figure 4.10b), as shown in Figure 4.12a. Therefore, the second delamination path at the "cl-2" ply cannot be captured (Figure 4.12b). The reason is that the average transverse shear stiffness of laminate is still governed by the shear modulus of the "cl-1" because G^{cl-2} is quite larger than G^{cl-1}.

Consequently, although delamination process has begun at bottom interface layer ($G^{cl-2} = 2.9 \times 10^{-6}$), it was not possible to capture the relative displacement at "cl-2" ply.

Note that, for this case, the difference of two orders of magnitude between the shear moduli implies a difference of the damage variable *d* equal to 9.9×10^{-7} % only.

Summarizing, in order to predict multi-delamination with the LRZ/QLRZ delamination model, the reduced shear properties of new degraded interfaces must be almost the same as that of the first damaged cohesive layer. This precaution allows the model to capture new relative displacement while maintaining previous delamination states.

In consequence, it is necessary to development an strategy for controlling the degradation process of each cohesive layer at Gauss point level. This topic is proposed as future work. Thus, the model is actually able to simulate single-delamination only.

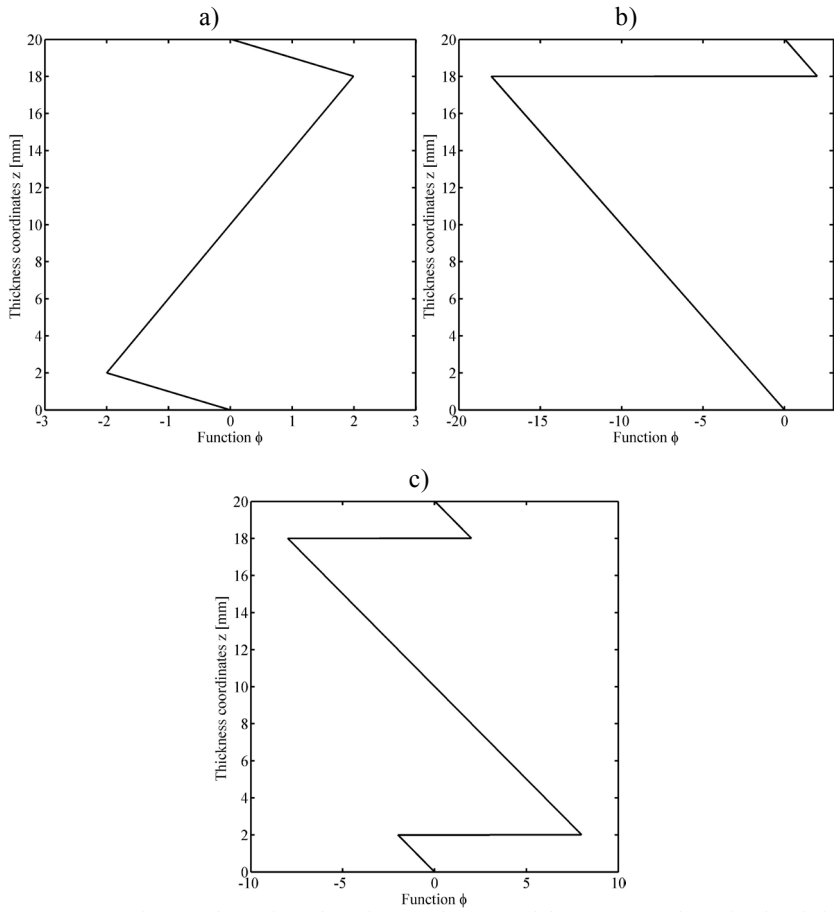

Figure 4.10 – Zigzag function for the undamaged beam (a), for single-delamination at the cohesive layer "cl-1" (b) and for multi-delamination (c).

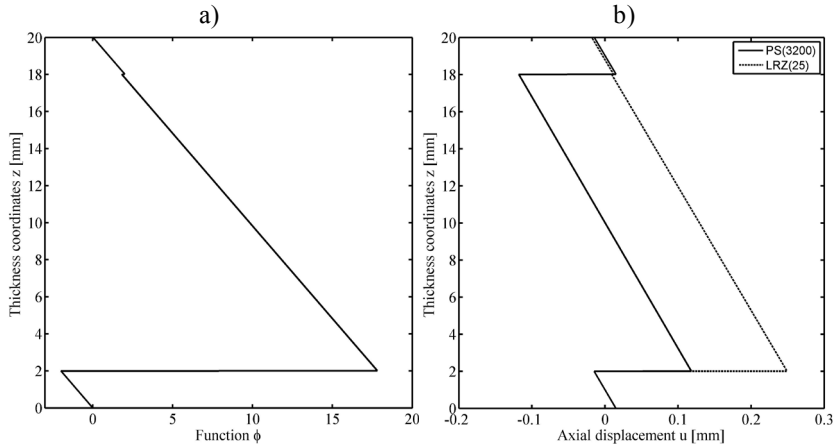

Figure 4.11 - Zigzag function (a) and axial displacement (b) for the case where the damage shear modulus of the bottom cohesive layer is smaller than that of the top damaged cohesive layer.

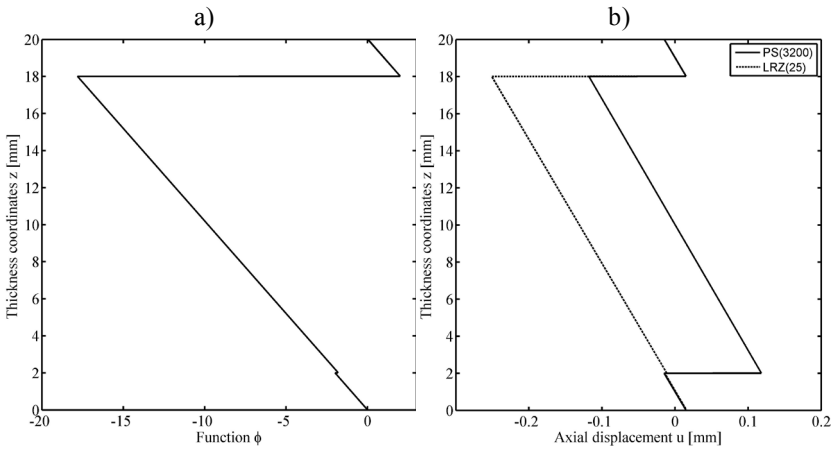

Figure 4.12 - Zigzag function (a) and axial displacement (b) for the case where the damage shear modulus of the bottom cohesive layer is higer than that of the top damaged cohesive layer.

4.6 Numerical examples

The performance of the LRZ/QLRZ delamination model is analyzed in this section. Only single-delamination cases are studied.

Simulations are carried out under the following considerations: quasi-static application of vertical displacement, geometrically linear problem and small deformation.

4.6.1 Delamination in beams

Sandwich clamped beam under vertical displacement

Skin-core delamination at the top interface (cl-1 ply) of the sandwich clamped beam of Section 4.5 is analyzed. The structure is subjected to a vertical displacement Δw = 10mm. Dimension, boundary conditions and layer stacking of the beam are schematized in Figure 4.7. Layer mechanical properties are listed in Table 4.1. Tensile strength and fracture energy of the "cl-1" layer are equal to f_t = 2MPa and G_f=5x10^{4}kN/m, respectively. The LRZ mesh contains 25 elements.

The reference solution is computed by a plane stress analysis (PS) using the mesh of Figure 4.8. The step increment is dw = 0.003mm for both solutions. The tolerance value is ζ = 1x10^{-3} for the LRZ analysis and ζ = 1x10^{-2} for the PS solution due to difficulties for getting convergence.

Figure 4.13 shows the load-displacement curve. Load P corresponds to the total vertical reaction computed at the clamped support whereas displacement w is the imposed vertical displacement Δw.

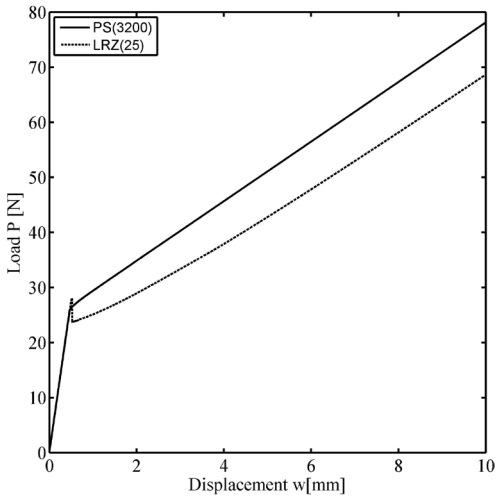

Figure 4.13 - Load vs. displacement curves for single-delamination in sandwich laminated materials.

Although the error at the end of simulation is approximately 12.0%, both, the onset and the growth of delamination are correctly predicted by the LRZ delamination model. Damage starts for Δw = 0.468mm and Δw=0.414mm for the PS and LRZ models, respectively.

After onset delamination, the LRZ solution exhibits a load drop at Δw=0.519mm, which is related to the update of the zigzag function.

At this increment, degradation of the "cl-1" layer is increased from d^{cl} = 0.98 (Δw=0.513mm) to d^{cl} = 0.998, approximately. This relatively small variation (2% approx.) of damage variable induces a significant change of the zigzag function, as shown in Figure 4.14, which provokes the load drop of Figure 4.13.

Figure 4.14a shows the zigzag function obtained with different degradation levels of the top cohesive layer. In other words, the sensibility of zigzag function to the damage variable is shown. It is observed that no major changes on the zigzag function are produced until damage variable d reaches values close to 0.998.

In order to reduce the load drop of Figure 4.13, smaller step increments can be used, as shown in Figure 4.14b. In this figure two LRZ solutions computed using dw=0.003mm (LRZ) and dw=0.00003mm (LRZ_{SI}) are compared.

Results show that immediately after onset delamination, i.e. at Δw = 0.417mm, a very small load drop is computed by the LRZ_{SI} solution when damage variable changes from 0.437 to 0.976 in a few number of finite elements. Although a degradation level of 0.976 does not induce relevant alterations in the zigzag function, it is enough to provoke a small fall.

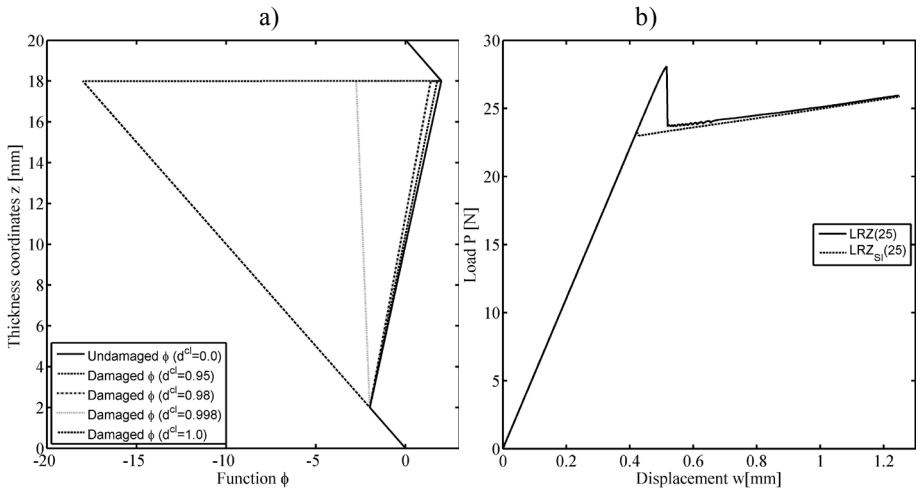

Figure 4.14 - Undamaged and damaged zigzag function (a) and load vs. displacement curves obtained by the LRZ model for two different step increments (b).

Figure 4.15 shows the evolution of the cl-1 damage variable for the LRZ and LRZ_{SI} solutions. The jump of d from 0.437 to 0.976 at Δw =0.417mm and from 0.98 to 0.998 at Δw =0.519mm for the LRZ_{SI} and the LRZ solutions, respectively, can be observed.

This figure also reveals that damage variable evolves faster for LRZ_{SI} than LRZ solution. The reason is that the strains $\boldsymbol{\varepsilon}$ used to calculate the predictor stresses ($\boldsymbol{\sigma} = \mathbf{D}\,\boldsymbol{\varepsilon}$) are computed from the previous delaminated kinematics. Consequently, the greater is the relative displacement at the *n-1*th step the higher is the predictor stresses at the *n*th step.

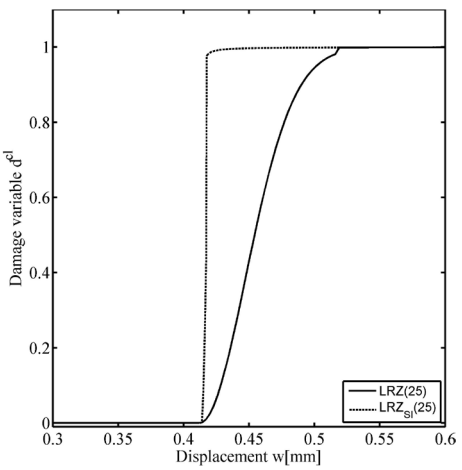

Figure 4.15 – Damage variable d of the "cl-1" ply at the Gauss point of the first finite element from the free end obtained by the LRZ model for two different step increments.

Figure 4.16 shows the thickness distribution of the axial displacement u at the free end for three different steps: before (a) (Δw =0.393mm) and after delamination onset (b) (Δw =2.013mm) and at the end of simulation (c) (Δw=9.993mm).

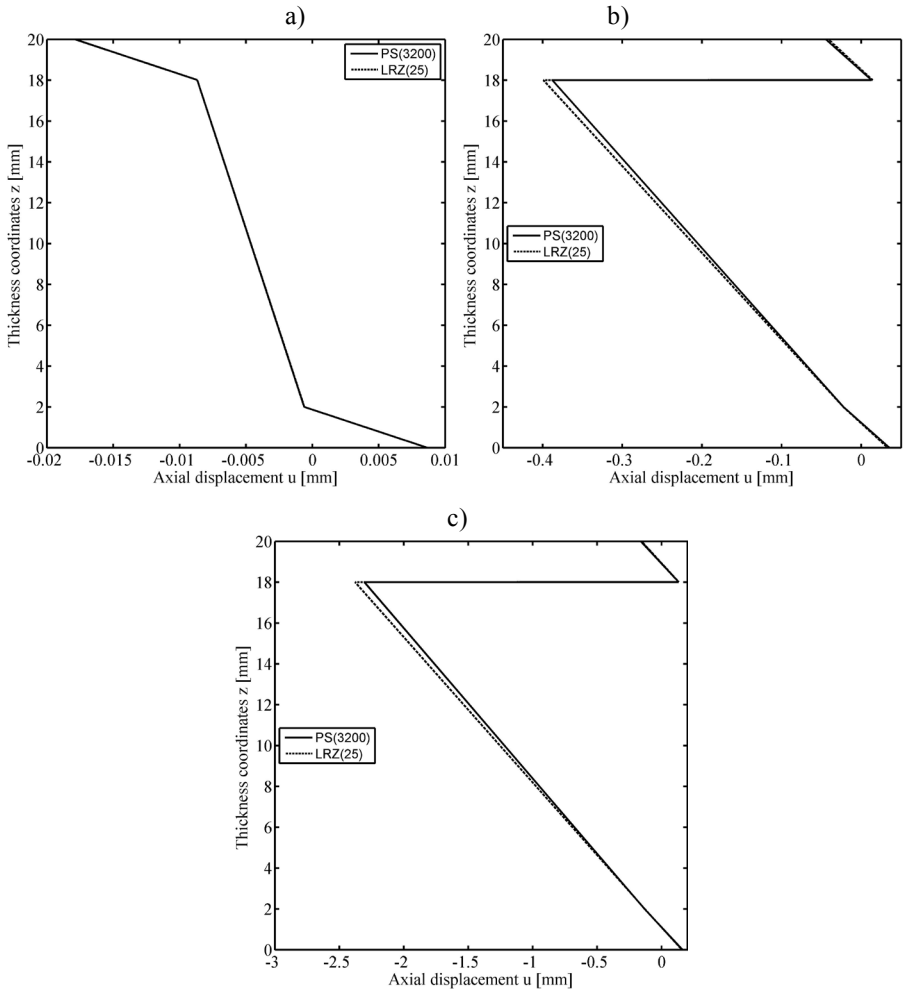

Figure 4.16 - Thickness distribution of the axial displacement u at the free end before (a) and after delamination (b) and at the end of simulation (c).

Multilayered clamped beams under vertical displacement

In this example single-delamination in multilayered beams is studied by modeling a beam of length L = 0.5m supported as shown in Figure 4.17. A vertical displacement Δw at the clamped support is imposed. The beam is analyzed for two laminates (L1 and L2) with properties listed in Table 4.2-Table 4.4. Location of the cohesive layer for both laminates is shown in Figure 4.18.

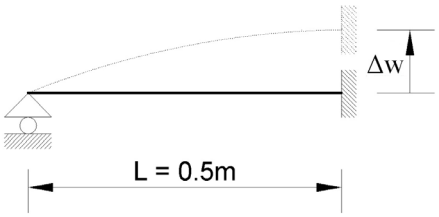

Figure 4.17 - Boundary conditions of the analyzed beam.

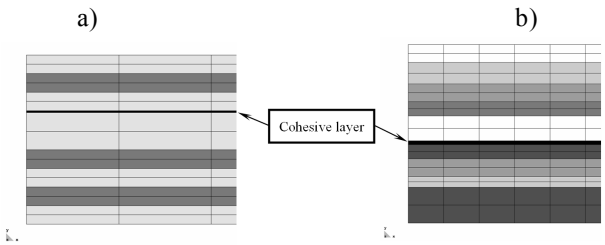

Figure 4.18 - Cohesive layer in laminate L1 a), and laminate L2 b).

Mechanical properties of *linear-elastic* plies [MPa]

Material	Young's Modulus (E_0)	Shear Modulus (G_0)
A	157.9×10^5	5.93×10^5
B	104.0×10^2	40.0×10^2
C	5.3×10^2	2.12×10^2
D	2.19×10^2	0.876×10^2
E	0.82×10^2	0.328×10^2
F	0.73	0.29
G	7.3×10^2	2.92×10^2

Table 4.2 - Mechanical properties of linear-elastic layers.

Mechanical properties of *cohesive* plies (cl)

Material	E_0 [MPa]	G_0 [MPa]	Tensile Strength (f_t) [MPa]	Fracture Energy (G_f) [kN/m]	
				Ductile (G_f^D)	Fragile (G_f^F)
H^{cl}	104.0×10^2	40.0×10^2	6.5	5.0×10^5	1.0×10^{-1}
I^{cl}	0.73	0.29	0.02	5.0×10^5	1.0×10^{-2}

Table 4.3 - Mechanical properties of cohesive layers (cl).

Laminated materials			
Laminate	Layer distribution	h_i / h	h [mm]
L1	(A/B/A/H^{cl}/A/B/A/B/A)	(0.11/0.11/0.11/0.01/0.22/0.11/0.11/0.11/0.11)	9.1
L2	(C/D/E/F/C/I^{cl}/G/E/D/G)	(1.0/0.12/0.1/0.08/0.14/0.02/0.08/0.1/0.06/0.2)	25.0

Table 4.4 - Layer distribution of laminated materials.

In order to show the influence of the fracture energy G_f^{cl} in the delamination process, two values of this parameter (a larger one and a smaller one) are adopted for the cohesive layer in each laminate. For clarity, in the followings the largest value (G_f^D) is associated to a "ductile" property whereas the smallest (G_f^F) to a "fragile" one.

LRZ meshes of 2, 16, 128 finite elements are used in the analysis. The reference solution is obtained by means of a plane stress analysis (PS) using 4-noded quadrilateral finite elements and the isotropic damage model presented in Section 4.2 for managing the degradation of the cohesive layer. The beam length, the thickness of the elastic layers and the thickness of the cohesive ply are discretized with 100, 2 and 1 finite elements, respectively. The discretization chosen leads to meshes of 1700 (Figure 4.19a) and 1900 (Figure 4.19b) 4-noded quadrilateral PS elements for the laminates L1 and L2, respectively.

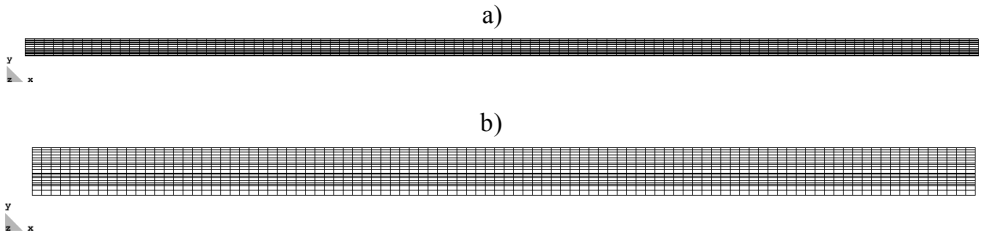

Figure 4.19 – Four-noded quadrilateral finite element meshes for laminate L1 a), and laminate L2 b).

Figure 4.20 and Figure 4.21 show the load-displacement curves for the laminates L1 and L2, respectively. The load corresponds to the vertical reaction at the clamped support. The displacement corresponds to the incremental displacement Δw applied at the clamped end (Figure 4.17). The curves shown in Figures a) are obtained when the "ductile" (G_f^D) fracture energy is considered. The response of the beam when the "fragile" (G_f^F) fracture energy is used is shown in Figures b). The fracture energy values are listed in Table 4.3.

Results reveal an admissible agreement between both solutions. The errors for the finest LRZ meshes at the end of simulation for the cases L1- G_f^D (Figure 4.20a), L1- G_f^F (Figure 4.20b), L2- G_f^D (Figure 4.20a) and L2- G_f^F (Figure 4.21b) are less than 11.0%, 2.5%, 7.5% and 2.9%, respectively. LRZ solution exhibits small drops of load for the case L1- G_f^D (Figure 4.20a), which are not present in the PS solution. The cause of these drops was mentioned in the previous skin-core delamination analysis.

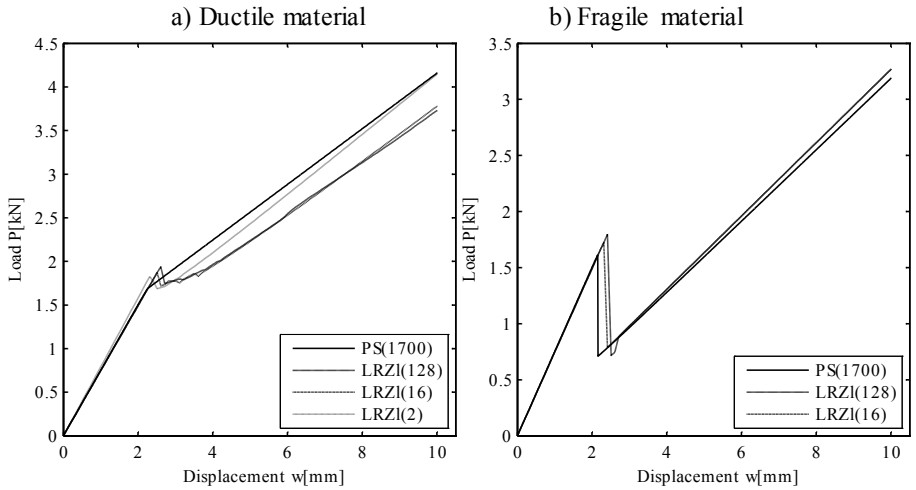

Figure 4.20 - Load vs. displacement curves for laminate L1 with ductile (a) and fragile (b) fracture energy.

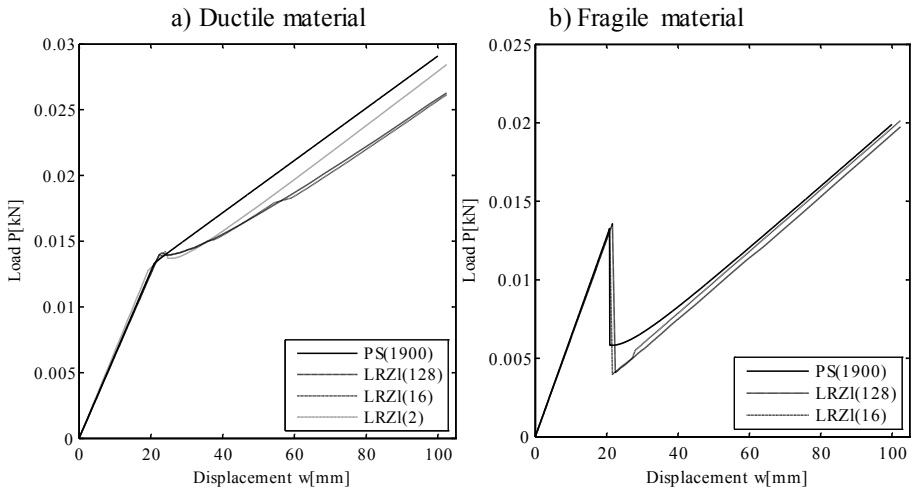

Figure 4.21 - Load vs. displacement curves for laminate L2 with ductile (a) and fragile (b) fracture energy.

When the "fragile" value of the fracture energy (G_f^F) is used, the cohesive layer completely loses its energy at the delamination onset, which provokes the sharp drop in the sample resistance, as shown in Figures b). The loss of resistance computed by the

PS solution is around 56% for both laminates, whereas LRZ solution gives 60% and 70% for L1 and L2, respectively.

The initial stiffness and the stiffness once delamination process has been started are very close to the stiffness obtained by 2D analysis in all cases. Also, is shown that delamination starts for similar values of displacement and load.

The thickness distribution of the axial displacement *u* at the simply supported end, before and after delamination onset, is shown in Figure 4.22 and Figure 4.23 for laminates L1 and L2, respectively.

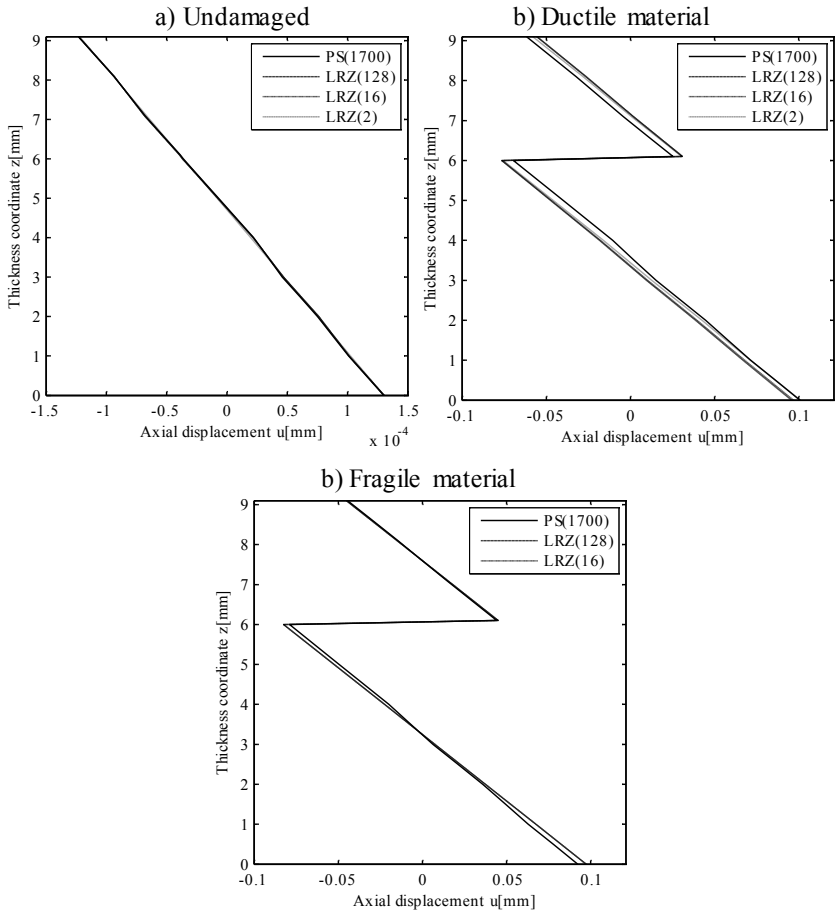

Figure 4.22 - Thickness distribution of the axial displacement *u* at the simply supported end for laminate L1. This figure shows the undamaged kinematics a) and the damaged kinematics when the "ductile" b) and the "fragile" c) fracture energy is used.

The undamaged kinematics is shown in Figures a), which make evident the very good match between PS and LRZ kinematics. Figures b) and c) show the delaminated kinematics at the end of simulation when the "ductile" and the "fragile" fracture energy

values are used, respectively. In the "ductile" case, the LRZ elements are capable to capture the relative displacement with errors around 11% and 16% for laminates L1 and L2, respectively. In the "fragile" case, the errors are less than 3.3% for both laminates.

Almost identical results are obtained with the quadratic LRZ beam element.

Figure 4.24 shows the thickness distribution of the zigzag function ϕ for laminate L1 (a) and laminate L2 (b). The solid line represents the initial zigzag function (undamaged), whereas the dashed and the dash-dot line correspond to the damaged zigzag function when the damage variable of cohesive layer is equal to 0.9 and 1, respectively. As mentioned in Section 4.4, the ability of the LRZ element to capture the relative displacement between plies during a delamination process lies in the zigzag function update according the layers are being damaged.

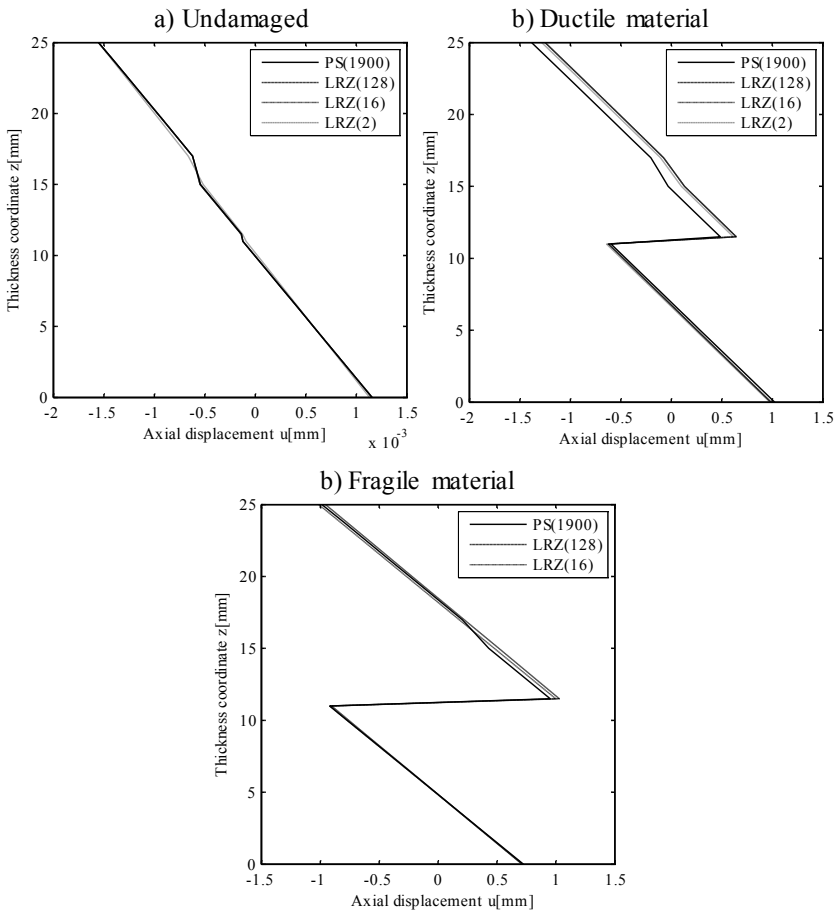

Figure 4.23 - Thickness distribution of the axial displacement u at the simply supported end for laminate L2. This figure shows the undamaged kinematics a) and the damaged kinematics when the "ductile" b) and the "fragile" c) fracture energy is used.

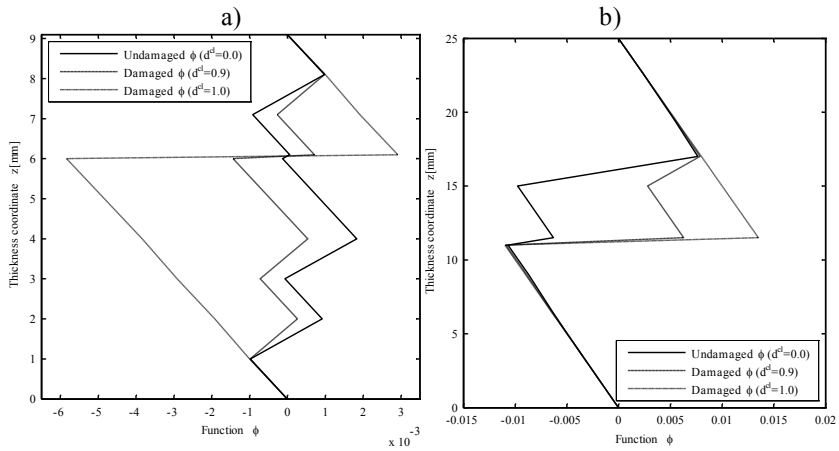

Figure 4.24 - Undamaged and damaged zigzag function for laminate L1 a) and laminate L2 b).

In order to compare the performance of the PS and the LRZ analyses, the total increment numbers and the incremental displacement values as well as the tolerance value (ζ = 1x10^{-4}) are the same for both methods. The total increment numbers are equal to 1000 and 7000 for laminates L1 and L2, respectively. The incremental displacement value applied in each increment is 1x10^{-3}mm and 4x10^{-3}mm for L1 and L2, respectively. Table 4.5 and Table 4.6 show the total number of iterations, the maximum number of iteration needed for achieving convergence in any increment and the total CPU time used in the simulation for L1 and L2, respectively.

As expected, the computation time needed for the PS analysis is several times greater than that required for LRZ solutions. Comparing with the finest 128-LRZ mesh, PS uses at best around 67 times the time used by LRZ solution for laminate L2 and G_f^F =1.0x10^{-3} (Table 4.6). At worst, the time used by PS is 156 times greater than that required by the LRZ solution for laminate L1 and G_f^D =5.0x10^4 (Table 4.5). If the comparison is made versus the 16-LRZ mesh, the time used by the PS solution is 530 and 1954 times of that needed by the LRZ solution at best and at worst scenarios, respectively.

Computational cost of the iterative process for laminate L1

Finite element		G_f = 5.0x10^4 (Ductile)			G_f = 1.0x10^{-2} (Fragile)		
		Total Iter.	Max. Iter.	Time [seg]	Total Iter.	Max. Iter.	Time [seg]
2D	1700	9308	485	3069.0	3465	254	1127.0
LRZ	2	1543	166	1.52	-	-	-
	16	1286	81	1.57	1009	9	1.27
	128	2291	225	19.61	1036	23	9.45

Table 4.5 - Computational cost of the iterative process for laminate L1.

Computational cost of the iterative process for laminate L2

Finite element		$G_f = 5.0\text{x}10^4$ (Ductile)			$G_f = 1.0\text{x}10^{-3}$ (Fragile)		
		Total Iter.	Max. Iter.	Time [seg]	Total Iter.	Max. Iter.	Time [seg]
2D	1900	18374	88	6967.0	10141	144	4223.0
LRZ	2	7298	76	8.10	-	-	-
	16	7131	53	8.11	7016	11	7.96
	128	7072	71	64.51	7372	101	65.46

Table 4.6 - Computational cost of the iterative process for laminate L2.

4.6.2 Delamination in plates

The capability of the QLRZ element for simulating the relative in-plane displacements (Mode II and III) between plies is studied by modeling a simply supported rectangular plate of length L=1.0m, depth D=0.5m and thickness h=0.025m with a center hole of radius R=0.0125m (Figure 4.25a). Taking advantage of symmetry, only one quarter of plate is studied (Figure 4.25b). The structure is subjected to bending by imposing a uniform vertical displacement Δw along the segment $\overline{CF}$ (Figure 4.25b). The plate is analyzed for two laminates (L1 and L2) with properties listed in Table 4.7-Table 4.9. The cohesive layers are denoted as I^{cl} and J^{cl} for the L1 and the L2 laminate, respectively.

The reference solution was obtained via a 3D finite element analysis using a mesh of 16416 8-noded hexahedral elements (HEXA8) involving 18620 nodes and 55860 DOFs (Figure 4.26). One and two finite elements are used to discretize the thickness of the cohesive layer and the thickness of the elastic layers, respectively. This mesh was used for both laminates as they share the same geometry.

Mesh convergence is studied using five QLRZ meshes of 44, 102, 216, 384 and 964 finite elements with 60, 126, 250, 429, 931 nodes and 420, 882, 1750, 3003, 6517 DOF, respectively, as shown in Figure 4.27.

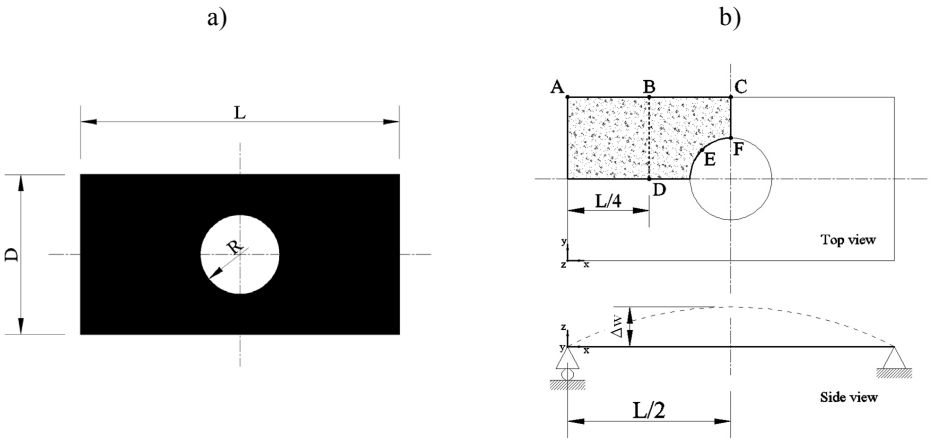

Figure 4.25 - Simply supported rectangular plate with a center hole. Whole structure dimensions a), quarter of plate under study with boundary conditions b).

Mechanical properties of *linear-elastic* plies [MPa]

Mat.	Young's Modulus			Shear Modulus			Poisson
	E_x	E_{xy}	E_z	G_{xy}	G_{xz}	G_{yz}	μ
A	$157.9\text{x}10^5$	$9.584\text{x}10^5$	$9.584\text{x}10^5$	$5.93\text{x}10^5$	$5.93\text{x}10^5$	$3.227\text{x}10^5$	0.32
B	$19.15\text{x}10^3$	$19.15\text{x}10^3$	$19.15\text{x}10^4$	$42.3\text{x}10^{-4}$	$36.51\text{x}10^3$	$124.8\text{x}10^3$	$6.58\ \text{x}10^{-4}$
C		$104.0\text{x}10^2$			$40.0\text{x}10^2$		0.30
D		$5.30\text{x}10^2$			$2.12\text{x}10^2$		0.25
E		$2.19\text{x}10^2$			$0.876\text{x}10^2$		0.25
F		$0.82\ \text{x}10^2$			$0.328\ \text{x}10^2$		0.25
G		0.73			0.29		0.25
H		$7.3\ \text{x}10^2$			$2.92\ \text{x}10^2$		0.25

Table 4.7 - Mechanical properties of linear-elastic layers.

Mechanical properties of *cohesive* plies (cl)

Materials	E_0 [MPa]	G_0 [MPa]	Tensile Strength (f_t) [MPa]	Fracture Energy (G_f) [kN/m]
I^{cl}	$104.0\text{x}10^2$	$40.0\text{x}10^2$	20.0	$5.0\text{x}10^5$
J^{cl}	0.73	0.29	$3.0\ \text{x}10^{-3}$	$5.0\text{x}10^5$

Table 4.8 - Mechanical properties of cohesive layers (cl).

Laminated materials			
Laminate	Layer distribution	h_i / h	h [mm]
L1	(A/C/A/C/B/I^{cl}/C/A/C/A)	(1.0/0.12/0.1/0.08/0.14/0.02/0.08/0.1/0.06/0.2)	25.0
L2	(D/E/F/G/D/J^{cl}/H/F/E/H)	(1.0/0.12/0.1/0.08/0.14/0.02/0.08/0.1/0.06/0.2)	25.0

Table 4.9 - Layer distribution of laminated materials.

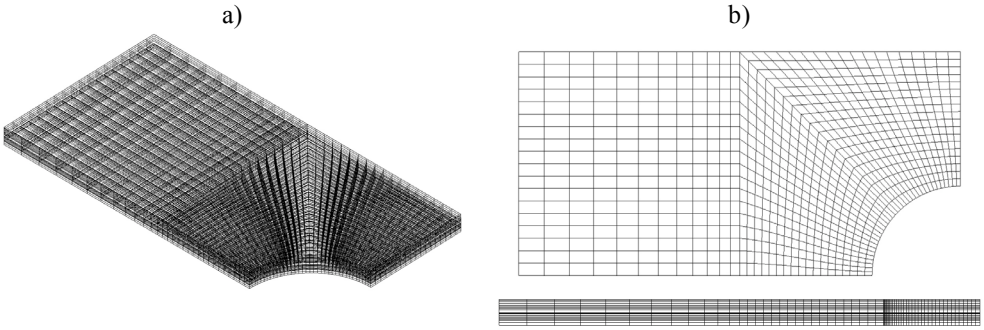

Figure 4.26 – HEXA8 mesh for both laminates. Isometric view a), top and side view b).

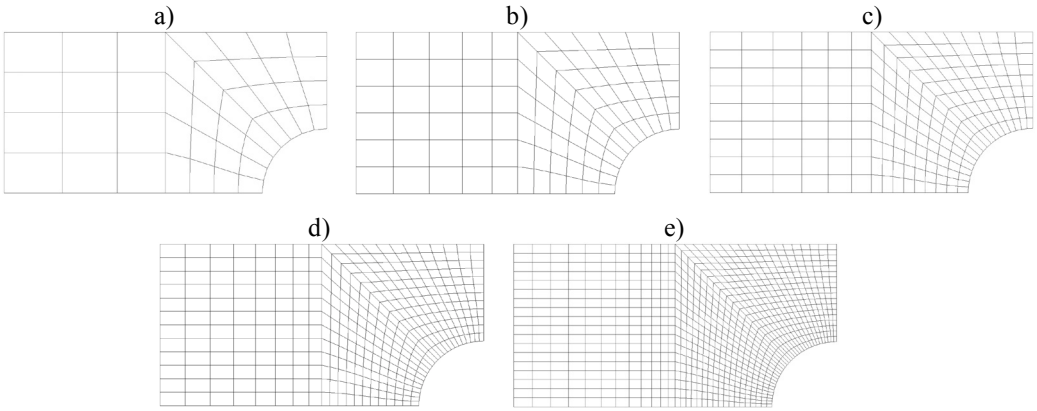

Figure 4.27 – QLRZ meshes of 44 a), 102 b), 216 c), 384 d) and 964 e) finite elements.

The load-displacement curves for both laminates are shown in Figure 4.28. The curves are obtained with the HEXA8 element (solid line) and the finest QLRZ mesh (dashed lines). The load corresponds to the total vertical reaction computed at the simply supported end whereas the displacement is the imposed vertical displacement Δw (Figure 4.25b). Results show a good agreement between both solutions. In all cases, the lineal-elastic QLRZ stiffness is very close to that computed by means of 3D analysis. Also, it is shown that delamination starts approximately at the same values of displacement and load.

Figure 4.29 shows the convergence of the normalized load value at the end of the simulation as the number of DOF is increased. The error for the coarser QLRZ mesh reaches almost 35% and 65% for the L1 and the L2 laminates, respectively. However, the error is around 1% (L1) and 10% (L2) for the finest QLRZ mesh.

The evolution of the transverse shear stress τ_{xz} for the cohesive layer for laminates L1 and L2 is shown in Figure 4.31 and Figure 4.32, respectively. For the linear-elastic state, the HEXA8 solution gives about 12% (L1) and 30% (L2) higher maximum value of τ_{xz} as appreciated for Δw =0.01mm. Because of this, damage starts a little later for the QLRZ solution. This mismatch between both solutions is more evident for the L2 laminate where the τ_{xz} distribution obtained with the HEXA8 mesh at Δw =0.41mm is similar to that computed with the QLRZ mesh at Δw =0.51mm. For the L1 laminate, no great differences are observed between both solutions. In all cases, approximately the same values of τ_{xz} are predicted at the end of the simulation (Δw =2.51mm).

Figure 4.33 and Figure 4.34 show the evolution of the transverse shear distribution along the segments AC and BD (Figure 4.25b) for the L1 and the L2 laminate, respectively. Results along segment AC are influenced by the mesh topology especially for laminate L2 as shown in Figure 4.34 for Δw =0.01mm. However, this mesh dependence disappears once delamination has started.

Taking into account that the degradation of the cohesive layer is governed by the transverse shear stress in these examples, the norm f of Eq.(4.5) can be approximated by

$$f \simeq \sqrt{\tau^2 / G_0}$$

Thus, equating the initial threshold c_0 of Eq.(4.4) and the preceding equation, the transverse shear stress for which delamination starts is approx. computed by

$$\tau \simeq \sqrt{G_0 / E_0}\ f_t$$

which reveals that delamination onset occurs for a transverse shear stress smaller than the tensile strength f_t, as appreciated in Figure 4.33 and Figure 4.34.

The gray-scale images shown in Figure 4.35 and Figure 4.36 illustrate the damage growth of the cohesive ply for laminates L1 and L2, respectively. The black color denotes a full damage state (d = 1). These images confirm that damage starts earlier when the HEXA8 finite elements are used, especially for the L2 laminate. However, the global response of the structure (Figure 4.28) is similar for both finite elements. Although the cohesive layer seems to be full damaged at the last step (Δw=2.51mm),

the damage variable just reaches at most a value of 0.997. For this reason, the transverse shear stress τ_{xz} did not decrease as expected in a softening process. Surely, if the test continues until the ply is full damaged, the stresses will be reduced to zero.

The thickness distribution of the axial displacement u at points A, B and E (Figure 4.25b), before (Δw =0.01mm) and after (Δw =2.51mm) delamination, is plotted in Figure 4.37 (L1) and Figure 4.38 (L2), respectively. The QLRZ element captures the relative displacement with errors less than 6% and 2% for laminates L1 and L2, respectively. For all cases, a very good match between 3D and QLRZ kinematics was found.

To emphasize the importance of the zigzag function update to capture relative displacement between layers during a delamination process, Figure 4.30 shows the change of the zigzag thickness distribution from an undamaged to a full damaged state for laminates L1 (Figure 4.30a) and L2 (Figure 4.30b).

In order to compare the performance of the 3D solution and the QLRZ analysis, both, the total increment numbers and the incremental displacement values as well as the error tolerance value are the same for both methods. As expected, the computation time needed for the QLRZ solution is several times less than that required for the 3D analysis. The time used by the finest QLRZ mesh is approximately 20 and 12 times less than that required by the HEXA8 mesh for laminates L1 and L2, respectively. In addition, the computation storage space during the simulation is much greater for the 3D analysis as expected.

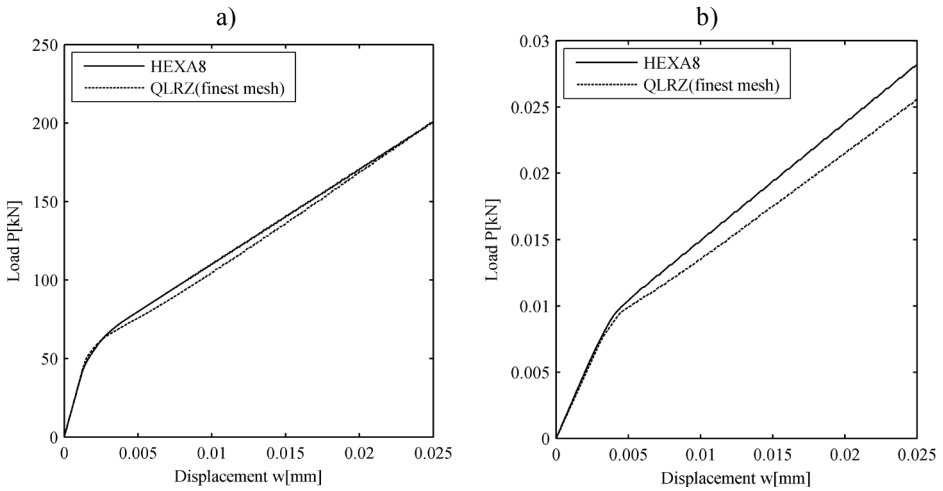

Figure 4.28 – Load vs vertical displacement for laminate L1 a) and L2 b).

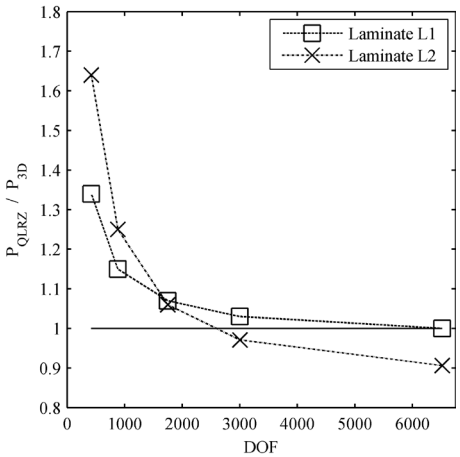

Figure 4.29 – Mesh convergence. Normalized load value for both laminates and all meshes.

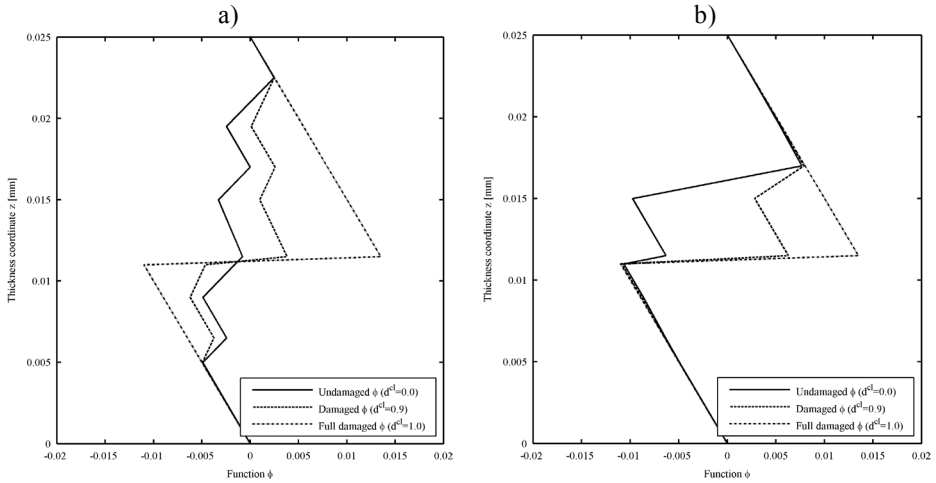

Figure 4.30 – Undamaged and damaged zigzag function ϕ_x for laminate L1 a) and L2 b).

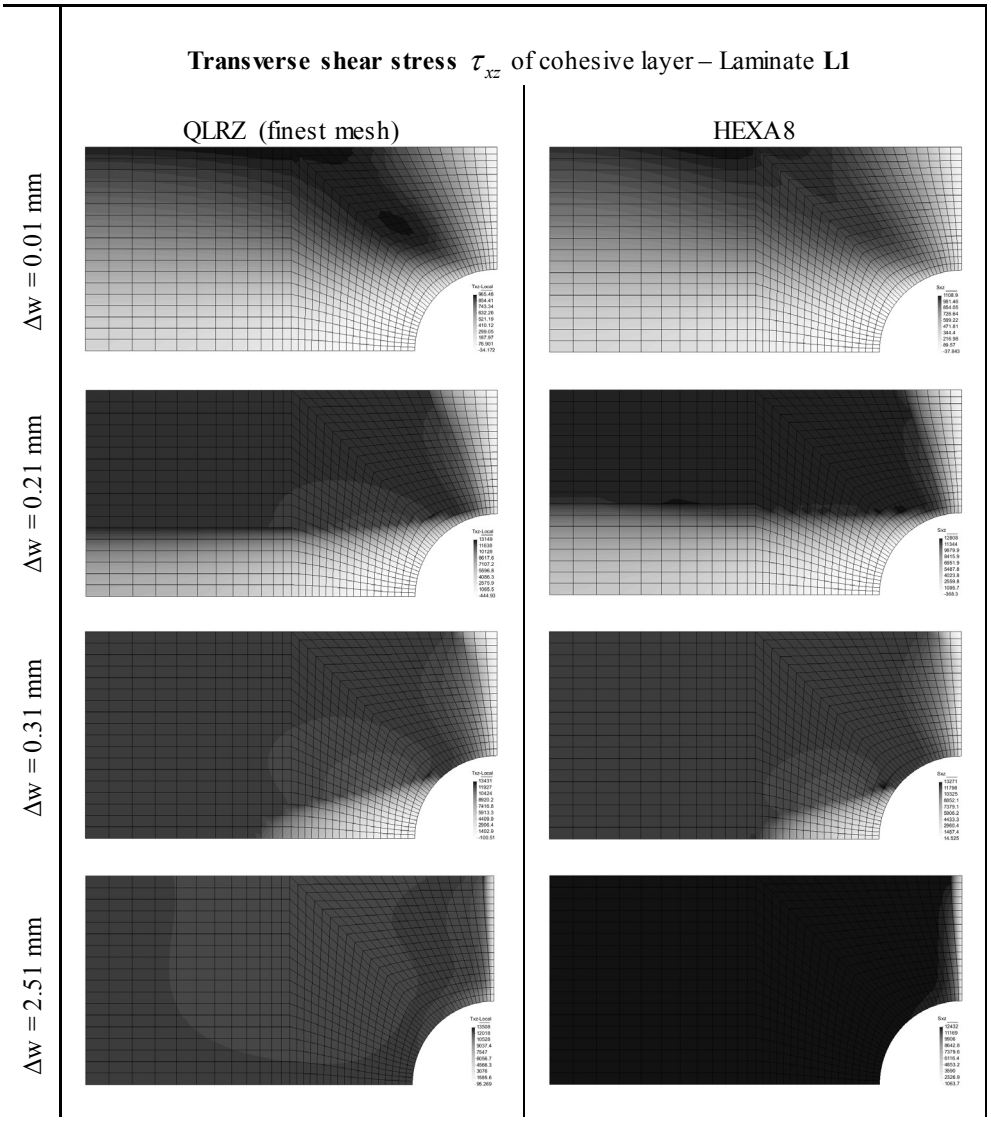

Figure 4.31 – Transverse shear distribution τ_{xz} of cohesive layer for laminate L1 computed with the finest QLRZ mesh (left) and the HEXA8 mesh (right) observed at four different Δw increments.

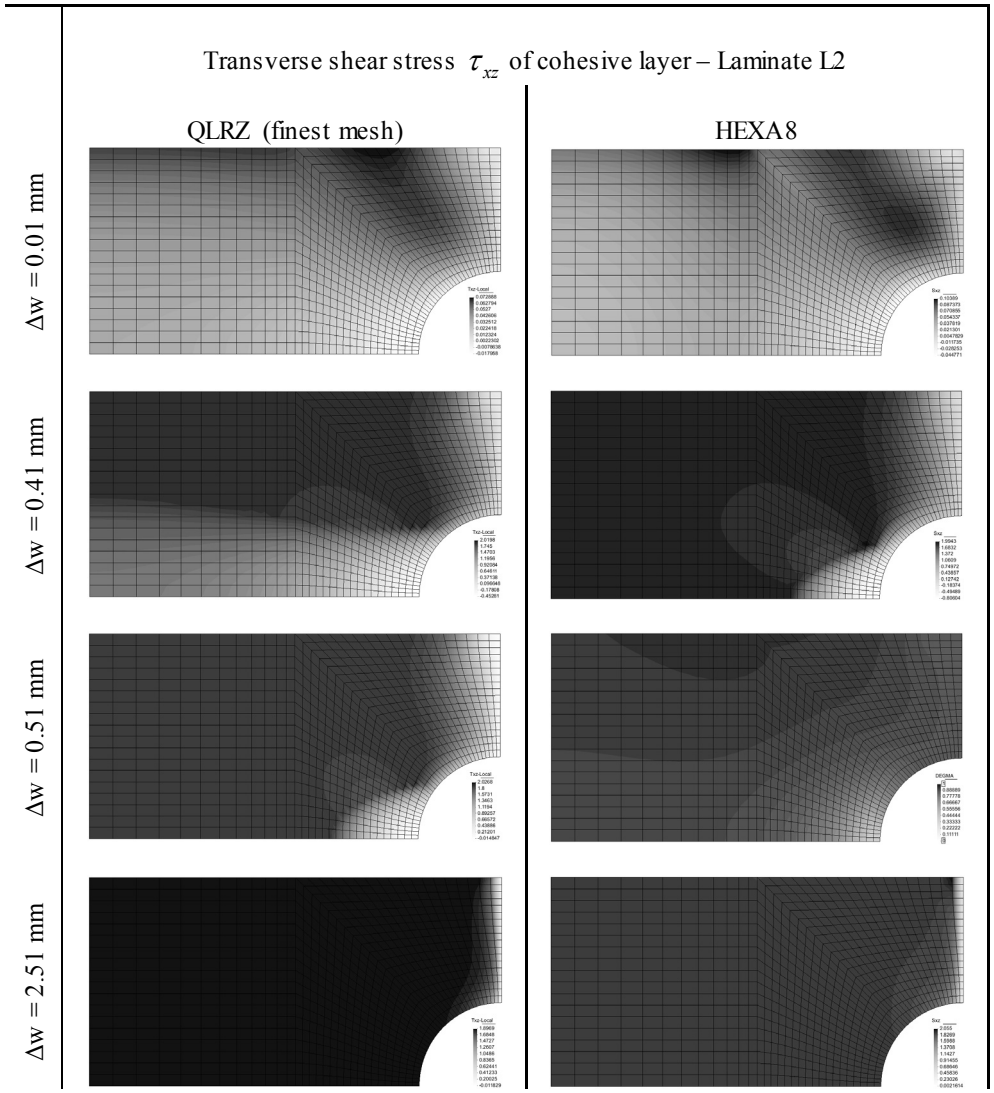

Figure 4.32 – Transverse shear distribution τ_{xz} of cohesive layer for laminate L2 computed with the finest QLRZ mesh (left) and the HEXA8 mesh (right) observed at four different Δw increments.

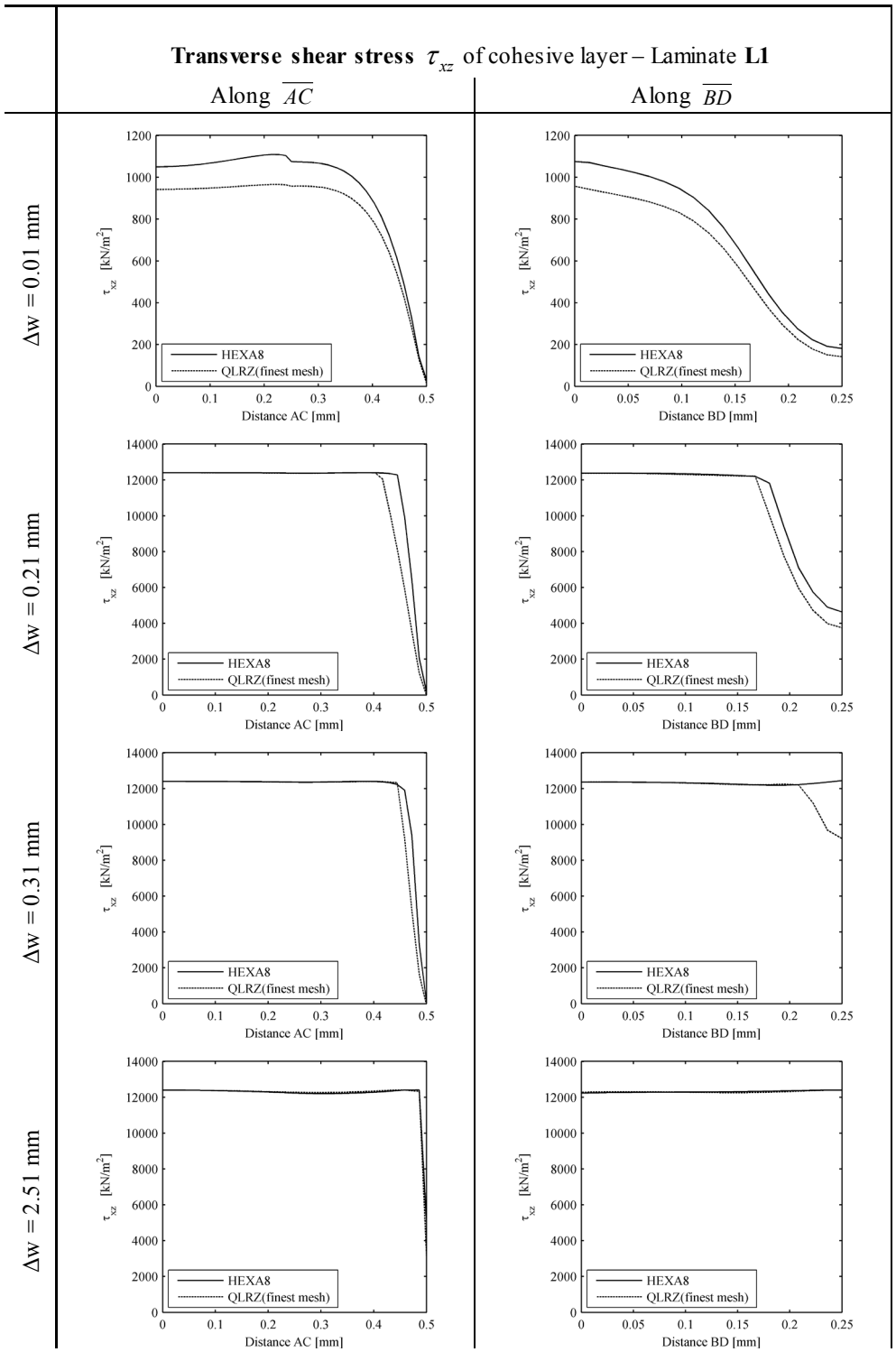

Figure 4.33 – Transverse shear distribution τ_{xz} of cohesive layer for laminate L1 along the segments $\overline{AC}$ (left) and $\overline{BD}$ (right), which were observed at four different Δw increments.

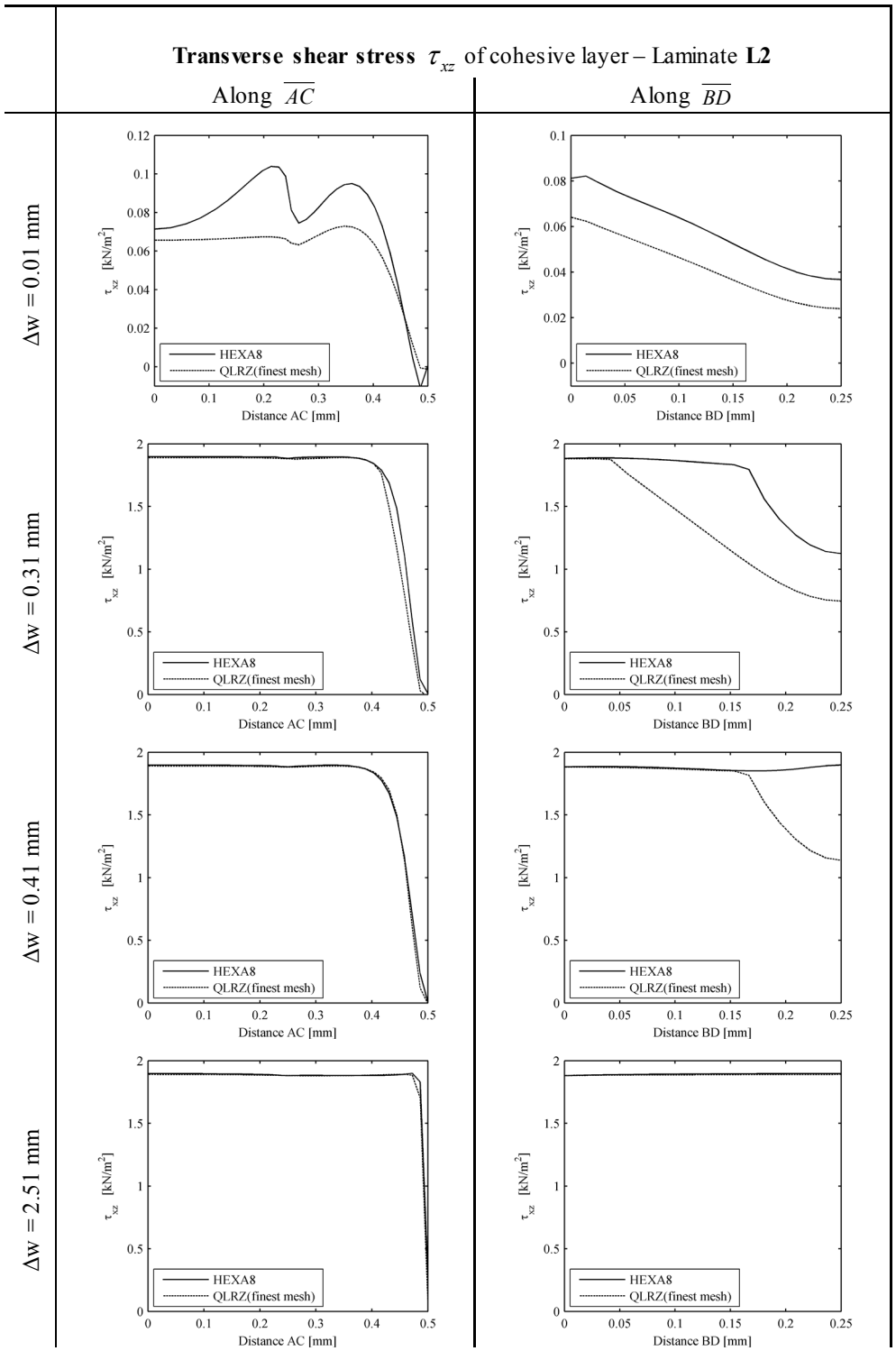

Figure 4.34 – Transverse shear distribution τ_{xz} of cohesive layer for laminate L2 along the segments $\overline{AC}$ (left) and $\overline{BD}$ (right), which were observed at four different Δw increments.

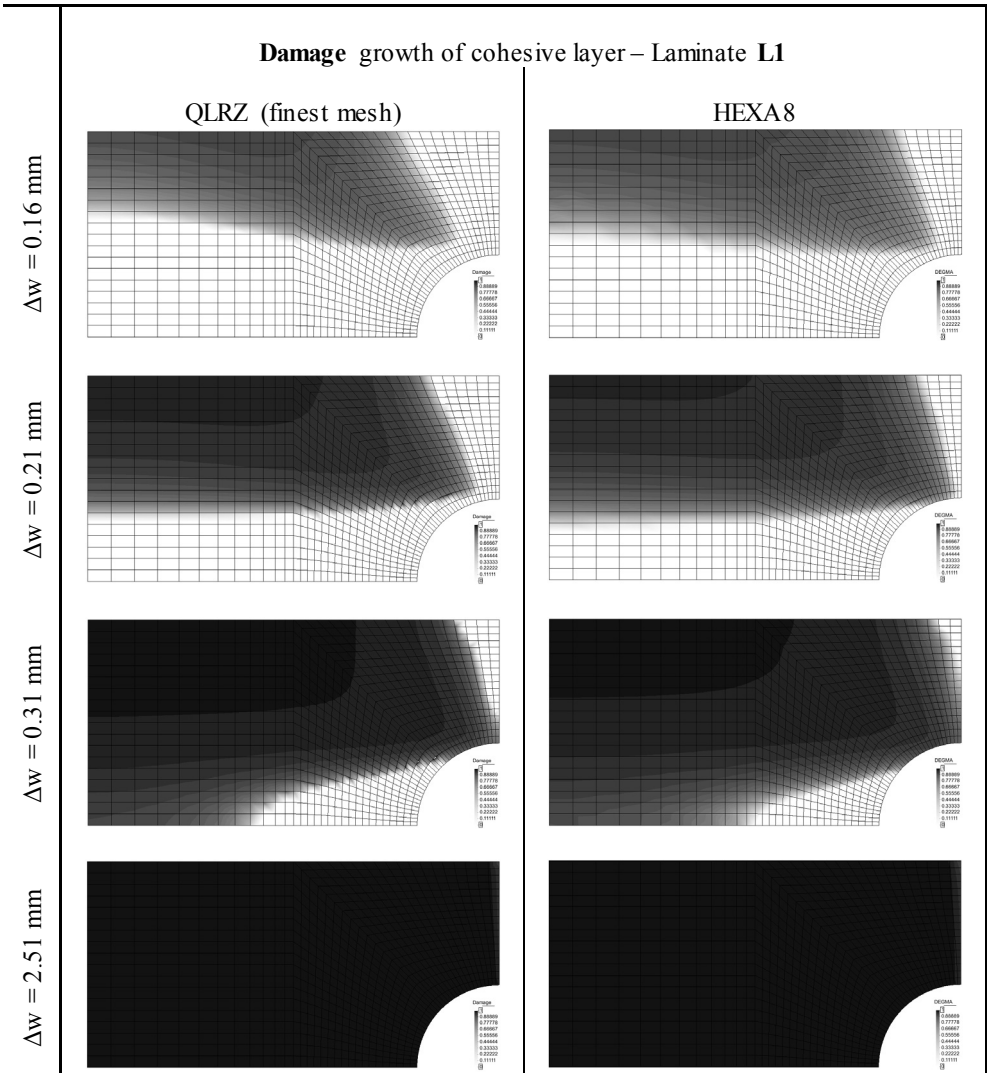

Figure 4.35 – Damage level of cohesive layer for laminate L1 computed with the finest QLRZ mesh (left) and the HEXA8 mesh (right) observed at four different Δw increments. White color is a sing of non-damage and black color indicates full damage.

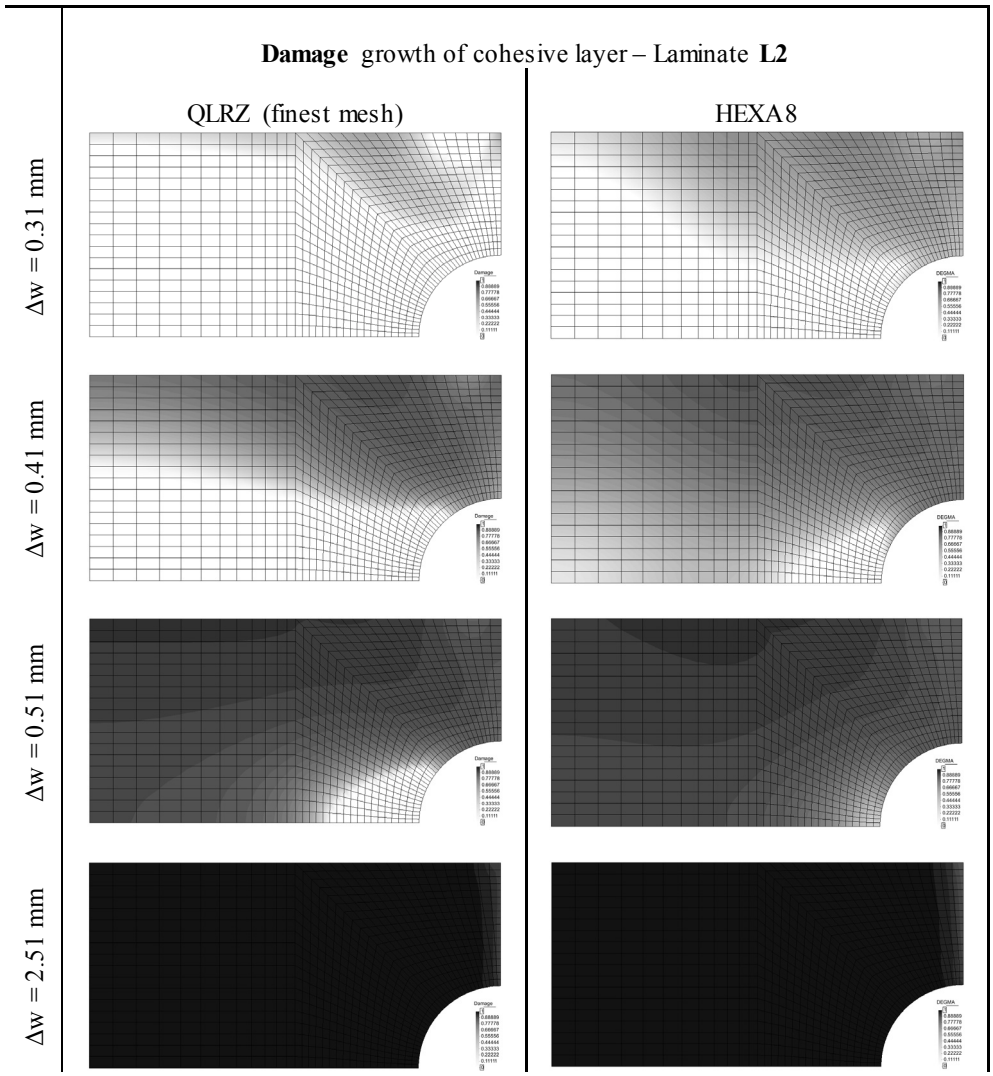

Figure 4.36 – Damage level of cohesive layer for laminate L2 computed with the finest QLRZ mesh (left) and the HEXA8 mesh (right) observed at four different Δw increments. White color is a sing of non-damage and black color indicates full damage.

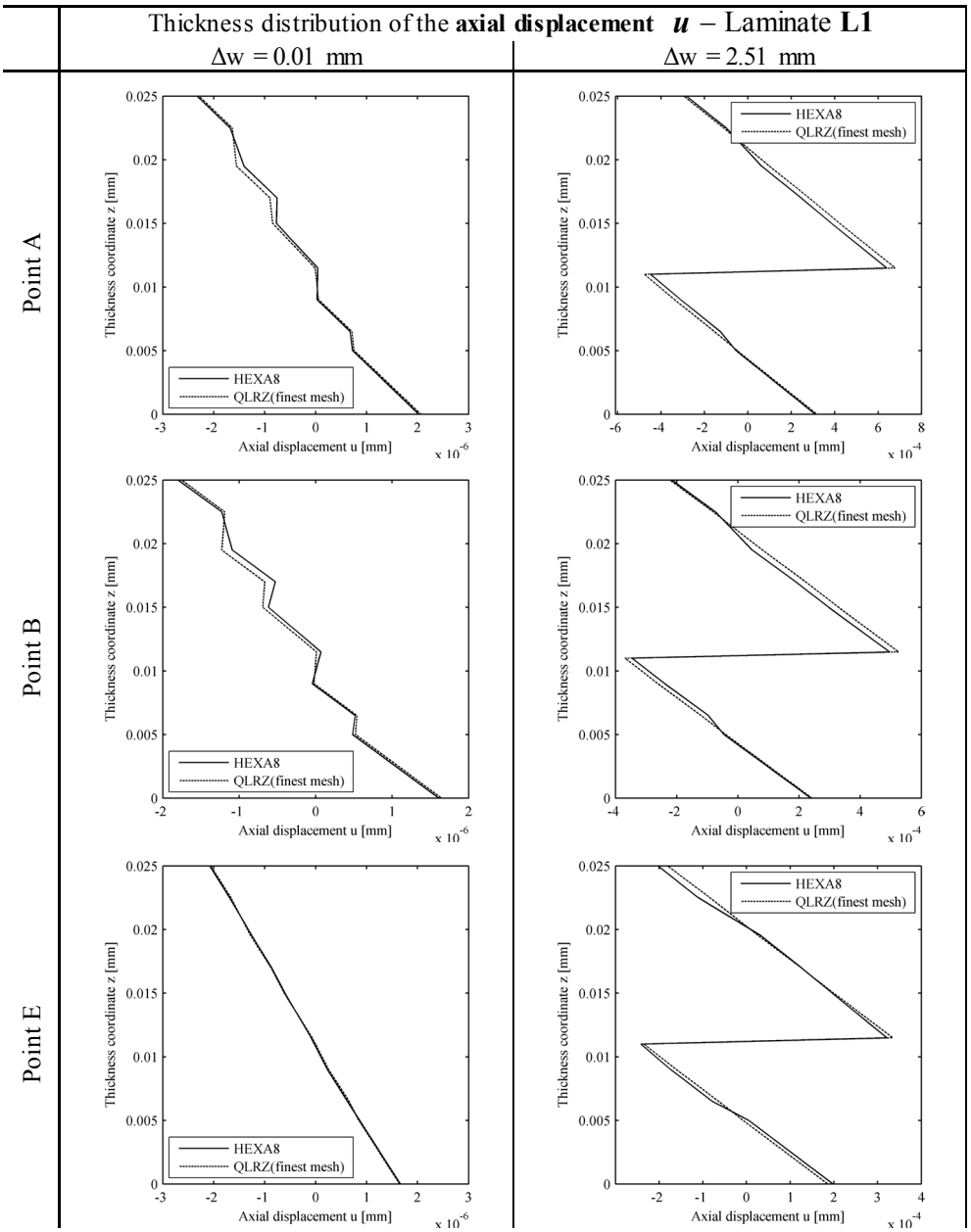

Figure 4.37 – Thickness distribution of the axial displacement u at three different points for laminate L1. Figures show the undamaged kinematics (left - Δw = 0.01 mm) and the delaminated kinematics at the end of simulation (right - Δw = 2.51 mm).

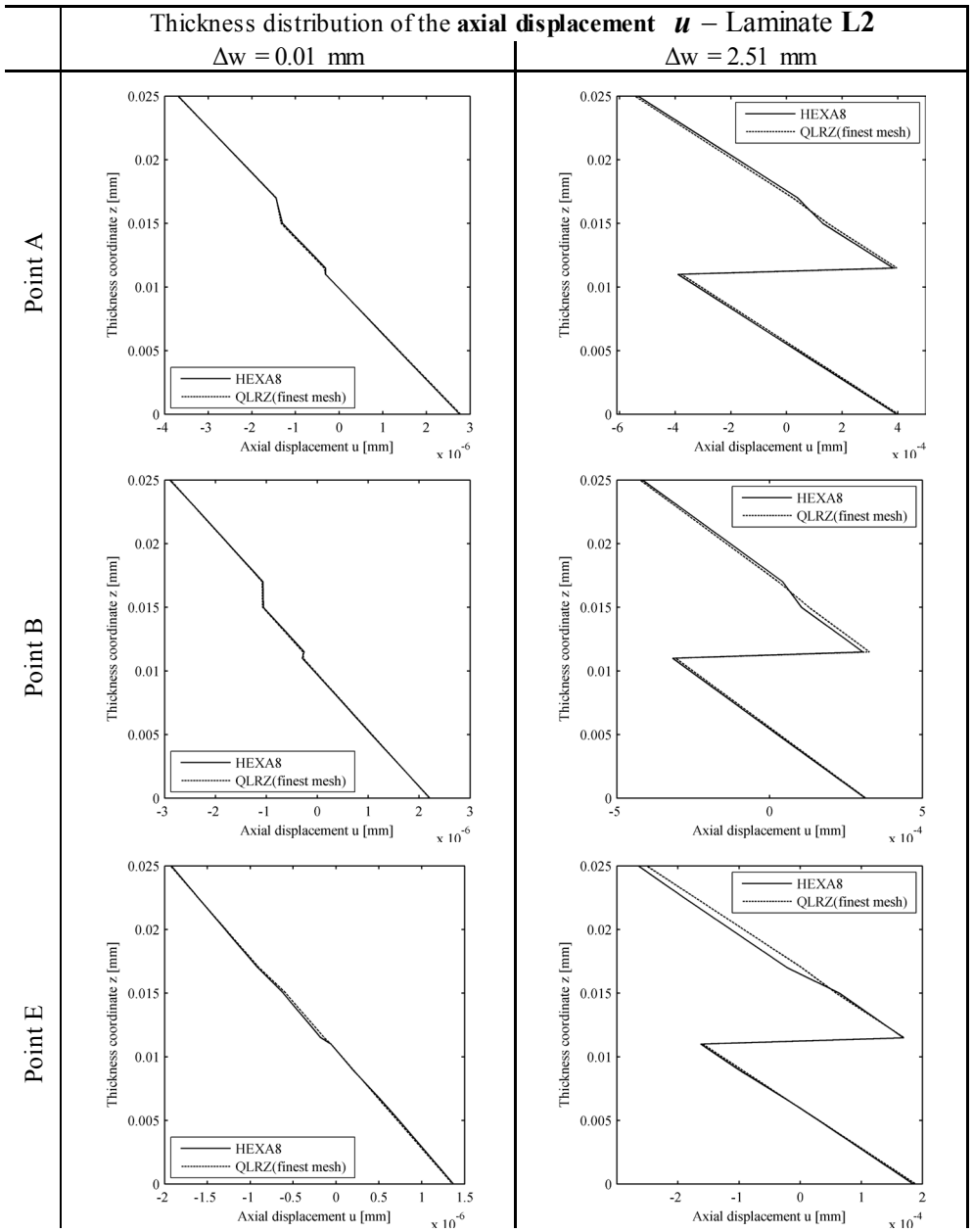

Figure 4.38 – Thickness distribution of the axial displacement *u* at three different points for laminate L2. Figures show the undamaged kinematics (left - Δw = 0.01 mm) and the delaminated kinematics at the end of simulation (right - Δw = 2.51 mm).

5 Conclusions and future work

This thesis dealt with the modeling of laminated materials. The formulation of the beam (LRZ) and plate (QLRZ) finite elements based on the RZT theory for simulating highly heterogeneous multilayered laminates and the development of a numerical method based on these elements for modeling mode II/III delamination in advanced composite materials were the main goals.

The contents and main achievements of the present work are summarized in the following.

In Chapter 2, a review of more common beam/plate theories for modeling laminated materials was presented. In particular, the Refined Zigzag Theory (RZT) was described in detail since the finite elements here developed are based on this zigzag theory. Then, the influence on the zigzag in-plane displacement of both, the material transverse anisotropy and the laminate span-to-thickness ratio was also studied. Results showed that the amplitude of the zigzag kinematics is increased according the transverse anisotropy is higher whereas it is reduced according the laminate is more slender. Furthermore, advanced composite materials and their failure mechanisms were treated, with special attention on delamination. Common numerical methods to predict intra- and inter-laminar failure modes were discussed.

Chapter 3 dealt with development of two simple, robust, shear locking free and accurate isoparametric finite elements based on the RZT theory for simulating laminated beam and plate structures, which constitute the first achievement. The LRZ beam element is a two-node element with four variables per node, whereas the QLRZ plate element is a four-node quadrilateral element with seven variables per nodes. Both elements were formulated on small deformation and displacement.

A key attribute of these elements is that the number of node variables is constant and independent of the analysis layers used to define the laminate. In order to overcome the shear locking defect, a selective numerical integration of the transverse stiffness matrix is adopted in the LRZ element, and a linear shear strain field is assumed in the QLRZ element.

The performance of these elements was investigated through several studies. Results showed that the elements are able to accurately model highly heterogeneous laminated materials under different loads and boundary conditions. The influence of the transverse anisotropy on the convergence and accuracy of the LRZ/QLRZ solutions was also studied. It was found that as the transverse anisotropy is greater the LRZ/QLRZ solution gives worse results.

A very important feature of these elements is their ability to accurately capture the through-thickness distribution of both, the zigzag in-plane displacement and the axial stress. On the contrary, however, the transverse shear stresses distribution is defined by the constitutive equations as a constant pricewise function, which is far from the real distribution. There, the post-processing computation of the transverse shear stresses by means of the equilibrium equations has demonstrated to be a suitable alternative.

An acceptable agreement between the LRZ/QLRZ solutions and the reference solutions was observed in all cases studied.

The development of a numerical model for modeling delamination in advanced composite materials was addressed in Chapter 4. The model uses the LRZ/QLRZ finite elements for describing the whole laminated material including the resin-rich zone at the interface between plies where delamination takes place. In other words, no additional technique for modeling the delamination paths is required. The interfaces are defined by means of additional layers (cohesive layer), which need to be enough thin to avoid membrane effect. It is important to mention that no additional kinematics variables are introduced in the model by incorporating interface layers. Their mechanical behavior is managed by an isotropic damage model. Thus, the relative displacement between two neighbor layers occurs when the transverse shear modulus of the cohesive layers between them is considerably reduced in comparison with those of the neighbor plies.

Only the shear fracture modes (mode II and III) can be captured with the LRZ/QLRZ delamination model because the vertical displacement in the RZT theory is defined constant through the thickness.

In addition, as a result of the definition of the zigzag function, the model cannot predict the zigzag pattern of the in-plane displacement of sub-laminates after delamination. This limitation causes that delamination in multilayered structures having low span-to-thickness ratio or high transverse anisotropy of shear properties cannot be

properly simulated with the LRZ/QLRL delamination model. However, that is not the case of advanced composite laminates where the shear modulus does not differ generally in more than one order of magnitude between layers [113]. Moreover, laminated structures of composite materials are generally characterized by high slenderness ratios. Furthermore, delamination in three-layered laminates can be modeled with independence of the level of transverse anisotropy and the slenderness of the structures, because the sub-laminates, for this kind of material, present a linear displacement distribution after delamination. Because of this, skin-core delamination in sandwich materials can be also modeled with the model, as showed the results.

It was demonstrated that, in order to simulate delamination with this model it is necessary to update the zigzag function. This update was performed by taking into account the level of degradation of the interface layer.

It was also observed that, in order to predict multi-delamination with the LRZ/QLRZ delamination model the reduced shear properties of new degraded interfaces must be almost the same as that of the first damaged cohesive layer. Otherwise, the model may predict wrong displacements obviating previous delamination states or ignoring new delamination paths.

The performance of the LRZ delamination model was analyzed through some single-delamination cases. The analyses include the skin delamination from the core in a clamped sandwich beam and the internal delamination within two different multilayered materials in a simple supported beam. Moreover, the influence on the structural response of the fracture energy of the cohesive layer was also analyzed.

A comparison of the computational cost between the LRZ delamination model and the reference solution, i.e. the finite element plane stress (PS) analysis, was performed. As expected, the results showed that the computation time and the memory space needed by the LRZ model is several times less than that required by a PS analysis.

The performance of the QLRZ delamination model has been studied by simulating internal delamination in a simply supported rectangular plate with a center hole subjected to bending. Two different multilayered materials were used and the results were compared with a reference solution obtained with a 3D finite element analysis.

It was observed that the LRZ/QLRZ delamination model predicts with an acceptable precision the onset and growth of delamination. In addition, the in-plane displacement after delamination is also well predicted.

Summarizing, the main achievement of this work is the development of a preliminary numerical model based on the LRZ/QLRZ finite elements for predicting delamination in advanced composite materials as well as in sandwich laminates. In addition, the LRZ beam and the QLRZ plate finite elements based on the RZT theory are also contributions of this thesis.

It should be noted that some aspects of the developments should be still improved in order to obtain more generality. The following are some of the most relevant aspects which deserve future attention.

- The LRZ and QLRZ elements could be improved in order to obtain more generality. Membrane locking should be investigated. Finite displacements and rotations may be accounted for to simulate geometrically non-linear problems.

- A better definition of the zigzag function is needed to capture zigzag patterns in sub-laminates after delamination with independence of the span-to-thickness ratio and the transverse anisotropy.

- A strategy for controlling the degradation process should be developed in order to simulate multi-delamination with the LRZ/QLRZ delamination model. This strategy has to be applied at each integration points.

- Although the adopted isotropic damage model demonstrated to be able to predict the onset and growth of delamination, it would be interesting to evaluate other damage laws which can simulate the delamination process as a combination of the fracture mode II and III, i.e. mixed mode delamination.

- In order to simulate the complex fracture behavior of advanced composites materials, intra-laminar failure mechanisms should be also accounted for.

All numerical tools developed in this thesis were implemented by the author in his own finite element code. The reference solutions were computed by using the PLCD [121] software developed by the International Center for Numerical Methods in Engineering (CIMNE). Pre- and post-process tasks were carried out employing the GID [122] software developed by CIMNE.

References

[1] Carrera, E. Theories and Finite Elements for Multilayered, Anisotropic, Composite Plates and Shells. *Arch. Comput. Meth. Engng.,* 9: 87-140, 2002.

[2] Reddy, J. N. Mechanics of Laminated Composite Plates and Shells: Theory and Analysis. 2nd Ed. United States of America, CRC Press, 2003.

[3] Tessler, A., Sciuva, M. D., and Gherlone, M., "Refinement of Timoshenko Beam Theory for Composite and Sandwich Beams Using Zigzag Kinematics," NASA, Technical Publication TP-215086, 2007.

[4] Tessler, A., Sciuva, M. D., and Gherlone, M. A consistent refinement of first-order shear deformation theory for laminated composite and sandwich plates using improved zigzag kinematics. *Mechanics of Materials and Structures,* 5: 341-365, 2010.

[5] Balzani, C., "Finite element modeling of intra- and interlaminar damage growth in composite laminates," Fakultät für Bauingenieur-, Geo- und Umweltwissenschaften der Universität Fridericiana zu Karlsruhe, Karlsruhe, Germany, 2009.

[6] Martinez, X., Rastellini, F., Oller, S., Flores, F., and Oñate, E. Computationally optimized formulation for the simulation of composite materials and delamination failures. *Composites: Part B,* 47: 134-144, 2011.

[7] Krueger, R. The Virtual Crack Closure Technique: History, Approach and Applications. *Applied Mechanics Reviews,* 57: 109-143, 2002.

[8] Aymerich, F., Dore, F., and Priolo, P. Prediction of impact-induced delamination in cross-ply composite laminates using cohesive interface elements. *Composites Science and Technology,* 68: 2383-2390, 2008.

[9] Sánchez-Palencia, E. S. Homogenization techniques for composite media. *Springer-Verlag, Berlin, Germany. Chapter: "Boundary layers and edge effects in composites",* 121-192, 1987.

[10] Oller, S., Miquel, J., and Zalamea, F. Composite material behavior using a homogenization double scale method. *Journal of Engineering Mechanics,* 131: 65-79, 2005.

[11] Carrera, E. C^{0z} Requirements-models for the two dimensional analysis of multilayered structures. *Composite Structures,* 37: 373-383, 1997.

[12] Kirchhoff, G. Über das Gleichgewicht und die Bewegung einer elastishen Scheibe. *J Angew Math,* 40: 51-88, 1850.

[13] Wanji, C. and Zhen, W. A Selective Review on Recent Development of Displacement-Based Laminated Plate Theories. *Recent Patents on Mechanical Engineering,* 1: 29-44, 2008.

[14] Timoshenko, S. P. and Woinowsky-Krieger, S. Theory of plates ans shells. 3rd Ed. New York, McGraw-Hill, 1959.

[15] Timoshenko, S. P. On the correction for shear of differential equations for transverse vibrations of prismatic bars. *Philosophical Magazine Series,* 41: 744-746, 1921.

[16] Reissner, E. The effect of transverse shear deformation on the bending of elastic plates. *Appl. Mech.,* 12: 69-79, 1945.

[17] Mindlin, R. D. Influence of rotatory inertia and shear in flexural motions of isotropic elastic plates. *Appl. Mech.,* 18: 31-38, 1951.

[18] Reddy, J. N. A simple higher-order theory for laminated composite plates. *Appl. Mech.,* 51: 745-752, 1984.

[19] Kant, T. and Swaminathan, K. Analytical solution for the static analysis of laminated composite and sandwich plates based on a higher order refined theory. *Composite Structures,* 56: 329-344, 2002.

[20] Matsunaga, H. Assessment of a global higher-order deformation theory for laminated composite and sandwich plates. *Composite Structures,* 56: 279-291, 2002.

[21] Auricchio, F. and Sacco, E. Partial-mixed formulation and refined models for the analysis of composite laminates within an FSDT. *Composite Structures,* 46: 103-113, 1999.

[22] Carrera, E. A priori vs. a posteriori evaluation of transverse stresses in multilayered orthotropic plates. *Composite Structures,* 48: 245-260, 2000.

[23] Reddy, J. N. and D. H. Robbins, J. Theories and computational models for composite laminates. *Applied Mechanics Reviews,* 47: 147-165, 1994.

[24] Robbins, D. H. and Reddy, J. N. Modelling of thick composites using a layerwise laminate theory. *Int. Journal for Numerical Methods in Engineering,* 36: 655-677, 1993.

[25] Carrera, E. Mixed layer-wise models for multilayered plates analysis. *Composite Structures,* 43: 57–70, 1998.

[26] Carrera, E. Evaluation of Layerwise Mixed theories for laminated Plates Analysis. *AIAA,* 36: 830-839, 1998.

[27] Murakami, H. Laminated composite plate theory with improved in-plane responses. *Journal of Applied Mechanics,* 53: 661-666, 1986.

[28] Murakami, H. A higher-order laminated plate theory with improved in-plane response. *Int. J. Solids Struct.,* 23: 111-131, 1987.

[29] Carrera, E. C0 Reissner-Mindlin multilayered plate elements including zigzag and interlaminar stress continuity. *Int. J. Numer. Meth. Engng,* 39: 1797-1820, 1996.

[30] Demasi, L. Refined multilayered plate elements based on Murakami zig–zag functions. *Composite Structures,* 70: 308-316, 2005.

[31] DiSciuva, M. A refinement of transverse shear deformation theory for multilayered orthotropic plates. *Atti Accademia delle Scienze di Torino,* 118: 279-295, 1984.

[32] DiSciuva, M. A third-order triangular multilayered plate finite element with continuous interlaminar stresses. *Int. J. Numer. Meth. Engng,* 38: 1-26, 1995.

[33] Cho, M. and Parmerter, R. An efficient higher-order plate theory for laminated composites. *Composite Structures,* 20: 113-123, 1992.

[34] Averill, R. C. Static and dynamic response of moderately thick laminated beams with damage. *Composites Engineering,* 4: 381-395, 1994.

[35] Averill, R. C. and Yip, Y. C. Development of simple, robust finite elements based on refined theories for thick laminated beams. *Computers & Structures,* 59: 529-546, 1996.

[36] Tessler, A., Sciuva, M. D., and Gherlone, M. A refined zigzag beam theory for composite and sandwich beams. *Journal of Composite Materials,* 43: 1051-1081, 2009.

[37] Tessler, A., Sciuva, M. D., and Gherlone, M. Refined zigzag theory for homogeneous, laminated composite, and sandwich plates: a homogeneous limit methodology for zigzag function selection. *Numerical Methods for Partial Differential Equations,* 27: 208-229, 2011.

[38] Oñate, E., Eijo, A., and Oller, S. Simple and accurate two-noded beam element for composite laminated beams using a refined zigzag theory. *Computer Methods in Applied Mechanics and Engineering,* 213–216: 362-382, 2012, DOI: http://dx.doi.org/10.1016/j.cma.2011.11.023.

[39] Eijo, A., Oñate, E., and Oller, S. A four-noded quadrilateral element for composite laminated plates/shells using the refined zigzag theory. *Int. J. Numer. Meth. Engng,* 95: 631-660, 2013, DOI: http://dx.doi.org/10.1002/nme.4503.

[40] Eijo, A., Oñate, E., and Oller, S. A numerical model of delamination in composite laminated beams using the LRZ beam element based on the refined zigzag theory. *Composite Structures,* 104: 270-280, 2013, DOI: http://dx.doi.org/10.1016/j.compstruct.2013.04.035.

[41] Eijo, A., Oñate, E., and Oller, S. Delamination in laminated plates using the 4-noded quadrilateral QLRZ plate element based on the refined zigzag theory. *Composite Structures,* 108: 456–471, 2014, DOI: http://dx.doi.org/10.1016/j.compstruct.2013.09.052.

[42] Gherlone, M., Tessler, A., and Di Sciuva, M. Cº beam element based on the refined zigzag theory for multilayered composite and sandwich laminates. *Composite Structures,* 93: 2882-2894, 2011.

[43] Versino, D., Gherlone, M., Mattone, M., Sciuva, M. D., and Tessler, A. C0 triangular elements based on the Refined Zigzag Theory for multilayer composite and sandwich plates. *Composites Part B: Engineering (online),* -: -, 2012.

[44] Barut, A., Madenci, E., and Tessler, A., "A refined zigzag theory for laminated composite and sandwich plates incorporating thickness stretch deformation," in *53rdAIAA/ASME/ASCE/AHS/ASC structures, structural dynamics, and materials conference,* Honolulu, Hawaii., 2012.

[45] Barut, A., Madenci, E., and Tessler, A. C0-continuous triangular plate element for laminated composite and sandwich plates using the {2,2} – Refined Zigzag Theory. *Composite Structures,* 106: 835-853, 2013.

[46] Harris, C. E., "Opportunities for Next Generation Aircraft Enabled by Revolutionary Materials," in *AIAA SDM Conference*, Denver, EEUU, 2011.

[47] Hill, R. A theory of the yielding and plastic flow of anisotropic metals. *Proceedings of the Royal Society of London, Serie A: Mathematical and Physical Sciences 193,* 1033: 281-297, 1948.

[48] Tsai, S. and Wu, E. M. A general theory of strength for anisotropic materials. *Journal of Composite Materials,* 5: 58-80, 1971.

[49] Hashin, Z. Failure criteria for unidirectional fiber composites. *Journal of Applied Mechanics,* 47: 329-334, 1980.

[50] Goyal, V. K., Jaunky, N. R., Johnson, E. R., and Ambur, D. R. Intralaminar and interlaminar progressive failure analyses of composite panels with circular cutouts. *Composite Structures,* 64: 91-105, 2004.

[51] Puck, A. and Schürmann, H. Failure analysis of FRP laminates by means of physically based phenomenological models. *Composites Science and Technology,* 58: 1045-1067, 1998.

[52] Dávila, C. G., Camanho, P. P., and Rose, C. A. Failure Criteria for FRP Laminates. *Journal of Composite Materials,* 39: 323-345, 2005.

[53] Pinho, S. T., Dávila, C. G., Camanho, P. P., Ianucci, L., and Robinson, P., "Failure models and criteria for FRP under in-plane or three-dimensional stress states including shear non-linearity," NASA, Technical Memorandum TM-2005-213530, 2005.

[54] ASTM Standard D3039 / D3039M - 00. *Standard Test Method for Tensile Properties of Polymer Matrix Composite Materials*. American Society for Testing and Materials, West Conshohokken, PA, USA, 2000.

[55] ASTM Standard D3410 / D3410M - 03. *Standard Test Method for Compressive Properties of Polymer Matrix Composite Materials with Unsupported Gage Section by Shear Loading*. American Society for Testing and Materials, West Conshohokken, PA, USA, 2003.

[56] DIN Standard DIN EN 2561. *Aerospace series - Carbon fibre reinforced plastics - Unidirectional Laminates - Tensile test parallel to the fibre direction*. Deutsches Institut für Normung, Berlin, Germany, responsible committee NA 131-02-01 AA, 1995.

[57] DIN Standard DIN EN 2597. *Aerospace series - Carbon fibre reinforced plastics - Unidirectional Laminates - Tensile test perpendicular to the fibre direction - German version EN 2597:1998*. Deutsches Institut für Normung, Berlin, Germany, responsible committee NA 131-02-01 AA, 1998.

[58] DIN Standard DIN EN 2850. *Aerospace series - Carbon fibre thermosetting resin unidirectional laminates - Compression test parallel to fibre direction*. Deutsches Institut für Normung, Berlin, Germany, responsible committee NA 131-02-01 AA, 1998.

[59] Oller, S., Martínez, X., Barbat, A., and Rastellini, F. Advanced composite material simulation. *Ciência e Tecnologia dos Materiais,* 20: 2008.

[60] Martinez, X., "Micro mechanical simulation of composite materials using the Serial/Parallel Mixing Theory," Dto. Resistencia de Materiales, Universidad Politécnica de Cataluña, Barcelona, Spain, 2008.

[61] Truesdell, C. and Toupin, R. The classical field theories, handbuch der physik iii/i ed. Berlin, Germany,, Springer-Verlag, 1960.

[62] Car, E., Oller, S., and Oñate, E. An anisotropic elastoplastic constitutive model for large strain analysis of fiber reinforced composite materials. *Computer Methods in Applied Mechanics and Engineering,* 185: 245–277, 2000.

[63] Rastellini, F., Oller, S., Salomon, O., and Oñate, E. Composite materials non-linear modelling for long fibre reinforced laminates: continuum basis, computational aspects and validations. *Computers & Structures,* 86: 879-896, 2008.

[64] Bolotin, V. V. Delaminations in composite structures: its origin, buckling, growth and stability. *Composites: Part B,* 27B: 129-145, 1996.

[65] Villaverde, B. N., "Variable mixed-mode delamination in composite laminates under fatigue conditions: Testing and analysis.," Departament of Physics of University of Girona, Girona, Spain, 2004.

[66] ASTM Standard D2344 / D2244M - 00 (2006). *Standard Test Method for Short-Beam Strength of Polymer Matrix Composite Materials and Their Laminates*. American Society for Testing and Materials, West Conshohokken, PA, USA, 2006.

[67] DIN Standard DIN EN 6033. *Aerospace series - Carbon fibre reinforced plastics - Test metod - Determination of interlaminar fracture toughness energy - Mode I - GIc*. Deutsches Institut für Normung, Berlin, Germany, responsible committee NA 131-02-01 AA, 1996.

[68] ASTM Standard D5528-01 (2007) E1. *Standard Test Method for Mode I Interlaminar Fracture Toughness of Inidirectional Fiber-Reinforced Polymer Matrix Composites*. American Society for Testing and Materials, West Conshohokken, PA, USA, 2007.

[69] DIN Standard DIN EN 6033. *Aerospace series - Carbon fibre reinforced plastics - Test metod - Determination of interlaminar fracture toughness energy - Mode II - GIIc*.

Deutsches Institut für Normung, Berlin, Germany, responsible committee NA 131-02-01 AA, 1996.

[70] Lee, S. M. An edge crack torsion method for mode III delamination fracture testing. *Journal of Composites Technology and Research 15,* 3: 193-201, 1993.

[71] ASTM Standard D6671 / D6671M - 06. *Standard Test Method for Mixed Mode I - Mode II Interlaminar Fracture Toughness of Inidirectional Fiber-Reinforced Polymer Matrix Composites*. American Society for Testing and Materials, West Conshohokken, PA, USA, 2006.

[72] Reeder, J. 3d mixed mode delamination fracture criteria-an experimentalist perspective. NASA Langley research center,M/S 188E, Hampton VA 23681-2199,USA.

[73] Benzeggagh, M. and Kenane, M. Measurement of Mixed-Mode Delamination Fracture Toughness of Unidirectional Glass/Epoxy Composites with Mixed-Mode Bending Apparatus. *Composite Science and Technology,* 56: 439, 1996.

[74] Wu, E. M. and Reuter-Jr., R. C. Crack Extension in Fiberglass Reinforced Plastics. *T and M Report, University of Illinois,* 275: . 1965.

[75] Greenhalgh, E., Asp, L., and Singh, S., "Delamination resistance, failure criteria and fracture morphology of 0º/0º, 0º/5º and 0º/90º ply interface in cfrp," in *5th International Conference on Deformation and Fracture of Composite*, London, United Kingdom, 1999.

[76] Rybicki, E. F. and Kanninen, M. F. A finite element calculation of stress intensity factors by a modified crack closure integral. *Engineering Fracture Mechanics,* 9: 931-938, 1977.

[77] Cherepanov, G. P. The propagation of cracks in a continuous medium. *Journal of Applied Mathematics and Mechanics,* 31: 503-512, 1967.

[78] Rice, J. R. A Path Independent Integral and the Approximate Analysis of Strain Concentration by Notches and Cracks. *Journal of Applied Mechanics,* 35: 379-386, 1968.

[79] Hellen, T. K. On the Method of Virtual Crack Extension. *Int. J. Numer. Meth. Engng,* 9: 187-207, 1975.

[80] Klug, J., Wu, X. X., and Sun, C. T. Efficient modeling of postbuckling delamination growth in composite laminates using plate elements. *AIAA,* 34: 178-184, 1996.

[81] Gaudenzi, P., Perugini, P., and Riccio, A. Post-buckling behavior of composite panels in the presence of unstable delaminations. *Composite Structures,* 51: 301-309, 2001.

[82] Liu, P. F., Hou, S. J., Chu, J. K., Hu, X. Y., Zhou, C. L., Liu, Y. L., Zheng, J. Y., Zhao, A., and Yan, L. Finite element analysis of postbuckling and delamination of composite laminates using virtual crack closure technique. *Composite Structures,* 93: 1549–1560, 2011.

[83] Wang, J. T. and Raju, I. S. Strain energy release rate farmulae for skin-stiffener debond modeled with plate elements. *Engineering Fracture Mechanics,* 54: 211-228, 1996.

[84] Krueger, R., Paris, I. L., O'Brien, T. K., and Minguet, P. J., "Fatigue Lifo Methodology for Bonded Composite Skin Stringer Configurations," NASA, Technical Memorandum TM-2001-210842 ARL-TR-2432, 2002.

[85] Krueger, R., Paris, I. L., O'Brien, T. K., and Minguet, P. J. Comparison of 2D finite element modeling assumptions with results from 3D analysis for composite skin-stiffener debonding. *Composite Structures,* 57: 161-168, 2002.

[86] Saeedi, N., Sab, K., and Caron, J. F. Cylindrical bending of multilayered plates with multi-delamination via a layerwise stress approach. *Composite Structures,* 95: 728-739, 2013.

[87] Barbero, E. J. and Reddy, J. N. Modeling of delamination in laminates using a layer-wise plate theory. *International Journal of Solids and Structures,* 28: 373-388, 1991.

[88] Dudgale, D. S. Yielding of steel sheets containing slits. *Journal of Mechanics and Physics of Solids,* 8: 100-104, 1960.

[89] Barenblatt, G. I. The mathematical theory of equilibrium cracks in brittle failure. *Advances in Applied Mechanics,* 7: 1962.

[90] Wagner, W., Gruttmann, F., and Sprenger, W. A finite element formulation for the simulation of propagating delaminations in layered composite structures. *Int. J. Numer. Meth. Engng,* 51: 1337-1359, 2001.

[91] Balzani, C. and Wagner, W. An interface element for the simulation of delamination in unidirectional fiber-reinforced composite laminates. *Engineering Fracture Mechanics,* 75: 2597-2615, 2008.

[92] Camanho, P. P. and Dávila, C. G., "Mixed-mode decohesion finite elements for the simulation of delamination in composite materials," NASA, Technical Memorandum TM-211737, 2002.

[93] Zou, Z., Reid, S. R., and Li, S. A continuum damage model for delaminations in laminated composites. *Journal of the Mechanics and Physics of Solids,* 51: 333-356, 2003.

[94] Turon, A., Camanho, P. P., Costa, J., and Da´vila, C. G. A damage model for the simulation of delamination in advanced composites under variable-mode loading. *Mechanics of Materials,* 38: 1072–1089, 2006.

[95] Balzani, C. and Wagner, W. Numerical treatment of damage propagation in axially compressed composite airframe panels. *Int. J. Struct. Stab. Dyn.,* 10: 683-703, 2010.

[96] Turon, A., "Simulation of delamination in composite under quasi-static and fatigue loading using cohesive zone models," University of Girona, Girona, Spain, 2007.

[97] Turon, A., Camanho, P. P., Costa, J., and Renart, J. Accurate simulation of delamination growth under mixed-mode loading using cohesive elements: Definition of interlaminar strengths and elastic stiffness. *Composite Structures,* 92: 1857–1864, 2010.

[98] Wagner, W. and Balzani, C. Simulation of delamination in stringer stiffened fiber-reinforced composite shells. *Computers and Structures,* 86: 930-939, 2008.

[99] Na, W. J. and Reddy, J. N. Delamination in cross-ply laminated beams using the layerwise theory. *Asian Journal of Civil Engineering,* 10: 451-480, 2009.

[100] Hosseini-Toudeshky, H., Hosseini, S., and Mohammadi, B. Delamination buckling growth in laminated composites using layerwise-interface element. *Composite Structures,* 92: 1846-1856, 2010.

[101] Williams, T. O. and Addessio, F. L. A general theory for laminated plates with delaminations. *International Journal of Solids and Structures,* 34: 2003-2024, 1997.

[102] Sciuva, M. D. and Gherlone, M. A global/local third-order Hermitian displacement field with damaged interfaces and transverse extensibility: FEM formulation. *Composite Structures,* 59: 433-444, 2003.

[103] Sciuva, M. D. and Gherlone, M. Quasi-3D static and dynamic analysis of undamaged and damaged sandwich beams. *Journal of Sandwich Structures and Materials,* 7: 31-52, 2005.

[104] Icardi, U. and Zardo, G. C0 Plate element for delamination damage analysis, based on a zig-zag model and strain energy updating. *International Journal of Impact Engineering,* 31: 579-606, 2005.

[105] Icardi, U. C0 plate element based on strain energy updating and spline interpolation, for analysis of impact damage in laminated composites. *International Journal of Impact Engineering,* 34: 1835-1868, 2007.

[106] Icardi, U. and Ferrero, L. Impact analysis of sandwich composites based on a refined plate element with strain energy updating. *Composite Structures,* 89: 35-51, 2009.

[107] Zienkiewicz, O. C. and Taylor, R. L. Finite element method. Vol. 1, 5 Ed. Oxford, UK, Butterworth-Heinemann, 2000.

[108] Oñate, E. Structural analysis by the finite element method. Vol. 2: Beams, plates and shells Barcelona, Springer-CIMNE, 2013.

[109] Dvorkin, E. N. and Bathe, K. J. A continuum mechanics based four node shell element for general non-linear analysis. *Engineering computations,* 1: 77-88, 1984.

[110] Bathe, K. J. and Dvorkin, E. N. A four node plate bending element based on Mindlin-Reissner plate theory and mixed interpolation. *Int. Journal for Numerical Methods in Engineering,* 21: 367-383, 1985.

[111] Hinton, E. and Huang, H. C. A family of quadrilateral Mindlin plate elements with substitute shear strain fields. *Computers & Structures,* 23: 409 - 431, 1986.

[112] Oñate, E., Zienkiewicz, O., Suárez, B., and Taylor, R. L. A general methodology for deriving shear constrained Reissner-Mindlin plate elements. *Int. Journal for Numerical Methods in Engineering,* 33: 345-367, 1992.

[113] Soden, S. P., Hinton, M. J., and Kaddour, A. S. Lamina properties, lay-up configurations and loading conditions for a range of fibre-reinforced composite laminates. *Compos Sci Technol,* 58: 1011-1022, 1998.

[114] Simo, J. C. and Ju, J. W. Strain - and stress - based continuum damage models - I. Formulation. *International Journal Solids Structures,* 23: 821-840, 1987.

[115] Simo, J. C. and Ju, J. W. Strain - and stress - based continuum damage models - II. Computational aspects. *International Journal Solids Structures,* 23: 841-869, 1987.

[116] Chaboche, J. L. Continuum damage mechanics: Part I - General concepts. *Journal of Applied Mechanics,* 55: 59-64, 1988.

[117] Chaboche, J. L. Continuum damage mechanics: Part II - Damage growth, crack initiation, and crack growth. *Journal of Applied Mechanics,* 55: 65-72, 1988.

[118] Oliver, J., Cervera, M., Oller, S., and Lubliner, J., "Isotropic damage models and smeared crack analysis of concret," in *Second international conference on computer aided analysis and design of concrete structures.* Zell am See, Austria, 1990.

[119] Oller, S. Fractura mecánica. Un enfoque global., 1ra Ed. Barcelona, España, CIMNE, 2001.

[120] Zienkiewicz, O. C. and Taylor, R. L. El método de los elementos finitos. Vol. 2, 5 Ed. Barcelona, CIMNE, 2004.

[121] International Center for Numerical Methods in Engineering, 2011. Implicit finite element code for the simulation of composite materials. https://web.cimne.upc.edu/users/plcd/.

[122] International Center for Numerical Methods in Engineering, 2010. Pre- and post-processor software. http://gid.cimne.upc.es/.

Appendix

Attention¡¡

Pages 153 to 249 of the thesis are available at the editor's web

- Oñate, E., Eijo, A., and Oller, S. Simple and accurate two-noded beam element for composite laminated beams using a refined zigzag theory. *Computer Methods in Applied Mechanics and Engineering* (IF: 2.617), 213–216: 362-382, 2012.
  DOI: http://dx.doi.org/10.1016/j.cma.2011.11.023.
  http://www.sciencedirect.com/science/article/pii/S0045782511003690

- Eijo, A., Oñate, E., and Oller, S. A four-noded quadrilateral element for composite laminated plates/shells using the refined zigzag theory. *Int. J. Numer. Meth. Engng* (IF: 2.068), 95: 631-660, 2013.
  DOI: http://dx.doi.org/10.1002/nme.4503.
  http://onlinelibrary.wiley.com/doi/10.1002/nme.4503/full

- Eijo, A., Oñate, E., and Oller, S. A numerical model of delamination in composite laminated beams using the LRZ beam element based on the refined zigzag theory. *Composite Structures* (IF: 2.231), 104: 270-280 2013.
  DOI: http://dx.doi.org/10.106/j.compstruct.2013.04.035.
  http://www.sciencedirect.com/science/article/pii/S0263822313002018

- Eijo, A., Oñate, E., and Oller, S. Delamination in laminated plates using the 4-noded quadrilateral QLRZ plate element based on the refined zigzag theory. *Composite Structures* (IF: 2.231), 108: 456–471, 2014
  DOI: http://dx.doi.org/10.1016/j.compstruct.2013.09.052.
  http://www.sciencedirect.com/science/article/pii/S0263822313004996